MAGNETO-TRANSPORT STUDIES ON THE SINGLE CRYSTALS OF $TaAs_2$ AND $NbAs_2$ SEMIMETALS

By

HARIMOHAN V

PHYS 02 2014 04 010

Indira Gandhi Centre for Atomic Research, Kalpakkam

A thesis submitted to the

Board of Studies in Physical Sciences

In partial fulfillment of requirements

for the Degree of

DOCTOR OF PHILOSOPHY

of

HOMI BHABHA NATIONAL INSTITUTE

November, 2020

Homi Bhabha National Institute

Recommendations of the Viva Voce Committee

As members of the Viva Voce Committee, we certify that we have read the dissertation prepared by Mr. **Harimohan V** entitled "**Magneto-transport Studies on the Single Crystals of $TaAs_2$ and $NbAs_2$ Semimetals**" and recommend that it may be accepted as fulfilling the thesis requirement for the award of Degree of Doctor of Philosophy.

G. Amarendra — April 13, 2021

Chairman: **Dr. G. Amarendra** Date:

C S Sundar — 13/04/2021

Guide/ Convener: **Dr. C. S. Sundar** Date:

E.V. Sampathkumaran — 13/04/2021

External Examiner: **Dr. E. V. Sampathkumaran** Date:

Awadhesh Mani — 13/04/2021

Member 1: **Dr. Awadhesh Mani** Date:

R Rajaraman — 13/04/2021

Member 2: **Dr. R. Rajaraman** Date:

by VC

Technology Advisor: **Dr. Shilpam Sharma** Date:

Final approval and acceptance of this thesis is contingent upon the candidate's submission of the final copies of the thesis to HBNI.

I hereby certify that, I have read this thesis prepared under my direction and recommend that it may be accepted as fulfilling the thesis requirement.

Date: 13/04/2021

Place: Kalpakkam

C S Sundar

Dr. C. S. Sundar

(Guide)

(This page is to be included only for final submission after successful completion of viva voce).

Homi Bhabha National Institute

Recommendations of the Viva Voce Committee

As members of the Viva Voce Committee, we certify that we have read the dissertation prepared by Mr. **Harimohan V** entitled "**Magneto-transport Studies on the Single Crystals of $TaAs_2$ and $NbAs_2$ Semimetals**" and recommend that it may be accepted as fulfilling the thesis requirement for the award of Degree of Doctor of Philosophy.

G. Amarendra — April 13, 2021

Chairman: **Dr. G. Amarendra** Date:

C S Sundar — 13/04/2021

Guide/ Convener: **Dr. C. S. Sundar** Date:

E.V. Sampathkumaran — 13/04/2021

External Examiner: **Dr. E. V. Sampathkumaran** Date:

Awadhesh Mani — 13/04/2021

Member 1: **Dr. Awadhesh Mani** Date:

R Rajaraman — 13/04/2021

Member 2: **Dr. R. Rajaraman** Date:

by VC

Technology Advisor: **Dr. Shilpam Sharma** Date:

Final approval and acceptance of this thesis is contingent upon the candidate's submission of the final copies of the thesis to HBNI.

I hereby certify that, I have read this thesis prepared under my direction and recommend that it may be accepted as fulfilling the thesis requirement.

Date: 13/04/2021

Place: Kalpakkam

C S Sundar

Dr. C. S. Sundar

(Guide)

(This page is to be included only for final submission after successful completion of viva voce).

Statement by Author

This dissertation has been submitted in partial fulfillment of requirements for an advanced degree at Homi Bhabha National Institute (HBNI) and is deposited in the Library to be made available to borrowers under rules of the HBNI.

Brief quotations from this dissertation are allowable without special permission, provided that accurate acknowledgement of source is made. Requests for permission for extended quotation from or reproduction of this manuscript in whole or in part may be granted by the Competent Authority of HBNI when in his or her judgment the proposed use of the material is in the interests of scholarship. In all other instances, however, permission must be obtained from the author.

Harimohan V

Declaration

I, hereby declare that the investigation presented in the thesis has been carried out by me. The work is original and has not been submitted earlier as a whole or in part for a degree / diploma at this or any other Institution / University.

Harimohan V

List of Publications

Journal

1. "Magneto-resistance in pristine and irradiated $TaAs_2$", V. Harimohan, A. Bharathi, R. Rajaraman, P. Magudapathy, C. David, C.S. Sundar, *AIP Advances*, **2019**, *9*, 045020.
2. "Validity of Kohler's rule for the magneto-resistance in pristine and irradiated $NbAs_2$", V. Harimohan, A. Bharathi, P.D. Babu, R. Rajaraman, P. Magudapathy, C. David, C.S. Sundar, *Solid State Communications*, **2020**, *305*, 113734.

Conferences

1. "A magneto-resistance and magnetisation study of $TaAs_2$ semimetal",V. Harimohan, A. Bharathi, R. Rajaraman, C.S. Sundar, *AIP Conference Proceedings*, **2018**, *1942*, 110019. Oral & Poster presentations at *'DAE Solid State Physics Symposium* 2017' held at BARC, Mumbai.
2. "Magneto-resistance study on single crystals of $NbAs_2$ semimetal", V. Harimohan, A. Bharathi, P.D. Babu, R. Rajaraman, C.S. Sundar, *AIP Conference Proceedings*, **2019**, *2115*, 030430. Oral & Poster presentations at '*DAE Solid State Physics Symposium* 2018' held at GJUST, Hisar, Haryana.
3. "A clue to the large magneto-resistance in the $NbAs_2$ semimetal", V. Harimohan, A. Bharathi, P.D. Babu, R. Rajaraman, C.S. Sundar, *AIP Conference Proceedings*, **2020**, *2265*, 030428. Oral & Poster presentations at '*DAE Solid State Physics Symposium* 2019' held at IIT Jodhpur, Rajasthan. Selected for 'Best Poster' award.

Conference Presentation

1. "Irradiation effects on the magneto-transport of $TaAs_2$ single crystals". V. Harimohan, A. Bharathi, R. Rajaraman, P. Magudapathy, C. David, C. S. Sundar. Poster presentation at the '*HBNI Research Scholars Meet* 2018', IGCAR, Kalpakkam.

Others (Not part of the thesis)

1. "Structural and electrical characterization of ion beam sputter deposited Mo/Cu films". V. Harimohan, Mukul Gupta, Shilpam Sharma, B. Sundaravel, P. Magudapathy, Awadhesh Mani, and C. S. Sundar. *AIP Conference Proceedings,* **2017**, *1832*, 110022. Poster presentation at '*DAE Solid State Physics Symposium* 2016' held at KIIT University, Bhubaneswar, Odisha.

Harimohan V

Dedicated To

The ultimate Taxpayer

For the credit, recognition, comfort, sense of identity/ego,…. all we earn or possess in the name of science come from the exchequer that also includes the tax rendered by those who are not able to have two proper meals a day. Let this thought be inscribed on our discretion for all time.

Acknowledgements

This thesis is the culmination of the dedication, cooperation, and effort received from a handful of people in the last few years, along with the encouragement and support of a large number of persons over a long time. As I recollect, let me express my gratefulness and appreciation to them in the following lines.

With deep sense of happiness and gratitude, I wholeheartedly thank my thesis advisors Dr. C. S. Sundar and Dr. A. Bharathi for their teaching, guidance, supervision, mentoring, and above all, for the commitment and dedication shown for the completion of my doctoral work. My learning and thesis have greatly benefitted from the scholarship of Dr. C. S. Sundar. His magnificent obsessions for perfection and high standards on research culture & practice have always helped in improving and refining my understanding and perspective on the subject, and in writing & presenting better technical papers. I am immensely grateful to him for his earnest efforts in patiently reading and correcting my manuscripts and thesis drafts, in spite of his personal time constraints and multiple commitments. I sincerely thank Dr. A. Bharathi for introducing me to this exciting area of research, and for the encouragement and the help that I received to grow as a young researcher. It is her excellent experimental acumen, expertise on the subject and continued support that has helped me to pursue this work. She has placed faith, instilled confidence and trained me to do low temperature experiments. It is her active involvement and guidance that has helped us to shape the methodology of my doctoral research and the analysis of the data therein. I have great admiration for her sustained enthusiasm to learn and the determination to take up research in the frontier topics of the field.

Let me express my wholehearted gratitude to Dr. G. Amarendra for the motivation and continuous encouragement given by offering his help and support through extending the facilities in his various capacities, as the Directors of Materials Science Group &

UGC-DAE CSR Kalpakkam node, and as the Chairman of my doctoral committee. His succinct comments and questions during review meetings have helped a lot to change the trajectory of my thesis to better directions. I always admire his presentation styles, inter-personal interaction & time management skills and excellent administrative capabilities.

I am very much indebted to Dr. R. Rajaraman, Academic Dean & my doctoral committee member, for teaching Raman spectroscopy experiments, data analysis & understanding, for the supervision, guidance, valuable suggestions for presentations, and continuous encouragement throughout my PhD. He has been amicable, supportive and approachable for various help & directions on multiple occasions.

I sincerely thank my doctoral committee members Dr. Awadhesh Mani and Dr. Shilpam Sharma for their suggestions, questions during review meetings and encouragement during my work.

I am highly indebted and thankful to the Consortium of Scientific Research facilities, since a large share of the experiments, in this thesis and outside, during my PhD tenure have been done at UGC-DAE centers at Kalpakkam, Mumbai and Indore. It is a great pleasure to express my deep gratefulness and appreciation to Dr. P. D. Babu, UGC-DAE CSR Mumbai, for the timely & cordial help, and for the active collaboration during the magneto-transport experiments, especially in the $NbAs_2$ system. He has shown immense interest, and put dedicated efforts to complete the scheduled experiments whenever we approached him. I extend my gratitude to Dr. V. Siriguri, Director CSR Mumbai, for the help in ensuring accommodation at Anushakthinagar during the experiments. I thank Dr. S. D. Kaushik, Dr. Sudeep Mukherjee, Shri. B. R. Mendole, Shri. M. Venugopal and Ms. Swati Pandey for various help and warm interactions at Mumbai centre. I specially thank the help and cherish the friendship of Shri. Srikanta Goswami.

I am happy to extend my sincere thanks and appreciation to Shri. P. Magudapathy and Dr. C. David for their earnest efforts in ion irradiation experiments. They have been very much supportive and helpful during the investigations using accelerator facilities and provided valuable inputs while preparing manuscripts & thesis.

It is my pleasure to thank Dr. D. Sornadurai, Dr. S. Ganesamoorthy, Dr. R. M. Sarguna and Shri. Raj for the x-ray diffraction experiments, especially the Laue measurements on single crystals. I gratefully remember the useful discussions with Dr. D. Sornadurai on Laue data analysis.

I sincerely thank the Centre Director Dr. A. K. Bhaduri for providing all facilities to carry out my doctoral work in this prestigious DAE centre, and for the privileges I have enjoyed as a research scholar of Indira Gandhi Centre for Atomic Research. His distinguished leadership has facilitated for the easy reach to access various academic locations at Kalpakkam. I also extend my gratefulness to former Directors Dr. S. A. V. Satyamurthy and Dr. P. R. Vasudeva Rao for their support.

For the generous and timely financial support during the PhD years, I am very much grateful to the Department of Atomic Energy. I sincerely thank the DAE, HBNI, IGCAR & GSO management, administration and staff for providing accommodation, various services & amenities at campus and in the serene, seashore township, which ensured a smooth and happy stay at Kalpakkam. The surrounding greenery has always been a solace in the scorching May, and that also provided a shimmering background during the mild chill of December. I specially thank the service of the Central Cafeteria and its staff.

I am grateful to the former Group Director Shri. M. P. Janawadker for pursuing my research in Materials Science Group, and also to the present Director Dr. Shaju K

Albert for allowing to continue the studies in MSG. It has always been a pleasure to attend their talks and addresses, often brief, but filled with a distinctive originality.

I am particularly happy to thank Dr. N. V. Chandra Shekar, Former Dean, for his timely interventions, continuous monitoring and for offering valuable suggestions for the progress of my PhD.

In the initial years, before settling on this thesis investigation, I was working on Mo-Cu thin films. I am very happy to thank Dr. Mukul Gupta, UGC-DAE CSR Indore, for his dedicated help in the preparation of Mo-Cu bilayers, and for the cordial interactions. I am grateful to Dr. V. Ganesan, Former Director, CSR Indore, for providing generous hospitality at CSR guest house by accepting our short notice requests for experiments. I am delighted to thank Shri. Layanta Behera and Shri. Anil Gome for their help in thin film preparations and x-ray reflectivity measurements. I wish to express great appreciation and thanks to CSR research scholars Atul Tiwari, Jagrati Dwivedi, Prabhat Kumar and Nidhi Pandey. They have offered valuable help, and extended cooperation without hesitation during the ion beam sputtering deposition and in the XRR analysis.

It is my pleasure to thank Dr. B. Sundaravel and Dr. K. Saravanan for the Rutherford backscattering spectroscopy studies on the Mo-Cu system. I remember with gratitude the discussions with Dr. B. Sundaravel on the RBS analysis and his kind help. I must specially thank the willingness, and the continuous help offered by Shri. P. Magudapathy whenever we approached him for large number of x-ray diffraction measurements on thin films. I express my sincere appreciation and respect for his distinguished service.

I have extreme pleasure to thank my senior colleague in lab, Dr. K. Vinod for his help and continuous support during my PhD. He has shown immense patience in explaining and teaching the low temperature systems, particularly liquid helium and

nitrogen based. I have been fortunate to associate with him, and admire his simplicity and the willingness to share knowledge.

I sincerely thank my senior colleague Dr. A. Edward Prabu for his help and useful discussions on the magneto-resistance measurements. I thank the senior members Dr. J. Janaki, Smt. M. Premila, Dr. T. Geetha Kumary, Dr. A. T. Sathyanarayana and Dr. Shamima H for their cordial interactions.

I have been really fortunate to be in the company of some wonderful research scholars over these years in low temperature lab. It gives me great joy to thank my seniors Dr. T. R. Devidas and Dr. N. Radhikesh Raveendran for their constant and friendly support. Dr. Devidas has shown extreme patience in teaching the basics of low temperature techniques, particularly to make electrical contacts on samples and doing resistivity measurements during the initial years, which greatly helped me in the later period. Dr. Radhikesh always extended his warm companionship & help, and it has been a delightful experience to have a conversation with him, which I enjoyed and cherish. I have great pleasure to thank my fellow research scholar, Mrs. Gayathri V for the pleasant interactions and help. It is always a joy to cherish the affectionate interactions of my beloved junior, Mr. Paban Kumar Patra.

With the help of Dr. P. Jegadeesan, the task of editing and formatting the thesis became less cumbersome, and I thank him for providing a thesis writing template. I once again extend my thanks to Dr. Vinod and Mrs. Gayathri for patiently reading the draft chapters and offering their valuable comments.

I am happy to thank MSG members, particularly, Dr. Kishore K Madapu, Dr. D. Karthikeyan, Dr. K. Yadagiri, Dr. C. Lakshmanan, Dr. Padmalochan Panda, Dr. Vairavel M, Shri. Arun K. C, Shri. Ravikumar Yadav and Mrs. M. Sinduja for their gracious help at various occasions like Raman measurements, heat treatment experiments,

single crystal cutting / polishing, discussions on RBS analysis, for providing / sharing materials at urgent requirements or for giving valuable directions.

I have great pleasure to thank Dr. Renjith Ramachandran for his affectionate interactions. It is a unique experience to reunite with classmates and old friends in a new place after a gap. It has been a feeling of great happiness that I could continue the friendship with Shri. Dheeraj S and Dr. Irshad K. A at Kalpakkam.

During the course of PhD, I could meet a large number of research scholars, and shared moments of joy and friendship at JRF Enclave and in campus; Dr. A. K. Sivadasan, Dr. Nidhin T. S, Anil Kumar Behera, Pradosh Kumar Sahoo, Sithara Vinod, Bijay Kumar Das, Prince Joseph, Gopinath Sahoo, Sarvajith M, Suman Sourav, Tanmay Mondal, Anoop K Unni, Manu Harilal, Parvathy N. S, Paulson Varghese, Sachin Tom, Mohasin S. N, Arjun A. R ….and many others. I cherish our interactions, however short or transient: chit-chats over a cup of tea or during lunch in cafeteria; in labs; when meeting in the corridors of MSL; while traveling to lab and back to enclave…….

Dr. Uttiyo Arnab Saha has been my esteemed companion and best friend at Kalpakkam. With enormous joy, I thank Arnab for his fellowship, concern and care for me.

…...It has been a long walk. ....I thank you all for helping me directly or indirectly.

When making a small step in physics learning, it will be ungrateful from my part, if I don't acknowledge my respected teachers of St. Berchmans College, Changanacherry. It is their blessings, devotion, philosophy, convictions, class and excellence that always motivate me to move ahead. I express my sincere gratitude to Prof. Baby Joseph, Dr. K. E. Abraham, Dr. Stephen Mathews, Prof. C. A. Xavier, Dr. George C Chennattucherry, Prof. Johny Joseph, Prof. V. Prabha, Dr. Jose Mathew, Dr. Issac Paul, Dr. Jacob Mathew M, Dr. Shajo Sebastian, Dr. K. C. George, Dr. P. J. Kurian, Dr. K. V.

Saban, Dr. Siby Kurian, Prof. Antony Mathew, Dr. P. C. Thomas, Dr. K. C. Philip, Dr. Antony Mathews, Dr. Tomlal Jose E, Dr. Shine C Mathew, Dr. Joji Madappattu, Prof. Siby Cherian, Prof. Ajith Kumar M, Dr. Mathew Jose K, Prof. George Thomas, Prof. P. J. Thomas, Dr. Raju Sebastian, Shri. Ajai Jose, Dr. Gijo Jose, Shri. Justin John, Shri. Sijo Sebastian .... and to all other teachers. Without a mention of my beloved classmates, this paragraph will be incomplete.

I am indebted to Shri. K. J. Yohannan, Fr. Koshy Abraham, Smt. Valsa Varghese, Smt. Annie Philip, Smt. Annie Valsam, Shri. Philip Varghese, Shri. Mathew Cherian, Smt. Jessan Varghese, Smt. Usha Susan Alex, Shri. Rosh V Kuriakose ..... and to other teachers, as the roots of my science education are grounded at Mar Gregorious Memorial Higher Secondary School, Thiruvalla.

I am always indebted to the constant support, encouragement, care and love from my beloved parents, Shri. P. S. Viswanadha Varrier and Smt. L. Padmadevi, and brother Mr. Sreemohan P. V. I must specially thank for the unconditional support of my mother at all moments of my education that enable me to pursue this degree.

When reflect back, I realize that the prayers of my family, well-wishers and the teachers of Lisiux Carmel primary school, Ithithanam, Changanacherry have been the strength to reach this point.

I bow before time and the almighty God for the kindness on me.

Harimohan V

Table of Contents

List of Figures

List of Tables

Chapter 6

Summary and Conclusions

When the investigation on the magneto-transport in the di-arsenides was initiated as a part of the thesis work, there was a considerable confusion in the literature on whether this then new family of materials belongs to the class of Weyl semimetals. There were experiments in the literature that pointed to negative LMR, a tell-tale signature of Weyl semimetal, as also experiments that showed only positive LMR. Further, the characteristic upturn in resistivity with the lowering of temperature under magnetic field has been attributed to a metal - insulator transition induced by magnetic field, or alternatively explained as arising due to the effect of magnetic field and temperature on the transport of carriers in the semi-metallic system characterized with high mobility and low density.

In this thesis, two related systems $TaAs_2$ and $NbAs_2$ were investigated, as also these systems in which disorder was introduced through low energy ion irradiation and heat treatment with a view to alter the carrier density and mobility. The principal findings are conveyed through figures in the following:

Figure 6.1a shows the variation of resistance with temperature under magnetic field in $TaAs_2$. The metallic behaviour at zero field shows an upturn with the application of magnetic field. The upturn temperature indicated by the stars (See Figure 6.1b) could not be fitted to a critical behaviour $T^* \sim (B - B_C)^n$, as would be expected for a metal - insulator transition driven by a magnetic field. In fact, in a few cases (See Figure 3.15 and Figure 4.10), the variation of T^* with B is almost linear that certainly cannot be fitted to a critical behaviour. However, it is seen that the magneto-resistance curves seen in Figure 6.1a can be scaled according to the Kohler's rule, $MR = \alpha \left(\frac{B}{\rho_0}\right)^m$, with $m \sim 2$, as indicated in Figure 6.1c. As discussed in Section 3.4, the Kohler rule also provides an

explanation for the upturn behaviour under magnetic field as arising due to competition between the opposing temperature behaviour of zero field resistivity, $\rho\,(T)$ and the increase in resistance due to magnetic field. This results in a broad minimum at T^* in the temperature dependence of the total resistivity, as shown in Figure 6.1d. Further, for $m = 2$, the value of minimum resistivity at T^* is $2\rho_{0,}$ and these, indicated as red dots, are in good agreement with data in Figure 6.1a. The variation of resistivity as a function of magnetic field at various temperatures for $TaAs_2$ is shown in Figure 6.1e. The near parabolic and non-saturating variation of resistivity at various temperatures is seen to scale according to Kohler rule as shown in Figure 6.1f. It is seen that while a single exponent is seen in the Kohler's plot obtained from isothermal measurements, there is a change of exponent in the Kohler scaling plot obtained from resistivity measurements as a function of temperature at various fields (See Figure 6.1c). This is linked to the temperature dependence of mobility, as also validated from the results shown in Figure 6.3. The results as seen in Figure 6.1 for pristine $TaAs_2$ are also seen for irradiated $TaAs_2$ and $NbAs_2$ systems.

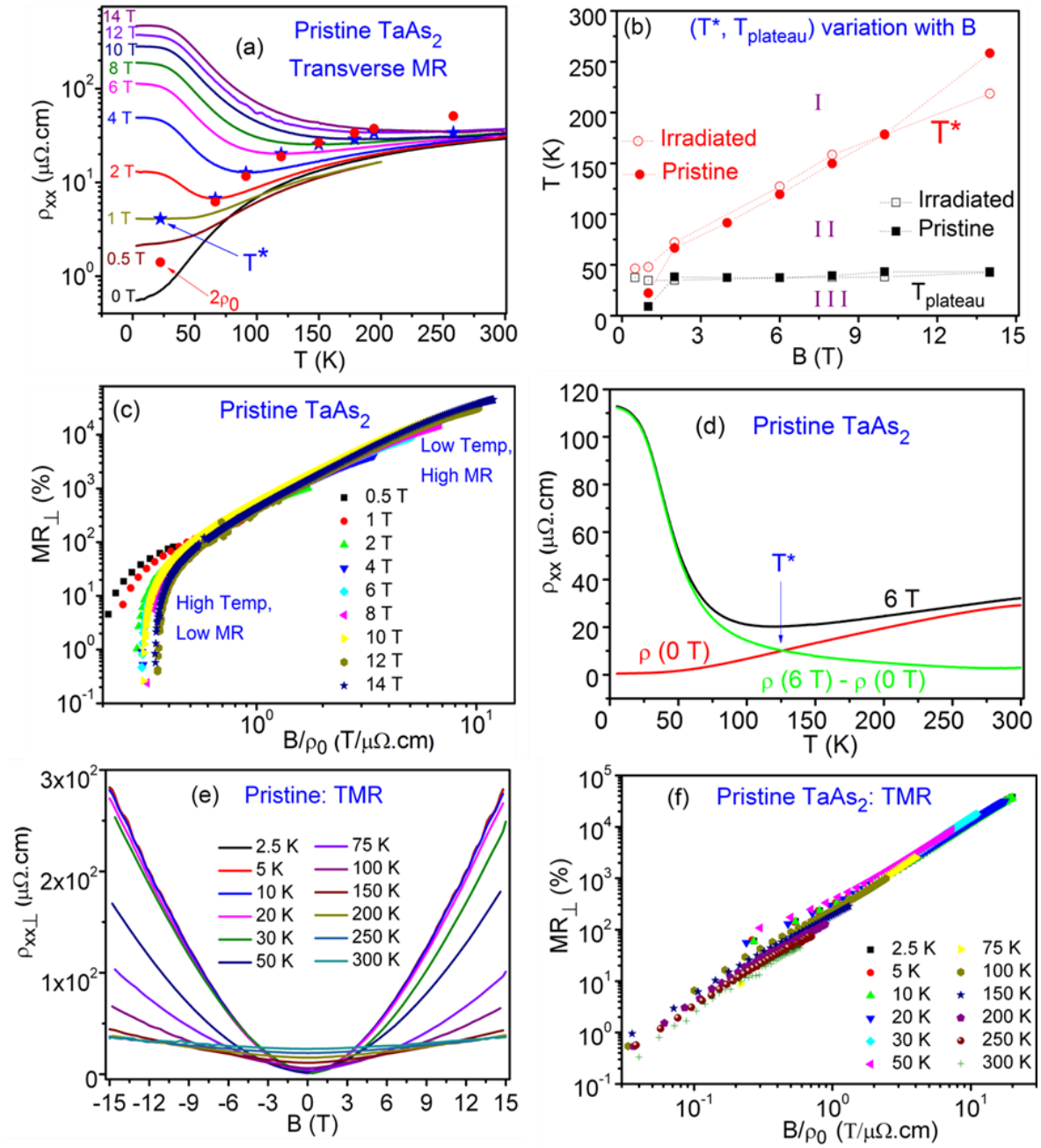

Figure 6.1 ***(a)*** *Temperature dependence of resistance under magnetic field in $TaAs_2$.* ***(b)*** *Variation of the resistivity minima temperature T^* and the plateau temperature $T_{plateau}$ as a function of magnetic field.* ***(c)*** *Kohler scaling of the magneto-resistance data shown in (a).* ***(d)*** *The origin of minima in the resistivity as a competition between $\rho_0(T)$ and the resistivity due to magnetic field.* ***(e)*** *Resistivity versus magnetic field at various temperatures for $TaAs_2$, and its excellent scaling according to Kohler rule is shown in* ***(f)***.

In the present study, the absence of negative longitudinal magneto-resistance in $TaAs_2$ and $NbAs_2$ has been established through angle dependent MR measurements and

careful LMR experiments. The results are summarized in Figure 6.2. The longitudinal MR is also seen to scale according to the Kohler's rule.

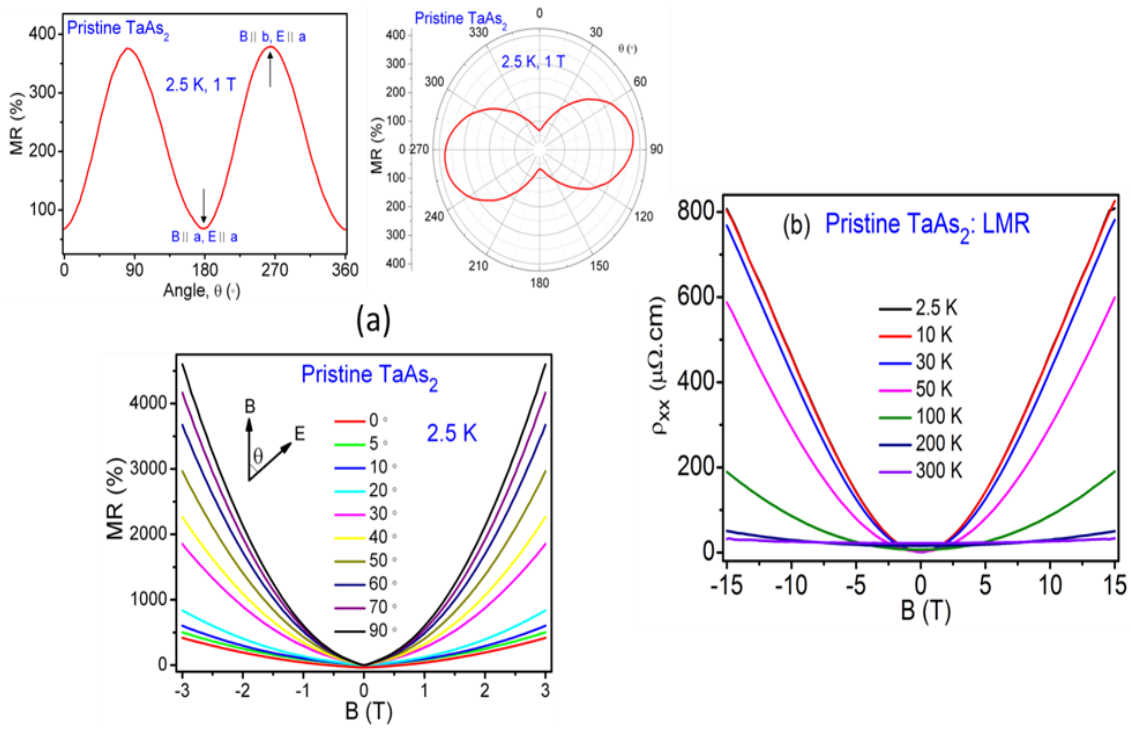

Figure 6.2 ***(a)*** *The variation of MR with magnetic field for various angles between the magnetic and electric fields for $TaAs_2$ is shown. It is seen that MR is positive even for longitudinal configuration, albeit smaller than for transverse configuration.* ***(b)*** *The parabolic variation of resistivity with magnetic field for $TaAs_2$, in LMR configuration.*

The large magneto-resistance seen in $TaAs_2$ $\sim 10^4$ % at low temperatures and magnetic fields ~14 T arises due to near compensation of charge carriers within the framework of the two-band model. For the semimetals, the MR varies as μH^2, and the results for various semimetals from the literature [12] are shown in Figure 6.3a. In this plot, we have now included (See the red dots in Figure 6.3a) the results from our MR studies on pristine $TaAs_2$ and $NbAs_2$, along with the mobility as obtained from Hall measurements. While, we do not have large variation in mobility with irradiation, as it occurs naturally across the various semimetals, the present data falls in place lends credence to the correlation between MR and mobility. Further, the similarity of the

temperature dependence of MR with that of mobility, as shown in Figure 6.3b, shows another facet of the correlation between large magneto-resistance and mobility.

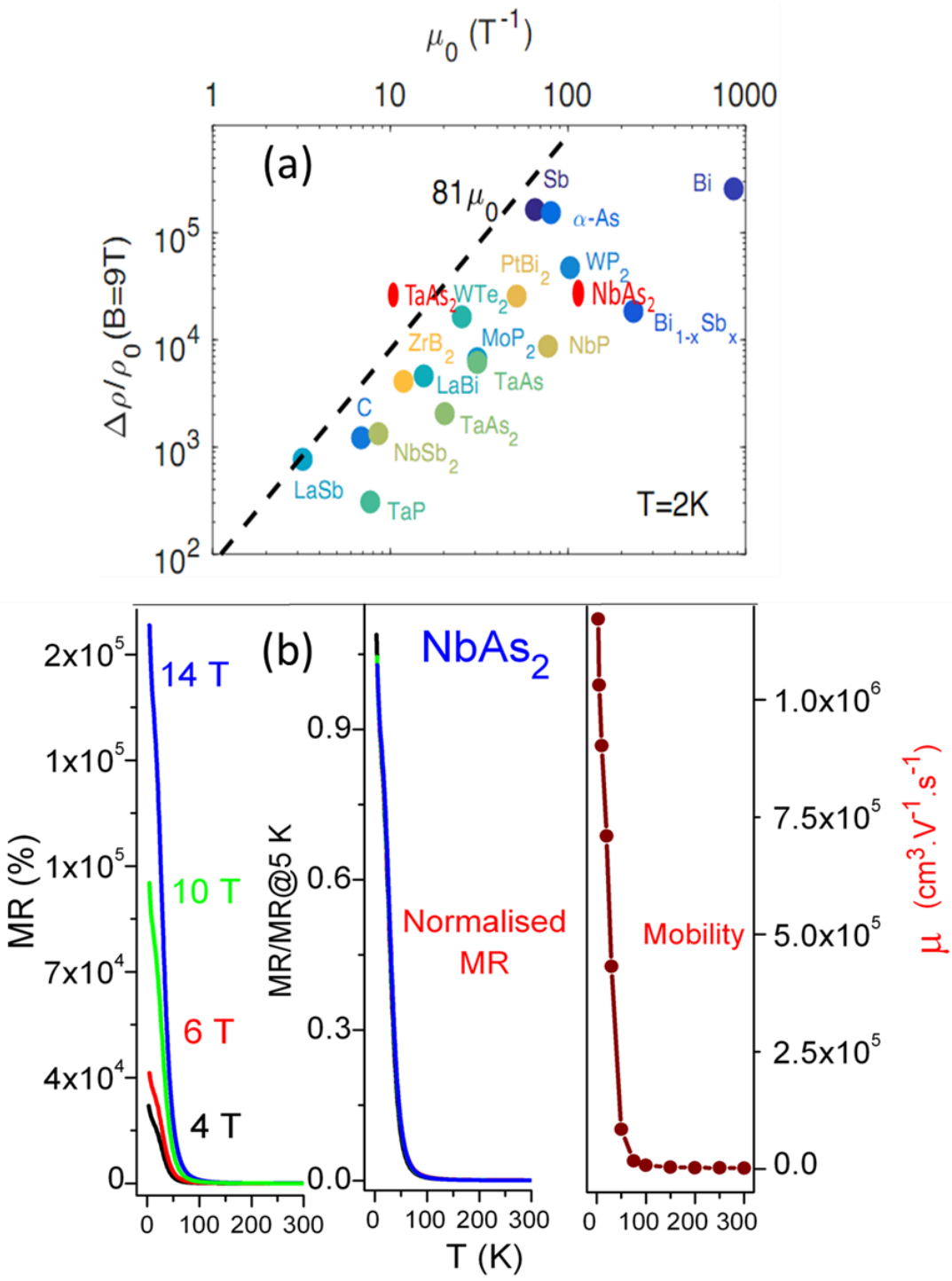

Figure 6.3 ***(a)*** *The variation of MR with mobility from Fauque et al [12]. The data from the present investigations (indicated in red) are in concurrence with the above correlation.* ***(b)*** *The similarity of the temperature dependence of normalized MR with mobility from Hall measurements in $NbAs_2$.*

Finally, the high quality of crystals with large mobility resulted in high quality de Haas - van Alphen oscillations as shown in Figure 6.4a for $TaAs_2$. The decay of these oscillations with magnetic field has been analyzed using the Lifshitz - Kosevich formula to extract important transport parameters in pristine and irradiated samples. With an analysis of these oscillations through the construction of the Landau Level - fan diagram, it is seen that $TaAs_2$ has a trivial Berry phase that indicates the non-topological nature of di-pnictides.

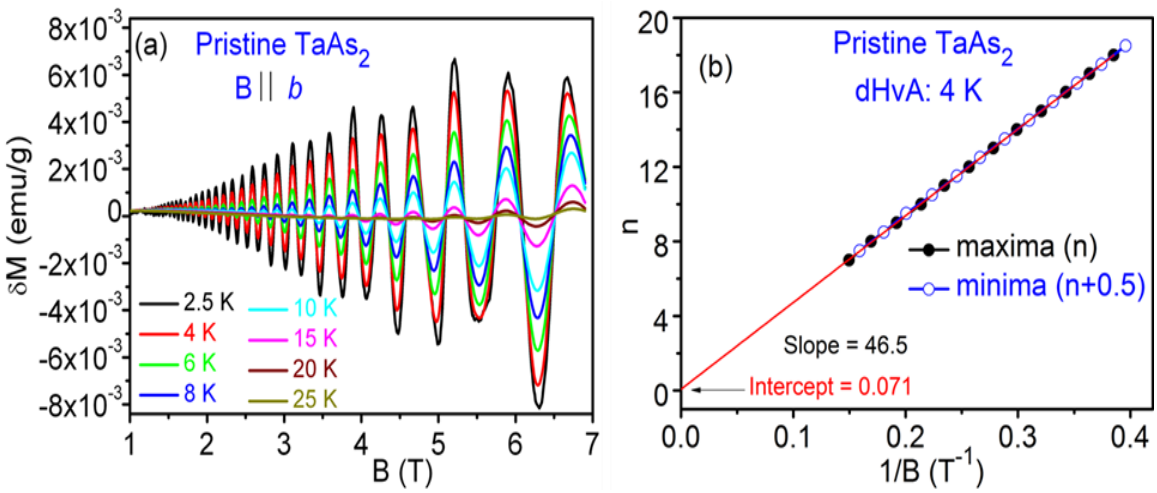

Figure 6.4 ***(a)*** *de Haas - van Alphen oscillations in $TaAs_2$ after the subtraction of the diamagnetic background.* ***(b)*** *Landau level-fan diagram constructed from the data shown in (a). The slope is consistent with that obtained from the fast Fourier transform of dHvA oscillations, and the intercept points to a trivial Berry phase.*

To conclude, through experiments reported in this thesis, we have shown that while the di-pnictides show several interesting magneto-resistance properties characteristic of a semimetal, it does not belong to the family of Weyl semimetals.

Abstract

Transport measurements in semimetals has emerged as a major field of research in condensed matter physics / material science in the last decade following the discovery of Weyl and Dirac semimetals. Similar to many other semimetals of recent focus, the low temperature resistivity in transition di-pnictides $TaAs_2$ and $NbAs_2$ shows large increase $\sim 10^5$ % under applied magnetic fields, leading to non-saturating magneto-resistance, and also features the characteristic resistivity minima and upturns in its temperature variation. In this thesis work, we have approached the magneto-resistance property in $TaAs_2$ and $NbAs_2$ single crystals of high purity, having micron to millimeter sizes that are grown via chemical vapour transport route, and characterized by Raman spectroscopy, from the rationale of Kohler's rule, which has its roots in the landscape of semi-classical metal physics. This helped us to establish the veracity and the universality of Kohler's scaling framework in dealing with the magneto-transport of semimetals for a wide range of temperatures ~300 K to 2.5 K, and magnetic fields up to ± 15 T. In doing so, we have excluded other propositions which are suggested in literature, viz., the existence of a critical field arising out of metal-insulator transition driven by magnetic fields, or a temperature / field induced Lifshitz transition etc., as role playing agents in the transport behaviour of di-pnictides. Further, combined with the Hall resistance measurements, we made a systematic investigation in uncovering the underlying relationship between the extremely large magneto-resistance and the ultra-high carrier mobility $\sim 10^6\ cm^2.V^{-1}.s^{-1}$ in these semimetals. Although this is a recurring theme present in literature, it has not been explored before in detail, and now we also show it as a reflection of the validity of Kohler's rule. This has been undertaken by extending the studies to samples of altered carrier density and mobility, which are created after modifying the as-grown crystals through ion irradiation and heat treatments. By supplementing these

magneto-resistance measurements with angle dependent studies, we show here that the di-arsenides does not exhibit negative longitudinal MR, a necessary requirement to be satisfied by archetypical Weyl semimetals. Quantum oscillation measurements are another frontier field where vigorous investigations have been pursuing to study transport properties in semimetals. In this thesis, using the spectacular de Haas - van Alphen oscillation measurements, which is a relatively less attempted area in di-pnictides, and by adopting the Lifshitz - Kosevich formalism for the oscillation decay, we also present the extracted transport parameters that can provide better insights on the carrier transport and magneto-response in $TaAs_2$ and $NbAs_2$. Also, with the help of a Landau level-fan diagram, we suggest that the energy bands in these systems are topologically trivial. We believe that the investigations and results in this work are of high value and relevance in the electron transport characterization in materials, in particular for semimetals.

Chapter 1

INTRODUCTION: Magneto-resistance in Semimetals

In this chapter, we first provide an overview of magneto-resistance in metals and semimetals, and then present an introduction to the recent interest in the novel topological semimetals, in particular their distinctive transport properties under magnetic fields. While the mono-pnictides have been established to be Weyl semimetals, the results in the new di-pnictide family of semimetals have been contradictory. We present a survey of these results drawn from the literature to set the stage for the contents of the thesis.

1.1. Magneto-resistance in Metals

The investigation of dynamics of electrons under the application of magnetic field is a rich field in condensed matter physics, that has spawned several areas of research, that include the elucidation of Fermi surface in metals, Landau quantization of energy levels leading to quantum oscillations in resistivity and magnetization, to the exotic phenomena such as fractional quantum Hall effect (FQHE) and the investigation of magneto-transport in novel materials [1, 2].

It is well known [3] that under the combined application of electric and magnetic fields, the conductivity of a metal becomes a tensor, with the component along the electric field varying with the magnetic field (H), and a transverse component – the Hall conductivity. An analysis of the dynamics of free electron described by the Langevin equation shows that the resistivity component ρ_{xx} is independent of the applied magnetic field, that is metals within the free electron approximation have no magneto-resistance (MR). However, metals do show positive magneto-resistance, that is $\rho_H > \rho_0$. At the simplest level, it requires the presence of two types of carriers such as the electrons and holes or electrons of two different masses, such as the 's' and 'd' electrons. The two-band model is described subsequently in Section 1.3.

In some metallic systems, the resistivity gets saturated as H increases in all crystalline directions, whereas in some systems it saturates in some directions, but not along others. This is related to the detailed topology of the Fermi surface. It is known [4, 5] that for closed orbits MR saturates with the increase of field, whereas for open orbits it increases as H^2 without saturation. This aspect is used in the determination of Fermi surface of metals through experiments on the study of high field MR in single crystals [4].

1.2. Magneto-resistance in Semimetals

The semi-metallic systems like Graphite, Bi and Sb display huge magneto-resistance, orders of magnitude higher than in metals. In contrast to metals, the semimetals are characterized by lower carrier density, lower cyclotron mass and higher mobility of carriers. This leads to very interesting transport characteristics with the variation of the magnetic field and temperature. We note that the relevant magnetic field parameter is the cyclotron frequency: $\omega_c = \frac{eB}{m^*}$, where e is the charge of the electron, B the magnetic induction and m^* the (cyclotron) effective mass. This together with the scattering time τ and temperature T helps to delineate the various magneto-transport regimes: (1) $\omega_c\tau \ll 1$, the low field limit, (2) $\omega_c\tau \approx 1$, the intermediate field limit, (3) $\omega_c\tau \gg 1$, the high field limit, (4) $\hbar\omega_c > k_BT$, the quantum oscillation regime and (5) $\hbar\omega_c > E_F$, the quantum limit, in which E_F corresponds to the Fermi level [6].

The low carrier density in semimetals implies that a moderately high field of 10 T is enough to drive the system to quantum limit. Further, the low effective mass leads to higher cyclotron frequency which in turn leads to quantum oscillations being observed at relatively high temperatures. This together with their high purity facilitates the observation of well-resolved oscillation patterns, in that the semimetals such as bismuth and graphite have been popular materials for studies of quantum magnetic-field effects [7].

Another interesting property is the variation of resistivity with temperature at various magnetic fields. Figure 1.1 shows the results in graphite [8]. The metallic behaviour seen at zero field shows an upturn with the lowering of temperature, as the magnetic field is applied. With the increase of field, on lowering the temperature, the resistance increases, as it does in an insulator but then saturates towards field-dependent constant values at the lowest temperatures.

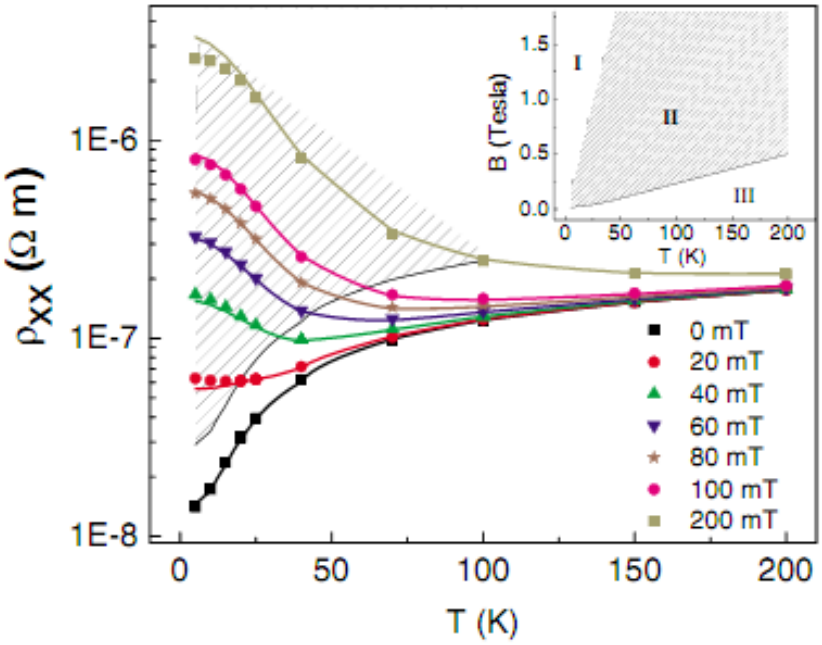

Figure 1.1 The temperature dependence of the ab-plane resistivity ρ_{xx} for graphite crystal along the c-axis magnetic fields indicated in the legend, showing the metal to insulator type behaviour. Adapted from Du et al [8]. The shadowed area in the inset and its mapping onto the data in the main panel indicates the interval defined by the condition $\frac{\hbar}{\tau} \leq \hbar\omega_c \leq k_B T$ (See text).

This has been attributed [9] to a metal – insulator transition (MIT) driven by the magnetic field. The magnetic field opens up an excitonic gap in the linear spectrum of the Coulomb interacting quasi-particles in graphite [10]. However, the upturn behaviour as seen in Figure 1.1 for graphite is also seen in other semimetals such as Bi that does not have a linear dispersion. This has prompted an alternate explanation [8] for the upturn behaviour that is based on the generic properties of semimetals, namely, the low carrier density, high purity, and an equal number of electrons and holes (compensation), rather

than the almost two-dimensional (2D) nature of transport and a Dirac-like spectrum in graphite.

Through a combined analysis of the temperature and field-dependent longitudinal resistivity $\rho_{xx}(T,B)$ (magneto-resistance) and transverse resistivity $\rho_{xy}(T,B)$ (Hall effect), it is shown that there exists a wide interval of temperatures and magnetic fields (shaded region in the inset of Figure 1.1), defined by the condition $\frac{\hbar}{\tau} \leq \hbar\omega_c \leq k_B T$. In the middle region, the effect of magnetic field on resistivity is large, viz., the MR is large. The large MR is also due to compensation between charge carriers. The inequality above defines the ordering of the three characteristic energy scales, viz., the width of the energy levels $\frac{\hbar}{\tau}$, where τ is the electron - phonon scattering time, the cyclotron energy $\hbar\omega_c$ and the thermal energy $k_B T$, and for the semimetals characterized by low carrier density and high mobility, there exists a wide range where the magnetic field has a large influence on the resistivity.

As we shall see, features similar to that shown in Figure 1.1 for graphite is also seen in the novel topological semimetals [11], and discussions based on MIT induced by magnetic field or as arising due to the compensation of charge carriers have been put forward. One of the aims in this thesis is to resolve between these alternative viewpoints in the magneto-transport studies on di-pnictides.

In addition to experiments where the resistivity is measured as a function of temperature at constant fields, experiments are also carried out with varying field, at constant temperatures. The variation of MR with H provides insight into the dynamics of electrons. As indicated earlier, in metals in some directions, MR increases and saturates, whereas in other directions, it does not saturate and increases as H^2. In the case of semimetals, the MR increases quadratically with applied transverse magnetic field, and does not saturate up to very high fields. This is shown in Figure 1.2, for the semimetals

Bi and Sb [12]. This un-saturating behaviour is responsible for the large MR observed in the semi-metallic systems, and finds justification within the two-band model, discussed below.

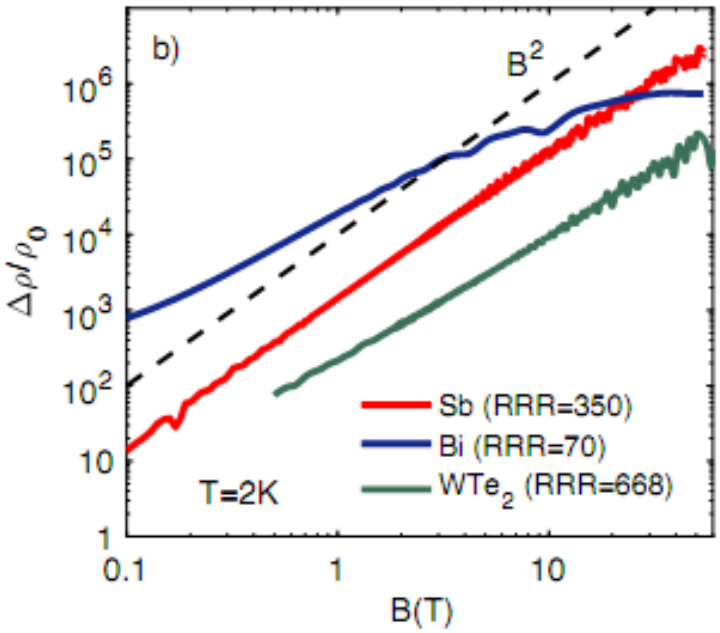

Figure 1.2 Magneto-resistance of elemental semimetals antimony, bismuth and WTe_2 at T = 2 K. Residual Resistivity Ratio (RRR) is equal to $\frac{\rho(T=300\ K)}{\rho(T=2\ K)}$. Adapted from Fauque et al [12].

1.3. Two-band Model

The magneto-resistance behaviour in a semimetal is understood within the framework of a two-band model. In the semi-classical two-band model [5], the longitudinal resistivity ρ_{xx} and the Hall resistivity ρ_{xy} are given by [13]

$$\rho_{xx} = \frac{\sigma_e + \sigma_h + \sigma_e\sigma_h\,(\sigma_e R_e^2 + \sigma_h R_h^2)\,B^2}{(\sigma_e + \sigma_h)^2 + \sigma_e^2\sigma_h^2\,(R_e + R_h)^2\,B^2} \tag{1. 1}$$

$$\rho_{xy} = B\,\frac{[R_e\sigma_e^2 + R_h\sigma_h^2 + \sigma_e^2\sigma_h^2 R_e R_h (R_e + R_h)B^2]}{(\sigma_e + \sigma_h)^2 + \sigma_e^2\sigma_h^2 (R_e + R_h)^2 B^2} \tag{1. 2}$$

where $\sigma_e = n_e e\mu_e$, $R_e = -\frac{1}{n_e e}$, n_e and μ_e ($\sigma_h = n_h e\mu_h$, $R_h = -\frac{1}{n_h e}$, n_h and μ_h) are longitudinal conductivity, Hall coefficient, carrier density, and mobility for electrons (holes), respectively.

In case of perfect compensation between electrons and holes, $n_e = n_h$, *i.e.*, $R_e + R_h = 0$, MR has a simple quadratic dependence on B in the formula $MR = \mu_e \mu_h B^2$, and does not saturate [3, 5]. A slight deviation from the perfect resonant condition can also lead to a large quadratic MR as long as B is not too strong. This is consistent with the results shown in Figure 1.2.

In Figure 1.3, we show the variation of MR with mobility. The amplitude of field-induced enhancement in resistivity is plotted [12] as a function of zero-field mobility, extracted from resistivity and carrier density: $\mu_0 = \frac{1}{\rho_0 (n+p) e}$. One can see that across more than three orders of magnitude, the MR of semimetals roughly scales with their zero-field mobility. The data from the recent topological semimetals are also included in this. The higher the mobility, the larger is the magneto-resistance. This is consistent with the two-band description of $MR = \mu_e \mu_h B^2$. In this thesis, we show that for the di-pnictide system too, MR scales with mobility. Experiments have been carried out on irradiated samples to control the mobility.

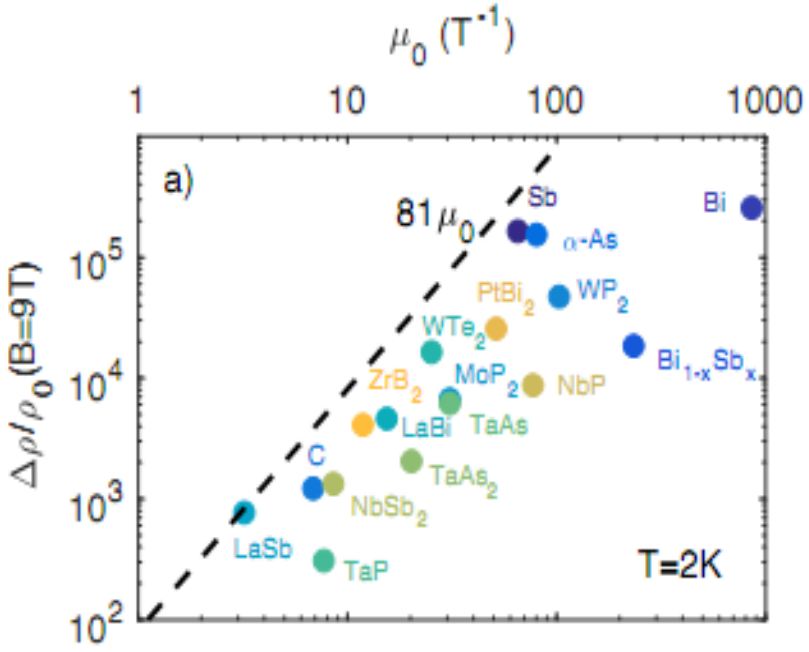

Figure 1.3 Magneto-resistance of various semimetals at B = 9 T and T = 2 K as a function of the mobility $\mu_0 = \frac{1}{\rho_0(n+p)e}$ where e is the charge of the electron, n and p are the electron and hole density and ρ_0 is the zero field resistivity at 2 K. μ_0 is expressed in Tesla^{-1} = 10^4 cm^2.V^{-1}.s^{-1}. Adapted from Fauque et al [12].

1.4. Kohler Scaling Relation

While the variation of resistivity with temperature under magnetic field is quite complicated (See Figure 1.1), Kohler pointed out that the MR can be described as a scaling relation: $\frac{\Delta\rho}{\rho_0} = F(\frac{H}{\rho_0})$ where $\Delta\rho = \rho_H - \rho_0$ and F represents a function of material properties [3]. The validity of Kohler's rule is seen in many systems, including high temperature superconductors [14, 15]. A recent result for the topological semimetal WTe_2 [16] is shown in Figure 1.4.

The temperature dependence of resistance under magnetic field in WTe_2 shows the characteristic feature of a resistivity minimum, followed by an upturn leading to a plateau at very low temperatures where the magnitude of the magneto-resistance reaches extreme values. The temperature at which the minimum occurs is found to increase systematically with the applied field. This upturn in resistivity on lowering the temperature has been attributed to a field induced metal to insulator transition invoking an excitonic model [9,

17]. Alternatively, the large variation of resistance with magnetic field has been understood within the framework of a semi-classical transport model for a semimetal characterized by low density and high carrier mobility [8]. It is seen from Figure 1.4 that the data scales according to Kohler's rule $MR = \alpha \left(\frac{H}{\rho_0}\right)^m$ with $m \sim 2$. The exponent $m = 2$ in the Kohler relation follows from the two-band model for the case of perfectly compensated system. For the two-band model, with $n_e = n_h$, $\rho_{xx}(T, H) = \rho_{xx}(T, 0) + \rho_{xx}(T, 0)\, \mu_e \mu_h H^2$, which leads to $MR = \alpha \left(\frac{H}{\rho_0}\right)^2$ [16].

The underlying physical reason for the applicability of the Kohler scaling relation can be understood as follows [18]: The applied magnetic field causes the electron to move in a circular / helical orbit. The ratio of H to resistivity depends on how many times the electron goes around in cyclotron orbit before collisions, which in turn depends on the ratio of the electron mean free path (l) to cyclotron radius (r). For a free electron, the mean free path, $l = \frac{mv}{e^2 n \rho_0}$, and $r = \frac{mv}{eH}$, giving $\frac{l}{r} = \frac{H}{\rho_0}$ apart from a constant involving electronic charge e and charge density n. Thus, the $\frac{H}{\rho_0}$ in the Kohler relation is a measure of $\frac{l}{r}$ that essentially vary with collisions [5, 19]. In a material, which conforms to Kohler's law, the role of magnetic field is merely to create cyclotron orbit rather than to change the scattering rate. The validity of Kohler's scaling relation expresses a self-similarity of the electronic orbital motion across different length scales: an invariance of the magneto response under the combined transformation of shrinking the orbital length $L \sim \frac{1}{H}$ by increasing H while, at the same time, also increase of the scattering rate $\frac{1}{\tau}$ by the same factor such that $H\tau$ remains unchanged [18, 20]. It can be appreciated that Kohler's rule breaks down if different scattering mechanisms emerge on different temperature or length scales or if Landau orbit quantization plays a role [20]. Further, deviations from the

Kohler rule may also point to electronic phase transitions, such as the Lifshitz transition [21]. More details on the Kohler rule are presented in Section 3.4.

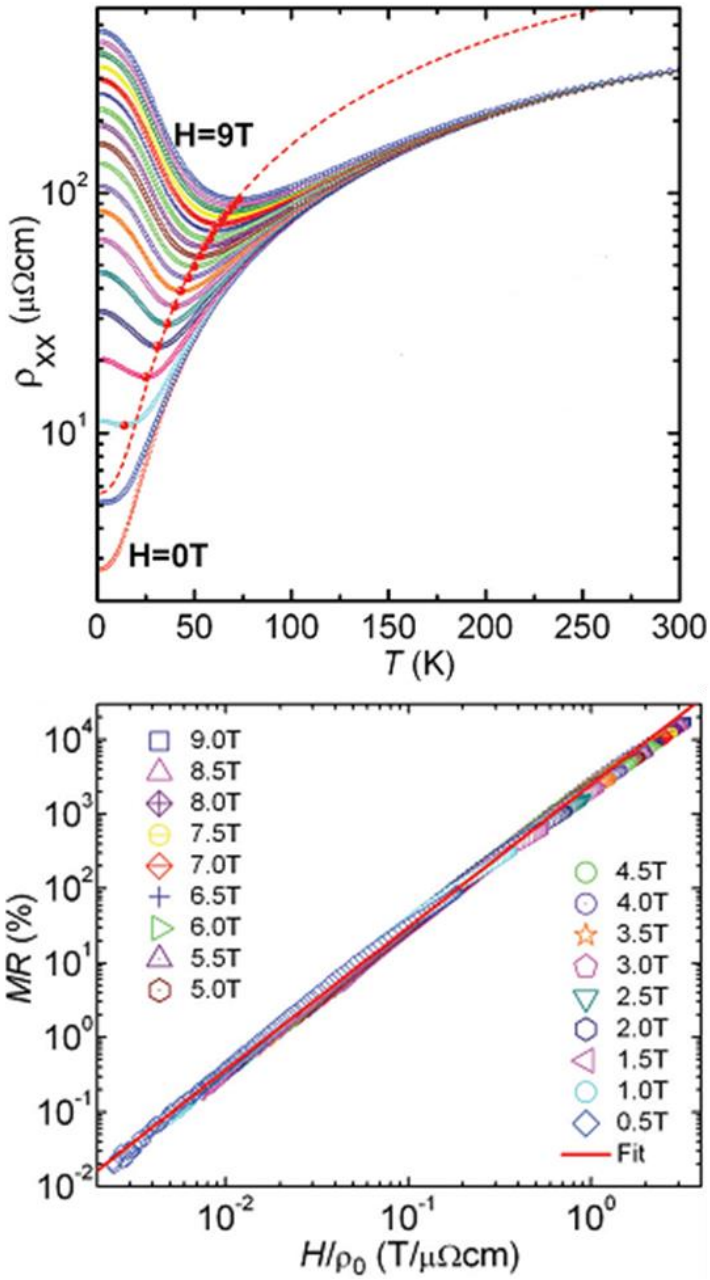

Figure 1.4 (Top) The temperature dependence of the resistivity, indicated by the open symbols, of WTe_2 in various magnetic fields from 0 to 9 T at intervals of 0.5 T. The red solid circles denote the locations of the resistivity minima, and the dashed red line represents its temperature variation, as derived from Kohler's scaling rule. (Bottom) The temperature dependence of the magneto-resistance of this sample follows the Kohler's scaling rule: $MR = \alpha \left(\frac{H}{\rho_0}\right)^m$ with m = 1.92 and $\alpha = 25$ [μΩ.cm/T]$^{1.92}$. Adapted from Wang et al [16].

1.5. Topological Semimetals

Starting with the discovery of topological insulators, the studies on the topological states of matter have been further enriched with the discovery of topological semimetals that are characterized by a linear energy band dispersion in the bulk state and topologically protected surface state with arc-like Fermi surface [22].

Figure 1.5a shows the sketch of the band structure of a topological insulator [23, 24]. It is constituted by a bulk valence band (green) and conduction band (blue) that exhibits a parabolic dispersion, and features additional topological surface states that exhibit a linear dispersion. Dirac and Weyl semimetals are 3-dimensional (3D) topological materials in which conduction and valence bands touch linearly close to the Fermi energy. In Dirac semimetals, both time-reversal and inversion symmetries are preserved, and the Dirac cone is degenerated, as shown in Figure 1.5b. Weyl states emerge when one of these symmetries is broken. As sketched in Figure 1.5c, the band touching point splits in momentum space into a pair of separated nodes (Weyl nodes) with opposite chirality, which refers to the handedness of the spin of electrons with respect to linear momentum. The Weyl nodes are the point-like crossings of two energy bands with linear dispersion. Locally, they can be described by a Hamiltonian of the form $H_k = \sum k_i a_{ij} \sigma_j$. Topologically, a Weyl node can be characterized as being a quantized source or sink of Berry curvature, depending on its chirality. Due to their quantized nature, Weyl points can only be created or annihilated in pairs of opposite chirality. The projections of the Weyl nodes with opposite chirality near the surfaces of Brillouin zone boundaries must be connected by surface Fermi arcs, as shown in Figure 1.5d. The two curves of the crescent are two Fermi arcs, and the two end points correspond to the projected Weyl nodes.

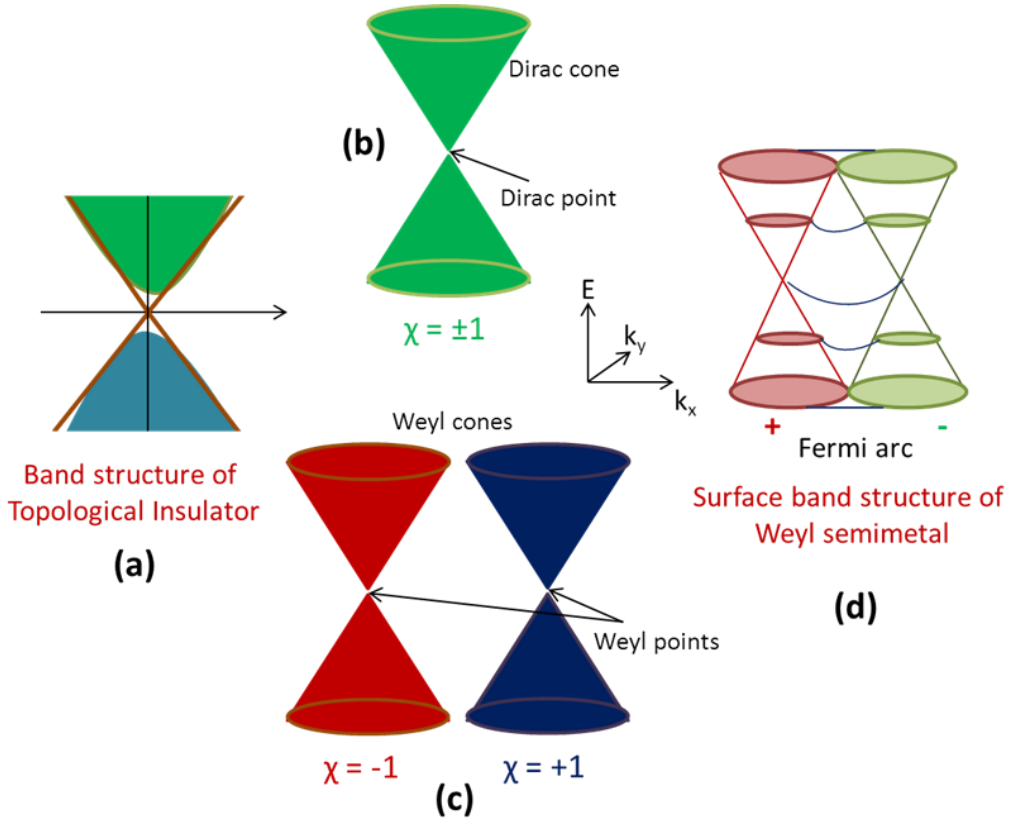

Figure 1.5 ***(a)*** *A topological insulator has a bulk band gap with band inversion, and a surface state with Dirac cone like dispersion (Left).* ***(b)*** *A Dirac semimetal has a degenerated Dirac cone (Middle Upper).****(c)*** *and* ***(d)*** *A Weyl semimetal is gapless in the bulk with a pair of band crossing points with opposite chirality (Middle Lower) which leads to a surface Fermi arc (Right) [23, 24].*

In the last few years, several Weyl semimetal (WsM) systems have been discovered such as TaAs, TaP, NbAs, NbP, $MoTe_2$ and WTe_2 [24, 25]. Niobium mono-arsenide (NbAs) crystallizes in a non centro-symmetric, body-centered tetragonal structure. The absence of a horizontal mirror plane in the unit cell makes this structure break the inversion symmetry, which is crucial to realize a time-reversal symmetric intact Weyl semimetal. Evidence for the presence of both the Weyl fermions in the bulk and the Fermi arcs on the surface have been obtained in these systems through angle-resolved photoemission spectroscopy (ARPES) experiments by choosing different incident photon energies [24].

Another class of materials, the transition metal di-pnictides of the type AB_2 [A = (Ta, Nb); B = (As, Sb)] have gained a lot of attention [17, 26-30] for their giant

magneto-resistance. The exact nature of magneto-resistance in these materials - especially the dependency on the direction of the magnetic field - is still under active investigation and is the subject of this thesis. Of particular importance is to know, whether these materials belong to the class of Weyl semimetals or not. Negative magneto-resistance, that is a distinctive signature of a WsM (See below) has been observed experimentally for $NbAs_2$ [28, 29], $TaAs_2$ [27, 29] and $TaSb_2$ [17, 28]. However, there are also experiments which point to the opposite, which is that there is no negative magneto-resistance in these materials [30, 31].

1.6. Structure and Electronic Structure of di-pnictides

The transition metal di-pnictides AB_2 (A = V, Nb, Ta, Cr, Mo, and W; B = P, As, and Sb) crystallize in the monoclinic $OsGe_2$-type structure [32]. The unit cell is having one crystallographic A site and two B sites [11] [See Figure 1.6a]. It can be seen that one of the two B sites is isolated from its nearby equivalent sites, while the other forms distinct B - B dimers. Further, each A atom is coordinated or surrounded by six B atoms, which form a trigonal prism with two more B atoms outside the rectangular faces. The prisms are stacked along the crystallographic *b* direction through their trigonal faces to form the monoclinic structure. The structure possesses an inversion centre and consequently not expected to host Weyl nodes.

The band structure of $TaAs_2$ is shown in Figure 1.6b [33]. It is seen that there is a pair of one electron band and one hole band which cross the Fermi level E_F, suggesting the two-band character and the coexistence of electron/hole carriers in these compounds. Moreover, two anti-crossing features within 0.2 eV of the Fermi level E_F are seen, as denoted by the blue circles. These band inversion properties have been verified with symmetry analysis for the states near the K-points. By explicitly calculating the coordinates of the nodal K-points, it has been shown that these band crossing K-points

form nodal lines. On taking into account the spin-orbit coupling it is seen [33] that the nodal lines become gapped, leaving a pair of fully gapped hole band and electron band. Furthermore, these bands are also completely separated from all other bands in the whole Brillouin Zone. Therefore, Z_2 invariants can be calculated for each of these bands. Thus, the band structure calculations indicate that these materials are semimetals, but without a direct closure of the band gap. Consequently, they do not host any Weyl or Dirac points. These compounds can be classified as weak topological insulators, with Z_2 indices $0;\ (111)$, in agreement with other studies [27, 28, 34].

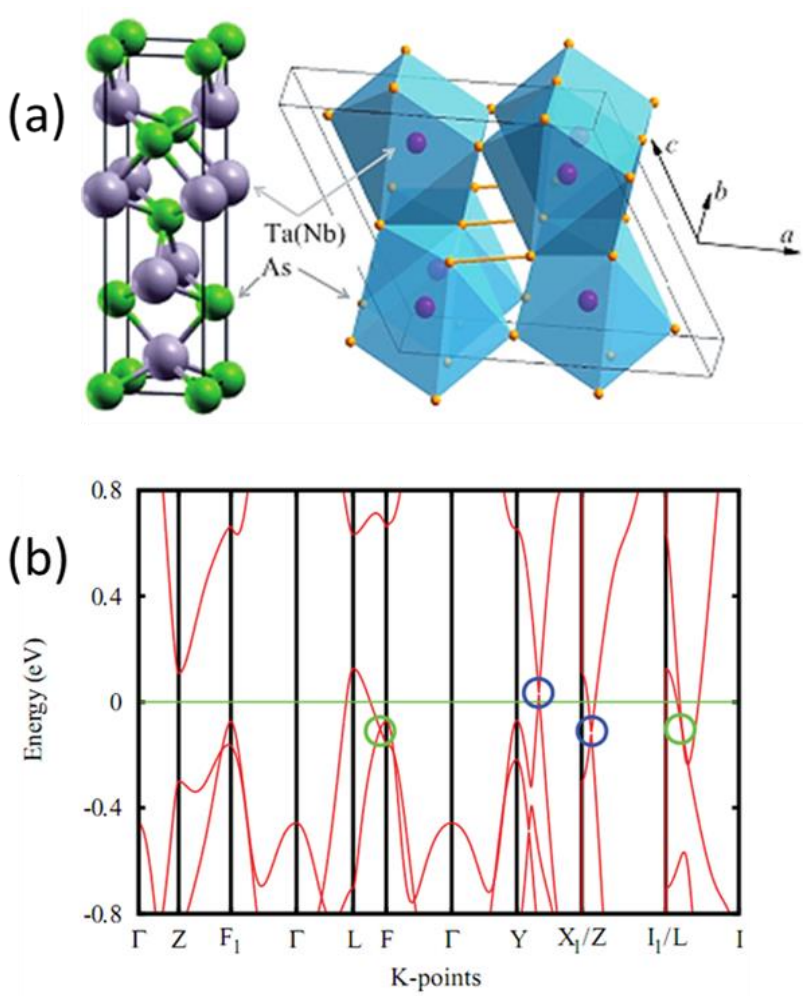

Figure 1.6 ***(a)*** *Unit cells for Ta(Nb)As$_2$ as adapted from Lu et al [11].* ***(b)*** *Bulk band structure of TaAs$_2$, calculated without considering spin-orbit coupling; taken from [33]. The circles denote anti-crossing features within 200 meV range of the Fermi level, aligned at 0.*

1.7. Magneto-transport in Topological Semimetals

Of particular interest have been the unique transport properties at low temperatures and high magnetic fields [35]. The topological semimetals show an ubiquitous non-saturating resistance with the applied magnetic field, that leads to extreme magneto-resistance $\sim 10^5$ %. There are some aspects of the MR behaviour that is related to the semi-metallic characteristics, and there are those that are intrinsically related to the topological nature of the electronic structure [36]. We shall present these in the following.

1.7.1. Magneto-resistance versus Temperature (MR versus T)

As an example of these studies, we present the results in $TaAs_2$, taken from Yuan et al [30]. Figure 1.7a shows the results of variation of resistivity with temperature under various magnetic fields. It is seen that with the application of magnetic field, the metallic variation of resistivity shows an insulating upturn and finally saturates at lowest temperature. This behaviour is similar to that seen in the case of graphite and WTe_2 (See Figure 1.1 and Figure 1.4). Figure 1.7b shows the parabolic and non-saturating variation of resistivity with magnetic field that in turn leads to extremely large MR in these systems. In order to understand the large MR, Hall measurements have proved very useful. Figure 1.7c shows the variation of transverse resistivity with magnetic field. A non-linear variation of Hall voltage is seen, that points to multiple charge carriers. An analysis in terms of two-band model indicates a near compensation of charge carriers that accounts for the large MR (See Equations (1. 1) and (1. 2) in Section 1.3 on two-band model). In the present thesis too, the MR data in di-pnictides have been analyzed in conjunction with the Hall data.

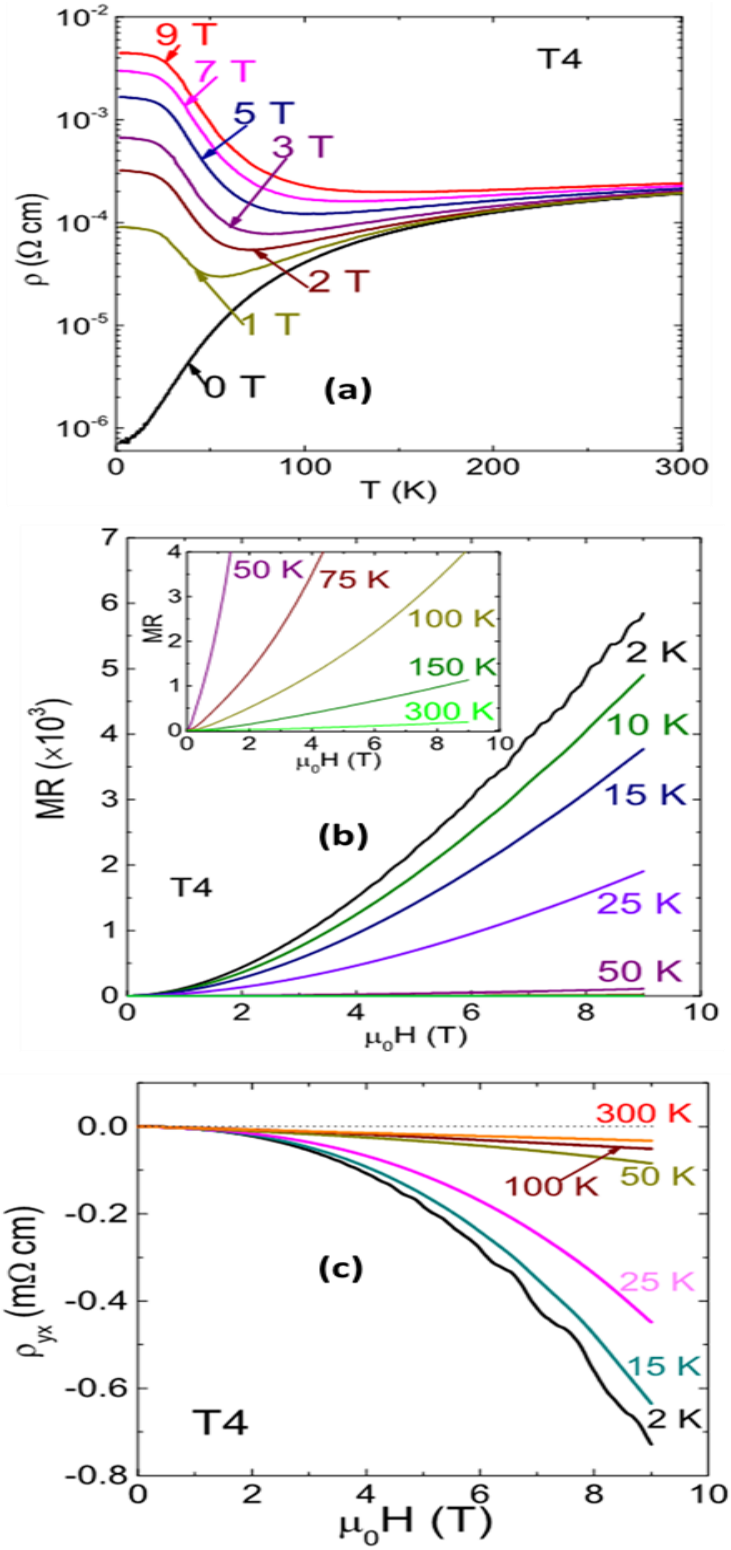

Figure 1.7 ***(a)*** *The temperature dependence of the longitudinal resistivity ρ in $TaAs_2$ at various magnetic fields (B=0 – 9 T).* ***(b)*** *The variation of MR with applied field at various temperatures.* ***(c)*** *The Hall resistivity ρ_{yx} at different temperatures and the fitted results by the semi-classical two-band model. Adapted from Yuan et al [30].*

1.7.2. Magneto-resistance versus Magnetic field (MR versus H)

In typical non-magnetic and semiconducting materials, the MR increases quadratically with applied transverse magnetic field and saturates to a constant value when the product of the applied field and the mobility (μ) approaches unity [37]. However, in the topological semimetals, the MR is seen to show a non-saturating behaviour, leading to record-high non-saturating MR, known as extreme magneto-resistance (XMR).

Two types of MR behaviour are seen as shown in Figure 1.8. The parabolic non-saturating MR is attributed to the semi classical two-band model, where electron-like and hole-like carriers are nearly compensated, resulting in rich magneto-transport characteristics that are strongly temperature (T) and applied transverse magnetic field (H) dependent. On the other hand, the linear behaviour of MR versus H is attributed to the squeezed trajectories of carriers (guiding center motion of charge carriers). In semi-classically large magnetic fields, $\mu B \geq 1$, that is easily achieved in linearly dispersing topological semimetals (See Leahy et al [37]).

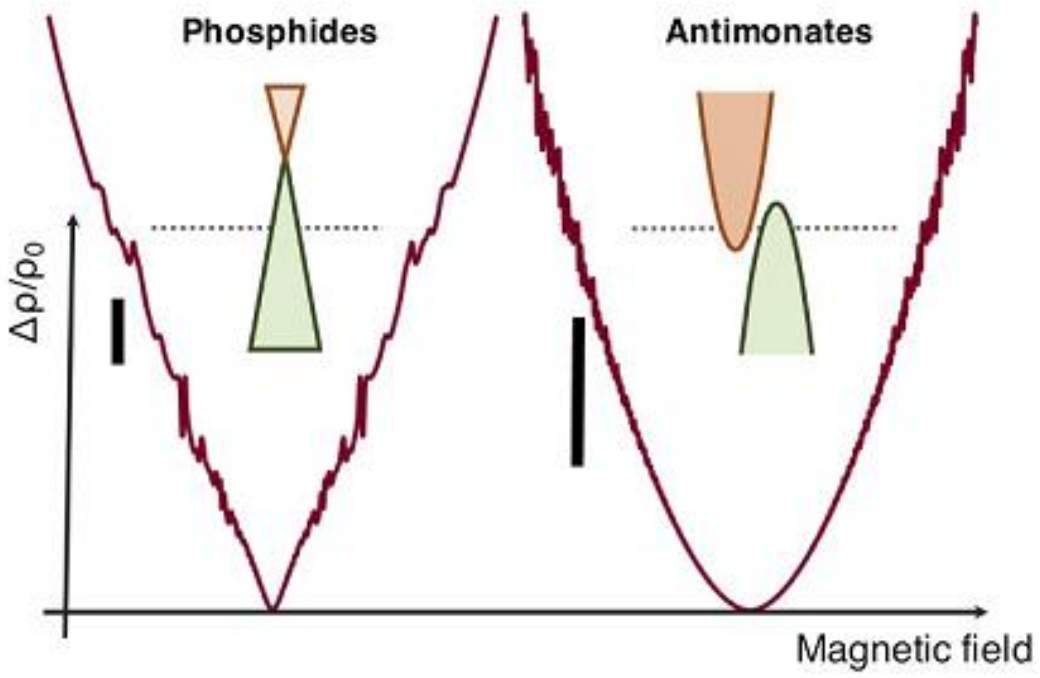

Figure 1.8 Non-saturating magneto-resistance phenomena and representative energy dispersions for phosphides [Left] (as in TaP) and antimonates [Right] (as in $TaSb_2$) are schematically depicted. Adapted from Leahy et al [37]. The MR in phosphides is characterized by quasi-linear to linear transition as field increases, while for the antimonates, MR is characterized by persistent quadratic H dependence, arising from semi-classical charge compensation. Each bar indicates $\frac{\Delta\rho}{\rho_0} = 5 \times 10^5$ *%. Magnetic field was applied up to* $\mu_0 H$ *= 31 T at 0.3 K.*

1.8. Influence of Topology on Magneto-transport

In a Weyl semimetal, the presence of Weyl nodes with opposite chirality leads to interesting topological features. There are two different manifestations of topology: First is the nontrivial surface state, and the second is to study the response to an applied electric and/or magnetic field [35]. The unusual response to electric and magnetic fields is due to the chiral anomaly, discussed in the following:

1.8.1. Chiral anomaly and negative LMR

The conservation law of chirality mandates that the number of left-handed and right-handed electrons must always be symmetric; in other words, more electrons of one chirality than of the other cannot exist [23]. When a magnetic field is applied in parallel to an electric field, the chiral symmetry scenario can be violated at the quantum level.

Simultaneous application of electric and magnetic fields to a Weyl semimetal leads to chiral charge pumping between the two branches of chiral energy levels (Landau levels), such that the flow rate is proportional to the product of the parallel magnetic and electric field components, as shown in Figure 1.9a [38].

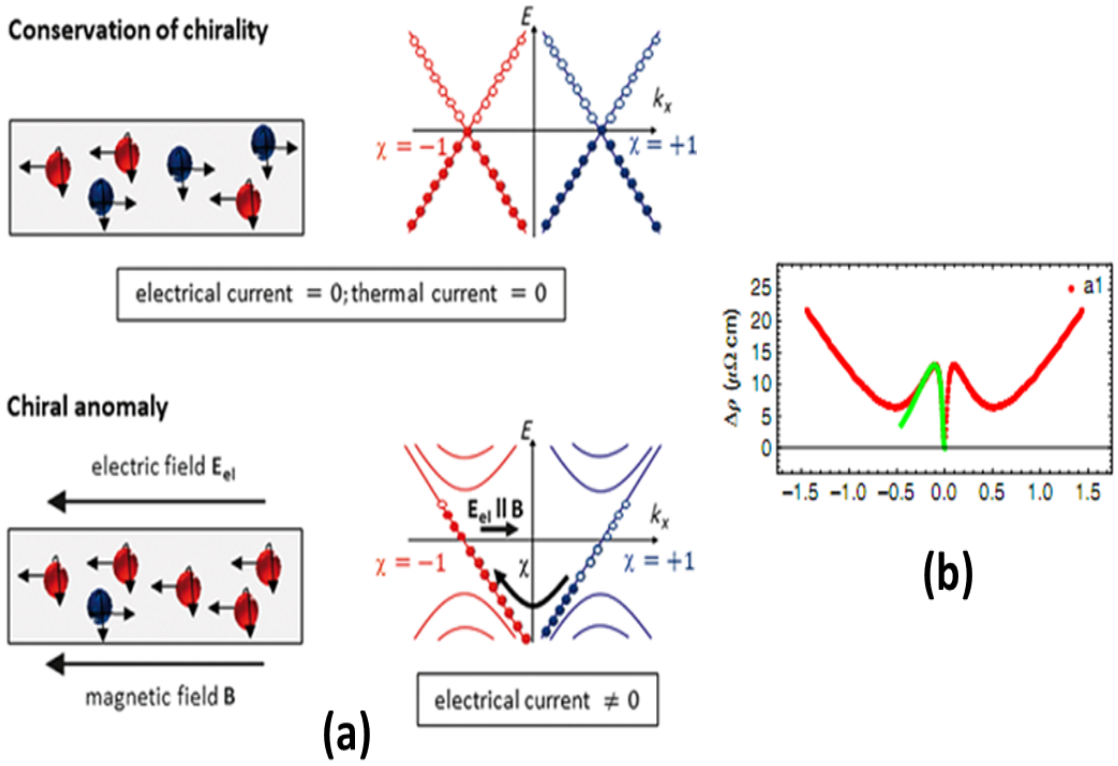

Figure 1.9 ***(a)*** *Left panels, adapted from Gooth et al [23], show the real space scheme of the charge-carrier flow and the associated band structure occupation in topological materials. Usually, the chirality is conserved, and consequently, the net current flow is suppressed. However, quantum mechanical fluctuations can break the conservation law of chirality under the parallel magnetic (B) and electric (E_{el}) fields (chiral anomaly).* ***(b)*** *Longitudinal MR for TaAs samples at 2 K for E and B along the 'a' crystallographic direction. The short (green) curve is a fit to the longitudinal MR data in the semi-classical regime based on a chiral anomaly model. Adapted from Zhang et al [38].*

While in TaP and TaAs, definitive evidence for the negative longitudinal magneto-resistance (NLMR) has been obtained (See Figure 1.9b), the results in the case of di-pnictides have been contentious. For example, while in the studies by Luo et al [27] on $TaAs_2$, clear signatures of LMR are seen; in the studies by Wu et al [13], positive LMR is seen. These are shown in Figure 1.10. This discrepancy, shown for the $TaAs_2$ system, is

also seen in the other di-pnictides such as $NbAs_2$ [29, 31]. As mentioned earlier (Section 1.6), $TaAs_2$ possesses an inversion centre, and further the electronic structure shows a band gap, rather than band touching points with linear dispersion, and hence not expected to host Weyl nodes [34]. There have been theoretical proposals [39] for mechanisms by which Weyl nodes to appear in these materials under the influence of a magnetic field. The chiral anomaly associated with these Weyl nodes is a possible source of negative magneto-resistance. Further, it has been demonstrated that the negative LMR observed in $TaAs_2$ may be an artefact of current jetting effect, when the contacts are not fully covering the sample, as discussed in more detail in Chapter 3 (See Section 3.8). This is shown in Figure 1.10c.

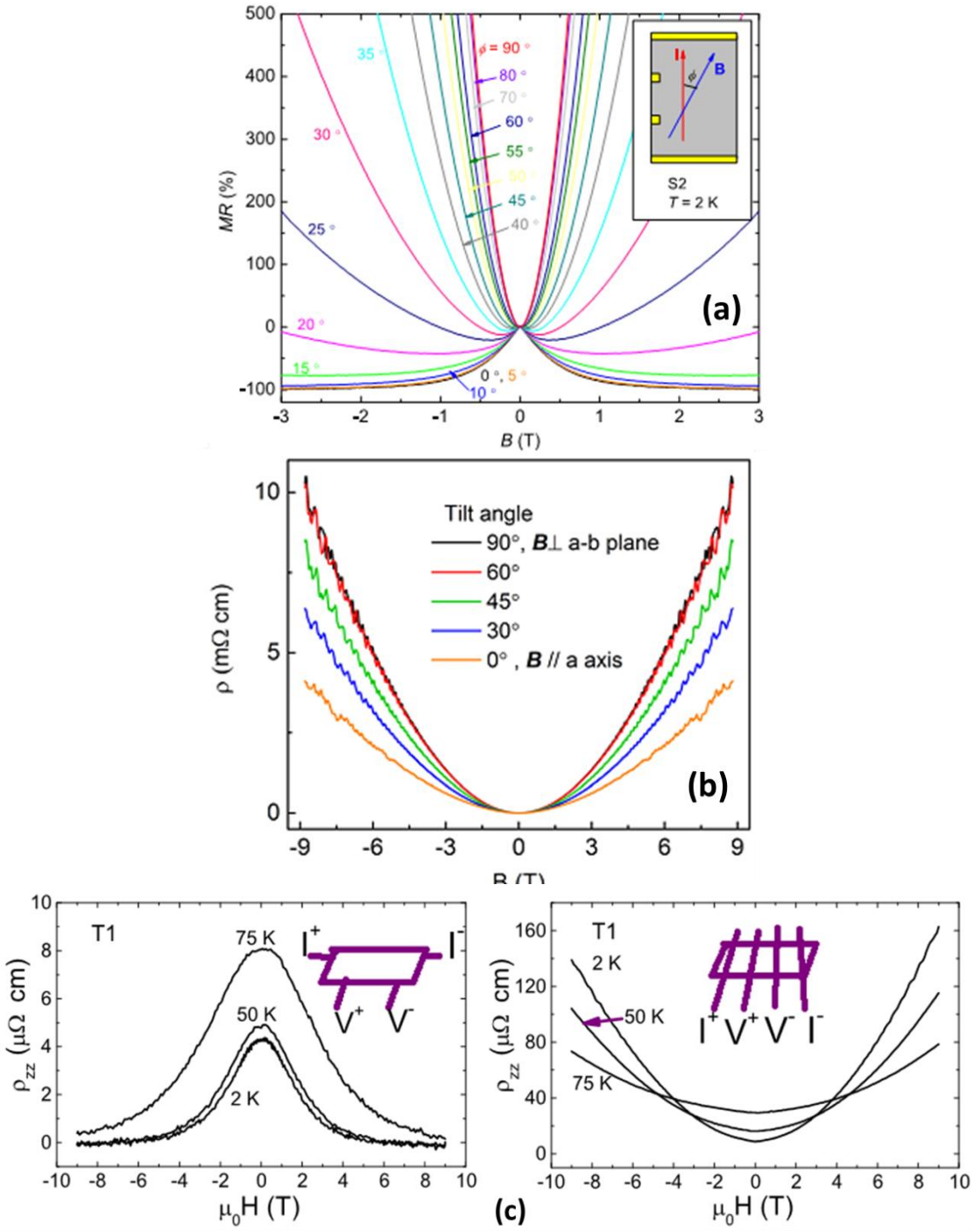

Figure 1.10 ***(a)*** *Field-dependent MR of $TaAs_2$ with various angles φ at 2 K that shows negative LMR as adapted from Luo et al [27]. The inset shows the configuration of the measurements.* ***(b)*** *Experimental results from Wu et al [13] that shows positive LMR. Resistivity versus magnetic field for various tilting angles at T = 1.6 K.* ***(c)*** *Demonstration of current jetting effect in $TaAs_2$ as adapted from Yuan et al [30]. Negative LMR is seen when the contacts are not fully covering the sample as shown in the left panel and that changes to positive LMR when the contacts are fully covering the sample (right panel).*

1.8.2. Berry phase

In addition to the presence of Fermi surface arcs and exotic signatures in electron transport such as chiral anomaly induced negative longitudinal magneto-resistance, the presence of nodes of opposite chirality in a Weyl semimetal leads to a Berry phase of π [40]. The Berry phase describes the additional geometrical phase factor acquired in the adiabatic evolution along a closed trajectory in the parameter space.

The Berry phase is characterized by the topological features of the electron bands in the Brillouin zone. A non-zero Berry phase indicates the existence of band touching point, such as Dirac nodes that manifests itself in observable effects in quantum oscillations. Under a magnetic field B, the cyclotron motion of Dirac fermions induces Berry phase, and it changes the phase of quantum oscillations [41]. Generally, through mapping the Landau level (LL) - fan diagram (the plot of n^{th} Landau level index versus $\frac{1}{B_n}$, the inverse of the applied magnetic field), the Berry phase can be conveniently extracted from the intercept of the linear extrapolation of Landau level index to the zero of inverse field ($\frac{1}{B}$). Experimentally, a Berry phase of π arising from the linear band dispersion of a Dirac cone has been obtained from the Shubnikov - de Haas oscillations in topological insulators and Dirac fermion systems [42].

In Weyl semimetals, a similar linear band dispersion also generates a non-trivial Berry phase of π. However, unlike the well-established π Berry phase in Dirac systems, the experimental determination of Berry phase using the LL - fan diagram remains challenging for mono-pnictide Weyl semimetals for several reasons [43]: Presence of quantum oscillations with multiple frequencies due to the existence of multiple Fermi pockets and complication due to the coexistence of Dirac and parabolic bands [42, 44]. In this thesis, we present the results on the estimation of Berry phase in the di-pnictides from de Haas - van Alphen (dHvA) oscillations, and these are presented in Chapter 5.

1.9. Contents of the Thesis

With the above background, the present thesis work is aimed at understanding the magneto-transport phenomena in di-pnictides, $TaAs_2$ and $NbAs_2$. Experiments have been carried out in pristine and low energy (Ar^+ ion) irradiated single crystals, the later with a view to affect the surface states and alter the mobility. It is shown that the observed MR behaviour can be rationalized using Kohler's rule. It is further shown that the origin of the XMR in these materials is strongly linked with the high mobility of the carriers and evidence for this is provided through a combined study of Hall and de Haas – van Alphen oscillations measurements. The thesis is organized into six chapters.

Chapter 2 describes the experimental methods and techniques used for the thesis work. These include the growth of single crystals, characterization of samples by Raman spectroscopy and the magneto-resistance and Hall measurements that forms the main thrust of the thesis. **Chapter 3** presents the results of magneto-resistance studies in $TaAs_2$ single crystals [45]. The temperature variation of resistivity under magnetic field in both the pristine and irradiated samples exhibits an upturn in resistivity with the lowering of temperature followed by a plateau resulting in extremely large magneto-resistance $\sim 10^5$ % at 2 K and 14 T. The characteristic temperature of resistivity minima that was seen to increase systematically with the applied field was shown not to follow a critical behaviour as expected for an MIT, induced by the applied magnetic field. However, the magneto-resistance data in both the pristine and irradiated $TaAs_2$ was seen to follow Kohler's scaling rule remarkably well as seen from the collapse of all the MR curves to a single curve in the whole range of temperature and field. In **Chapter 4**, we present the results of magneto-transport investigations in an iso-structural compound $NbAs_2$ [46]. Transverse MR in $NbAs_2$ showed qualitatively similar behaviour as in $TaAs_2$ and angle dependent MR measurements unambiguously confirmed the absence of negative

LMR in $NbAs_2$. Combining with Hall measurements, a clear correlation of temperature dependence of magneto-resistance and mobility was seen across the three set of samples, viz., pristine, irradiated and heat treated.

Chapter 5 describes the studies from the de Haas - van Alphen oscillations in the pristine and irradiated $TaAs_2$ and $NbAs_2$. This study is aimed to give support to the results of Chapters 3 and 4, rather than to explore the Fermiology of the materials. The isothermal magnetization measurements up to 7 T exhibited spectacular dHvA oscillations at low temperatures, where the resistivity plateau appeared in the MR experiments. A fast Fourier transform (FFT) analysis was used to resolve the oscillation frequencies and it revealed multiple charge carrier pockets. The field variation of the oscillation amplitudes at various temperatures was analyzed using the Lifshitz - Kosevich (L-K) formalism [47] to estimate the cyclotron mass of the charge carriers and the Dingle temperature. Further, a Landau level - fan diagram was constructed for pristine $TaAs_2$ from the dHvA oscillations to extract the Berry phase [41, 44] that points to the topologically trivial nature of the band structure in the materials. In **Chapter 6**, we present the summary of the main findings of the thesis.

Chapter 2

Experimental Methods and Techniques

This chapter describes the experimental techniques and the instruments used for the present thesis work. $TaAs_2$ and $NbAs_2$ single crystal samples were synthesized by chemical vapour transport method. The characterization of the single crystals was carried out with Raman spectroscopy and Laue x-ray diffraction. Arsenic vacancies were introduced in the pristine samples via argon ion irradiation. Ion implantation was carried out using 150 kV accelerator. Electron transport measurements, magneto-resistance and Hall resistance, were carried out using Cryogenic Ltd (U.K) cryostat (2 K, 15 T) and Quantum Design make PPMS DynaCool cryostat (2 K, 14 T). Angle dependent magneto-resistance measurements were also performed using the DynaCool system.

2.1. Sample Preparation

Single crystals of $TaAs_2$ and $NbAs_2$ were grown by chemical vapour transport using iodine in two stages [27, 30]. Polycrystalline material was prepared in the first step from the precursor elements (See Figure 2.1a for the schematic of crystal growth). High purity tantalum / niobium and arsenic powders taken in stoichiometric ratios were separately ground and mixed together. The mixtures (Ta, As) and (Nb, As) were collected in separate alumina containers and covered their mouth by alumina wool. These were vacuum sealed in quartz tubes. The quartz ampoules were kept for heat treatment in a box furnace. It was heated to 1123 K in steps of 1 K per minute, and allowed to stay there for 48 hours followed by slow cooling to room temperature. The recovered polycrystalline pellets were again ground well and transferred into alumina containers along with iodine shots (13 mg/cc). It was vacuum sealed in a quartz tube of 12 cm length and having 12 mm diameter. These ampoules, for vapour transport, were placed in a horizontal furnace (See Figure 2.1b), programmed to a temperature gradient of approximately 100 K

between 1123 K and 1223 K such that the source material is at the hot end. The correctness of the gradient was ensured by calibrating the furnace using a K-type thermocouple. The required temperature level was reached by 1 K per minute heating rate, and maintained it for 10 to 14 days. Then the furnace was slow cooled (1 K per minute) to room temperature. $TaAs_2$ single crystals (shown in Figure 2.1c) of dodecahedron morphology were found at the cold end of the quartz ampoule [48]. For the case of $NbAs_2$, similar protocol was followed [49]. Flat $NbAs_2$ crystals (shown in Figure 2.1d) were found at the hot end. Crystals were found to have 1 to 2 mm x 1 mm sizes (length x width) and were having thickness less than 1 mm. The collected crystals were cleaned with isopropyl alcohol to remove the iodine stains from the surface before further measurements.

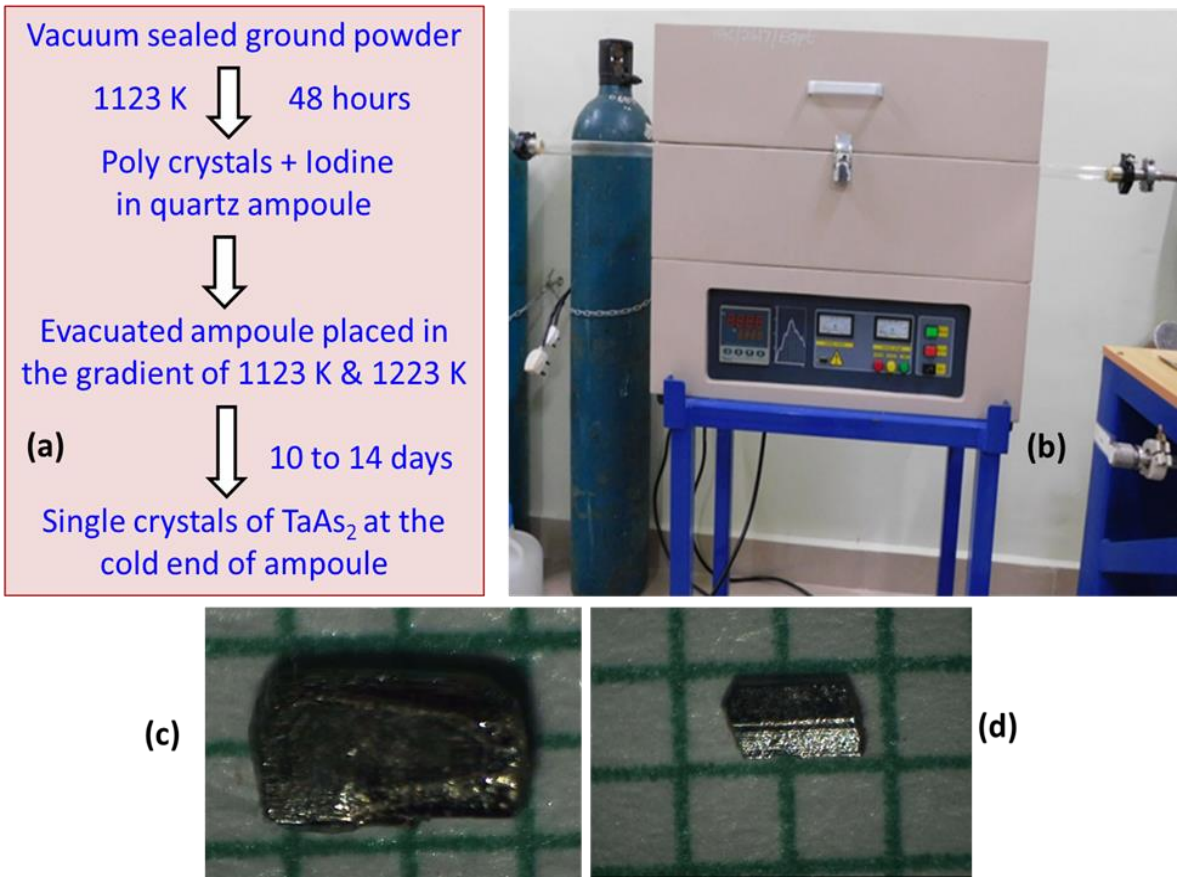

Figure 2.1 ***(a)*** *Flow chart of the synthesis of single crystals by chemical transport using iodine vapour.* ***(b)*** *The two-zone furnace used for sample synthesis in the second stage. Photographs of as-grown samples on (1 mm x 1 mm grid) graph paper are shown.* ***(c)*** *Thick $TaAs_2$ single crystal* ***(d)*** *Flat $NbAs_2$ single crystal.*

2.2. Irradiation Experiments

In this thesis, apart from magneto-transport studies on pristine di-pnictides, experiments were also carried out on irradiated and heat treated samples with a view to investigate the role of disorder. There has been one earlier study on irradiation effects on topological semimetals [50]. Low energy, 30 keV, argon ion (Ar^+) irradiation was carried out to introduce arsenic (As) vacancies near the surface. The ion irradiation experiments were carried out at room temperature using a 150 kV gaseous ion implanter. Figure 2.2a shows photograph of the accelerator facility. A radio-frequency ion source produced the gaseous ions. Argon ions, accelerated at low energies (30 keV) were used to irradiate the as-grown pristine samples. The samples were attached on a copper block using silver paste and it was mounted on the sample manipulator. The copper block was electrically isolated from the rest of the irradiation chamber to enable beam current measurements. The chamber was evacuated to a pressure of 5×10^{-7} mbar with a turbo molecular pump. A beam current of 0.3 μA was generated and the ion beam size was 12 mm. This resulted in an ion fluence of 1×10^{16} ions per cm^2. Sputtering yield and implantation depth were calculated with 'Stopping and Range of Ions in Matter' (SRIM) software [51]. These results are given in Figure 2.2b and Figure 2.2c. The sputter yield of As estimated from SRIM calculations is much higher as compared to Ta/Nb, resulting in predominantly As vacancies at the surface.

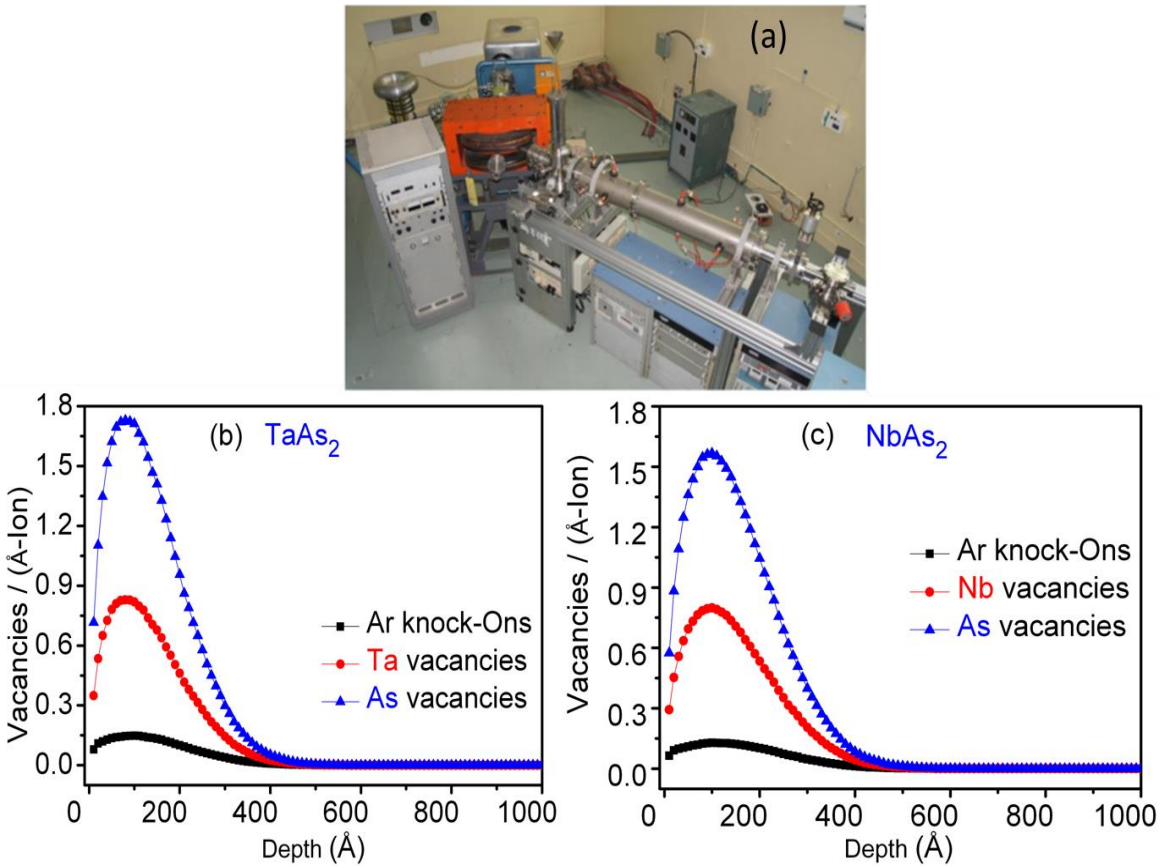

Figure 2.2 ***(a)*** *Photograph of the 150 kV accelerator facility, showing high voltage power supply units and accelerating tube. Vacancy distribution due to irradiation, as a function of depth, was calculated using SRIM and are shown for* ***(b)*** *$TaAs_2$* ***(c)*** *$NbAs_2$.*

2.3. Sample Characterization

2.3.1. Raman spectroscopy

Raman spectroscopy has been found useful to characterize the di-pnictide samples as discussed in detail by Jin et al [52], and we have employed the same in the present investigations. Raman spectroscopy experiments were carried out with RENISHAW inVia make Raman spectrometer equipped with a 514.5 nm argon laser and a 785 nm solid state diode laser. Figure 2.3a shows the Raman spectrometer and the computer controlled data acquisition system. The acquisition of data and analysis were done with a dedicated communication interface called 'Windows-based Raman Environment' (WiRE) software. The instrument is also equipped with a temperature control cell so that sample temperature can be varied between 80 K and 900 K (See inset in Figure 2.3a). Sample was cooled

below room temperature up to 80 K by passing cold nitrogen vapour to the sample cell. We have recorded each spectrum with argon laser with 10 mW power, after illuminating it for 300 seconds on a 1 μm spot on the crystal. Spectra were collected from different spots on the sample to ensure reproducibility.

Figure 2.3b shows the Raman spectrum obtained from the pristine $TaAs_2$ sample. The nine modes exhibited by the pristine crystal viz., ^1A_g, ^1B_g, ^2A_g, ^2B_g, ^3B_g, ^3A_g, ^5A_g, ^4A_g and ^6A_g could be indexed with all the Raman active modes, as given by Jin et al [52]. The sharp peaks revealed the high crystalline quality. In the case of irradiated sample, discussed later in Chapter 3 (See Section 3.2), while all the modes were present, they were observed to be hardened by ~2 cm^{-1}.

The sample stage of the Raman spectrometer was also used to heat treat the sample, as the Raman spectra was being monitored in-situ. Figure 2.3c shows the Raman spectra in $TaAs_2$ at various temperatures. Spectrum was recorded in 40 K intervals after a residence time of 5 minutes at each temperature. The recovered sample was designated as the heat treated $TaAs_2$ sample. As the temperature was increased from 80 K, Raman modes were seen to shift. For example, the highest intensity mode ^6A_g at 80 K shifts to low wave number side as temperature was increased, that can be attributed to lattice expansion (See Figure 2.3d). The width of this peak was broadened with increase of temperature. Apart from this, a large increase of background (predominantly between 200 cm^{-1} and 275 cm^{-1}) can be seen from Figure 2.3c at higher temperatures. This increase in the background was retained when the sample was cooled back to room temperature. This heat treated sample, in which disorder was introduced, was used in the magneto-transport experiments for comparison with pristine sample, as discussed in Chapter 3. For the case of $NbAs_2$ sample, discussed in Chapter 4, the heat treatment was

done, without the attendant in-situ Raman measurements, in a box furnace at 700 K, after vacuum sealing in a quartz ampoule.

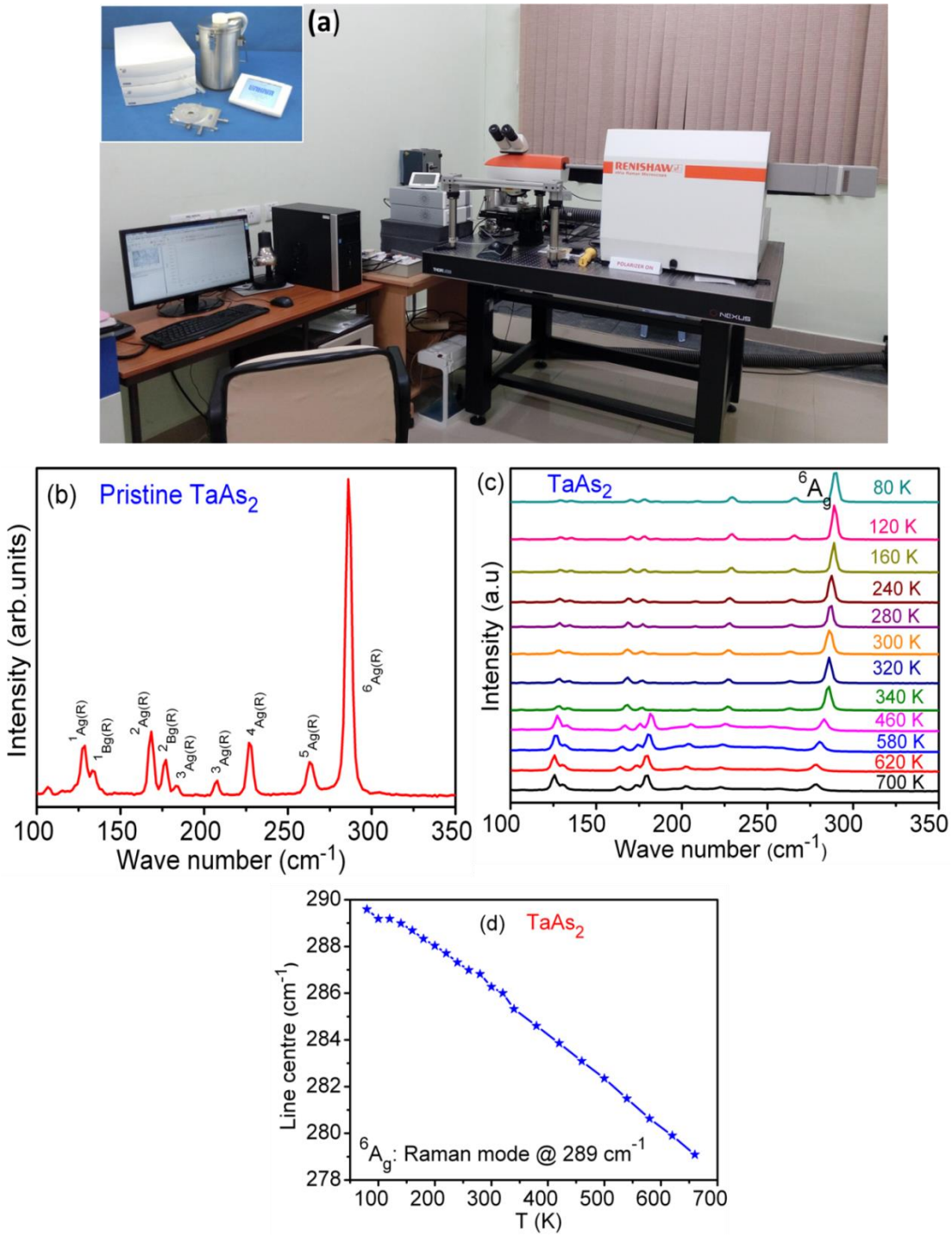

Figure 2.3 ***(a)*** *Photograph of the Renishaw inVia Raman spectrometer system. Inset shows the cryostat/heater setup that is used for temperature variation. It includes the sample cell, nitrogen container and the temperature controller. This was used for heat treating the sample.* ***(b)*** *The Raman spectra of pristine $TaAs_2$.* ***(c)*** *The Raman spectra of $TaAs_2$ at various temperatures.* ***(d)*** *The softening of the ^6A_g mode at 289 cm^{-1} with the increase of temperature due to thermal expansion.*

2.3.2. Laue x-ray diffraction

The samples were also characterized with Laue x-ray diffraction technique. The Laue patterns for the pristine and irradiated $TaAs_2$ and $NbAs_2$ are given in Figure 2.4. Experiments were performed using a molybdenum x-ray source. An HD-CR-35 NDT image plate system was used to record the diffraction pattern. The measurements were carried out in the back-reflection geometry. The array of spots in the Laue pattern of the pristine $TaAs_2$ (See Figure 2.4a) indicates the high quality of the synthesized single crystal samples. While, we have not analyzed the x-ray diffraction pattern in any detail, the streaks or the broad spots appears on the pattern of irradiated $TaAs_2$ (See Figure 2.4b) indicate the disorder caused by irradiation, consistent with the Raman spectroscopy results indicated in the previous section. Similar observations can be made from the Laue patterns of pristine and irradiated $NbAs_2$ as shown in Figure 2.4c and Figure 2.4d respectively.

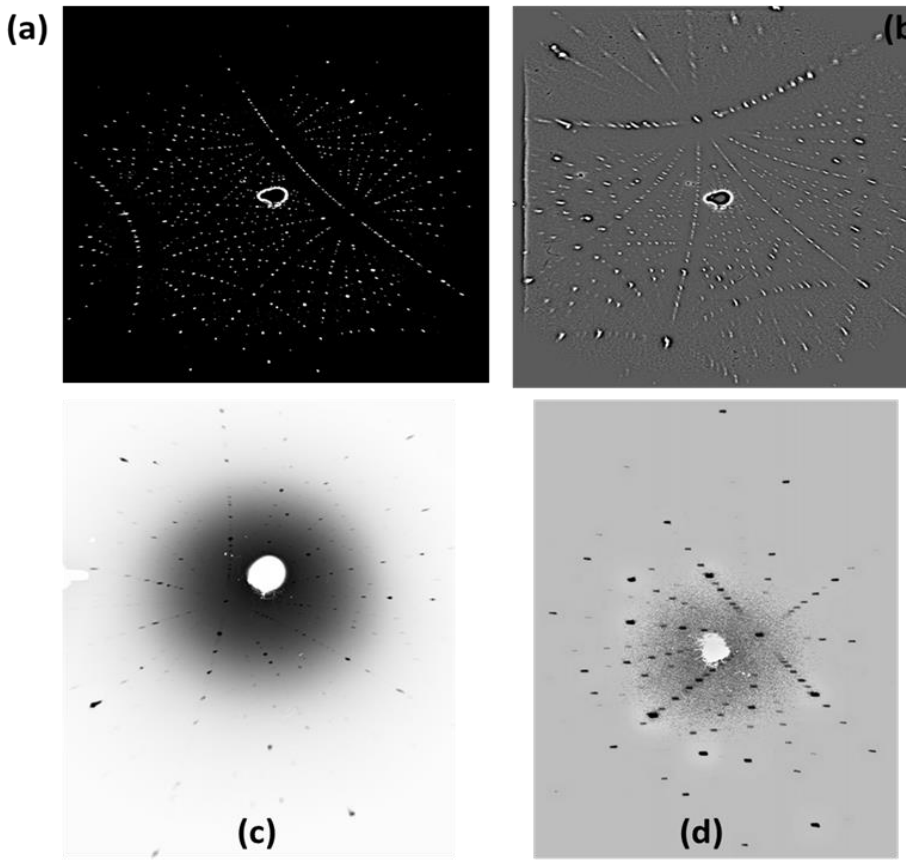

*Figure 2.4 Single crystal x-ray diffraction pattern obtained for the **(a)** pristine $TaAs_2$ **(b)** irradiated $TaAs_2$ **(c)** pristine $NbAs_2$ and **(d)** irradiated $NbAs_2$.*

2.4. Magneto-transport Experiments

The main thrust of the thesis is on magneto-resistance (MR) measurements in the di-pnictides. MR and Hall resistance measurements were performed using the liquid cryogen free Cryogenic Ltd (U.K) 2 K, 15 T cryostat and PPMS (2 K, 14 T) cryostat, in which the latter was also enabled to make angle dependent magneto-resistance measurements. Experiments were carried out in the 2 K to 300 K temperature range.

2.4.1. Liquid free (2 K, 15 T) Cryogenic Ltd cryostat

Figure 2.5a shows the Cryogenic Ltd cryostat set up. It consists of cryostat & magnets, cryo-cooler system, variable temperature insert (VTI), electronic units and measurement system software. The schematic diagram of the VTI cooling circuit as adapted from the cryostat user manual [53] is shown in Figure 2.5b**.** The vacuum insulated cryostat chamber provides a thermal shield to the superconducting magnet and the VTI. The magnet is a vertically oriented solenoid wound from superconducting NbTi (low field) or NbTi with Nb_3Sn (high field) wires. In the first stage of the cooling process, the cryo-cooler cools the radiation shield in the chamber. The helium gas at room temperature is stored in the reservoir. The second stage involves cooling of the magnet to 4 K and the VTI to below 4 K using the circulating helium gas. A needle valve is used to adjust the gas flow to the sample space. A heat exchanger below the VTI maintains the required sample temperature with the help of a heater, controlled by the temperature controller. The VTI helps in varying the sample temperature between 1.6 K and 325 K. An oil free pump drives the warm gas back to the helium dump. A CERNOX thermometer attached to the sample platform monitors the sample temperature. The sample is inserted to the sample space through an airlock provided on the top plate of the cryostat without contaminating the sample chamber. The electronic units include temperature controllers (to control and measure the VTI & sample probe temperatures), Keithley 2700 multi-meter, probe current source and magnet controls.

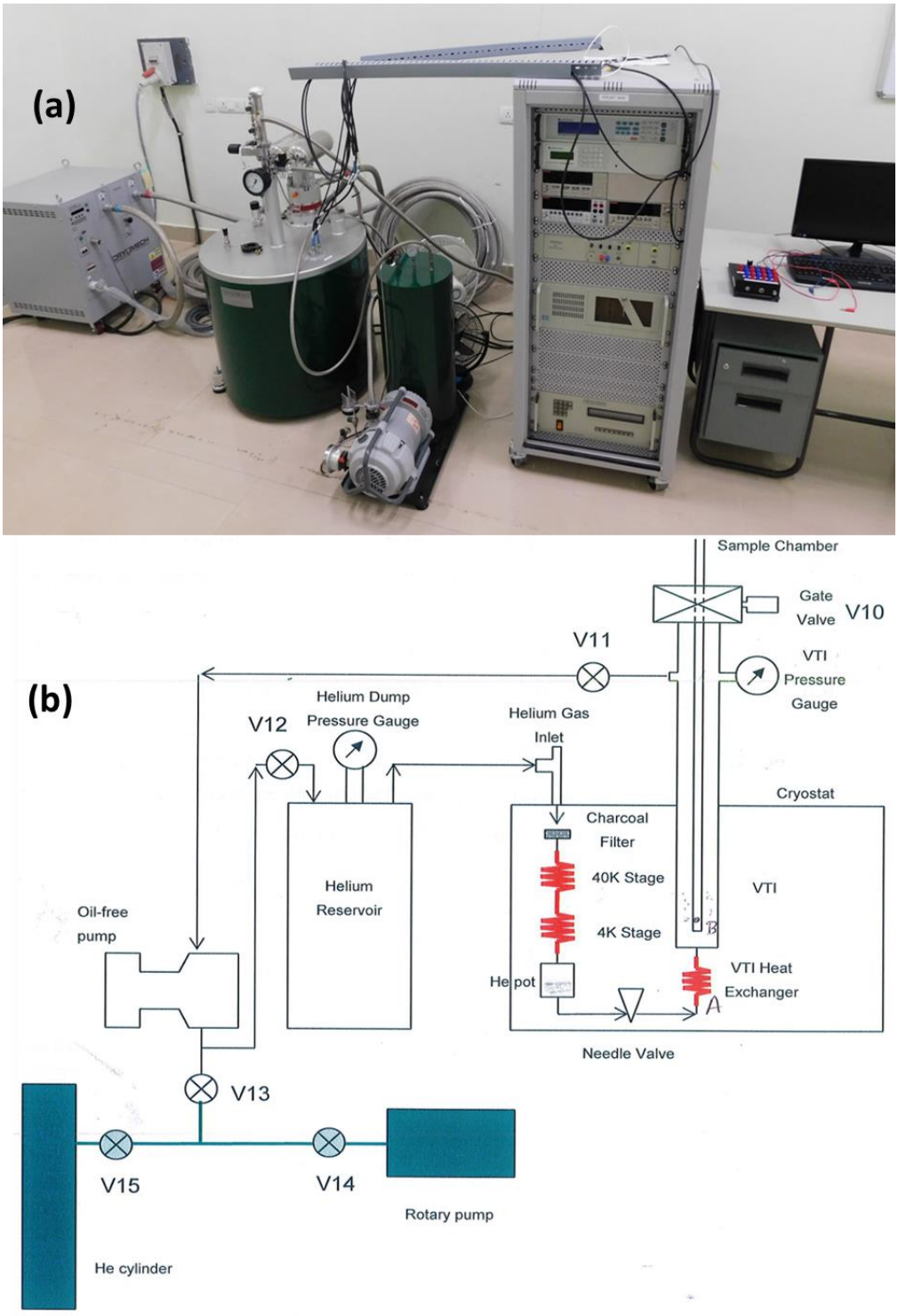

Figure 2.5 ***(a)*** *Photograph of the Cryogenic Ltd 2 K, 15 T cryostat. It shows the cryo-cooler, the cryostat chamber, helium reservoir and the system control units.* ***(b)*** *The schematic of the VTI cooling circuit, as adapted from the user manual [53].*

Photographs of the sample mounting puck and measurement probe platform are shown in Figure 2.6a and Figure 2.6b respectively. Samples of dimensions up to 10 mm x

5 mm (length x width) can be measured using this puck. Single crystal samples were polished to uniform thickness for measurements. The sample was mounted at the middle of the puck (Figure 2.6a) using double sided sticky tape. Four insulated copper wires (44 SWG) de-enameled at the tips were used to make electrical contacts on the sample under a microscope. The wires were attached on to the sample surface using silver paste. The other ends of the copper wires were soldered on any four gold coated pads on the puck. Any extra length of the contact wires was arrested on the puck using double sided sticky tape to avoid any spurious signal during field measurements. The puck, after mounting the sample, was inserted to any one of the two sockets on the probe platform shown in Figure 2.6b. For the transverse magneto-resistance (TMR) measurement, the puck was inserted to the socket at the tip, while for the longitudinal magneto-resistance (LMR) geometry, the socket on the side was used. The puck was also wrapped around with teflon tape on the platform to avoid the accidental fall of the crystal in the sample space during measurement. The probe platform was then connected to the measurement probe using a 19 - pin connector.

The magneto-resistance data were collected in both linear and van der Pauw geometries. A photograph of the electrical contacts on the pristine $TaAs_2$ crystal made in the van der Pauw geometry is shown in Figure 2.6c. The crystal is shown alongside a graph paper of grid size 1 mm x 1 mm. The approximate sample dimensions (length x width x thickness) were 1 mm x 1mm x 0.3 mm.

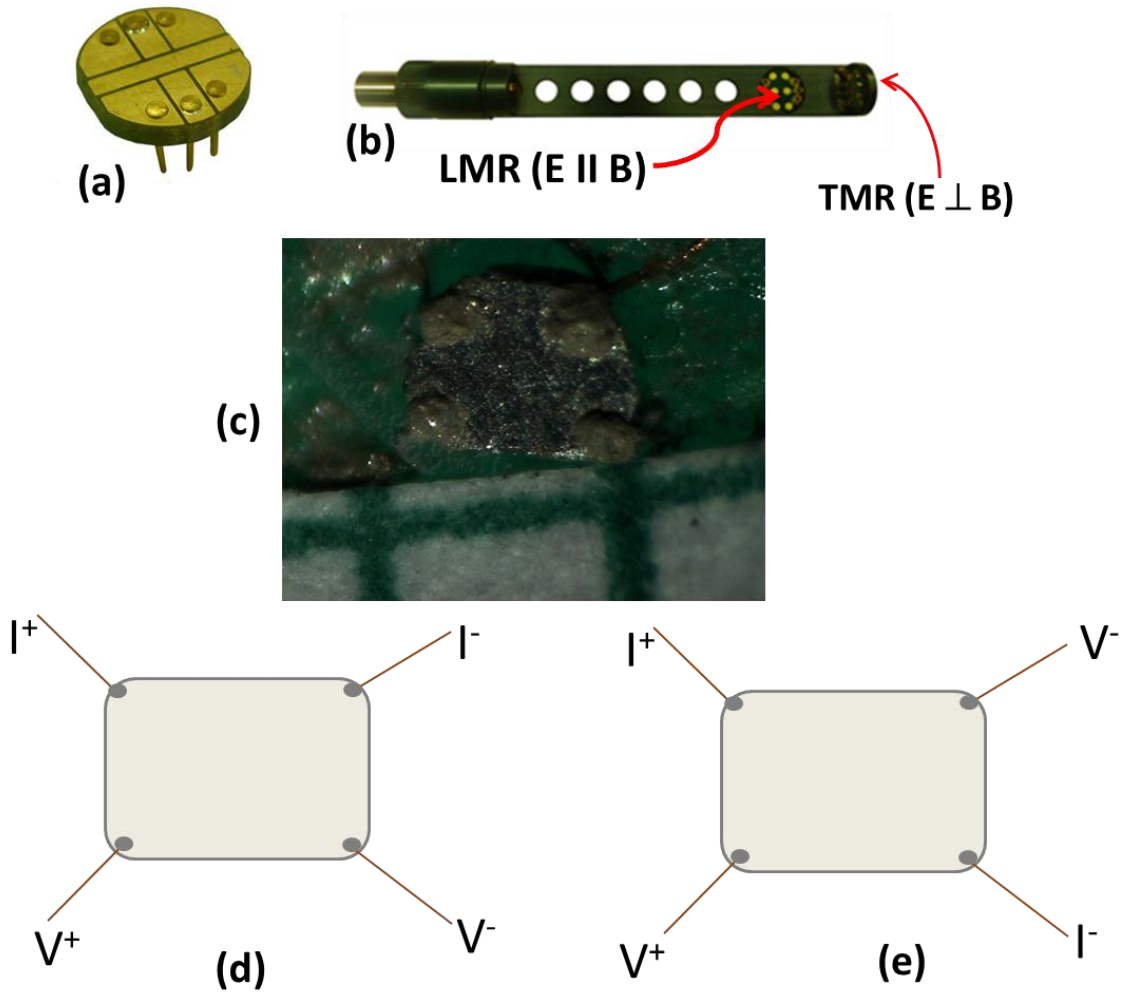

Figure 2.6 Measurement using Cryogenic Ltd system. ***(a)*** *The sample mounting puck.* ***(b)*** *The sample probe platform. Note the two sockets (one facing the reader and the other on the right end) for inserting the puck.* ***(c)*** *Photograph of electrical contacts made in the van der Pauw geometry on the pristine* $TaAs_2$. ***(d)*** *The schematic of van der Pauw geometry for resistance measurement. Transverse and Longitudinal resistances* (R_{xx}) *were obtained from the average of 8 van der Pauw voltages, as explained in the text.* ***(e)*** *The schematic of the Hall resistance* (R_{xy}) *measurement. Four Hall voltages were collected using this geometry. The magnetic field was applied perpendicular to the sample surface.*

The schematic of the resistance measurement is depicted in Figure 2.6d. In the van der Pauw geometry, eight voltages (V_1 to V_8) were collected by swapping the voltage and current terminals, and also after reversing the current directions. Following David et al [54], two resistivities were then evaluated as given below.

$$\rho_A = 1.133\, f_A\, t_S \frac{V_2 - V_1 + V_4 - V_3}{I} \quad \textbf{(2. 1)}$$

$$\rho_B = 1.133\, f_B\, t_S \frac{V_6 - V_5 + V_8 - V_7}{I} \quad \textbf{(2. 2)}$$

where ρ_A and ρ_B are resistivities in $\Omega.\,\mathrm{cm}$, t_S is the sample thickness in cm, V_1 through V_8 are the measured voltages, I is the current in ampere. Typically 10 mA current was sent through the sample. f_A and f_B are geometrical factors based on sample symmetry and are defined as $f_A = 1.0545 - 0.0478\, Q_A$ and $f_B = 1.0545 - 0.0478\, Q_B$. Here, Q_A & Q_B are the resistance ratios given as $Q_A = \frac{V_2 - V_1}{V_4 - V_3}$ and $Q_B = \frac{V_6 - V_5}{V_8 - V_7}$.

Sample resistivity was obtained from the average of ρ_A and ρ_B. Magnetic field was respectively applied perpendicular and parallel to the sample surface in transverse and longitudinal MR measurements. The data were collected under positive and negative magnetic fields, and averaged to eliminate the effect of non-symmetrical contributions of the contacts.

Hall resistance was also measured alongside the transverse magneto-resistance experiments. Figure 2.6e depicts the schematic of Hall resistance measurement. Four diagonal Hall voltages (V_1 to V_4) were measured by reversing the current direction (V_1 & V_2), and also after swapping the voltage and current terminals (V_3 & V_4). Here, magnetic field was applied perpendicular to the sample surface. The resultant Hall voltage was then obtained as

$$V_{Hall} = \frac{V_1 - V_2 + V_3 - V_4}{4} \quad \textbf{(2. 3)}$$

and the Hall resistance is given as $R_{Hall} = \frac{V_{Hall}}{I}$ where 'I' is the magnitude of the current passed.

Figure 2.7a shows the representative results of resistivity versus temperature measurements in $TaAs_2$. It is seen that the metallic behaviour of resistivity at zero field shows an upturn to an "insulating" behaviour in the presence of applied field. Figure 2.7b shows the variation of resistivity with applied field at 2.5 K in $TaAs_2$. A near parabolic variation of resistivity and a non-saturating behaviour with applied field, leading to extreme magneto-resistance, is one of the distinguishing features of these systems. The underlying reason for the metal to insulator type behaviour with applied field is the subject of the thesis. Towards developing an understanding of magneto-transport, Hall effect plays an important role, and the representative result is shown in Figure 2.7c. The Hall data were analyzed in terms of one/two carrier models [30, 55], and these are indicated at respective places in Chapters 4 and 5.

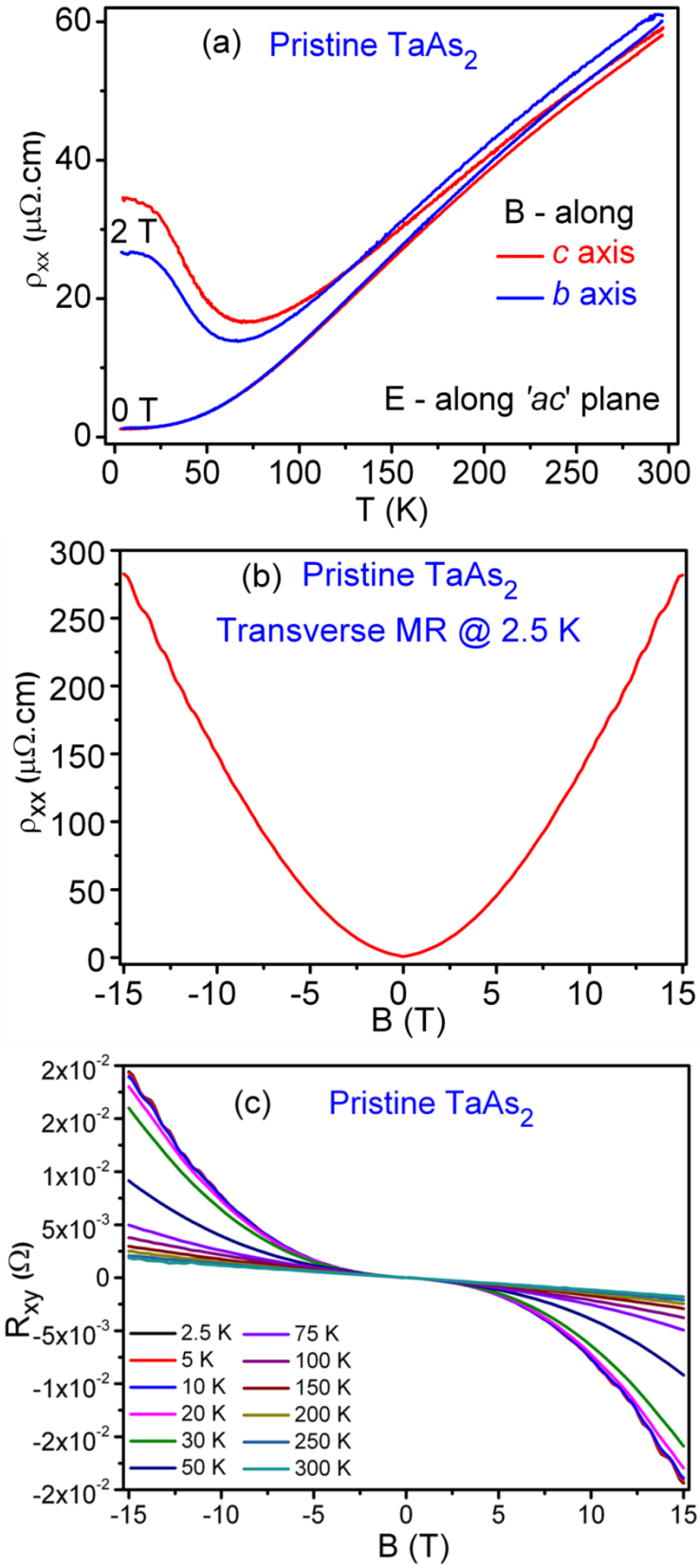

Figure 2.7 Representative results from pristine $TaAs_2$. ***(a)*** *Resistivity as a function of temperature at zero field and at 2 T.* ***(b)*** *Variation of resistivity as a function of field at T = 2.5 K.* ***(c)*** *Hall resistance as function of field at various temperatures.*

2.4.2. Liquid free (2 K, 14 T) PPMS DynaCool cryostat

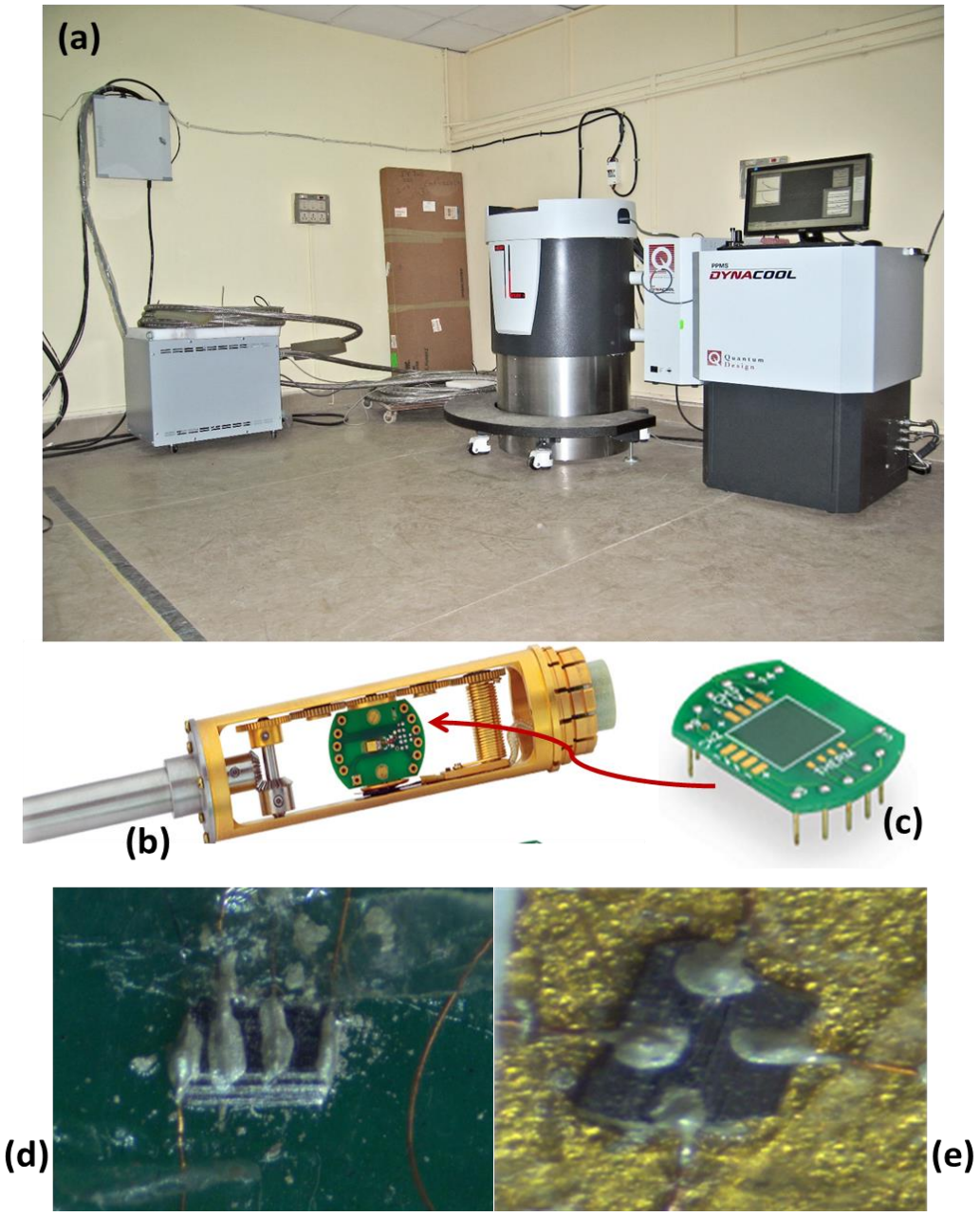

Figure 2.8 ***(a)*** *Photograph of the 14 T Quantum Design PPMS DynaCool setup showing the pulse tube cryo-cooler (left), cryostat cabinet (middle) and the computer controlled data collection system (right).* ***(b)*** *Image of the horizontal rotator of the PPMS cryostat.* ***(c)*** *The Electro Transport Option puck on which samples are mounted.* ***(d)*** *and* ***(e)*** *Four probe electrical contacts made on the pristine $NbAs_2$ sample in linear geometry for magneto-resistance (d), and in cross geometry for Hall resistance measurements (e).*

In addition to Cryogenic Ltd cryostat, some of the experiments were carried out using the Quantum Design make 14 T Physical Property Measurement System (PPMS)-DynaCool experimental facility as shown above in Figure 2.8a. The PPMS

DynaCool employs a two-stage pulse tube cryo-cooler for cooling the superconducting magnet and the temperature control systems. The temperature control can adjust the temperature from 400 K to 1.8 K. The system is equipped with either a 9 T or 14 T conduction-cooled superconducting switch-less magnet system.

The sample was mounted on an Electro Transport Option (ETO) puck that was operated in conjunction with horizontal rotator of the PPMS that are shown in Figure 2.8b and Figure 2.8c. With this, sample could be rotated through 360°, with magnetic field B along the vertical axis, enabling angular dependent magneto-resistance studies. Special attention was given to orient the crystal while mounting it on the puck so that the electric current direction changes as the platform rotate during measurement. Figure 2.8d and Figure 2.8e show photographs of the electrical contacts made on the pristine $NbAs_2$ sample for the magneto-resistance and Hall measurements respectively. In MR measurements, the electrical contacts were made in the four probe linear geometry with 44 SWG copper wires using silver paste. Hall resistance data were collected with a four point cross Hall structure contact geometry.

Representative results from the above PPMS-DynaCool system are shown in Figure 2.9. The system was used to investigate the angular dependence of magneto-resistance that was very useful in clarifying the absence of negative longituinal MR in the di-pnictides. Figure 2.9a shows the result for the pristine $TaAs_2$. This exhibits a cosine variation of magneto-resistance with respect to the angle between magnetic field B and electric field E (or current direction, I). Electric current (typically 10 mA) was sent along the a-axis. The polar plot of the variation of magneto-resistance is shown in Figure 2.9b. It is seen that the magneto-resistance reaches maximum when E and B are mutually orthogonal, and the magneto-resistance shows a minimum when these two fields are

parallel to each other. In particular, the magneto-resistance is positive even in the longitudinal MR configuration. Here both *E* and *B* are along the *a*-axis.

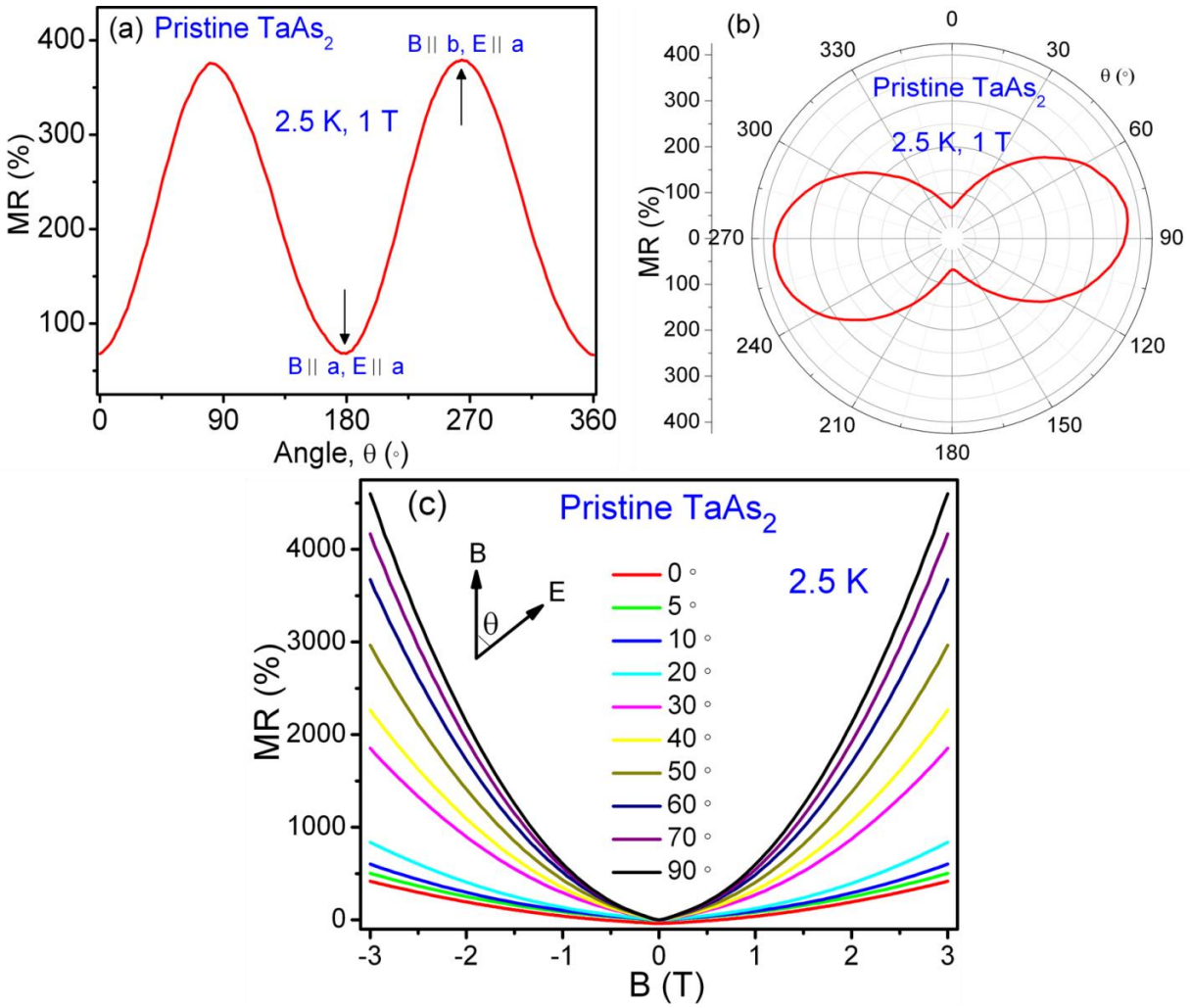

Figure 2.9 ***(a)*** *The angular dependence of magneto-resistance in pristine $TaAs_2$ crystal at 2.5 K with 1 T, measured using the PPMS cryostat in conjunction with the horizontal rotator. MR shows a sinusoidal variation.* ***(b)*** *The polar plot of the angle dependent magneto-resistance in pristine $TaAs_2$ measured at 2.5 K with 1 T field, showing dipolar behaviour.* ***(c)*** *Magneto-resistance measured at the various indicated fixed angles at 2.5 K as function of magnetic field showing a parabolic behaviour. It can be seen that highest MR is observed when sample (electric current) is oriented perpendicular (viz., 90°) to the magnetic field, and it is lowest when current is parallel to B (viz., 0°).*

The variation of resistivity with magnetic field could be carried out at various pre-set angles, and the representative result for pristine $TaAs_2$ is shown in Figure 2.9c. It shows parabolic and non-saturating property of magneto-resistance in $TaAs_2$ at all the angles from 0° (red curve) to 90° (black curve). It is seen that as the angle between *E*

and B fields is changed from orthogonal to parallel orientation, the magneto-resistance shows a gradual decrease and reaches a lowest value when the fields are collinear. Detailed angular dependence of magneto-resistance was performed for the pristine, irradiated and heat treated $NbAs_2$ samples and they are presented in Chapter 4.

In this thesis, apart from magneto-resistance measurements on $TaAs_2$ and $NbAs_2$, de Haas - van Alphen oscillation measurements have been carried out to obtain information on electron transport parameters such as the carrier density and mobility. The relevant experimental facilities and data analysis protocols are described in Chapter 5.

Chapter 3

Magneto-resistance in $TaAs_2$ Single Crystals

This chapter presents the magneto-transport results of chemical vapour transport grown $TaAs_2$ single crystals, performed in magnetic field up to 15 T, from room temperature to 2.5 K. Samples were characterized by Raman spectroscopy. Experiments have been performed in pristine and irradiated samples. It is inferred that the turn on temperature behaviour can be better understood by Kohler's scaling rule rather than as arising due to a metal to insulator transition. Hall resistance studies indicated the role of electrons and holes in the transport, and a two-band analysis provided a nearly carrier compensation picture of the material. By careful measurements performed on both pristine and irradiated samples, the absence of negative longitudinal magneto-resistance in $TaAs_2$ has been confirmed.

3.1. Introduction

Following the experimental realization of Weyl fermions in the transition pnictide mono-arsenide TaAs, there has been an unprecedented surge of interest in the magneto-transport of topological semimetals [56]. Of particular interest has been the family of di-pnictides, such as $TaAs_2$ and $NbAs_2$ [11]. The di-pnictides AB_2 (A = Ta, Nb; B = As, P, Sb) has base centered monoclinic structure (See Figure 1.6a), and belongs to the space group C12/m1 [27, 33]. They are centro-symmetric in contrast to their mono-pnictide counterparts, which lacks an inversion-centre [33], and hence not expected to host Weyl fermions. The electronic structure calculations in $TaAs_2$ (See Section 1.6) indicate that the density of states (DOS) of $TaAs_2$ shows a pseudo gap at the Fermi level, suggesting its semi-metallic character [57]. The density of states calculated by Xu et al [33] is 0.583 states per unit cell per electron volt. The Fermi surface calculations revealed three isolated carrier pockets [33]. The ratio of electron to hole DOS has been estimated

as 1:1.16, suggesting that $TaAs_2$ is nearly compensated [33]. The carrier densities reported in the literature [11, 13, 30] are seen to be in the range of 10^{18} cm^{-3} to 10^{19} cm^{-3}. Thus, while it is clear that $TaAs_2$ is a semimetal, the crucial issue is whether it is a topological semimetal, on which the experimental results reported in the literature have been divergent.

As indicated in Chapter 1, magneto-transport studies in $TaAs_2$ (See Figure 1.7) shows that, with the application of magnetic field, the metallic variation of resistivity exhibits an insulating upturn, and finally saturates at the lowest temperature. This 'upturn temperature' systematically increases with the applied field, and these features are similar to that seen in other semimetals such as graphite and WTe_2 [8, 16]. Experiments on the variation of resistivity as a function of magnetic field show a parabolic and non-saturating nature of resistivity that in turn leads to extremely large MR ~10^5 % in these systems. Previous investigations on $TaAs_2$ present different arguments on the mechanism for the extremely large magneto-resistance (XMR) and the reason for the upturn in resistivity under a magnetic field [11]. The upturns arising due to the large increase in the resistivity in magnetic fields at low temperatures has been interpreted as a metal to insulator transition (MIT) induced by the field [31]. Such a feature was also viewed as arising out of the high mobility of the charge carriers in semimetals [13]. Alternatively, the unique resistivity behaviour under magnetic field has been explained in terms of Kohler's scaling rule (described later in this chapter) in related semimetals WTe_2, LuBi etc. [16, 58]. The magnitude of the resultant XMR has been ascribed to the compensation of electron and hole carriers based on semi-classical approximation [13, 30].

As shown in Figure 1.10, there exist contradictory experimental results on the observation of negative longitudinal MR (NLMR). In the experiments of Luo et al [27], clear signatures of NLMR are seen that has been taken as a signature of chiral anomaly in

Weyl semimetals. However, in the experiments of Wu et al [13], NLMR is not seen (See Figure 1.10b). In fact, the observation of negative MR in di-pnictides has been attributed to measurement related artefacts such as 'current jetting effects' [30].

The discrepancies, as indicated above, compelled us to undertake detailed investigations to get better insights on $TaAs_2$ system. The magneto-resistance data, collected in both transverse and longitudinal geometries, have been analyzed in terms of MIT and on the basis of Kohler's rule. As will be shown, the later methodology provides consistent understanding of the upturn behaviour in temperature dependent resistivity. Further, Hall measurements have been carried out to estimate the carrier density and mobility, with a view to check the importance of charge compensation mechanism on the observed XMR [30, 59].

In the present investigations [45], in addition to experiments on as-grown pristine single crystals of $TaAs_2$, we have carried out experiments on irradiated and heat treated crystals. These studies have been undertaken to alter the density and mobility of carriers, and to see the effect on magneto-transport. In this chapter, we discuss the results of pristine and irradiated samples together.

3.2. Raman Characterization

The synthesized crystals have been characterized by Raman spectroscopy (See Section 2.3.1 for measurement details). Figure 3.1 shows the Raman spectrum obtained from the pristine, irradiated and heat treated $TaAs_2$ samples. Based on the report by Jin et al [52], the nine modes exhibited by the pristine crystal viz., ^1A_g, ^1B_g, ^2A_g, ^2B_g, ^3B_g, ^3A_g, ^5A_g, ^4A_g and ^6A_g were indexed as the Raman active modes (See Figure 3.1a). A systematic shift of all the modes by ~2 cm^{-1} have been observed in the irradiated sample (See Figure 3.1b) which can be understood as mode hardening from irradiation. In non-metallic materials, mode hardening results from the strengthening of bonds between

1^{st} and 2^{nd} neighbour atoms around a vacancy [60]. Sputter yield of As estimated from SRIM calculations showed one order higher magnitude as compared to Ta. Also, As vacancy concentration was double that of Ta (See Figure 2.2b). Hence it is reasonable to state that the irradiation induced defects were mainly due to arsenic vacancies.

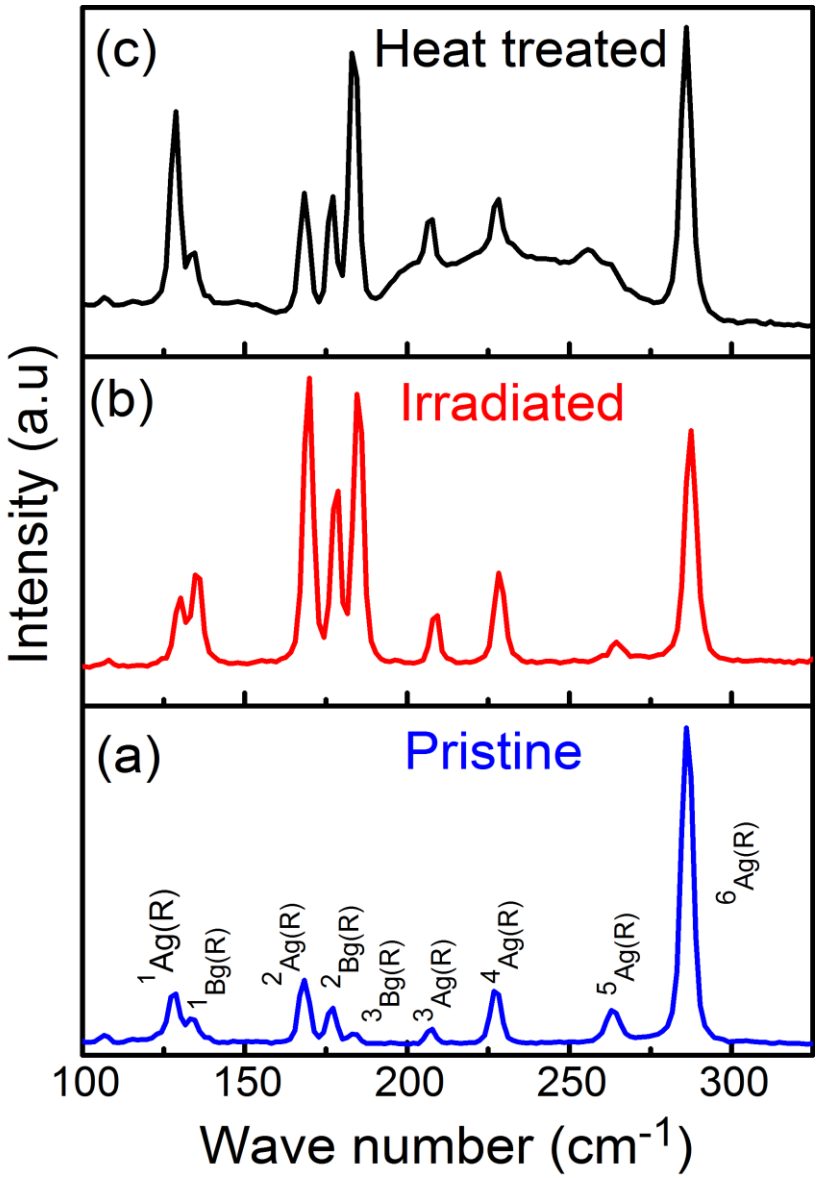

Figure 3.1 Raman spectra of pristine, irradiated and heat treated samples of $TaAs_2$. The mode assignment from Jin et al [52] is shown in the bottom panel.

The Raman spectrum for the sample heat treated at 700 K is shown in Figure 3.1c. Here, the mode hardening is negligible except for $^{4}A_g$ & $^{1}B_g$. However, there is considerable increase in background, observed between 200 cm^{-1} and 275 cm^{-1}, that

suggests disorder. Also, one new peak was seen in the broader region which was identified as an oxide mode (256 cm^{-1}) corresponding to the O-Ta-O bending vibrations in TaO_6 octahedra [61]. Table 3.1 lists all the Raman modes obtained from the pristine, irradiated and heat treated samples.

Table 3.1 Raman modes identified in the $TaAs_2$ samples at each stage. The first two columns are the standard reported data from references [52, 61]. *Columns 3, 4 and 5 give the values obtained from the present studies.*

Mode	Reported value [52] (cm^{-1})	Pristine (cm^{-1})	Irradiated (cm^{-1})	Heat Treated (cm^{-1})
^1A_g (R)	129.0	129	130	129
^2A_g (R)	168.7	168	170	168
^3A_g (R)	207.6	208	209	208
^4A_g (R)	227.9	227	228	228
^5A_g (R)	263.5	263	264	263
^6A_g (R)	286.3	286	287	286
^1B_g (R)	134.6	133	135	135
^2B_g (R)	177.0	177	179	177
^3B_g (R)	183.9	183	184	183
O-Ta-O bending mode (Dobal et al [61])				256

3.3. Transverse Magneto-resistance: Resistance versus Temperature shows upturn under a Magnetic field

The transverse magneto-resistance measurements in the pristine $TaAs_2$ sample have been carried out with four probe method in linear and van der Pauw geometries, as discussed in Section 2.4.1 of Chapter 2. The magnetic field was applied along the *b*-axis of the crystal. Uniformly polished crystals were used for measurements. The approximate sample dimensions (length x breadth x thickness) used for the linear geometry was 2.3 mm x 1.1 mm x 0.88 mm, while for the van der Pauw geometry it was 0.5 mm x 0.5 mm x 0.29 mm. Experiments on the irradiated sample (0.5 mm x 0. 5 mm x 0.41 mm) and heat treated sample (1 mm x 0.5 mm x 0.34 mm) have been performed in the van der Pauw geometry. For resistance measurements, an electrical current of 10 mA was sent along the *a*-axis in linear geometry or along the *ac*-plane in van der Pauw geometry such

that in either case the magnetic field and electric current were mutually perpendicular to each other. Magneto-resistance measurements have been carried out between ±15 T field in the 300 K to 3 K temperature interval using the facility described in Section 2.4.1.

Figure 3.2 shows the temperature variation of magneto-resistivity, $\rho\,(T, B)$ in the pristine and irradiated samples, measured under magnetic fields up to 14 T. We will initially look at the resistivity behaviour upon varying the temperature, $\rho\,(T)$ in the absence of an externally applied magnetic field. The zero field resistivity is metallic in pristine and irradiated samples as seen from the black curves of Figure 3.2. Upon lowering temperature from 300 K, the resistivity was seen monotonously decreasing with a positive temperature coefficient and finally saturates below 50 K. In the pristine sample, resistivity at the lowest temperature ($\rho_{residual}$) was $0.54\ \mu\Omega.\,\mathrm{cm}$ and the residual resistivity ratio (RRR) was 53. Surprisingly, the irradiated sample exhibited slightly lower residual resistivity ($0.39\ \mu\Omega.\,\mathrm{cm}$) and a higher RRR (62). The high residual resistivity ratios indicate the good quality of the synthesized crystals. The resistivity data below 80 K could be fitted to the Fermi liquid model $\rho\,(T) = \rho_{residual} + a \star T^m$ where 'm' was found to be 2.52 ± 0.01 and 2.62 ± 0.01 in the pristine and irradiated samples respectively. These values of 'm' lies between that reported for $TaAs_2$ by Butcher et al [62] (m = 2.4) and Yuan et al [30] (m = 2.7 to 3). It indicates that the scattering in the system is not purely due to electron - electron interactions for which m = 2 [3, 16]. Identical values of 'm' in other semimetals such as WTe_2 (m = 2.7) [63], LaBi (m = 2.99) [64] and $NbSb_2$ (m = 2.5) [65] have been observed [66].

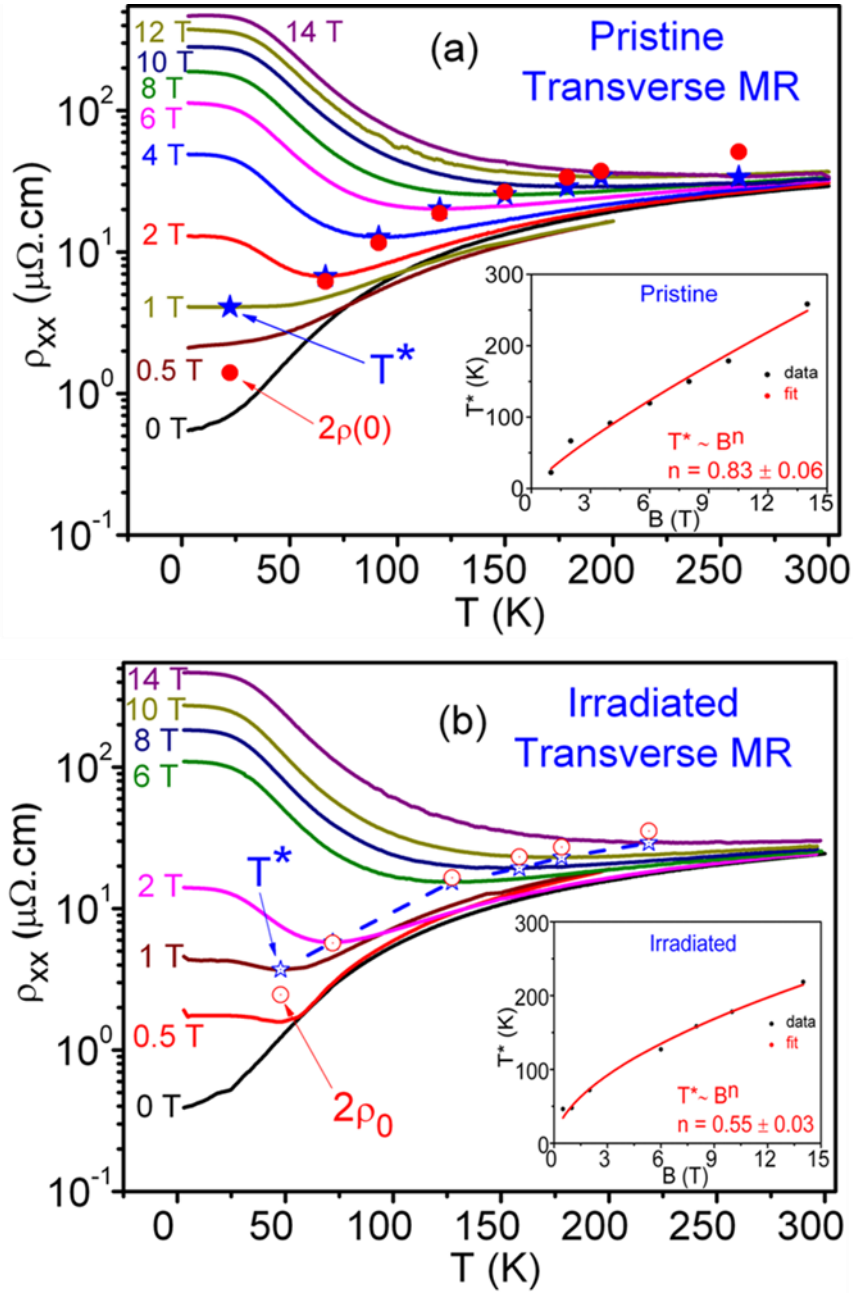

Figure 3.2 The temperature variation of resistivity at various constant magnetic fields in ***(a)*** *Pristine $TaAs_2$ and* ***(b)*** *Irradiated $TaAs_2$, displaying upturns below a resistivity minimum ρ^*. Resistivity saturates at very low temperatures. The temperature T^*(shown by stars), corresponding to ρ^* location, match with the respective points of $2\rho_0$ (circles) with respect to the zero field profile as predicted by the Kohler's rule (See Section 3.4.1). The insets depict the fit of the B^n behaviour of T^* (See Section 3.3).*

In measurements under a magnetic field, $\rho\,(T, B)$, the pristine sample (See Figure 3.2a) retains the metallic behaviour with 0.5 T also, but with an increase of residual resistivity. Upon increasing the field to 1 T, the resistivity shows a minimum around 50 K.

When the sample is cooled beyond this resistivity minimum, the temperature coefficient of resistivity becomes negative and with further cooling resistivity increases, resulting in an upturn in the $\rho\ (T, B)$ curve and finally saturates at the lowest temperatures. With higher magnetic fields, as the sample is cooled, resistivity shows clear upturns at certain temperature and saturates below ~ 40 K where it give rise to resistivity plateaus. It is noted that with an increase of magnetic field the resistivity minimum (ρ^*) shifts to higher temperature (T^*) values as indicated by the stars in Figure 3.2, producing clear resistivity upturns and leading to an extremely high magneto-resistance in the plateau region. With 14 T, the pristine sample shows an XMR $\approx\ 8.47 \times 10^4$ % at 2.5 K. These kinds of resistivity profile can essentially be summarized as metallic at high temperatures, which turns to semiconducting like variation at an intermediate temperature and finally shows plateaus in the lowest temperatures. This type of resistivity variation has observed in $TaAs_2$ [13, 27], in other transition di-pnictides [17, 65] and in many novel semimetals such as WTe_2 [59], LaBi [64], $PtBi_2$ [67], transition metal pnictides [11, 42, 68] as also in archetypical semimetals bismuth and graphite [69]. Such a resistivity behaviour has been variously interpreted as a metal to insulator transition in an applied magnetic field [55] or a temperature induced Lifshitz transition caused by significant electronic structure change [70], as alluded to in Chapter 1 (See Section 1.2).

The measurements from the irradiated $TaAs_2$ also displayed qualitatively similar features such as upturns in resistivity curves and the subsequent formation of plateaus in magnetic fields as evident from Figure 3.2b. But, a distinguishing feature is that the resistivity minimum appears with 0.5 T itself. This is clearer when we look at the low field resistivity behaviour, as shown in Figure 3.3. The higher MR 1.2×10^5 % seen in the irradiated sample is due to the lower zero field resistivity.

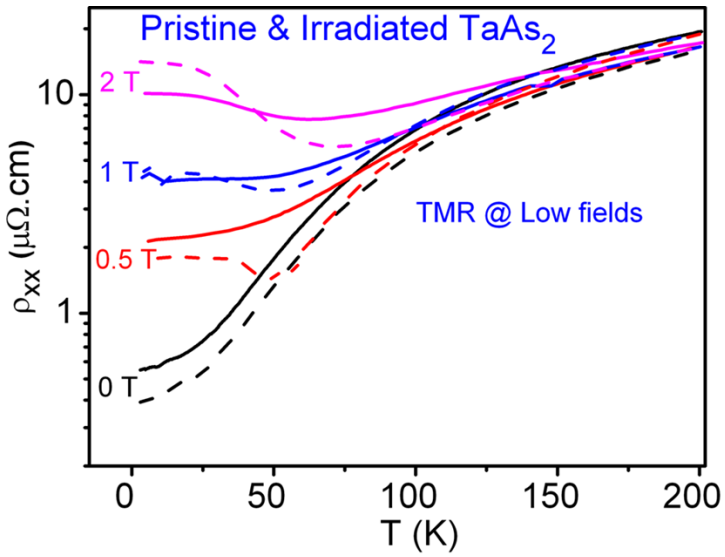

Figure 3.3 The resistivity variation of pristine (solid lines) and irradiated (dashed lines) $TaAs_2$ samples at low values of magnetic field. Note the decreased zero field resistivity after irradiation.

The temperature at which the upturn in resistivity occurs (See Figure 3.2), designated as the 'turn on' temperature (T^*) and that of the beginning of the resistivity plateau, while cooling, is $T_{plateau}$, and their variation with magnetic field are plotted in Figure 3.4. These temperatures have been deduced from a plot of differential resistivity ($\frac{\partial \rho}{\partial T}$) against temperature [31], with the points where $\frac{\partial \rho}{\partial T} = 0$ correspond to the values of T^* (indicated by the stars in Figure 3.2), and the minimum of the differential resistivity is considered as $T_{plateau}$. It can be seen that T^* increases with an increase of magnetic field while $T_{plateau}$ remains more or less the same. It is to be noted that T^* and $T_{plateau}$ values are more or less identical in both pristine and irradiated samples.

Qualitatively, the results in Figure 3.4 can be partitioned into three regions to differentiate the MR behaviour in a varying temperature and magnetic field. In the region-I wherein $T > T^*$, the resistivity follows a metallic temperature dependence and magneto-resistance is very small or negligible. The region-II, defined by $T_{plateau} < T < T^*$, is the region where upturn in resistivity is seen. The MR is determined by both magnetic field and temperature, and its rate of change is largest in this

region. The third region ($T < T_{plateau}$), where resistivity plateaus appear, exhibits the highest MR. Resistance in this area is affected by magnetic field only. This "phase diagram" serves to illustrate that the effect of temperature and magnetic field on the resistance of $TaAs_2$ is intricately intertwined to each other, and is challenging to delineate the role of one from the other, as also seen in the case of other topological semimetals [64, 71].

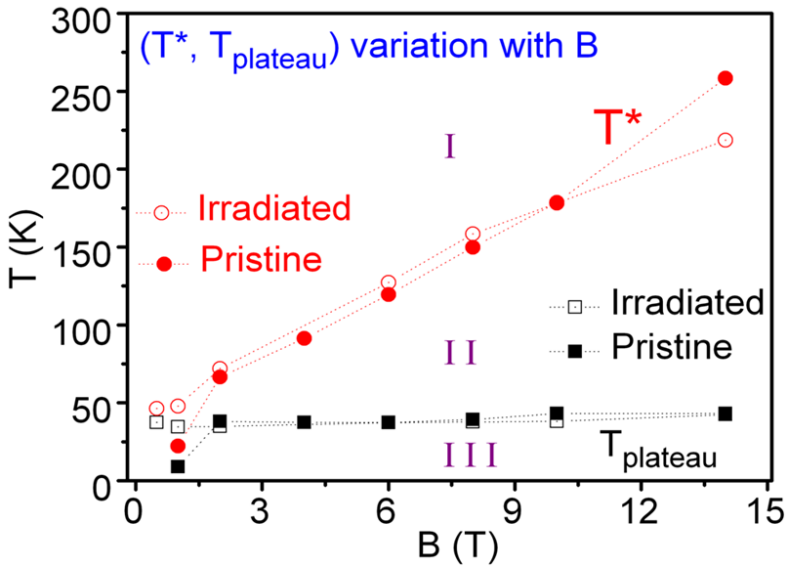

Figure 3.4 The upturn temperature T^* and $T_{plateau}$ are plotted against the applied magnetic field for the pristine and irradiated samples. The T^* value grows with increasing field, while $T_{plateau}$ remains the same.

The origin of the observed resistivity upturns under an applied magnetic field, as seen in Figure 3.2, has been a widely debated issue in the magneto-transport investigations of many semimetals, particularly in XMR materials [16, 20, 59, 64, 70-72]. The nature of T^* growth with B has been ascribed to a critical field behaviour [73] leading to a magnetic field induced metal to insulator transition [17], as has been done in the semimetals like graphite and Bi [9] and also in the novel semimetals [17]. The critical field B_C that triggers the semimetal to insulator transition and the temperature at which this behaviour sets in follows the relation, viz. $T^* \approx (B - B_C)^{\frac{1}{2}}$. Although we see a field dependent characteristic temperature T^* in the present studies (See Figure 3.4), our

attempt to fit the data to a critical behaviour was unsuccessful. In our case, the 'turn on' temperature fitted to $T^* \sim B^n$, rather than $(B - B_C)^n$, with $n = 0.83 \pm 0.06$ in the pristine and $n = 0.55 \pm 0.03$ in the irradiated samples. These fits are given as insets of Figure 3.2. Having failed to explain the variation of T^* with applied field in terms of the critical behaviour, we rationalize the upturn behaviour, as seen in Figure 3.2, in terms of the Kohler's rule, as has been done in the case of WTe_2 [16]. We pursue this in the next section.

3.4. Kohler's Rule: Magneto-resistance follows Scaling Laws

Before we analyze the experimental data as shown in Figure 3.2 in terms of the Kohler's scaling relation, we provide a brief introduction to the Kohler's rule and its validity, to supplement the contents in Section 1.4. The magneto-resistance due to the orbital motion of the charge carriers can be understood using a classical law known as the Kohler's scaling rule [3]. According to this rule, the magneto-resistance measured at various temperatures and magnetic fields can be scaled to a single curve, if the relaxation rate of the carriers has single temperature dependence at all points on the Fermi surface during the magneto-transport [74]. i.e., in order for Kohler's rule to hold, the anisotropy in the relaxation rate should be temperature independent [75].

The Kohler's rule expresses the MR due to an applied magnetic field B as a function of the product of the cyclotron frequency (ω_c) of the carriers and the relaxation time (τ) for the orbits in a plane orthogonal to B [4]:

$$MR = f(\omega_c \tau) \qquad \textbf{(3. 1)}$$

Since relaxation time has a reciprocal relationship with the zero field resistivity, $\rho_0 = \frac{m^*}{(ne^2\tau)}$, and $\omega_c = \frac{eB}{m^*}$ where n, e and m^* are the volume density, charge and the effective mass of the carrier, the Kohler's relation can be written as

$$MR = f\left(\frac{B}{ne\rho_0}\right) = \alpha\left(\frac{B}{ne\rho_0}\right)^m$$

(3. 2)

wherein α and m are constants depending on the external geometry of the material and its intrinsic electronic structure [14]. In general, they are independent of the value of ρ_0 and the defect concentration in the material [76]. If the carrier density does not change with temperature, this can be further simplified to

$$MR = \alpha\left(\frac{B}{\rho_0}\right)^m$$

(3. 3)

This essentially defines the Kohler's rule, and the plots of $\frac{\Delta\rho}{\rho_0}$ (MR) versus $\frac{B}{\rho_0}$ are known as Kohler plots [4]. In general, the Fermi surface geometry and topology does not matter for its validity across samples [74].

Kohler's rule is obeyed by conventional metals with Fermi liquid behavior. In conventional metals having quadratic MR, (See Chapter 1) the coefficient of B^2 is proportional to the transport scattering time (τ) associated with the orbital MR effect [77]. Since ρ_0 is proportional to $\frac{1}{\tau}$, plots of $\frac{\Delta\rho}{\rho_0}$ versus $\frac{B}{\rho_0}$ should collapse on a single line. The scaling can be understood as follows [4]: an increase of B results in a higher collision rate that only scales down the pattern of electron behavior without changing the character. As distinct charge carrier species will have different effective masses and a resulting spread in their velocities, they may encounter dissimilar scattering mechanisms resulting in distinct relaxation times, given their varied concentration and mobilities [78]. Hence systems with multiple types of carriers, as in the case of most semimetals, can show deviation from the Kohler's scaling [79, 80].

Historically, Kohler's rule has been formulated as an empirical relation to explain the magneto-resistance in single band metals for which carrier density, to an extent,

independent of temperature variation and impurity content [81]. Basically, it says that if we make a metal with higher and higher purity, it will show larger and larger magneto-resistance [82]. This is ingrained in the Kohler relation as it is defined in terms of the zero field resistivity (ρ_0) which is an indicator of the purity of the material. Over time, Kohler's law has been found useful in interpreting the magneto-resistance data in a variety of systems [75, 77] including, but not limited to, superconductors [14, 15], iron arsenide systems [80, 83] etc. Recently, this rule has gained attention to account for the extremely large MR in the novel topological materials [20, 82] that includes the Weyl [78] and Dirac [67] semimetals [72]. Investigations on the layered transition metal di-chalcogenide member WTe_2 have regenerated interest in the applicability of Kohler's scaling relations to interpret the XMR [16, 21]. Now we are demonstrating that Kohler's rule can really help us in understanding the magneto-resistance behaviour in our $TaAs_2$ samples.

3.4.1. Transverse MR obeys Kohler's Rule

We have analyzed our resistivity data of Figure 3.2 in terms of Kohler's rule and the results are given in Figure 3.5. The plots show that the visibly diverging $\rho(T)$ curves exhibiting large resistivity variations when measured under several constant magnetic fields collapse into a single curve, endorsing Kohler's scaling relation. A noticeable feature in the Kohler's plot of the pristine sample (See Figure 3.5a) is that the collapsed curve is not a straight line, but it has different slopes in the low and high MR regions. The low MR and high MR regions respectively correspond to the higher and lower temperature sides. However, for the irradiated sample (See Figure 3.5b) there is no apparent slope change. The agreement of Kohler's scaling implies that the application of magnetic field does not change the scattering process in the $TaAs_2$ samples [19]. The exponent 'm' in equation (3. 3) can be evaluated from the slope of the Kohler plot. A fit of the collapsed

line in the high MR region in the pristine sample gave $m \approx 2 \pm 0.01$, while in the irradiated sample $m \approx 2.1 \pm 0.01$, close to the value reported for WTe_2 ($m = 1.92$) [16]. The value of 'm' has often been considered as a measure of the degree of compensation of various types of charge carriers in the system [58, 72]. In particular $m = 2$ is taken to be an indication of perfectly balanced electron – hole densities [84].

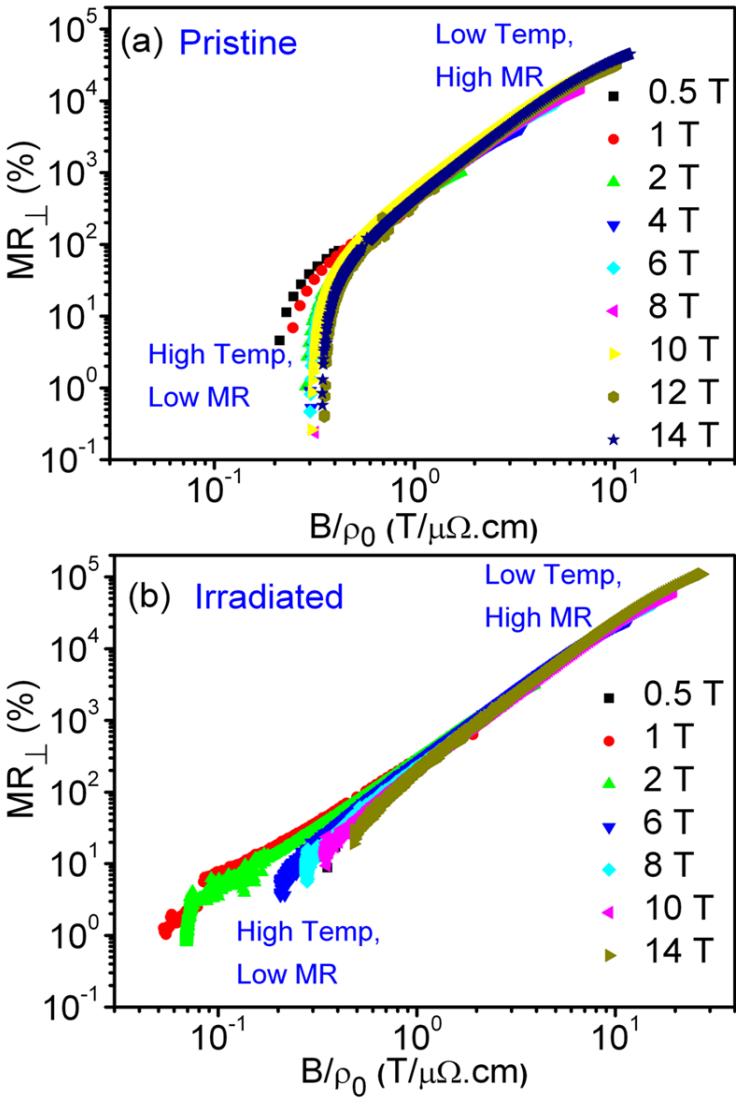

Figure 3.5 ***(a)*** *and* ***(b)*** *Kohler plots, generated from the temperature dependence of transverse magneto-resistivity, for the pristine and irradiated $TaAs_2$ samples. All the curves measured at various constant magnetic fields collapse on to a single curve in agreement with Kohler's scaling rule. It is to be noted that the pristine sample exhibits two slopes, while the irradiated sample bears a single slope.*

As will be shown in the following, the Kohler scaling behaviour also helps to rationalize the upturn behaviour seen in Figure 3.2. Following Wang et al [16] and other related reports [20, 58, 85], we can recast equation (3. 3) as

$$\frac{(\rho - \rho_0)}{\rho_0} = \alpha \left(\frac{B}{\rho_0}\right)^m$$

Further rearrangement will give us

$$\rho(T,B) = \rho_0(T) + \frac{\alpha B^m}{\rho_0^{m-1}}(T,B)$$

(3. 4)

Thus, it is seen that the change of resistance upon varying temperature under an applied magnetic field can be decomposed into two parts: The zero field resistivity $\rho_0(T)$ and the field induced resistivity component contained in the second term on the right of equation (3. 4). We see that the first term is proportional to ρ_0, while the second term has an inverse dependence on ρ_0 when $m = 2$. Since both components are functions of temperature (T), a variation in T will result in their reciprocal variations that show opposing changes. These mutually competing terms will result in a minimum at certain temperature in the total resistivity profile of $\rho\,(T,B)$, which we had assigned as the 'turn on' or 'resistivity minimum' temperature T^*.

In order to illustrate this, we show the temperature variation of resistivity at zero field and at 6 T in both pristine and irradiated samples in Figure 3.6a and Figure 3.6b respectively. It can be seen from the figures that at some temperature, the 0 T resistivity and the difference component reaches the same value and a minimum in the total resistivity appears at this temperature (T^*). If we plot Figure 3.6 with different fields, it will be clear that the resistivity minimum occurs corresponding to the temperature where the difference component crosses the 0 T curve. This is why the T^* values are seen varying as a function of magnetic field. It is also seen that equation (3. 4) predicts a rather

simple relation for the resistivity minima [16]: $\rho^*(T) = [1 + (m-1)^{-1}]\,\rho_0(T)$. Further, since $m \approx 2$ in both of our samples, the resistivity minima are expected to have a value of $\rho^*(T) = 2\rho_0(T)$. Thus obtained $\rho^*(T)$ values at various applied fields are indicated as closed circles in Figure 3.2a that is seen to match with the numerically estimated minima positions indicated by stars. The corresponding results for the irradiated sample of $TaAs_2$ are shown in Figure 3.2b. This good agreement of the minima positions provides another support that the temperature dependence of resistivity under magnetic field can be well explained with the Kohler rule.

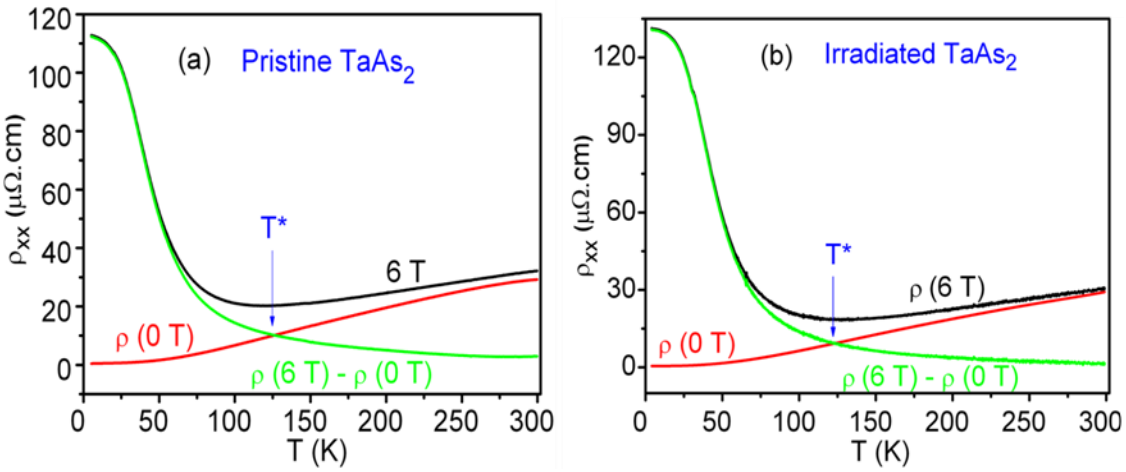

Figure 3.6 ***(a)*** *and* ***(b)*** *Decomposition of resistivity under an applied magnetic field (6 T) as suggested by Kohler scaling relation in the pristine and irradiated $TaAs_2$ samples. The red curve is the zero field profile. The green curve depicts the difference component from the total resistivity (black curve) with 6 T.*

3.5. Normalized Magneto-resistance has Identical Temperature Dependence: No Signatures of MIT

We have seen the applicability of Kohler's rule to explain the upturn in resistivity. The absence of MIT can also be appreciated in another way. The calculated transverse MR at the indicated fixed magnetic fields from the data in Figure 3.2a for the pristine sample is given in Figure 3.7a. The magneto-resistance increases monotonically with the lowering of temperature, with a larger increase at higher magnetic fields. There is no evidence for a jump / discontinuity that signals sudden gap opening. When the MR curves are normalized

with their corresponding values at 6 K, all the curves are seen to collapse onto a single curve as shown in Figure 3.7b. The results obtained from the analysis of the data from the irradiated sample are given in the lower panels of Figure 3.7. The normalized MR at all the fields has similar temperature dependence. Hence the upturn behaviour, starting at T^*, cannot be considered as an indication of the onset of a metal to insulator transition. A drastic increase in MR is observed below 100 K at all fields, irrespective of the position of T^* in the various resistivity curves of Figure 3.2. As will be shown in the next chapter, this temperature dependence of MR is linked to the temperature dependence of mobility.

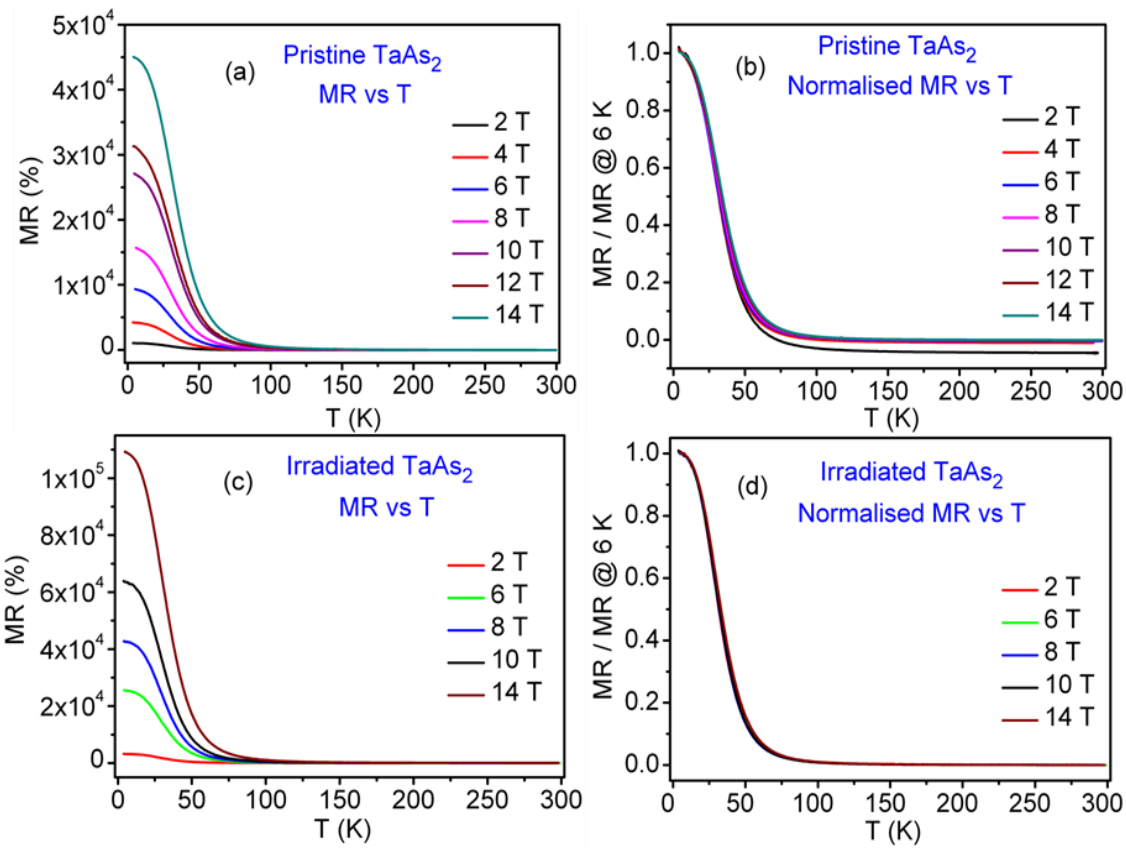

Figure 3.7 ***(a)*** *The temperature variation of transverse MR for the pristine sample. The data when normalized with the MR at 6 K collapse to single line as seen in* ***(b)****. Similar plots for the irradiated sample are given in the bottom panels* ***(c)*** *and* ***(d)****.*

3.6. Field dependent (Isothermal) Resistivity Measurements: Non-saturating MR

In addition to resistivity measurements by varying temperatures under constant fields (described in Section 3.3), experiments were also carried out by varying the magnetic field under isothermal conditions. The field dependent resistivity measurements have been performed up to ±15 T at several temperatures from 2.5 K to 300 K. The results are given in Figure 3.8a and Figure 3.8b respectively for the pristine and irradiated $TaAs_2$. The resistivity in both samples shows non-saturating, near parabolic variation with magnetic field. This will be discussed subsequently in Section 3.6.1. The curves for the four lowest values of temperatures are collapsed on each other as they come within the plateau region of Figure 3.2, where magneto-resistance is independent of temperature. It is noted that (See Figure 3.8a) at the lowest temperatures, magneto-resistivity displays Shubnikov - de Haas (SdH) oscillations and these are analyzed and discussed in Chapter 5.

The plots in Figure 3.8c and Figure 3.8d show that the transverse MR measured at various constant temperatures, from 2.5 K to 300 K, in pristine and irradiated $TaAs_2$ samples can be scaled into a single line conforming to Kohler's law. Remarkably, the two slope feature present in the Kohler plot of pristine sample generated from the $\rho(T)$ data (See Figure 3.5a) is now absent when the Kohler plot is constructed from $\rho(B)$ curves. We also note that, now the slope of the Kohler plot of the pristine and irradiated samples are 1.6 ± 0.1 and 1.8 ± 0.1 respectively.

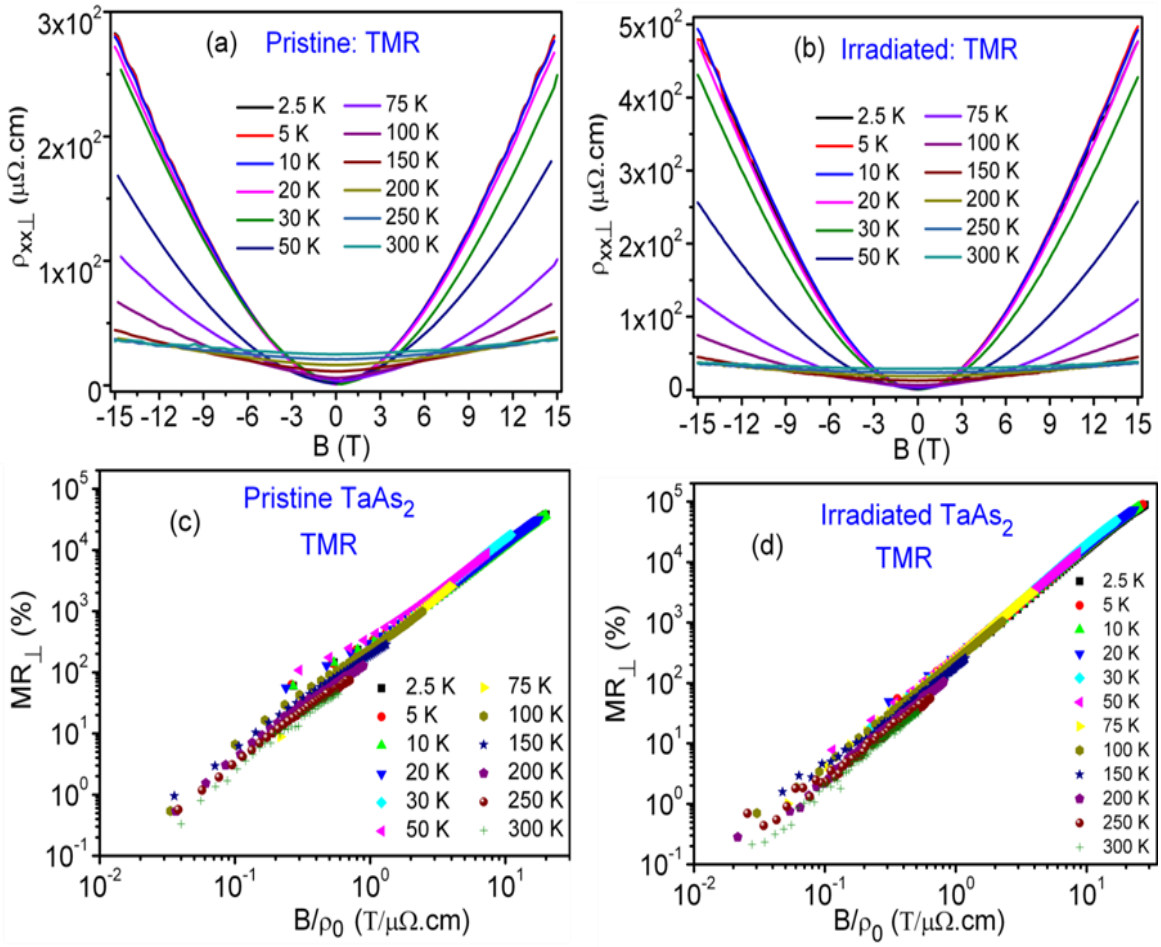

*Figure 3.8 The isothermal transverse magneto-resistance measurements in the **(a)** Pristine and **(b)** Irradiated $TaAs_2$ samples, exhibit a parabolic and non-saturating resistivity behaviour. **(c)** and **(d)** Kohler plots generated from various isothermal conditions for the pristine and the irradiated samples showing agreement with Kohler scaling law.*

In addition to experiments on pristine and irradiated crystals, MR measurements were also carried out on heat treated samples. Magneto-resistance of the $TaAs_2$ sample, heat treated at 700 K, was measured in the transverse geometry at selected isothermal conditions from 5 K to 200 K, and is shown in Figure 3.9a. Resistance variation was nearly quadratic (B^m with $m \approx 1.8 \pm 0.1$) with the applied field. MR reaches a non-saturating value of 8.7 x 10^4 % at 3 K and 14 T, close to the MR in pristine sample. All the isotherms in Figure 3.9a could be scaled to a single line in accordance with Kohler's rule and is presented in Figure 3.9b. The scaled curves fall on a straight line with a slope of 1.8 ± 0.1.

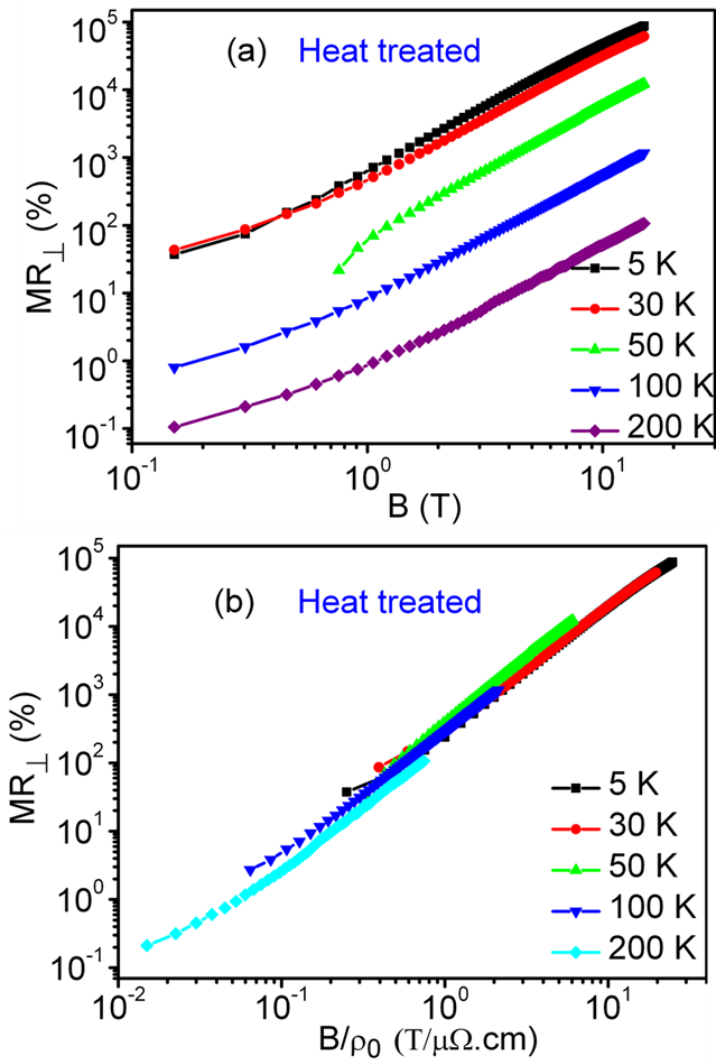

Figure 3.9 ***(a)*** *Transverse magneto-resistance of the heat treated $TaAs_2$ sample is plotted against the applied field at the indicated isothermal conditions.* ***(b)*** *MR versus $\left(\frac{B}{\rho_0}\right)$ plot generated from the data in (a) shows agreement with Kohler scaling rule.*

Thus, through experiments on pristine, irradiated and heat treated samples of $TaAs_2$, we have shown the validity of the Kohler's scaling relation, with an exponent ~ 2. The significance of the exponent value of 2 can be appreciated as follows: The Kohler's rule is derived from the Boltzmann transport relation [3], and the magnetic field enters in Boltzmann equation as a combination of $(B\tau)$. As will be shown in the next section, MR has a quadratic dependence on the magnetic field. Hence a plot of MR against $(B\tau)^2$ or

equivalently $\left(\frac{B}{\rho_0}\right)^2$ should collapse onto a temperature independent single line [15], as is reflected from the exponent 2 in the above Kohler plots.

3.6.1. Functional dependence of MR on Magnetic field

As mentioned in Chapter 1 (See Section 1.1), the functional behaviour of resistivity with magnetic field provides insights into the transport behaviour [4, 5]. For example, the resistivity has a B^2 dependence for compensated semimetals bismuth and graphite in weak fields, and at high fields when the quantum effects are dominant, the resistivity has a linear behaviour [86, 87]. The non-saturating nature of resistivity provides information on the extent to which charge carriers are compensated in semimetals [3]. Figure 3.10a shows the resistivity variation with magnetic field, $\rho_{xx}(B)$, at the four lowest temperatures for the pristine (solid lines) and irradiated (dashed lines) $TaAs_2$ samples. The $\rho_{xx}(B)$ values have been calculated as the average of resistivity from $\rho_{xx}(+B)$ and $\rho_{xx}(-B)$ measurements, obtained during the positive and negative directions of magnetic field. This is converted to magneto-resistance using the formula $(\frac{\rho_{xx}(B)-\rho_{xx}(0)}{\rho_{xx}(0)}) \times 100\ \%$ and is shown in Figure 3.10b in a log-log plot. Magneto-resistance reaches beyond 10^4 % at 2.5 K under 14 T without any sign of saturation.

We see from Figure 3.10b that magneto-resistance in both samples exhibit a power law, $MR = a \star B^m$, on the field B in which 'a' is a constant. However the power law behaviour is dependent on the strength of the applied magnetic field, the temperature and the sample in agreement with other reports [11, 30]. In the pristine sample, around 2 T, the exponent 'm' changes its value from $m = 1.25 \pm 0.01\ to\ 1.7 \pm 0.004$. While this feature of change of slope is prominent at temperatures below 30 K viz., in the resistivity plateau region, for higher temperatures the MR follows near quadratic behaviour ($m > 1.7$) all throughout the magnetic field. The corresponding measurements on the

irradiated sample display near quadratic MR variation ($m \approx 1.80 \pm 0.04$) in the entire measured field range as evident from the dashed lines of Figure 3.10b.

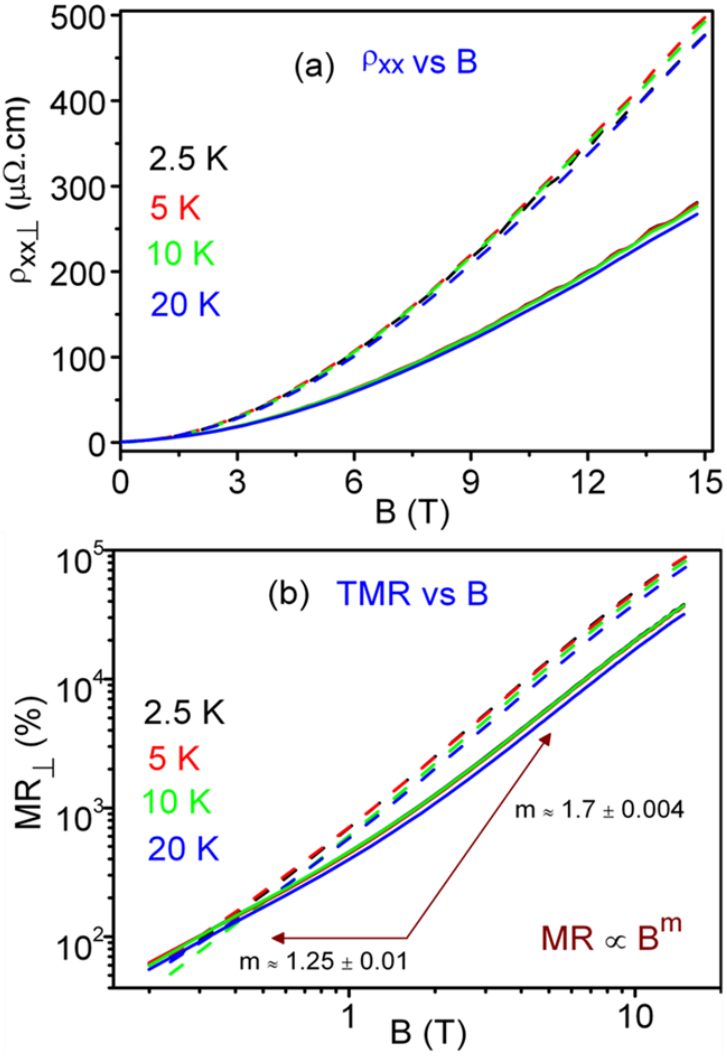

Figure 3.10 ***(a)*** *The isothermal resistivity variation with magnetic field in the resistivity plateau region for the pristine (solid curves) and the irradiated (dashed curves) $TaAs_2$ samples showing parabolic behaviour.* ***(b)*** *The resistivity data when converted to MR exhibits two slopes in the pristine sample. The varying curvature between the pristine and irradiated samples may be due to the difference in the coefficient of B^m.*

The literature [13, 30, 31] on $TaAs_2$ report that magneto-resistance is found to have nearly a parabolic dependence on the field, although Luo et al [27] mentions that the exponent 'm' decreases slightly at higher fields. In the case of $TaSb_2$, another transition di-pnictide, a change of slope in MR versus B and a lower exponent at fields less than 1 T

has been reported [73]. This has been attributed to the existence of an 'activation field' that triggers magneto-resistance [73]. While we find a change of slope in the pristine $TaAs_2$, we do not find that in the irradiated sample of $TaAs_2$, though both of these samples show upturn behaviour in resistivity beyond a certain field during the temperature dependent measurements (See Figure 3.2). It indicates that the assignment of the knee to a critical field may not be appropriate [77].

3.7. Hall Experiments: Non-linear Hall resistance and Charge Carrier Compensation

As indicated in Chapter 1, the large and non-saturating magneto-resistance property in semimetals has been ascribed to the charge compensation involving different types of carriers belonging to various energy bands [3]. In order to check this for $TaAs_2$, as suggested in some reports [13, 30], we have performed detailed Hall resistance experiments in both pristine and irradiated $TaAs_2$ samples.

Hall measurements have been carried out at different isothermal conditions in a varying magnetic field alongside the transverse magneto-resistance experiments (described in Section 3.6) in the van der Pauw geometry. A total of four Hall voltages have been collected by reversing the polarity of the current, and suitably averaged [88]. The resistance obtained in both directions of the field, $R_{xy}(+B)$ and $R_{xy}(-B)$ from +15 T to -15 T, was averaged properly in order to remove any asymmetry caused by the misalignment of voltage leads. The symmetrized Hall resistance $R_{xy}(B)$ for the pristine sample at the indicated temperatures is given in Figure 3.11a. It is linear at low fields and higher temperatures, but turns to non-linear at temperatures below 100 K. This indicates the role of multiple carriers [3, 4] - electrons and holes - in the transport of $TaAs_2$ [30]. It is seen that the Hall coefficient (R_H), depicted in Figure 3.11b is negative in the whole measurement without changing its sign. This indicates that electrons are the dominant charge carriers in the 2.5 K - 300 K range. We recall that band structure calculations by

Xu et al [33] predicted a hole dominant system. However, the earlier studies [13, 27] showed a slightly higher electron concentration in $TaAs_2$ in agreement with the present observations. The measurements on irradiated sample also gave qualitatively similar variation of $R_{xy}(B)$ and $R_H(B)$, though with higher non-linearity, as shown respectively in Figure 3.11c and Figure 3.11d.

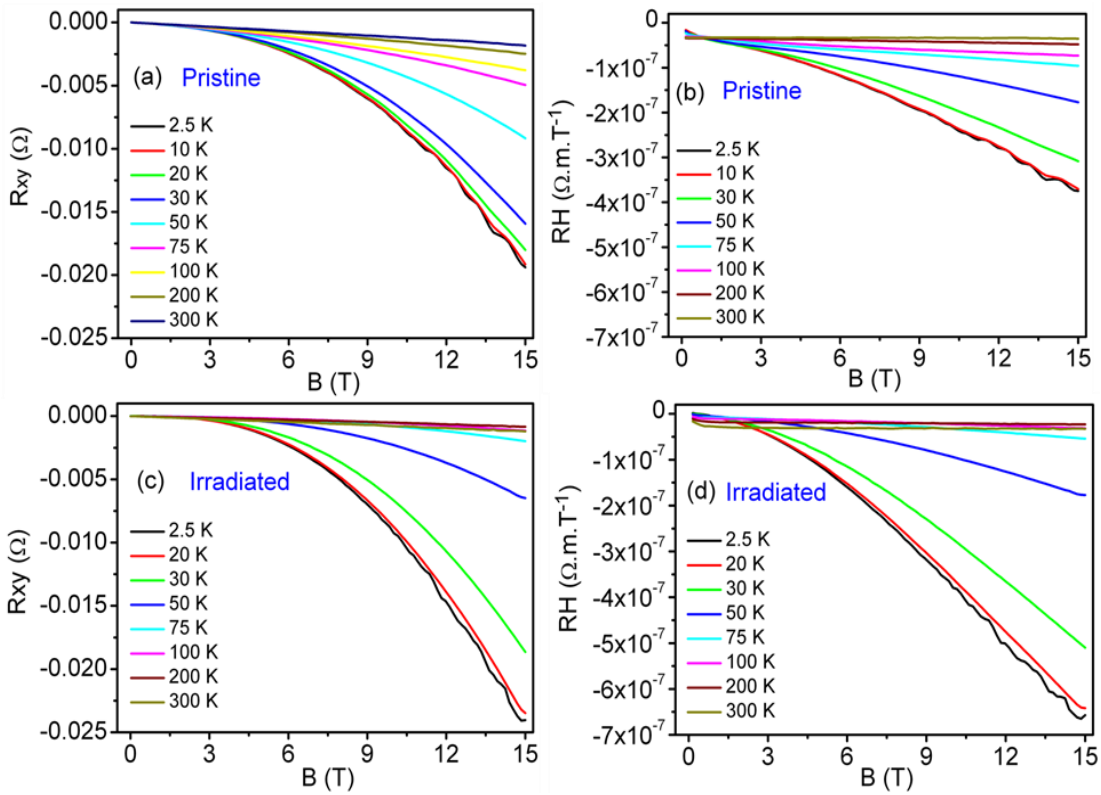

Figure 3.11 ***(a)*** *Hall resistance R_{xy} and* ***(b)*** *Hall coefficient R_H are plotted as a function of magnetic field for the pristine $TaAs_2$. The linear R_{xy} at high temperatures turns to non-linear below 100 K, indicating the appearance of multiple carriers. The negative R_H indicates that electrons are the dominant carriers in the magneto-transport. Similar results for the irradiated $TaAs_2$ are shown in* ***(c)*** *and* ***(d)****.*

We have adopted a multi-band model [3] to analyze the data in Figure 3.11. A two-band fit of the data has been done through an analysis of the field dependent conductivity tensor components $\sigma_{xx}(B)$ and $\sigma_{xy}(B)$ [88].

$$\sigma_{xx}(B) = \frac{1}{\rho(B)\left[\left(\frac{R_H(B)B}{\rho(B)}\right)^2 + 1\right]} \quad \textbf{(3. 5)}$$

$$\sigma_{xy}(B) = \frac{R_H(B)B}{\rho^2(B)\left[\left(\frac{R_H(B)B}{\rho(B)}\right)^2 + 1\right]} \quad \textbf{(3. 6)}$$

The carrier densities and mobilities obtained from the two-band analysis are shown in Figure 3.12 and Figure 3.13. It is seen from Figure 3.12 that below 100 K, hole carriers emerge along with the already existing electrons. In the pristine sample (See Figure 3.12a) the electron density $n_e \sim (1.0 \pm 0.5) \times 10^{26}\, m^{-3}$, exhibits a marginal decrease with lowering temperature. The hole density n_h ($\sim 6.3 \times 10^{25}\, m^{-3}$), which appears below 100 K, slowly rises as temperature is lowered, leading to better compensation. Both carrier densities saturate below 30 K. At 2.5 K, the densities of electrons ($\sim 9.4 \times 10^{25}\, m^{-3}$) and holes ($\sim 7.7 \times 10^{25}\, m^{-3}$) are nearly equal.

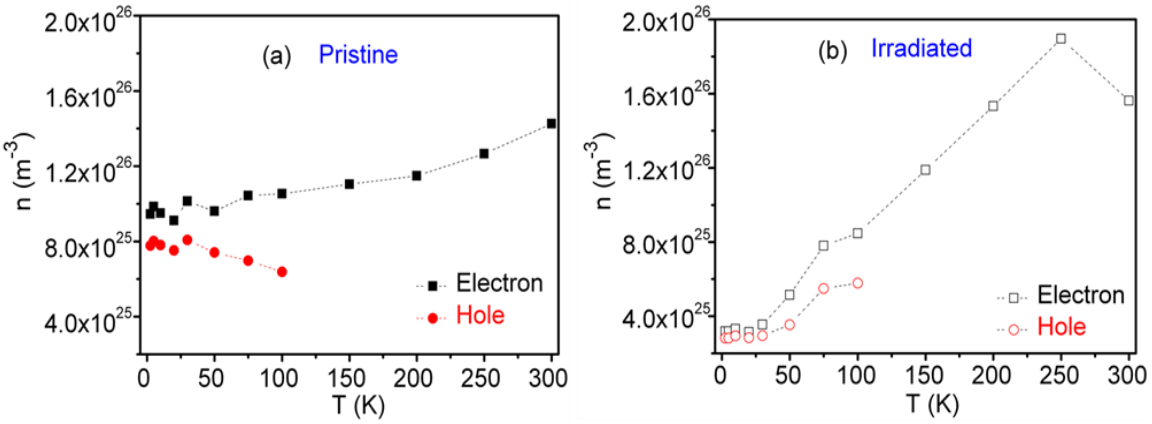

Figure 3.12 ***(a)*** *and* ***(b)*** *The temperature dependent carrier density for the pristine and irradiated $TaAs_2$ samples, obtained from the two-band analysis of Hall resistance and transverse magneto-resistance data. Both electron and hole charge carriers are present below 100 K, indicating the role of carrier compensation in the MR. Note the marginally higher electron density in both the samples. Better carrier compensation can be observed in the irradiated sample.*

In the irradiated sample (See Figure 3.12b), there exists a noticeable temperature dependent carrier density. The electron concentration at 300 K ($\sim 1.56 \times 10^{26}\, m^{-3}$) shows a monotonous drop with decrease in temperature until 30 K, and then saturates. A similar trend is exhibited by hole carriers which emerges from 100 K onwards. At the lowest temperature, n_e and n_h are closer than that seen in the pristine sample, viz. $\sim 3.18 \times 10^{25}\, m^{-3}$ (n_e) and $\sim 2.81 \times 10^{25}\, m^{-3}$ (n_h). This indicates that charge carriers are better compensated in the irradiated sample. It is to be noted that the resistivity plateaus in the $\rho\,(T, B)$ profile (Refer Figure 3.2) appear where carrier density saturates (below ~30 K) and the carrier compensation characteristic is observed. We note that the analysis from the measurements on heat treated $TaAs_2$ sample also provided evidence for the multi-carrier nature of magneto-transport.

According to the semi-classical model [3, 4, 89] of magneto-transport involving two carriers, the magneto-resistance is expressed as [90]

$$MR = \frac{\rho_H - \rho_0}{\rho_0} = \frac{n_e \mu_e n_h \mu_h (\mu_e + \mu_h)^2 H^2}{(n_e \mu_e + n_h \mu_h)^2 + \left((n_e - n_h)\mu_e \mu_h H\right)^2} \quad \textbf{(3. 7)}$$

In the case of perfect balance [13, 91] between electrons and holes, $i.e,\ n_e = n_h$, it follows a simple quadratic dependence leading to $MR = \mu_e\, \mu_h\, B^2$. This scenario has been recently invoked in the case of WTe_2, $PtBi_2$, LaBi, LuBi, YBi etc. which exhibit non-saturating MR [58, 59, 64, 67]. Yuan et al [30] and Wu et al [13] proposed that the XMR in their $TaAs_2$ samples are due to perfect compensation. On the other hand, the imbalances between n_e and n_h in $TaAs_2$ have also been observed [27]. In the present study, the carrier density ratio $\left(\frac{n_e}{n_h}\right)$ was found to be temperature dependent. For the pristine sample, it is ~1.6 at 100 K that reduces to ~1.2 at the lowest temperatures where the MR increases. The corresponding values for the irradiated sample are ~1.4 and ~1.1,

indicating that the degree of compensation is better. This accounts for the higher MR in the irradiated sample as we have earlier observed (See Figure 3.10b). The ratios deviate from the requirement of $\frac{n_e}{n_h} = 1.0$ for perfect compensation in line with the departure from B^2 response of MR (See Figure 3.10b).

The second parameter obtained from the two-band analysis is the mobility of carriers. The temperature variation of electron and hole mobility for pristine and irradiated samples are given in Figure 3.13a and Figure 3.13b respectively. The electron mobility (μ_e), in both samples, shows significant temperature dependence below ~100 K. In the pristine sample at 100 K, $\mu_e \approx 7000\, cm^2.V^{-1}.s^{-1}$ while it reaches to ~$31330\, cm^2.V^{-1}.s^{-1}$ at 2.5 K, an increase of ~4.5 times by variation of temperature. This very high mobility at low temperatures results in the low residual resistivity of the sample, although the carrier densities are rather small compared to typical metals. The hole mobility (μ_h) also shows similar trend of variation in the corresponding temperature range although their magnitude is quite small. On an average μ_h is eight times smaller than μ_e.

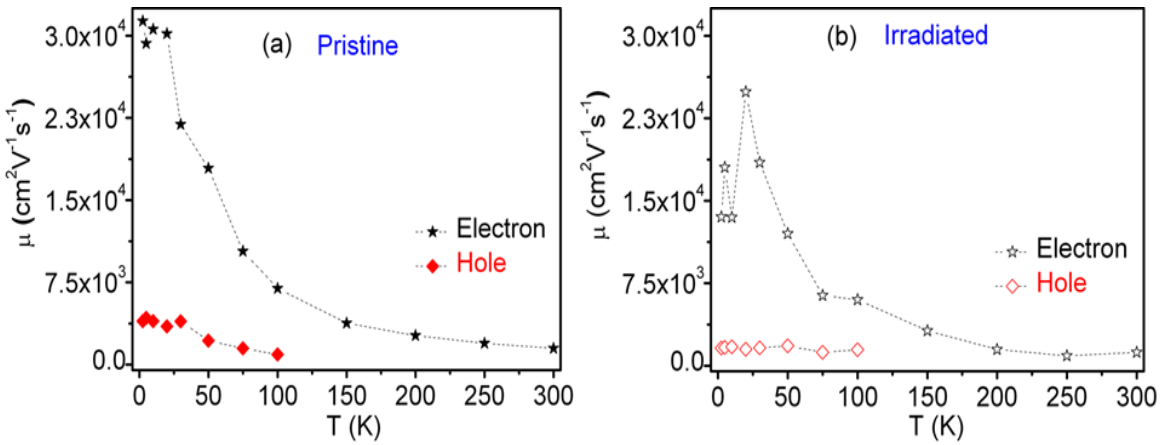

Figure 3.13 ***(a)*** *and* ***(b)*** *Mobility of charge carriers are plotted against temperature for the pristine and irradiated $TaAs_2$ as obtained from two-band model. Note that electron mobility increases to very high values below 100 K in both samples.*

In the irradiated sample, the electron mobility (See Figure 3.13b) has comparable magnitudes down to 100 K, while below this temperature its increase is not as steep as that in the pristine sample; $\mu_e \approx 25000\, cm^2.V^{-1}.s^{-1}$ at 20 K. The smaller mobility in the irradiated sample may be linked to the arsenic vacancies created by irradiation. While the mobility is smaller, the carrier density is increased upon irradiation, as seen in Figure 3.12.

We have earlier observed in Figure 3.5a that the slope of the pristine Kohler plot changes around ~170 K. This has similarities with the temperature variation of electron mobility which shows strong temperature dependence below ~100 K. However, the change of slope is absent when Kohler plot was constructed from the magnetic field dependent MR data measured at isothermal conditions (See Figure 3.8c). Thus the explicit temperature dependence of μ_e is reflected only when MR is measured in a varying temperature at a set field that is absent when the Kohler plot is generated from the isothermal field dependent MR measurements. A comparison of the collapsed MR curves in Figure 3.7b and Figure 3.7d with the mobility versus temperature plots in Figure 3.13 reveals that the temperature dependence of magneto-resistance has good similarities with that of mobility, particularly electron mobility μ_e. This emphasizes that any temperature dependent alteration in magneto-resistance in a system obeying Kohler's scaling can be completely attributed to the mobility changes of its charge carriers upon varying temperature [81]. This is discussed in more detail in Chapter 4 for the $NbAs_2$ system.

3.8. Longitudinal Magneto-resistance in $TaAs_2$

As indicated in Chapter 1, the measurement of longitudinal magneto-resistance under collinear electric and magnetic fields holds particular importance as it provides a direct evidence for the condensed matter realization of chiral anomaly [92]. A negative longitudinal magneto-resistance (NLMR) is the most sought-after magneto-transport signature for the existence of bulk chiral Weyl fermions in topological materials [35]. However, there exist a variety of situations which can give a negative magneto-resistance, misleading the experimentalist to conclude it as NLMR generated from chiral fermions. Most prominent among them are electrical contact geometry related artefacts [93]. An improper placement of voltage leads can often lead to the measurement of lower potential difference brought about by the non-uniform distribution of current in the sample. In the presence of a magnetic field, point contacts on the surface of a sample can inject an inhomogeneous distribution of current in the entire cross section of the sample. If the magnetic field is parallel to the line connecting the point current contacts, the electric current acts as a jet between those points. This 'current jetting effect' can cause the voltage probes on the sample to decouple from the actual current path, and record a smaller or even no potential difference across it (See the schematic in Figure 3.14a) [93]. If the voltage pair is close (V_1) / away (V_3) from this current line (indicated by I^+ to I^- line in the schematic), it can detect a higher / smaller resistance than the intrinsic longitudinal MR. In that case, the lower resistance detected can be interpreted as negative MR. This is significant in high mobility samples that show large transverse magneto-resistance. In order to avoid such an error, we have taken care to cover the four linear contact leads on the entire width of the sample so that the voltage probes will be able to intercept the current paths spread across the sample surface. A misalignment of electric and magnetic fields from the exactly parallel condition can render the negative magneto-resistance get

undetected. Given this, special care was taken while mounting the sample on the puck, and orienting it with magnetic field. Carefully polished flat samples were used for the experiments to avoid geometrical issues while mounting on the sample puck. Magneto-resistance data have been collected in both positive and negative directions of the magnetic field, and properly averaged to remove the Hall resistance contribution due to a probable minor misalignment of contact leads. Experiments have been repeated at least on two crystals in two different cryostats (Cryogenic & PPMS) that also helped to ascertain the reproducibility of the results. In addition, we have also collected data from a sample using the van der Pauw configuration, albeit the rationality of adopting such contact geometries in the search for negative magneto-response is not discussed in literature.

We have loaded the sample puck in the parallel slot of the sample holder in the Cryogenic Ltd cryostat such that magnetic field was along the *a*-axis. An electric current of 10 mA was sent along the *a*-axis (or *ac*-plane) so that ***B*** and ***I*** are parallel to each other. As for the measurement protocols, both temperature dependent and magnetic field dependent magneto-resistances were measured as was done for transverse MR experiments. During the isothermal field dependent experiments, between ±3 T, in order to discern any feeble negative magneto response, if present, data have been collected from very close field intervals (0.005 T) at the lowest temperature (2.5 K). Beyond ±3 T, field intervals were kept as 0.05 T and continued up to 14 T. Experiments have been repeated at higher temperatures up to 300 K with field intervals of 0.2 T. In all these measurements, magneto-resistance was seen to be positive, and no signature of a negative MR could be seen as shown in the results given in Figure 3.14b and Figure 3.14c for the pristine and irradiated $TaAs_2$. For the irradiated sample, measurements have been performed only up to 5 T at the indicated temperatures below 100 K. A double log plot of the longitudinal MR

against magnetic field in the pristine sample, shown in Figure 3.14d presents an increasing resistance profile with increase of field. The LMR was also found to follow a B^m dependence on the field B. In pristine sample $m \approx 1.79 \pm 0.01$ which indicate a near parabolic MR growth. In the irradiated sample for the measured range up to 5 T, this parabolic behaviour is less prominent as the exponent $m \approx 1.5 \pm 0.03$.

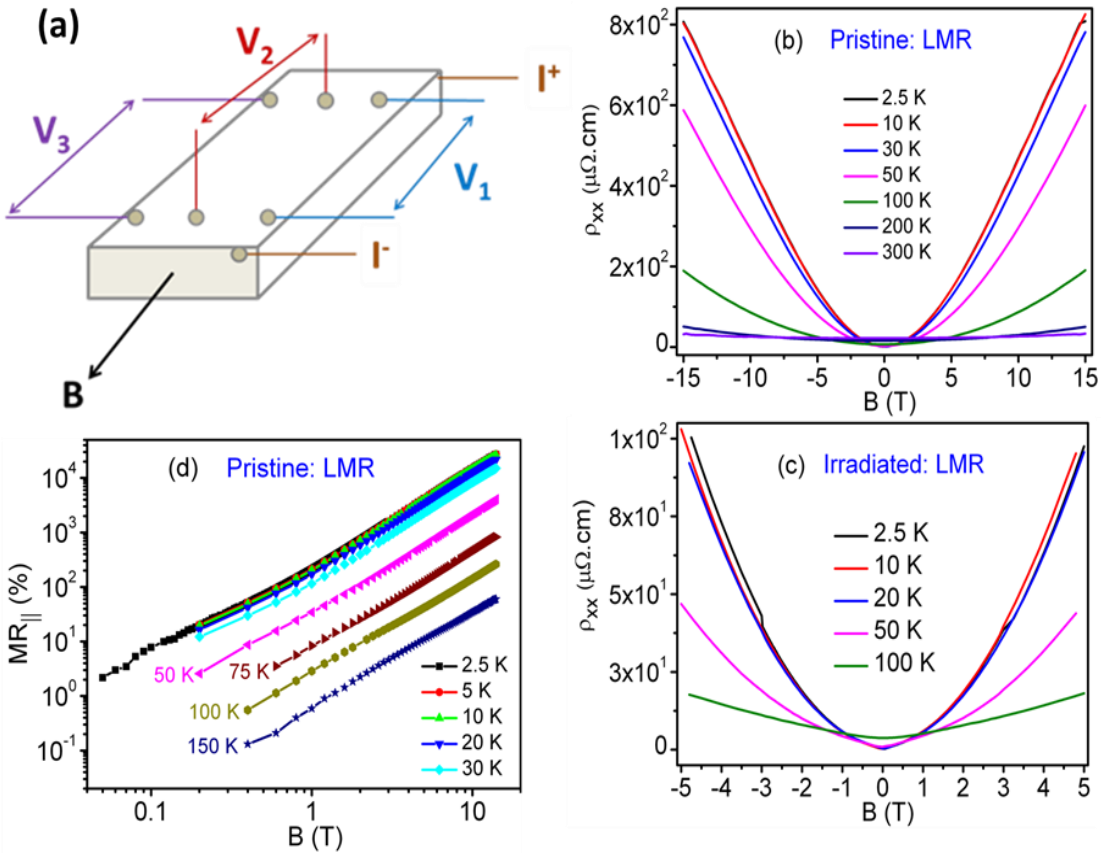

Figure 3.14 ***(a)*** *A schematic diagram to explain the current jetting effects, that can creep into resistance measurements under fields.* ***(b)*** *&* ***(c)*** *Isothermal longitudinal resistivity as a function of magnetic field for the pristine and irradiated $TaAs_2$ samples, showing a parabolic and positive MR.* ***(d)*** *The LMR as a function of field is plotted in a double log plot for the pristine sample, showing monotonously increasing positive MR.*

The evidence for positive LMR is also seen from the temperature dependent measurement with successive increase of magnetic field, $\rho\,(T, B)$, as shown in Figure 3.15a. The resistivity variation with temperature at various constant magnetic fields is qualitatively similar to TMR (See Figure 3.2), viz., a metallic profile in 0 T, upturns under

fields and resistivity plateaus at low temperatures. However, there are significant differences between pristine and irradiated samples when comparing the present LMR data against the corresponding results of TMR (See Figure 3.2). For a closer look of these differences, the temperature dependence of magneto-resistivity of pristine and irradiated samples in the LMR configuration is presented in Figure 3.15b. It is well discernible from the figure that the minimum magnetic field in LMR to produce a resistivity upturn is 1 T for the pristine sample, while a higher field of 2 T is required in the irradiated sample. But in TMR, an opposite trend is seen: with a lower field of 0.5 T, the irradiated sample displayed a resistivity minimum while in the pristine, a clear minimum occurred only with 2 T (See Figure 3.3 for TMR at low fields). The variation of T^* and $T_{plateau}$ with magnetic field is shown in the inset of Figure 3.15b. It is seen that T^* increases almost linearly with the applied field, and cannot be fitted to a critical field behaviour. However, the upturn behaviour can be understood in terms of the Kohler's scaling rule, as presented subsequently.

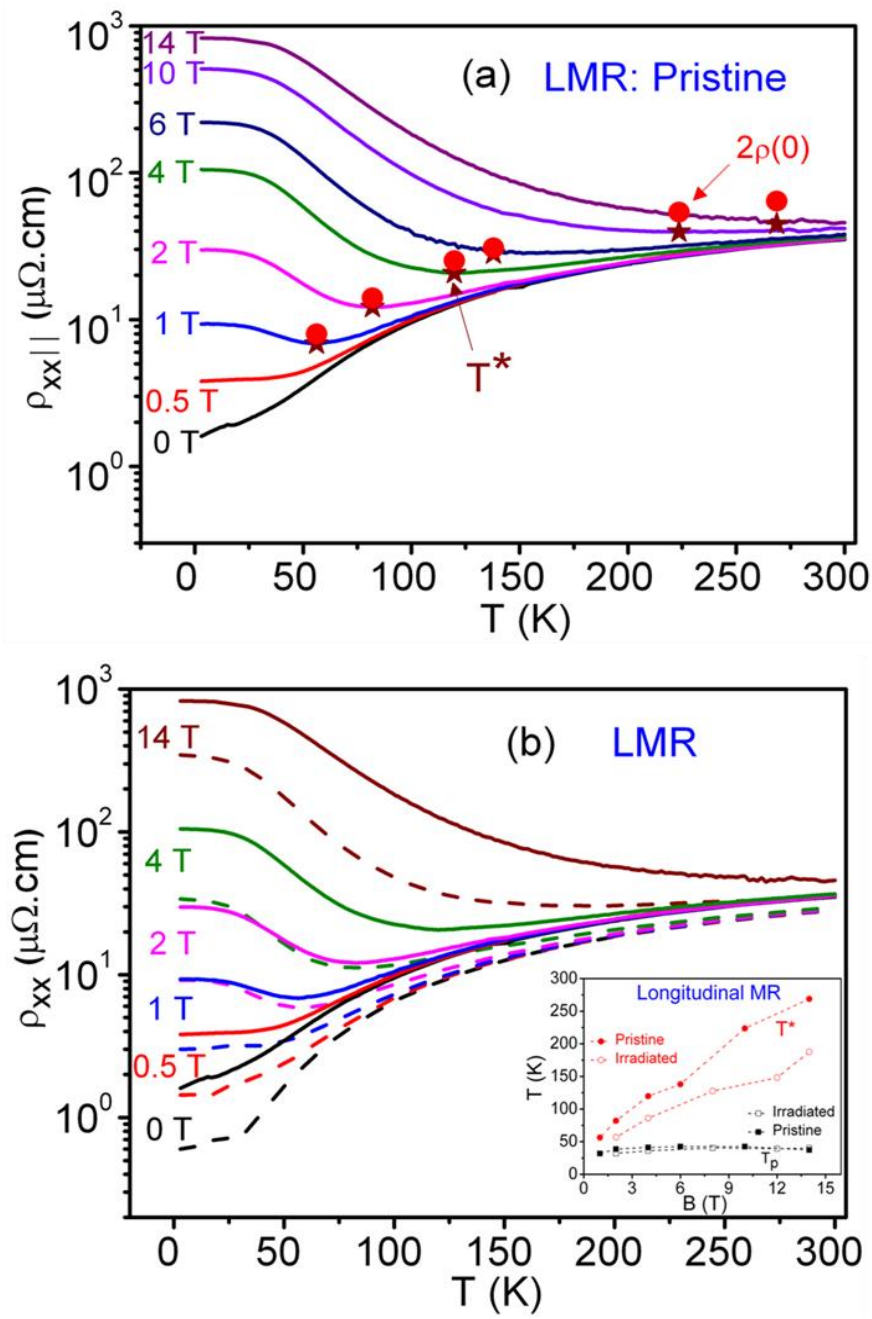

Figure 3.15 ***(a)*** *The temperature variation of resistivity in the LMR configuration in the pristine $TaAs_2$ sample at various constant magnetic fields. The stars and circles are points of T^* and $2\rho_0$, indicating the agreement with the Kohler rule prediction (Refer Section 3.4.1).* ***(b)*** *Comparison of the temperature variation of LMR in pristine and irradiated $TaAs_2$. Solid and dashed lines respectively indicate data from pristine and irradiated samples. Inset: T^* and $T_{plateau}$ variation with field.*

3.8.1. Longitudinal MR also Scales with Kohler's Rule

From Figure 3.16a and Figure 3.16b, we see that the temperature variation of longitudinal MR resulted in a scaling analogous to that of transverse MR. As observed in TMR (See Figure 3.5), a marked change of slope is present in pristine sample while that is not so prominent in the irradiated sample. The value of the exponent 'm' (See equation (3. 3)) obtained from the slope of linear region in the pristine sample is 1.9 ± 0.1, while for the irradiated sample it is 1.8 ± 0.1, both slightly differ from its value obtained in the Kohler analysis of TMR data ($m \approx 2$).

The longitudinal isothermal MR data measured up to 150 K also shows agreement with Kohler scaling as seen from the result in Figure 3.16c for the pristine sample. Up to 150 K, all the isotherms fall on a line that has a single slope. Above this temperature, the magneto-resistance data was noisy and hence we did not consider for analysis. The fit of the plot yielded the slope as 1.77 ± 0.07, slightly smaller than obtained from the $\rho\ (T, B)$ data ($m = 1.9 \pm 0.1$). Since isothermal MR for the irradiated sample was measured only up to 5 T, we have not done the Kohler analysis.

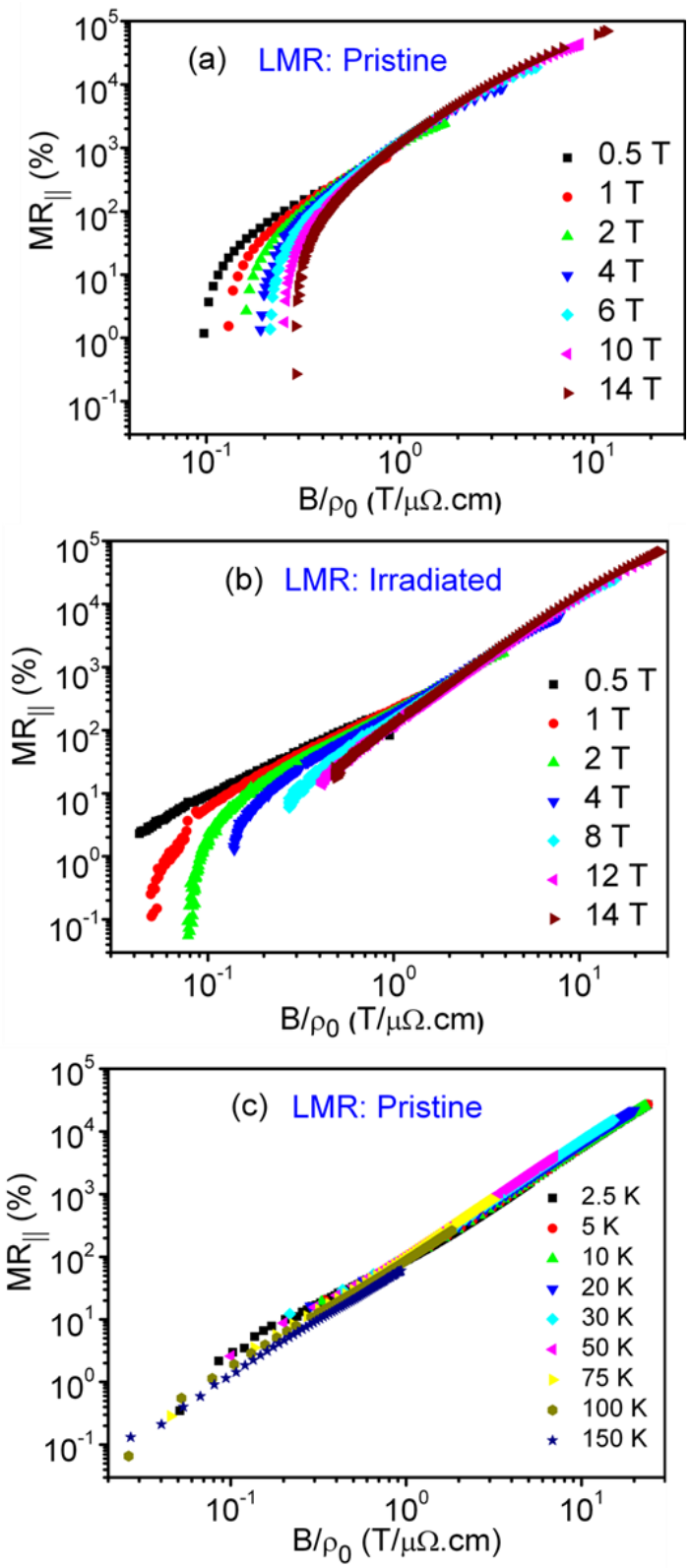

Figure 3.16 Kohler plots generated from the temperature variation of longitudinal magneto-resistance measured at various magnetic fields for ***(a)*** *Pristine and* ***(b)*** *Irradiated $TaAs_2$. Note the change of slope in the pristine sample towards the low MR region.* ***(c)*** *The isothermal LMR curves of pristine $TaAs_2$ collapses to a single straight line in the Kohler diagram.*

3.8.2. Negative MR is absent under collinear fields: $TaAs_2$ is not a Weyl semimetal

Through experimental results presented in this section, we have shown that there is no negative LMR in the $TaAs_2$ system. Hence, it cannot be considered as a Weyl semimetal, and is consistent with the band structure calculations [35]. The magneto-resistance, while positive in the longitudinal geometry, its magnitude is significantly smaller compared to that in the transverse geometry. For example, at 2.5 K the pristine sample exhibited an LMR of 27000 % at 14 T, only one third of the TMR value of 85000 %. This appreciable change in the magneto-resistance upon shifting the field orientation by 90° (to align along the *a*-axis) indicates that the magneto-transport in the system is not contributed by a 3-dimensional Fermi surface. There have been investigations of MR by changing the orientation of the magnetic field in XMR materials such as $PdSn_4$, $PtSn_4$ [20], LaBi [84] and $TaSb_2$ [94, 95]. Hence, transverse magneto-resistance for the pristine sample was also measured by applying the magnetic field along *c*-axis by keeping the current direction as before. The results for the 0 T and 2 T field were shown earlier in Figure 2.7a in Chapter 2. This has been performed without altering the electrical contacts. We note that MR in $TaAs_2$ is higher when the magnetic field was applied along *b*-axis (85000 %) and *c*-axis (89300 %), but decreased along *a*-axis (27000 %). In all the three instances, electric current direction was kept the same (*a*-axis). Hence it is reasonable to believe that magneto-dynamics is anisotropic in $TaAs_2$ system with respect to the magnetic field and is dominated by a 2-dimensional Fermi surface sheet [20].

The origin of positive magneto-resistance in the longitudinal configuration is not well understood. In the Lorentz force formulation, resistance will not have a response to magnetic field when it is applied parallel to the electric current [5]. In the quantum limit, the large degeneracy of Landau levels can contribute to LMR [96]. But within the limit of our field magnitudes, we do not expect any quantum effects that can yield a

longitudinal MR. A parallel magnetic field can couple only to the spin of the charge carriers and spin dependent scattering can generate an LMR [69]. However, the Kohler's rule scaling that is seen to be valid is usually used for dealing with MR contributed by the orbital motion of the charge carriers [3, 4]. Pal and Maslov [97] proposed that if the Fermi surface shape is having some angular anisotropy with respect to the magnetic field orientation, it can give rise to a quadratically increasing longitudinal magneto-resistance. This could be the possible reason for the positive LMR observed in the present experiments.

3.9. Conclusions

The detailed magneto-resistance investigations in the pristine and irradiated $TaAs_2$ single crystals revealed an extremely large magneto-resistance at low temperatures (Figure 3.2 and Figure 3.8). The observed MR behavior, exhibiting upturns and plateaus in the temperature variation of resistivity have been rationalized by scaling the magneto-resistance data in terms of Kohler's rule (Figure 3.5 and Figure 3.6). This approach, along with the normalized MR plots (Figure 3.7), has been used to negate the possibility of a magnetic field induced metal to insulator transition in the system. The Hall resistance experiments indicated the role of multiple charge carriers in the magneto-transport (Figure 3.11) and carrier compensation has been found to have an effect on the large parabolic MR, as revealed from the comparison of MR magnitudes in the pristine and irradiated samples. It was also understood that for a low density carrier system, when Kohler's rule is obeyed, the features in the magneto-resistance variation have its origin in the temperature variation of carrier mobility (Figure 3.13). Careful experiments in the parallel geometry (Figure 3.14) have confirmed the absence of negative longitudinal magneto-resistance, suggesting that $TaAs_2$ is not a Weyl semimetal.

Chapter 4

Magneto-resistance in $NbAs_2$ Single Crystals

Magneto-transport studies, in the range of 2.5 K to room temperature under magnetic fields between 0 to ±14 T, have been carried out in as-grown $NbAs_2$ crystals, and also after deliberately introducing disorder in the samples. Angle dependent measurements did not exhibit negative magneto-resistance, an important signature of Weyl semimetals. The large resistivity changes in a varying temperature and magnetic field showed consistent agreement with Kohler's rule, that is at variance to a behaviour expected in metal - insulator transition induced by magnetic field. The temperature variation of magneto-resistance is well correlated to that of charge carrier mobility. The origin of the extremely large magneto-resistance in the high pure semimetal system has been ascribed to the low density and high mobility of carriers.

4.1. Introduction

In Chapter 3, we have seen that the resistance in $TaAs_2$ shows tremendous changes upon varying temperature under magnetic field, resulting in large magneto-resistance values. Here, we are examining these observations in a related binary compound, niobium di-arsenide ($NbAs_2$), which belongs to the same di-pnictide family, and is iso-structural to $TaAs_2$. $NbAs_2$ crystallizes in the $OsGe_2$ prototype structure with an inversion-centre [33, 98, 99]. The crystal structure is described in Chapter 1 (Refer Section 1.6).

Figure 4.1 shows the band structure of $NbAs_2$ reported by Xu et al [33]. They predict that, without taking into account the spin - orbit coupling (SOC), one electron band and one hole band, each crossing the Fermi level, are present in the system. This suggests the coexistence of electron and hole carriers characteristic of two-band materials. Apart from this, within 0.2 eV of Fermi level, anti-crossing features are also present that form

nodal lines. When SOC effect is taken into consideration, the nodal line features become gapped, and leaving a fully gapped electron band and hole band. The gapped states lead to the formation of two large and one small isolated carrier pockets. These electronic structure calculations indicate that $NbAs_2$ is a compensated semimetal with electron and hole density of the order of 10^{19} to 10^{20} cm^{-3} [29, 30], with an electron to hole density in the ratio 1: 1.13 [29, 33]. The surface states arising out of the weakly topological electron band and hole band are not robust as that seen in strong topological insulators [33, 35].

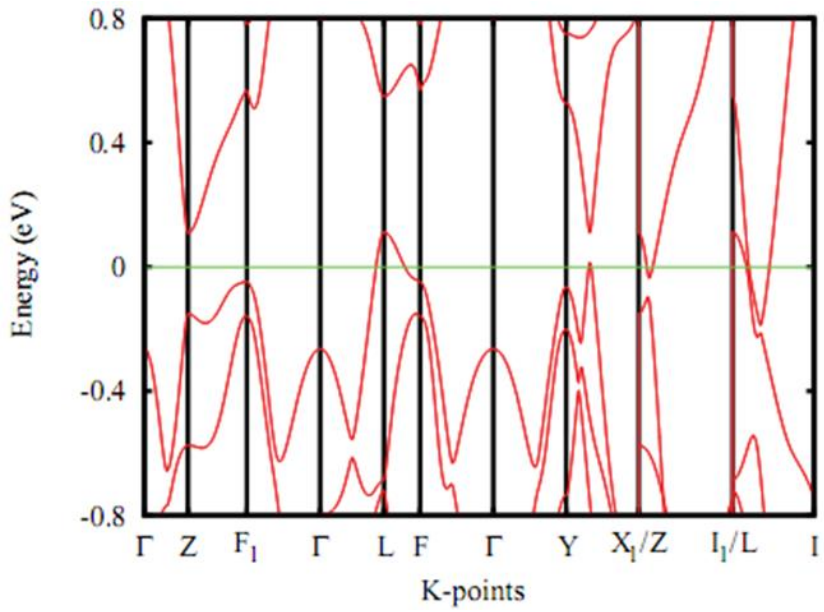

Figure 4.1 Band structure of $NbAs_2$ computed with spin - orbit coupling effect as adapted from Xu et al [33].

4.1.1. Issues in the Magneto-transport of $NbAs_2$

There have been several magneto-transport studies in $NbAs_2$, and in Figure 4.2, we present the representative results from the literature [28-31, 90, 100] to bring out the agreements and discrepancies. As can be seen from Figure 4.2a, the transverse magneto-resistance experiments show the characteristic upturn behavior under magnetic field, and resistivity saturation at low temperatures [11], resulting in extremely large magneto-resistance (XMR) ~10^5 % at 2.5 K and 14 T. The resistivity upturn has been interpreted as arising due to metal to insulator transition induced by magnetic field, and

the resistivity plateau as a consequence of the topological mechanism providing protection from backscattering [31]. Alternatively, the origin of large MR has been ascribed as due to the compensation of charge carriers in compensated semimetals [30]. There have been a few experiments that show Negative Longitudinal Magneto-resistance (NLMR) [29] (See Figure 4.2b), while not reproduced in several other experiments [30, 31]. The existence of negative LMR in $NbAs_2$, like in $TaAs_2$, is a highly debated issue. This has been attributed to measurement artefacts due to current jetting effects [30], or as an indication of chiral Weyl Fermions [29].

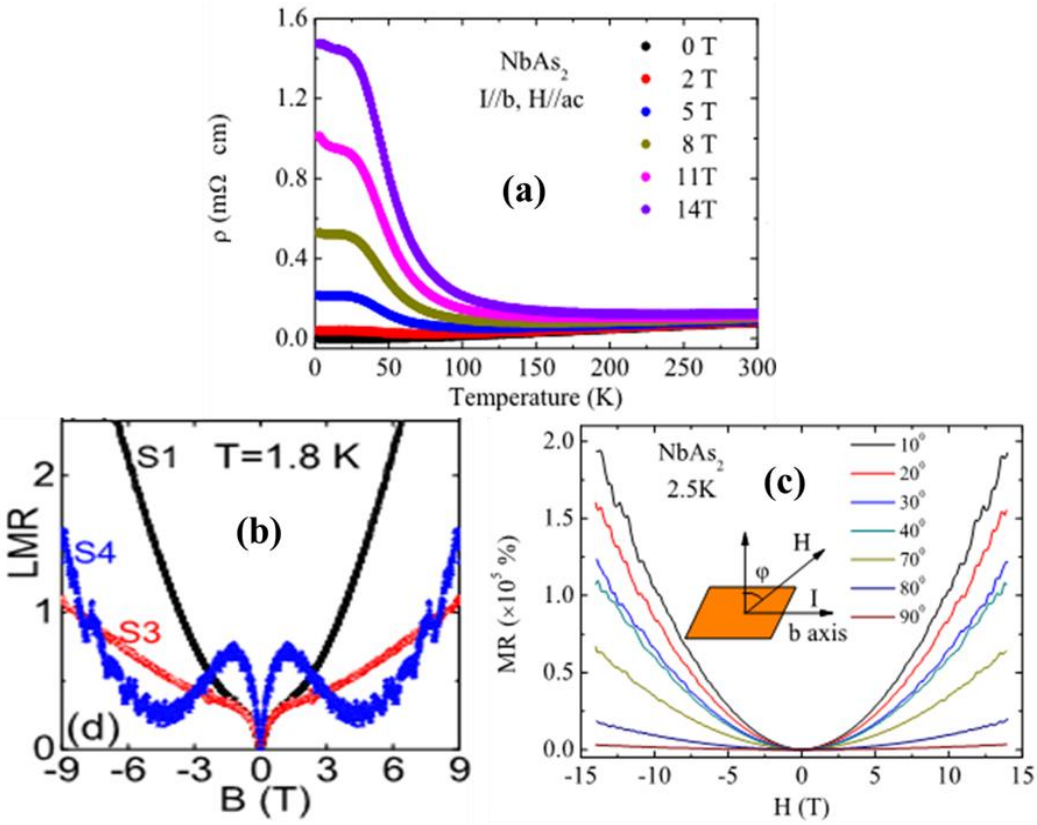

Figure 4.2 Representative results on the magneto-transport in $NbAs_2$ from the literature. ***(a)*** *Resistivity upturns and plateaus in the temperature variation of magneto-resistance reported by Wang et al [31]. Field dependent longitudinal MR measurements of* ***(b)*** *Shen et al [29] show negative MR, while that of* ***(c)*** *Wang et al [31] exhibit positive MR at all the angles between electric and magnetic fields including the Longitudinal MR geometry (See $\varphi = 90°$ orientation).*

Given this back ground, we have carried out systematic magneto-transport investigations on $NbAs_2$ single crystals that were characterized by Raman spectroscopy.

We have carried out these experiments in conjunction with angle dependent measurements, so that unambiguous Transverse MR (TMR) and Longitudinal MR (LMR) experiments could be undertaken. We have not observed negative LMR, and a consistent interpretation of both the TMR and LMR data could be done within the framework of the Kohler's scaling rule [46, 49]. Since the carrier density and mobility play a crucial role in the observed XMR [30], we have carried out Hall measurements, in addition to magneto-resistance experiments. With a view to control the mobility, experiments have been carried out with $NbAs_2$ crystals in which controlled disorder was introduced through low energy ion irradiation and heat treatment. These experiments, coupled with investigations on pristine $NbAs_2$, help to establish a clear correlation between the observed MR behavior and mobility variation with temperature [101].

4.2. Crystal Growth and Raman Characterization

As presented in Chapter 2 (Refer Section 2.1), single crystals of $NbAs_2$ have been prepared by the standard two-step chemical vapour transport route from the ground niobium and arsenic powders. The synthesis procedure and temperature protocols were the same as that adopted for the $TaAs_2$ crystals, described in Section 2.1. After the heat treatment of the polycrystalline material in the second step, $NbAs_2$ single crystals of thin rectangular plate type were seen towards the cold end of the quartz ampoule. The obtained crystals were of 1 to 2 mm long, and 0.2 mm or less thick (See Figure 2.1d). It looks very much similar to the rod-like crystals obtained by Wang et al [31]. The as-grown samples have been characterized by illuminating with a 514.5 nm argon laser from RENISHAW inVia Raman spectrometer. The obtained Raman spectrum is given in Figure 4.3a. The well-defined and sharp peaks evidence the high quality of the synthesized single crystals. Peaks were indexed based on the report by Jin et al [52]. All the modes, viz., $^{1}A_g$, $^{1}B_g$, $^{2}A_g$, $^{2}B_g$, $^{3}A_g$, $^{4}A_g$, $^{5}A_g$, and $^{6}A_g$ were identified as Raman active. The absence of extra

peaks ensured the purity of the crystal, and is thus free from impurities. We also saw some thicker (0.7 mm to 1 mm) dodecahedron type crystals that also showed similar Raman spectra (See Figure 4.3b). We have done experiments on both crystal types, and the MR results are nearly identical.

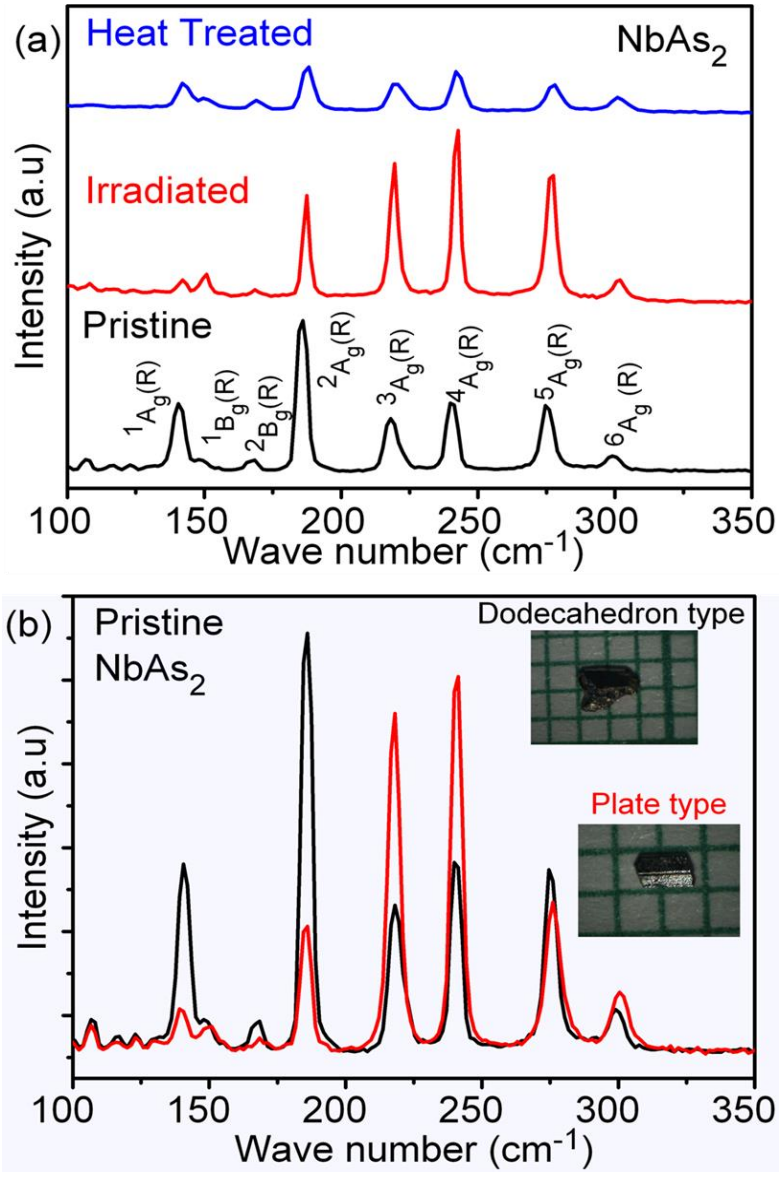

Figure 4.3 ***(a)*** *Raman spectra obtained from the Pristine, Irradiated and Heat treated $NbAs_2$ crystals. Modes in the pristine sample, indexed as per the report by Jin et al [52], displayed hardening of 2 to 3 cm^{-1} after irradiation and heat treatment. In the irradiated sample, the relative intensities of modes have been changed compared with the pristine sample, indicative of arsenic vacancies. After heat treatment, although relative intensity changes are less, peaks have been broadened which suggests the introduction of disorder.* ***(b)*** *Raman spectrum of the dodecahedron type and the plate type pristine $NbAs_2$ crystals. Both types show identical spectrum.*

Figure 4.3a also shows the Raman spectra of irradiated and heat treated samples. The details of irradiation experiments were given in Section 2.2 of Chapter 2. The Raman spectrum of the irradiated crystal retained all the modes of the pristine crystal, but showed a hardening of ~2 cm^{-1} that can be understood due to vacancies created upon irradiation [60]. The SRIM calculations revealed that 0.65 atoms/ion of Nb and 7.44 atoms/ion of As were respectively sputtered with a total yield of 8.1 atoms/ion. The higher sputter yield of As indicates that it was predominantly sputtered out from the surface (See Figure 2.2c for the vacancy profile). Considering the low implantation range, this gives rise to more arsenic vacancies near the surface. The heat treatment experiments were used as another method to create disorder in the bulk crystal. Here, crystals have been gradually heated in vacuum to 700 K, and quenched in liquid nitrogen after a residence time of 2 hours. The Raman measurement result of the heat treated sample is given in the top panel of Figure 4.3a. Similar to the Raman spectra of the irradiated crystals, mode hardening has been observed in samples obtained after heat treatment. Table 4.1 summarizes the Raman modes in the pristine, irradiated and heat treated $NbAs_2$ crystals.

Table 4.1 Raman modes of the pristine, irradiated and heat treated $NbAs_2$ crystals. The first and second columns are the theoretically predicted modes and the experimentally observed values reported by Jin et al [52]. Values in the third column are obtained from the as grown samples of the two morphologies. The wave numbers in the fourth and fifth columns are obtained respectively after the irradiation and heat treatment.

Mode	Report (cm^{-1})	Pristine (cm^{-1})		Irradiated (cm^{-1})	Heat treated (cm^{-1})
		Plate type	Dodecahedron type		
$^{1}A_g$ (R)	140.8	139	141	142	142
$^{2}A_g$ (R)	185.6	186	186	187	188
$^{3}A_g$ (R)	217.8	218	218	219	221
$^{4}A_g$ (R)	240.6	240	240	243	242
$^{5}A_g$ (R)	275.6	274	274	277	278
$^{6}A_g$ (R)	300.0	299	299	302	301
$^{1}B_g$ (R)	148.7	148	148	151	150
$^{2}B_g$ (R)	167.3	168	168	168	169
$^{3}B_g$ (R)	221.7	-	-	-	-

4.3. Angle Dependence of Magneto-resistance: Positive and dipolar MR

The angular dependence of magneto-resistance (AMR) of a material has been used in various contexts [67, 102] to obtain much useful information like anisotropic magneto-transport [90], Fermi surface topology [103] etc. But we have measured the angle dependence of MR in $NbAs_2$ to precisely orient the electric current direction with respect to the magnetic field in the sample, in view of its significance to search for the negative longitudinal magneto-response in (Weyl) semimetals [92]. It has been carried out at 2.5 K, by rotating the sample around the *b*-axis through 360° in a fixed magnetic field of 1 T, using the apparatus described in Section 2.4.2. Four electrical contacts in the linear geometry, covering the entire sample width, have been made on a plate type crystal of approximate dimensions 1 mm x 0.5 mm x 0.17 mm. Resistance data has been collected after sending an electric current of 10 mA through the *a*-axis of the sample. The result of such an experiment at 2.5 K, as a polar plot is shown in Figure 4.4a. Such a dumb-bell type MR variation suggests that magneto-resistance in the sample has classical Lorentz type behaviour [65, 72]. Also, the two-fold symmetry reflects the mirror plane or the inversion plane in monoclinic crystal systems [30, 104]. Figure 4.4a shows that maximum MR is obtained when $\boldsymbol{I}$ and $\boldsymbol{B}$ fields are mutually perpendicular, viz., $\theta = 90°\theta$ and 270°, and reaching a minimum when the fields become collinear, viz., $\theta = 0°$ and 180°. It is to be noted that magneto-resistance is positive at all the orientations including the longitudinal configurations in which $\boldsymbol{I}$ and $\boldsymbol{B}$ are parallel to each other. The absence of negative longitudinal magneto-resistance suggests that $NbAs_2$ is not a Weyl semimetal, contrary to some of the experiments [28, 29] (See Figure 4.2). The results of MR measured at 2.5 K for various angles by varying the magnetic field between ±3 T is shown in Figure 4.4b. It is seen that the MR increases systematically as $\boldsymbol{I}$ and $\boldsymbol{B}$ are made orthogonal to each other from a longitudinal configuration, and at all the angles, it has a

parabolic variation with the field. Having measured the angular dependence, the results of the transverse magneto-resistance and longitudinal magneto-resistance will be presented in the subsequent sections.

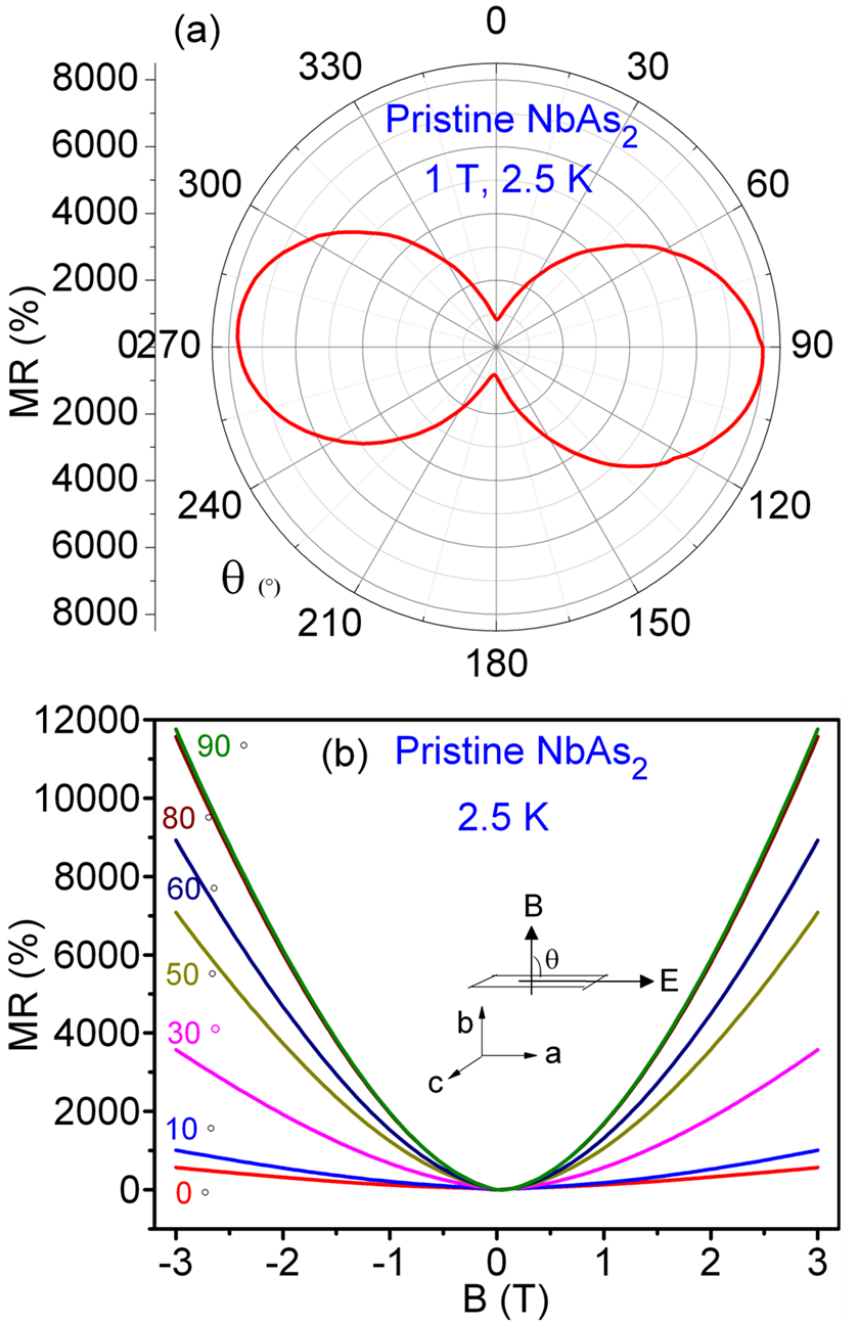

Figure 4.4 ***(a)*** *The angular magneto-resistance of pristine $NbAs_2$ measured at 2.5 K with 1 T showing a di-polar character.* ***(b)*** *The isothermal magneto-resistance for the pristine sample at various indicated angles measured as function of magnetic field shows a parabolic dependence on the field. The schematic of the measurement configuration with respect to crystalline axes is depicted as inset.*

4.4. Transverse Magneto-resistance in Pristine Crystal

In order to carry out the transverse magneto-resistance measurements, the pristine $NbAs_2$ sample was fixed at the angle where the maximum MR was observed during the angle dependent measurements described in the previous section. Here, the electric current is along the *a*-axis and the magnetic field is along the *b*-axis of the crystal. Figure 4.5a shows the observed temperature variation of resistivity $\rho\ (T)$ measured at various fixed magnetic fields. The results are similar to other references on $NbAs_2$ [11, 29-31]. We note the following features from our experiments. Without an applied magnetic field, the resistivity exhibits metallic nature (See the black curve) and saturates to $0.113\ \mu\Omega.cm$ at 3 K resulting in a residual resistivity ratio (RRR) of 150. This very low value of residual resistivity and high RRR shows the high quality of the crystals. With the application of a magnetic field, the resistivity profile changes from the metallic behavior at high temperatures to insulating at low temperatures, followed by a plateau at the lowest temperatures. The temperatures at which these two features appear, viz., minimum of resistivity and the plateau, while cooling the sample are respectively called T^* (turn on or upturn temperature) and $T_{plateau}$, conforming to the nomenclature used for $TaAs_2$ and in literature [31]. The smallest field with which a resistivity minimum was observed is 0.5 T. With higher applied fields, the upturn origin temperature T^* shifts to higher temperature side, while the $T_{plateau}$ remains the same, as can be seen from Figure 4.5a. The magnetic field variation of these two temperatures as obtained from a plot of differential resistivity against temperature is given in Figure 4.5b. It shows qualitatively the same behavior as seen in $TaAs_2$ (See Figure 3.4) and these results are in agreement with earlier studies on $NbAs_2$ [11]. The large changes in resistance with the magnetic field resulted in a resistivity of more than 110 μΩ.cm at 3 K with 14 T that reveals an MR of $\sim 1.8 \times 10^5$ %. The characteristic behavior of T^* with B has been interpreted as a metal to insulator transition

in many topological semimetals [27, 31, 45, 55, 58, 59, 64, 65] as arising out of an excitonic gap opening at the band touching points [17, 31]. However, our attempt to show critical behavior, $T^* \sim (B - B_C)^n$ was not successful. As will be shown in Section 4.5, the upturn behavior can be understood in terms of Kohler's rule.

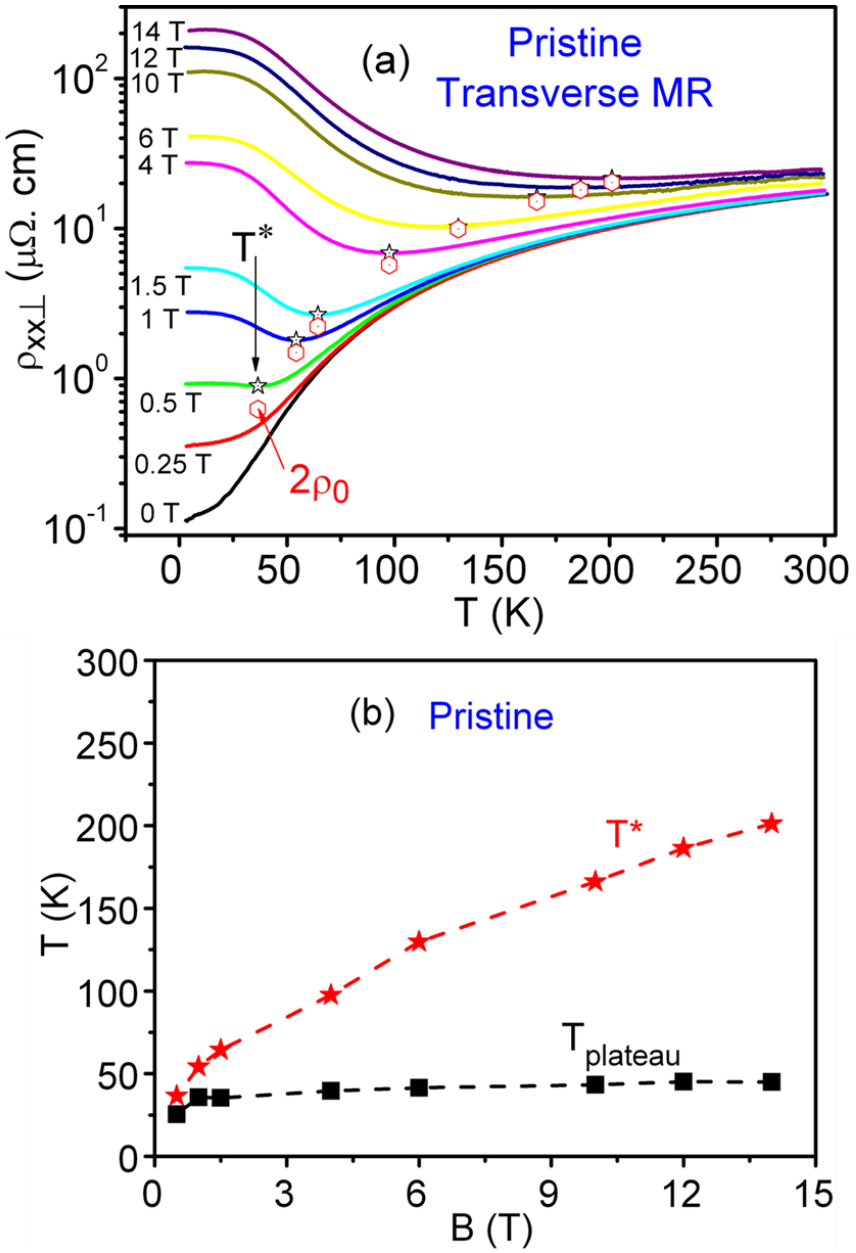

Figure 4.5 ***(a)*** *The temperature dependence of resistivity at various magnetic fields in pristine $NbAs_2$ in the transverse geometry. This shows upturn and resistivity saturation at low temperatures with the application of magnetic field. The upturn temperatures are denoted by 'stars'. The circles indicate the $2\rho_0$ values (See Kohler analysis in Section 4.5).* ***(b)*** *The T^* and $T_{plateau}$ are plotted as a function of magnetic field. The variation of T^* has been analyzed in literature in terms of critical field behavior.*

4.4.1. Isothermal MR Measurements

In addition to the measurements of resistivity versus temperature at various magnetic fields, we have also carried out resistivity versus field at various temperatures, as it will enable us to understand the functional dependence of magneto-resistance on the magnetic field. These isothermal MR experiments have been carried out at various constant temperatures from 2.5 K to 300 K with fields varying up to ±14 T, and the results are shown in Figure 4.6a. The resistivity is observed to have nearly a parabolic variation with applied field that is non-saturating up to the highest field measured. The increase in resistance with fields increases drastically at low temperatures, particularly below 30 K (the plateau temperature in Figure 4.5), leading to a very large magneto-resistance reaching ~ 1.1×10^5 % at 2.5 K with 14 T. A log-log plot of MR against field B is depicted in Figure 4.6b. A fit of the data shows that MR has B^m dependence, and the exponent 'm' changes with field B and temperature T.

It is seen that while the exponent is 1.7 over a large range of T and B, a change in the exponent to 1.4 at higher field and lower temperature is noticed. Such a change in the exponent has been seen in several systems including the di-pnictides [11, 13, 17, 30], and the topological semimetals such as the mono-pnictides [68, 105] and WTe_2 [106]. Several reasons have been attributed, such as the dispersive nodal line features in the $NbAs_2$ band structure [100]. However, given that the exponent 2 is expected for a fully compensated system (See Chapter 1), such a deviation from the quadratic behavior is more likely linked to the variation in the degree of compensation within the two-band model.

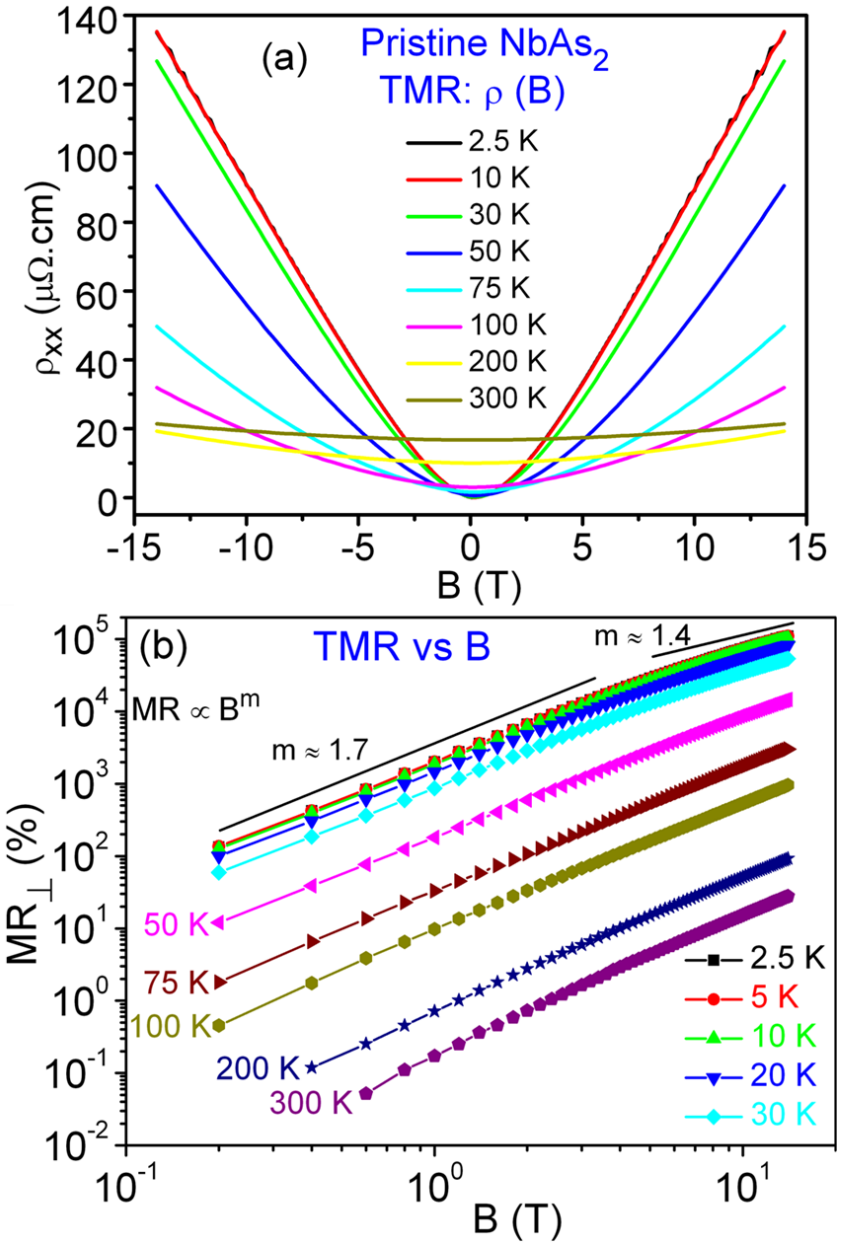

Figure 4.6 ***(a)*** *The transverse magneto-resistance of pristine $NbAs_2$ measured at various isothermal conditions shows a parabolic, non-saturating behavior with the applied magnetic field.* ***(b)*** *The resistivity data in the top panel is converted into magneto-resistance and plotted on a log-log scale. The exponent in the B^m fit is seen to decrease from 1.7 at low fields (less than ~3 T) to 1.4 at higher fields.*

4.5. Kohler's Analysis

In this section, we try to understand the variation of resistance with temperature and various magnetic fields (See Figure 4.5 and Figure 4.6) in terms of the Kohler's scaling relation. As described in Chapter 3, according to Kohler's rule, MR scales with $\frac{B}{\rho_0}$ as per the formula

$$\frac{\Delta\rho}{\rho_0} = F\left(\frac{B}{\rho_0}\right) = \alpha\left(\frac{B}{\rho_0}\right)^m$$

(4. 1)

Using the data shown in Figure 4.6, transverse MR is plotted against $\frac{B}{\rho_0}$ and the results are shown in Figure 4.7a, and the collapse of data collected at various temperatures from 2.5 K to 300 K is striking. Using the data in Figure 4.5a, the Kohler's plot is generated and these are shown in Figure 4.7b. Here we see that the data at various fields from 0 to 14 T collapse to a single curve. A fit of the collapsed line in Figure 4.7a has been used to estimate the value of 'm' as 1.6 ± 0.1. The exponent (m) in the Kohler's rule has been often considered as a measure of the degree of compensation of charge carriers and $m = 2$ indicates a perfectly compensated material [58, 85]. Hence, deviation of 'm' from the value 2 suggests that the carriers are weakly compensated in our $NbAs_2$ sample.

As indicated in Chapter 3 (Refer Section 3.4.1), the validity of Kohler's rule helps us to understand the resistivity upturn. The Kohler's relation can be recast to express the temperature variation of total resistivity in an applied magnetic field B as the sum of zero field resistivity $\rho_0\,(T)$ and the field induced resistivity [16]. This decomposition of resistivity when measured with 10 T field is shown in Figure 4.7c. The two components will result in a minimum in the total resistivity at an intermediate temperature as shown in Figure 4.7c. The position of this minimum (T^*) varies with the magnitude of the magnetic field (See Figure 4.5b). Thus the upturn and other features in the resistivity versus temperature curves (See Figure 4.5a) are natural consequences of the temperature dependence of the zero field resistivity [16, 20]. Further, the T^* points were found to be matching with $2\rho_0$ values as explained in Chapter 3. This is indicated by the stars and circles in Figure 4.5a.

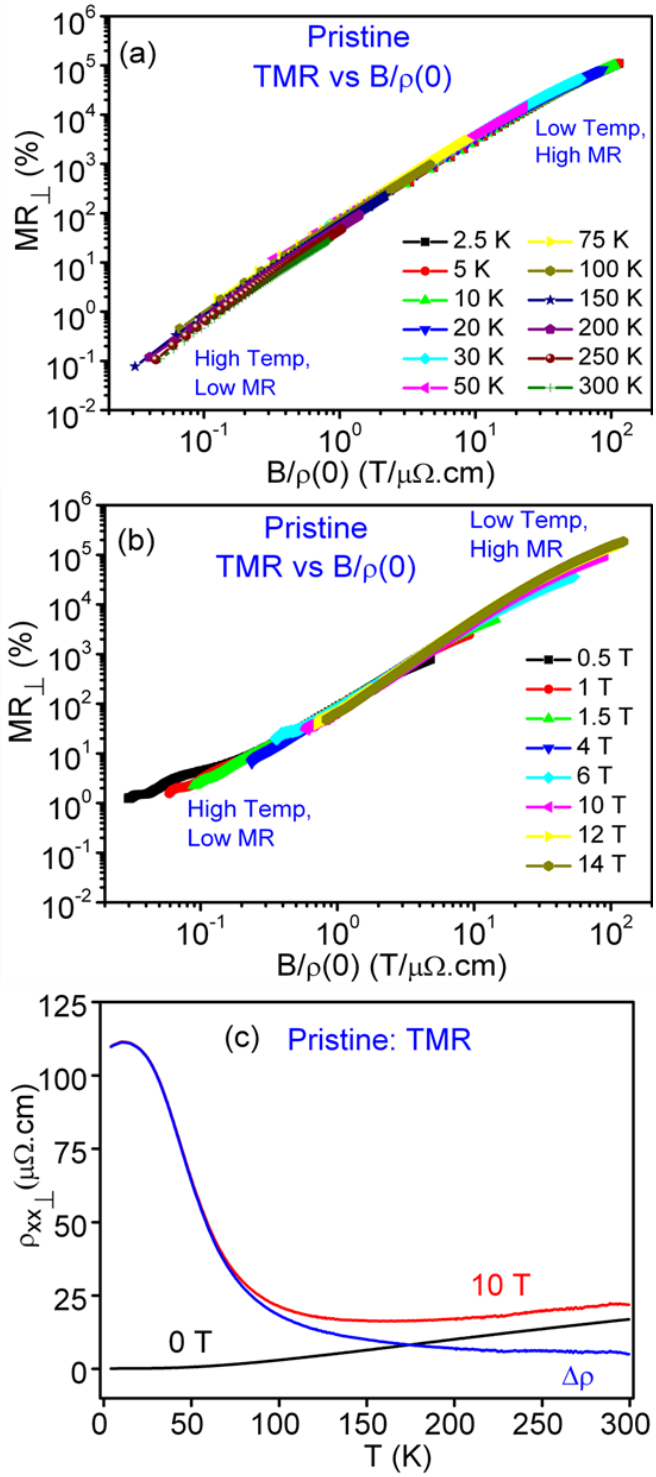

Figure 4.7 Kohler plots obtained for the pristine $NbAs_2$ sample from the transverse geometry during ***(a)*** *Isothermal magneto-resistance measurements and* ***(b)*** *Temperature variation of magneto-resistance carried out at various fixed magnetic fields. The collapse of MR data into a single line in both the figures shows validity of Kohler's rule in $NbAs_2$.* ***(c)*** *The decomposition of magneto-resistance in the temperature variation measurement to demonstrate the origin of resistivity upturns. The red curve shows the total resistivity at 10 T. The black curve is the zero field resistivity. The blue curve is the difference component between 10 T and 0 T measurements.*

The results shown in Figure 4.7, viz., the collapse of MR curves following the Kohler's scaling law, and the understanding of the upturn behavior, rules out the possibility of metal - insulator transition induced by magnetic field. Further, the validity of Kohler's rule indicates that a single dominant scattering process exists in $NbAs_2$ across the measured temperature ranges. This implies that the relaxation rate does not vary due to the application of magnetic field during magneto-transport between 2.5 K and 300 K.

4.6. Longitudinal Magneto-resistance in $NbAs_2$ is Positive

Our earlier section on the measurement of angular dependence of MR indicated that Longitudinal MR is positive in $NbAs_2$ (See Section 4.3). Here, we report the temperature and magnetic field dependence of MR, measured in the LMR configuration. The sample has been fixed such that magnetic field is also along the electric current direction through the *a*-axis. We note that the crystalline axes along which electric or magnetic fields are applied is immaterial for the chiral anomaly induced negative MR to occur [35]. Linear electrical contacts covered the entire width of the sample to keep a homogeneous current distribution and to ensure an error free voltage measurement [93]. Extra lengths of the contact wires have been arrested on the puck to avoid the generation of spurious signals in the presence of magnetic field. During isothermal measurements, LMR data has been collected in both $+B$ and $-B$ directions of the field (between ±14 T) and averaged properly to remove any Hall components. The raw isothermal longitudinal resistivity data is shown in Figure 4.8a. The corresponding log-log plot of LMR versus field is given in Figure 4.8b. It is seen that LMR is positive at all instances, indicating that $NbAs_2$ is ineligible to be categorized as a Weyl semimetal [107]. The isothermal plot for LMR appears different from TMR (See Figure 4.6a), because for LMR, the increase in resistivity with field is much smaller.

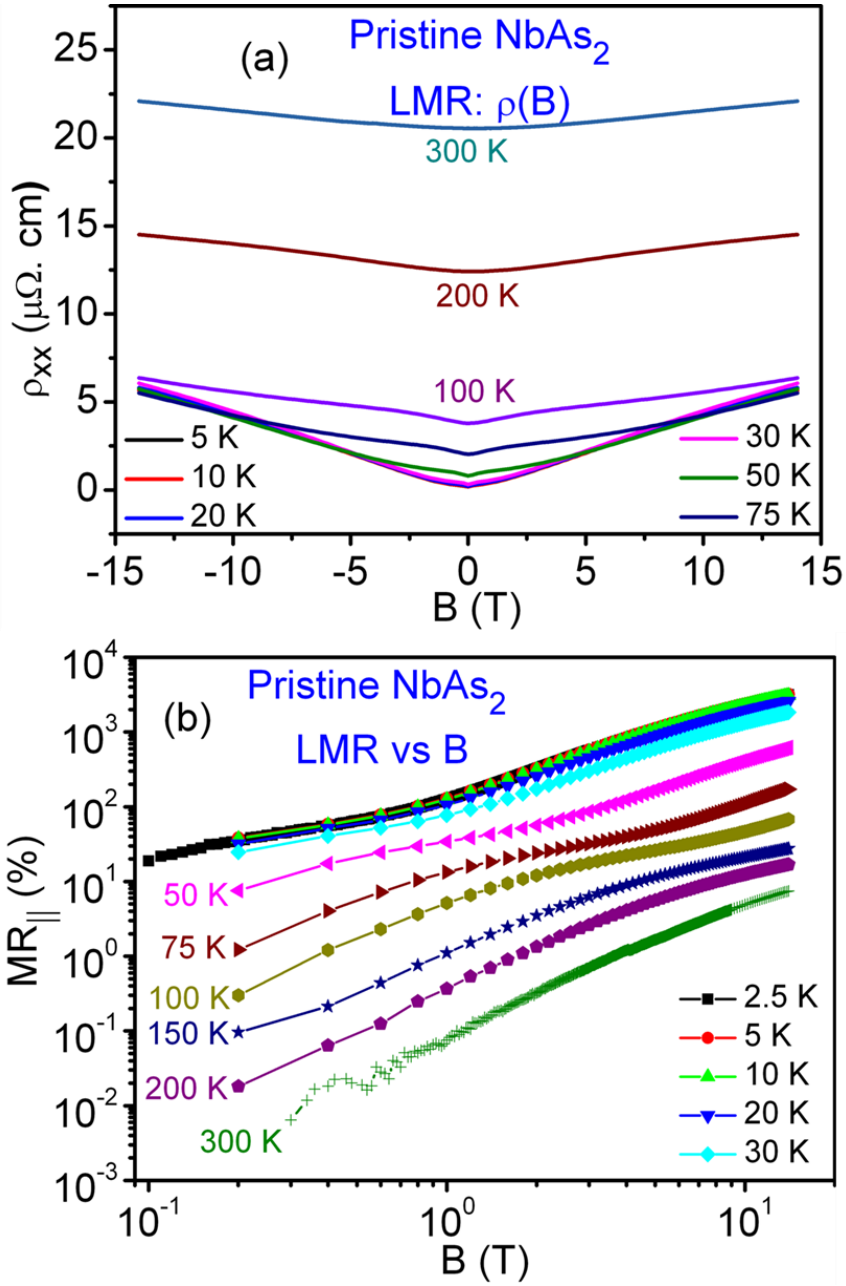

Figure 4.8 ***(a)*** *The field variation of longitudinal magneto-resistance measured at different temperatures.* ***(b)*** *The log-log plot of isothermal LMR versus magnetic field. Both results show positive LMR.*

The LMR, while positive is much smaller than TMR, viz., 5×10^3 % at 2.5 K against 1.1×10^5 %. In the semi-classical Drude theory of electron transport, a carrier moving along the magnetic field direction should not be affected by it [5]. As explained in Chapter 3 (Refer Section 3.8.2), the angular anisotropy of the Fermi surface with respect to the magnetic field direction can give rise to a quadratically increasing longitudinal MR [97]. This could be a possible reason for the positive LMR shown in Figure 4.8a.

In Figure 4.9a, we show the temperature dependence of resistivity at various fields in the LMR configuration. It is seen that as in the case of TMR (See Figure 4.5a), the resistivity shows an upturn as the field is increased. However, the resistivity upturns are not as distinct as that observed in TMR. Further, in LMR the minimum field at which an upturn originates is much higher, viz., 8 T in contrast to 0.5 T in TMR. The variation of 'turn on' temperature (T^*) with field is shown in the inset of Figure 4.9a. It is seen that it cannot be fitted to a critical behaviour at all. However, it is shown that the longitudinal MR data follows the Kohler's rule as seen from Figure 4.9b. While the flat T^* versus B cannot be fitted to a critical field behavior, it is seen (Figure 4.9c) that the observed minima in resistivity with temperature under magnetic field can be explained in terms of the decomposition of resistivity according to Kohler's rule (See equation (3. 4)). This further supports that an analysis of the results in terms of Kohler's scaling rule is better than in terms of the existence of a critical field, viz., MIT induced by magnetic field.

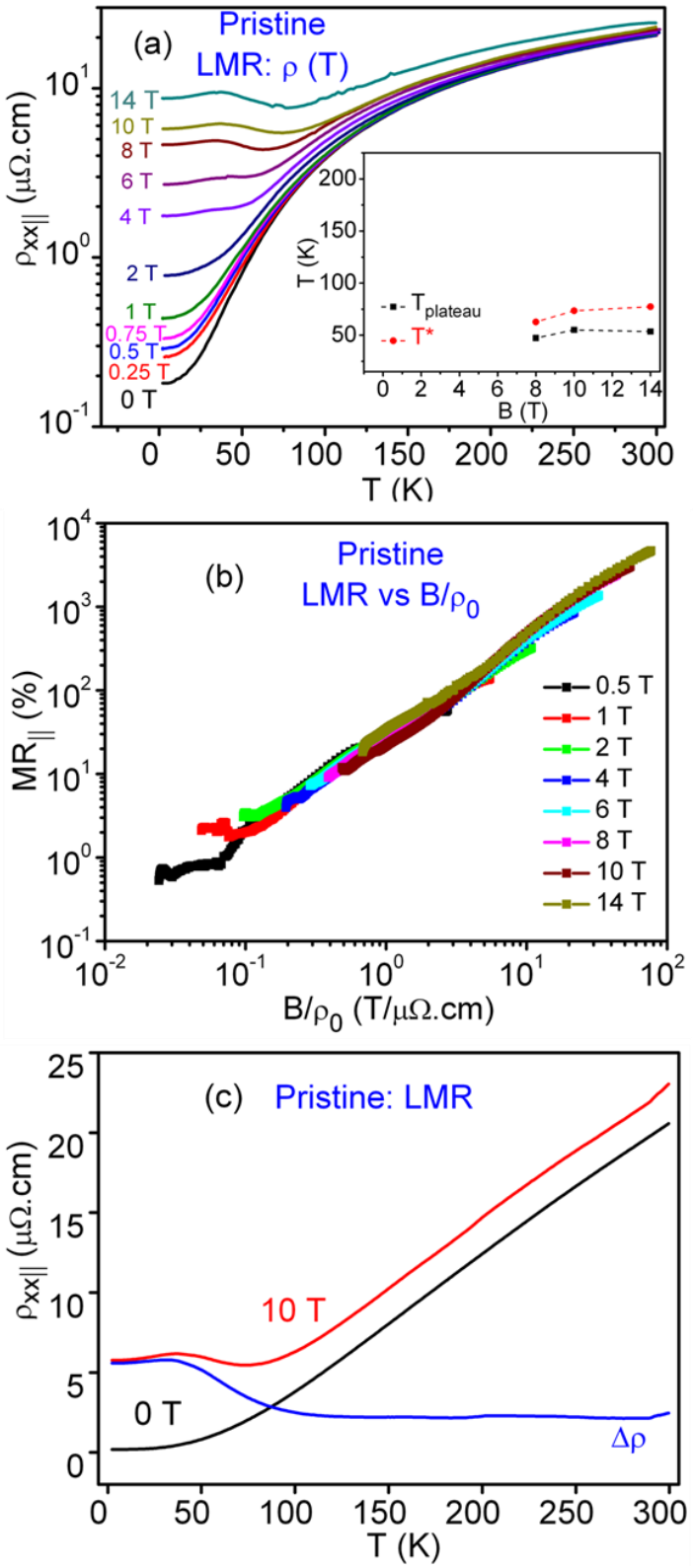

Figure 4.9 ***(a)*** *The temperature variation of LMR measured at various fixed magnetic fields. Inset shows the variation of* T^* *and* $T_{plateau}$ *with field.* ***(b)*** *Kohler plot generated from the temperature variation measurements shows collapse of LMR data into a single line.* ***(c)*** *The decomposition of the magneto-resistance at 10 T (red) into the zero field component (black) and the difference component (blue).*

4.7. Magneto-resistance in Irradiated $NbAs_2$ Crystals

As indicated in Section 4.2, we have irradiated the $NbAs_2$ crystals with Ar^+ ions at low energies to create arsenic vacancies so that carrier mobility is altered, and transport measurements were carried out. A crystal with approximate size of 1.8 mm x 0.8 mm x 0.69 mm was used for irradiation. The magneto-resistance measurements have been carried out in the same geometry with respect to the crystal axes identical to that done for the pristine sample (Refer schematic in the inset of Figure 4.4b). In Figure 4.10, we present the angle dependence of isothermal MR in the irradiated sample across ± 3 T field, carried out at the various indicated angles between the electric and magnetic field directions. It is seen that while the magneto-resistance retains the positive and parabolic character in the irradiated $NbAs_2$ at all the angles, its magnitude has reduced by almost six times compared to that in the pristine sample (See Figure 4.4b).

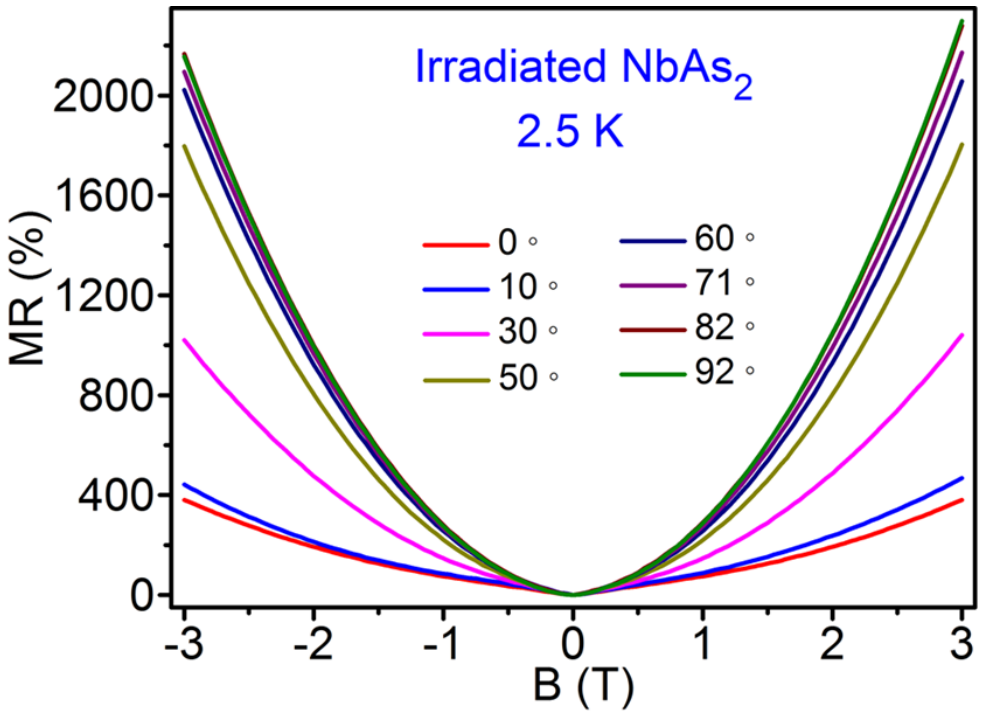

Figure 4.10 The magneto-resistance in the irradiated $NbAs_2$ at 2.5 K, measured as a function of magnetic field at various pre-set angles between the electric and magnetic fields. It shows positive MR at all the angles, irrespective of the relative orientations of the E and B fields. Note the decrease in the MR magnitude after irradiation (See Figure 4.4b).

Figure 4.11a shows the resistivity variation with temperature at various fields in the irradiated $NbAs_2$. Although the resistivity in the transverse geometry bears qualitatively similar features to that in the pristine sample (See Figure 4.5a) such as metallic profile under zero field, resistivity minimum followed by upturns and subsequent saturation at low temperature, there are certain differences. The irradiated sample has a higher residual resistivity of $0.511\,\mu\Omega.cm$ and a lower RRR of 36 against the corresponding values of $0.113\,\mu\Omega.cm$ and 150 for the pristine sample. At 3 K magneto-resistance of 5×10^4 % was observed with 14 T field, although quite high, reduced by three times from the pristine sample. The initial resistivity upturns are seen only with fields beyond 2 T, in contrast to the 0.5 T in the pristine sample. The field variation of T^* and $T_{plateau}$ are depicted as an inset to Figure 4.11a.

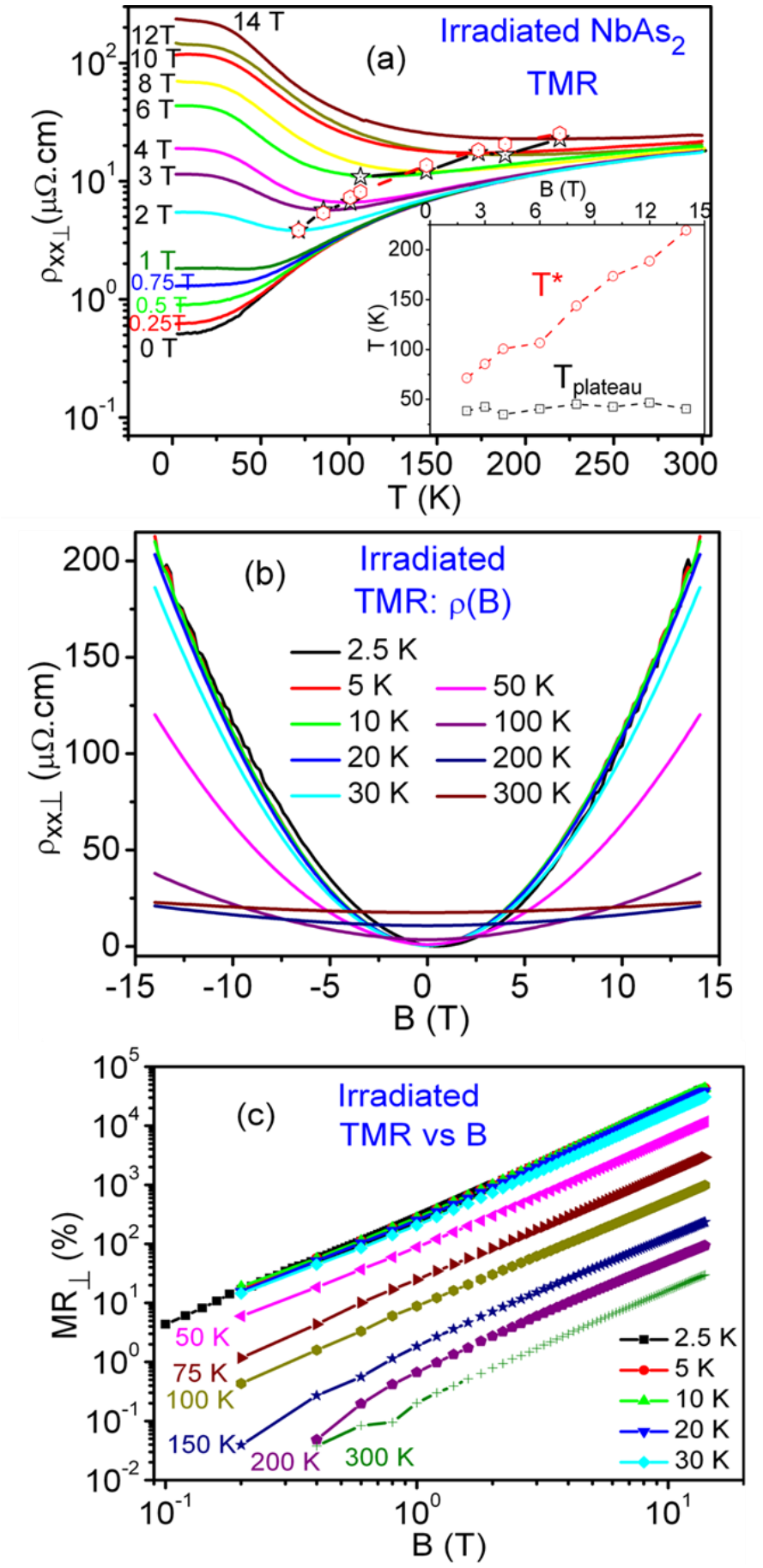
(a)
Irradiated NbAs2
TMR
14 T
12T
10 T
8 T
6 T
4 T
3 T
2 T
1 T
0.75 T
0.5 T
0.25T
0 T
ρxx⊥ (μΩ.cm)
T (K)
B (T)
T*
Tplateau
T (K)
(b)
Irradiated
TMR: ρ(B)
2.5 K
5 K
10 K
20 K
30 K
50 K
100 K
200 K
300 K
ρxx⊥ (μΩ.cm)
B (T)
(c)
Irradiated
TMR vs B
50 K
75 K
100 K
150 K
200 K
300 K
2.5 K
5 K
10 K
20 K
30 K
MR⊥ (%)
B (T)

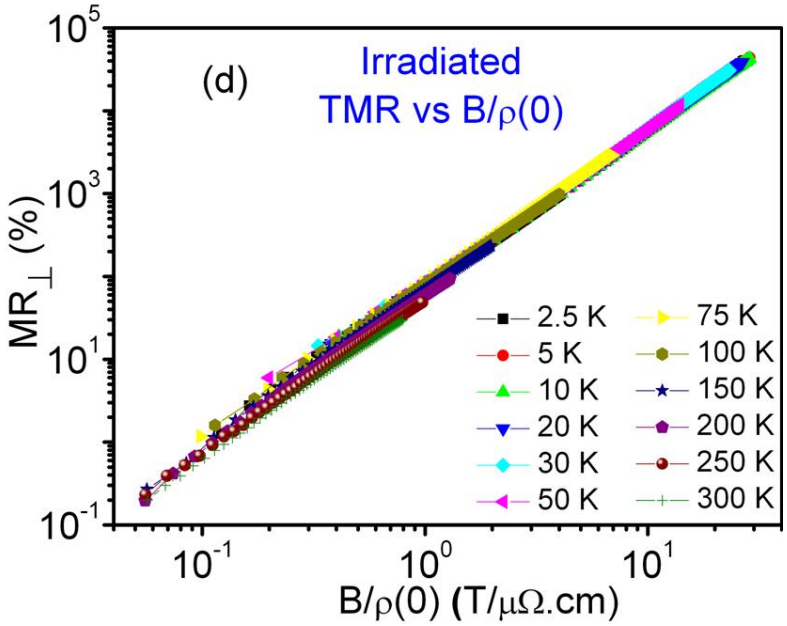

*Figure 4.11 Transverse magneto-resistance results from the measurements on the irradiated $NbAs_2$. **(a)** The temperature variation of MR measured at various indicated constant magnetic fields. **(b)** The isothermal TMR shows parabolic behaviour. The ripples at low temperatures are Shubnikov – de Haas oscillations. **(c)** The double log plot of isothermal TMR data exhibit a near quadratic dependence on the field B. **(d)** Kohler plot generated from the data in 'c' show a collapsed straight line conforming to Kohler's scaling rule.*

The isothermal TMR measurements showed non-saturating, parabolic magneto-resistance behaviour as seen from Figure 4.11b. The double log plot of MR versus B from the irradiated crystal is shown in Figure 4.11c. It exhibits B^m dependence of MR on field with $m \approx 1.85$ across the whole range of field measured (0 T to ±14 T). Here the functional dependence of MR on the field B does not change as we increase the field in contrast to the pristine sample where a quadratic to quasi-linear dependence was seen at low temperatures (See Figure 4.6b). The MR versus B data in Figure 4.11c, when scaled with zero field resistivity, collapsed on to a single straight line in excellent agreement with Kohler's scaling law, as shown in Figure 4.11d. The results from isothermal longitudinal MR measurements in the irradiated $NbAs_2$ are shown in Figure 4.12a. The LMR was found to be positive also in the irradiated sample. As seen from Figure 4.12b, the longitudinal magneto-resistance data also validated Kohler's rule.

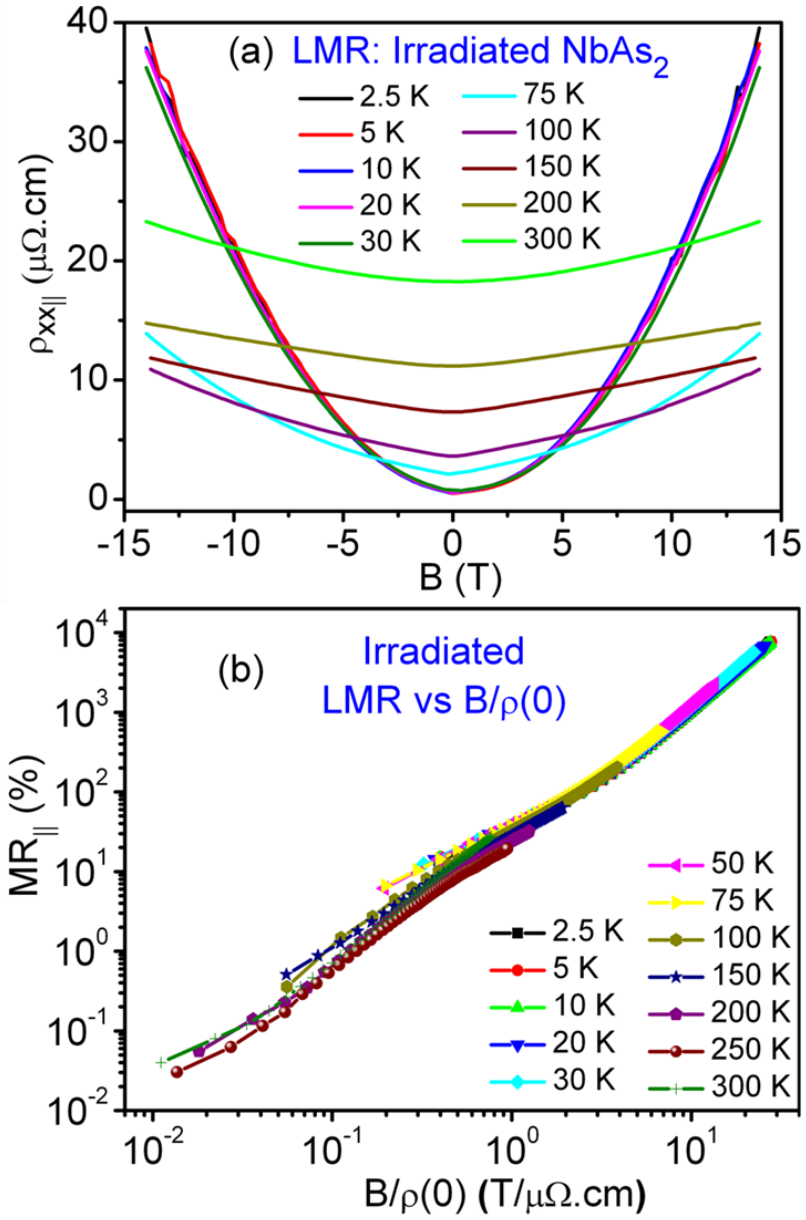

Figure 4.12 ***(a)*** *The isothermal longitudinal MR measurements on irradiated $NbAs_2$ shows positive MR.* ***(b)*** *The collapsed LMR versus B data shows that the irradiated sample follows Kohler's rule.*

So what have we learnt from the studies on irradiated sample? If we take the irradiated sample as another $NbAs_2$ system, with altered defects/disorder, then the present observations provide further vindication of the robustness of the positive LMR in $NbAs_2$, negating that it is a Weyl semimetal. The altered mobility due to irradiation and its relation to the MR value itself will be discussed in Section 4.9.

4.8. Experiments on Heat treated $NbAs_2$ Crystals

As an alternate way of creating disorder in the crystals, heat treatment experiments have been conducted. Crystal has been heat treated after vacuum sealed in a quartz ampoule. The ampoule was slowly heated to 700 K at the rate of 1 K per minute in a box furnace. After reaching 700 K, it was kept at this temperature for two hours and quenched in liquid nitrogen. The recovered sample is designated as HT700K. It has been characterized via Raman measurements as indicated in Section 4.2. It was followed by magneto-resistance and Hall resistance measurements from 2.5 K to 300 K with magnetic fields up to ±9 T. The approximate sample dimension was (1 mm x 0.5 mm x 0.13 mm). MR has been measured in four-probe linear geometry, while four-point cross Hall geometry has been used for collecting Hall resistance as described in Section 2.4.2.

The resistivity measured in the transverse geometry by varying temperature at several fixed fields is given in Figure 4.13a. It exhibit resistivity upturns in magnetic fields starting at 2 T onwards. Figure 4.13b shows the isothermal measurements, displaying near parabolic MR. Magneto-resistance attains a value of over 3×10^4 % at 2.5 K with 9 T. The Kohler plot from the isothermal measurements of HT700K is given in Figure 4.13c. The overlap of MR curves perfectly supports Kohler's scaling. The adherence to Kohler's rule in all the three samples, viz., pristine, irradiated and heat treated, emphasize the fact that the magneto-transport in $NbAs_2$ is characterized by a single dominant scattering mechanism.

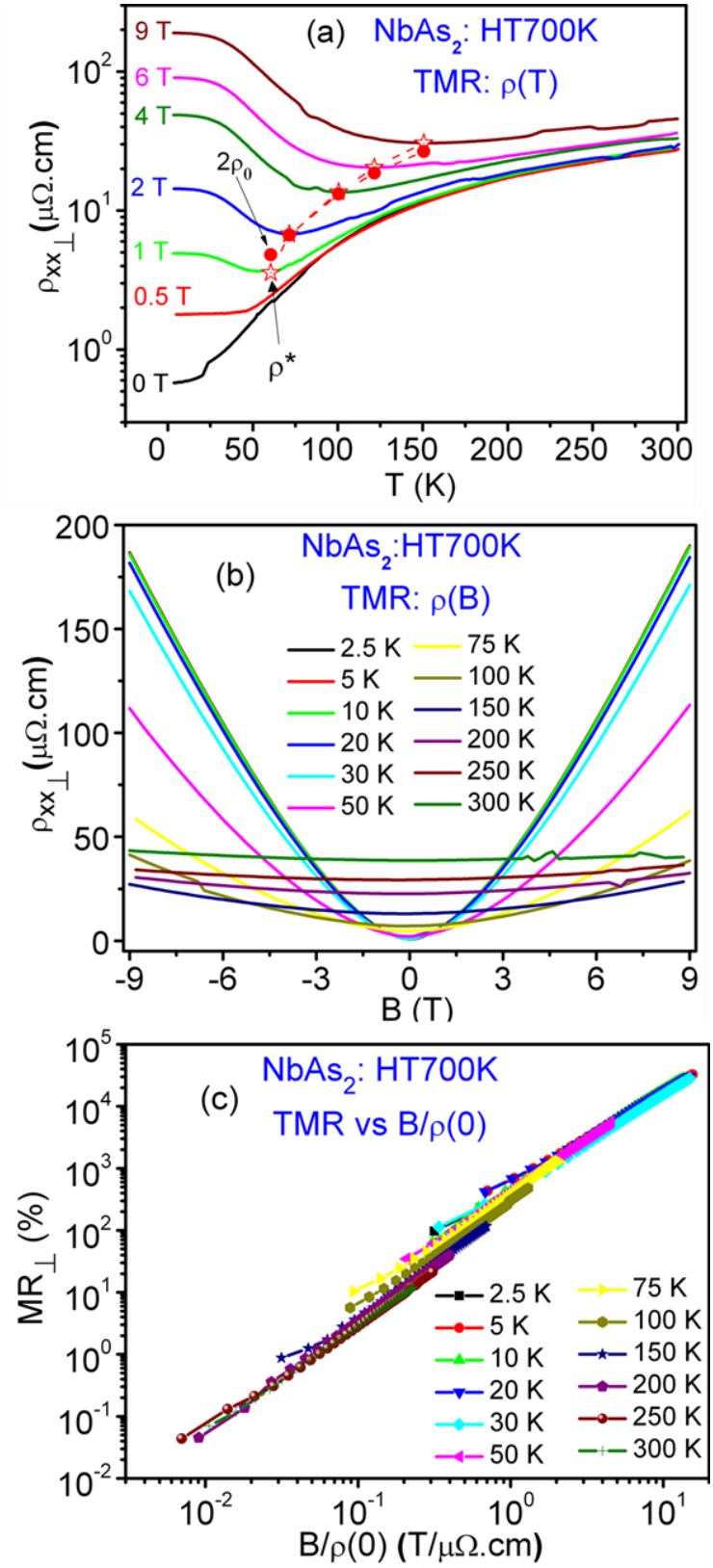

Figure 4.13 Results from the transverse magneto-resistance measurements in the heat treated $NbAs_2$ sample. ***(a)*** *The temperature variation of resistivity at different magnetic fields shows minima and upturns at low temperature.* ***(b)*** *Field variation of isothermal resistivity shows a near parabolic behaviour.* ***(c)*** *The isothermal MR scales to a single curve in the Kohler plot.*

4.8.1. Angular variation of MR: Temperature and Magnetic field dependence

Another aspect investigated in the heat treated sample is the study on the temperature and magnetic field dependence of angular variation of MR discussed in Section 4.3. It is known that insights on the nature of Fermi surface can be obtained from angular dependent magneto-resistance measurements [7, 108]. This is because the symmetry of the Fermi surface influences the resistivity anisotropy when projected onto a plane orthogonal to the electric current [104]. Given this, for the heat treated sample, we have carried out angular MR experiments as a function of temperature. For this, sample has been rotated through 360° at various isothermal conditions from 2.5 K to 100 K under a constant magnetic field of 6 T. As seen from Figure 4.14a, MR exhibits the two-fold symmetric dumb-bell behaviour. This implies that the crystal retains the inversion symmetry across this temperature range where the large MR was seen. Such an observation has been used in literature to negate an electronic structure change in the material brought about by a possible temperature induced Lifshitz transition [108]. A Lifshitz transition can also be driven by magnetic fields [109]. Hence, we have checked the angular dependence with various fixed magnetic fields in an isothermal condition at 2.5 K, and the results are shown in Figure 4.14b. This also gave two-fold symmetric MR variation confirming the centro-symmetric nature. Hence our angular dependent magneto-resistance measurements do not provide any signatures indicating modification of the Fermi surface in $NbAs_2$ with temperature and magnetic fields.

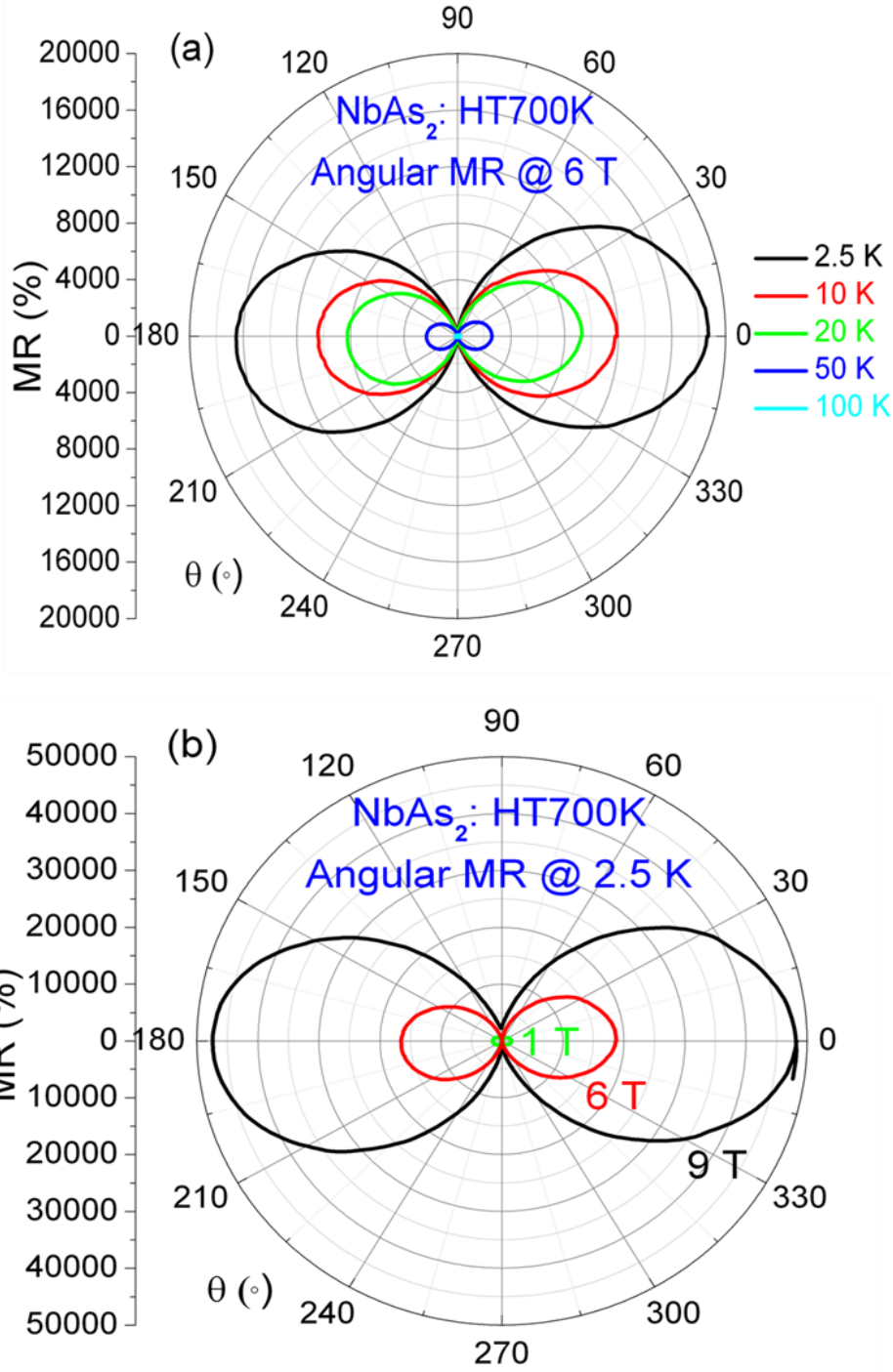

Figure 4.14 The angular dependence of magneto-resistance performed on the heat treated $NbAs_2$ sample. ***(a)*** *With 6 T, at various isothermal conditions.* ***(b)*** *At 2.5 K, with different fields. At all instances the sample retains the dipolar behaviour which negates a temperature or magnetic field induced Liftshitz transition.*

4.9. Hall Measurements: Mobility, Carrier density and linkage to MR

The mechanism behind the extremely large, non-saturating and parabolic magneto-resistance in semimetals has often been ascribed to the compensation of charge carriers from different energy bands [3]. The characteristic of such systems is that MR increases as $(\mu B)^2$ at low fields and saturates to a constant value at high B, where μ is the carrier mobility [4, 13, 59]. Resonant compensation or exactly matching carrier densities has been ascribed to the B^2 behaviour of the XMR (which is non-saturating even at 60 T) in WTe_2 [59, 65, 110].

To have an idea on the magneto-transport in $NbAs_2$, we carried out Hall measurements in the pristine and disordered samples at isothermal conditions by varying the magnetic field from 0 to ±14 T [for heat treated sample up to ±9 T]. The resistances $R_{xy}(+B)$ and $R_{xy}(-B)$ obtained from each directions of the field have been averaged for removing any asymmetry from a possible minor mismatch of the placing of voltage leads. The resultant Hall resistance as a function of field, $R_{xy}(B)$, for all the samples is depicted in Figure 4.15a to Figure 4.15c. It shows that the linear Hall resistance at low fields turns to non-linear with higher applied fields and this is increasingly prominent below 100 K. The non-linear $R_{xy}(+B)$ indicates the role of more than one type of carriers, electrons and holes, in the transport process which is consistent with other XMR systems [64, 65, 70, 103]. However, in the present investigation, we wanted to see the effect of mobility on XMR. Hence, we confined to a single band analysis. Further, we wanted to compare trends across three sets of samples, viz. pristine, irradiated and heat treated. Also, several authors have carried out single band analysis [55, 103]. The Hall coefficient was found to be positive in all samples and it indicates a hole dominant system in agreement with the reported band structure calculations [33].

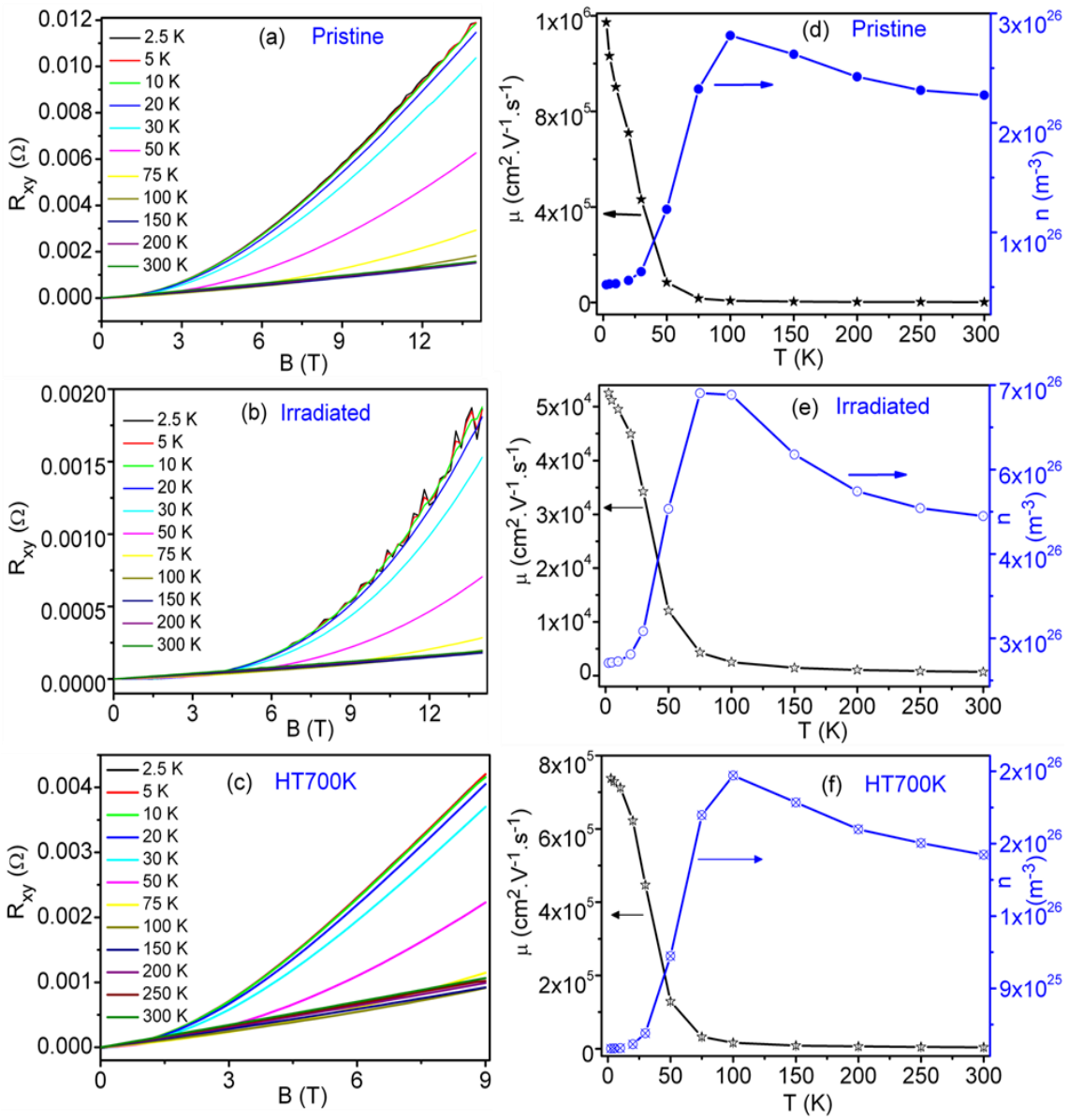

Figure 4.15 Results from Hall measurements. Panels (a) to (c) show the field variation of isothermal Hall resistance from different temperatures for the pristine, irradiated and heat treated $NbAs_2$ samples respectively. Hall resistance is linear at low fields & high temperatures and becomes non-linear at high fields & low temperatures. The right panels display the temperature variation of density and mobility of carriers in the corresponding samples as estimated from a single band model analysis.

The temperature variation of carrier density (n) and their mobility (μ) calculated from the single carrier model is plotted in Figure 4.15d to Figure 4.15f. Both parameters display strong temperature dependence below ~100 K. While the carrier density marginally decreases below 100 K, carrier mobility increases significantly below 100 K with lowering of temperature and reaches very high values at the lowest temperatures.

For example, in the pristine sample $\mu \sim 10^6$ $cm^2.V^{-1}.s^{-1}$ at 2.5 K. When μ is expressed in inverse tesla (10^4 $cm^2.V^{-1}.s^{-1}$ = 1 T^{-1}), the mobility of pristine $NbAs_2$ is ~100 T^{-1}. In the pristine and disordered samples, carrier mobility lies between 1 to 100 T^{-1} ($\approx 10^4$ - 10^6 $cm^2.V^{-1}.s^{-1}$) below 50 K. It is to be noted that the temperature region where mobility attains ultra-high values and carrier density saturates has remarkable resemblance with the temperatures in which large MR has been observed (See Figure 4.5a).

Now we look at the MR data to figure out its correlation with mobility. We present in Figure 4.16a to Figure 4.16c the temperature dependence of the transverse magneto-resistance measured at various fixed fields of the $NbAs_2$ samples. Upon normalizing these MR curves by the corresponding MR at 5 K, we see that all the curves collapse to a single line as depicted in the second columns of the Figure 4.16 (See panels 'd to f'). The magneto-resistance is seen to vary monotonically as temperature is lowered and for T < 100 K, MR shows tremendous increase. The collapse of MR data provides another evidence for the absence of a metal - insulator transition that can make the resistivity upturns and plateaus in the ρ (T) curves of Figure 4.5a.

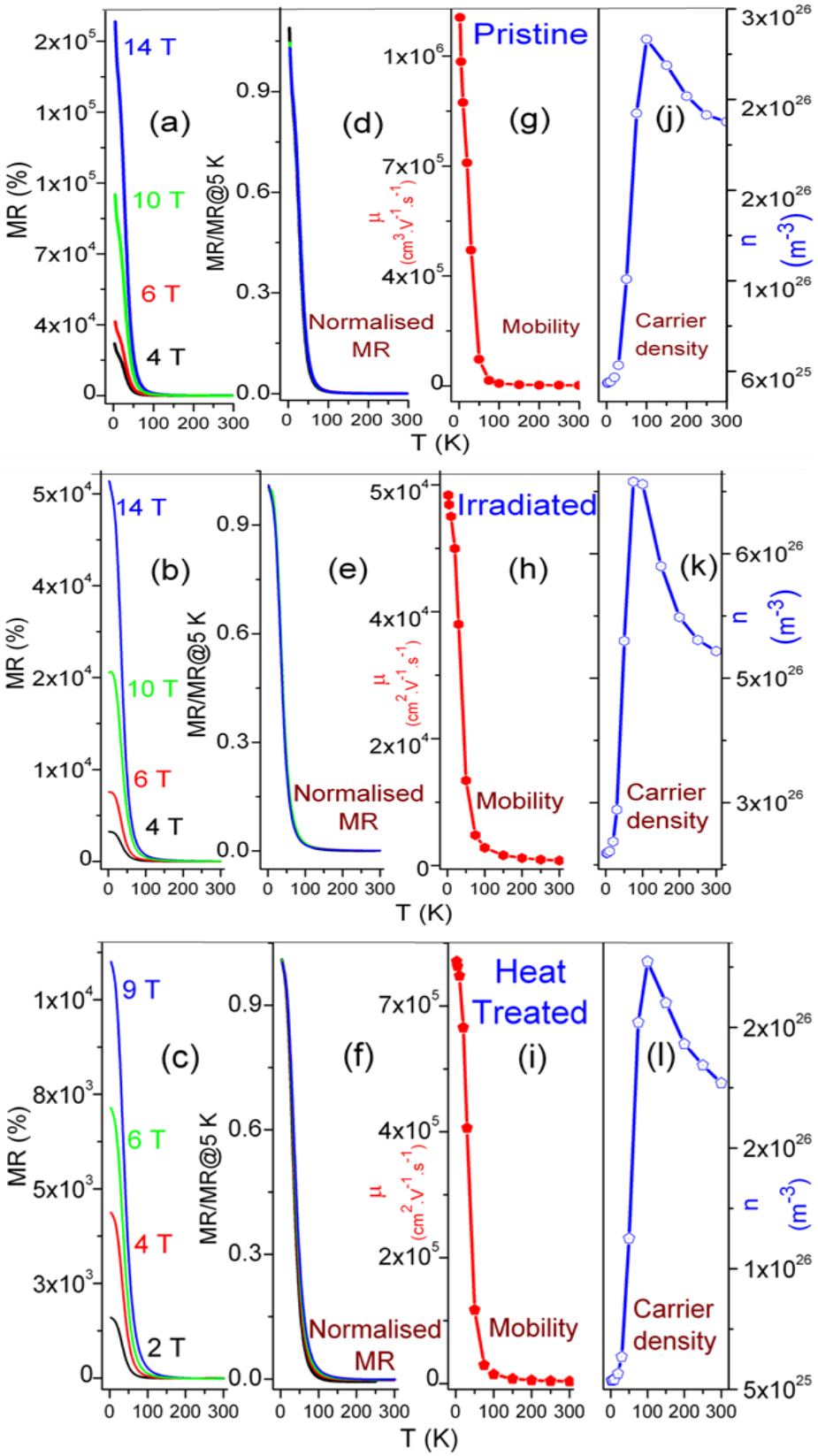

Figure 4.16 Correlation between the temperature dependence of magneto-resistance with that of carrier mobility and carrier density in the $NbAs_2$ system. The results are compiled in different panels for the pristine (top), irradiated (middle) and heat treated (bottom) samples. It is clearly seen that the magneto-resistance tracks the variation of mobility with temperature.

The temperature variation of mobility of the carriers is plotted in Figure 4.16g to Figure 4.16i. We note that the variation of mobility with temperatures is similar to the magneto-resistance behaviour as shown by the collapsed curves. It is known that for multi-carrier systems, Kohler's rule can often be modified as $MR = F(\mu' B)$, where μ' is the mean electron and hole mobility [81]. Further, it is to be recalled that when Kohler's rule is valid, the temperature dependent changes in the magneto-resistance are attributed to the variation of the carrier mobility in the system [14, 81]. Another notable feature is that the mobility increases rapidly in the temperature range where the carrier density decreases as depicted in Figure 4.16(j, k & l). A low density of carriers together with high purity of the sample (evidenced by the low residual resistivity and high RRR) effectively reduces the electron - phonon and impurity scattering events, leading to large MR [8].

4.10. Conclusions

Angle dependent magneto-resistance experiments confirmed the absence of negative MR in $NbAs_2$ (Figure 4.4). It was also shown to negate temperature and field induced electronic structure changes as a probable reason for the large magneto-resistance effect (Figure 4.14). The MR behaviour in the whole range of temperature and magnetic field followed Kohler's scaling rule in transverse (Figure 4.7) and longitudinal (Figure 4.9) measurement configurations. The temperature dependence of MR was found to follow the corresponding variation of charge carrier mobility, as estimated from Hall resistance measurements (Figure 4.16). These observations have also been validated through experiments with disordered $NbAs_2$ crystals of altered mobility, created via ion irradiation and heat treatments. The investigations point out that the extremely large MR is a characteristic of high purity semimetals having high mobility and low density carriers.

Chapter 5

de Haas - van Alphen Measurements in $TaAs_2$ and $NbAs_2$ Single Crystals

In this chapter, we present the results of de Haas - van Alphen (dHvA) experiments, carried out using the SQUID magnetometer, to obtain the transport parameters in the pristine and irradiated di-pnictides. The oscillation frequencies have been obtained by fast Fourier transform of the de Haas - van Alphen oscillations, and the transport parameters such as cyclotron mass, Dingle temperature etc. were extracted using Lifshitz - Kosevich analysis of the amplitude dampening of oscillations. The oscillation frequencies in pristine samples have also been obtained through the analysis of Shubnikov - de Haas measurements, and the results show good agreement with each other. The diamagnetic background of the dHvA oscillations is seen to be influenced by temperature, and disorder introduced by irradiation. From a Landau level-fan diagram analysis of the dHvA oscillations, the Berry phase has been extracted, to look for the topological signatures in the di-arsenides.

5.1. Introduction

When an external magnetic field (B) is applied to a metallic crystal, the energy of the conduction electrons is quantized by the applied field into a series of Landau sub bands. As the magnetic field increases, the Landau sub bands successively pass through the Fermi level (E_F). The resultant fluctuations of the density of states at E_F result in the oscillations of the magnetization in the de Haas - van Alphen (dHvA) effect. Further, as the probability of the scattering in electrical transport is also proportional to the density of states, the resistance oscillates with increasing magnetic field leading to the Shubnikov - de Haas (SdH) effect. The oscillations are periodic in $\frac{1}{B}$, and their frequency is given by the Onsager - Lifshitz relation [111]

$$B_F = \frac{1}{\Delta\left(\frac{1}{B}\right)} = \frac{\hbar}{2\pi e} A_{ext}$$

(5. 1)

where A_{ext} is the extremal Fermi surface cross sectional area (or extremal orbits) in k-space perpendicular to B direction. Thus by changing the direction of the field orientation, several frequencies can be obtained, leading to different extremal areas, and consequently the whole Fermi surface shape of the material can be mapped out [4, 111].

With the increase of temperature, the quantum oscillations are damped out, that reflects the broadening of the Landau levels due to temperature and disorder. Lifshitz and Kosevich [112] modeled the oscillations as a Fourier series, periodic in inverse magnetic field, in terms of the characteristic parameters of the electronic band structure [111]. From Lifshitz - Kosevich (L-K) analysis of the thermal damping effect of the quantum oscillations, it is possible to extract some critical parameters of the electron and hole pockets, such as the cyclotron mass and relaxation time.

Furthermore, the analyses of the phase shift of SdH and dHvA oscillations have been used to determine the Berry phase of the electron pockets [113] which is an important signature of their non-trivial topology. The Berry phase, that is the additional geometrical phase factor acquired in the adiabatic evolution along a closed trajectory in the parameter space, is determined by the topological characteristics of the electron bands in the Brillouin zone. For a band with linear energy dispersion, the cyclotron motion of Dirac fermions under magnetic field B induces Berry phase of π in the phase of quantum oscillations, in contrast with a zero Berry phase for a topologically trivial parabolic dispersive band. In the data analyses, the resistivity / magnetization peaks and valleys were used to identify the Landau indices (n) and a plot of n versus $\frac{1}{B}$, called the Landau Level - fan diagram, is used to extrapolate the phase shift.

The SdH / dHvA measurements along with band structure calculations in the transition mono-pnictides have been used to probe the topology of the Fermi surface. As an example of these studies, we present in Figure 5.1, the results in Weyl semimetals NbP [114] and TaP [42] from the literature. In comparison to mono-pnictides, there are fewer studies in di-pnictides. Mention can be made of the studies by Shen et al [29] in which SdH oscillations have been investigated in $NbAs_2$.

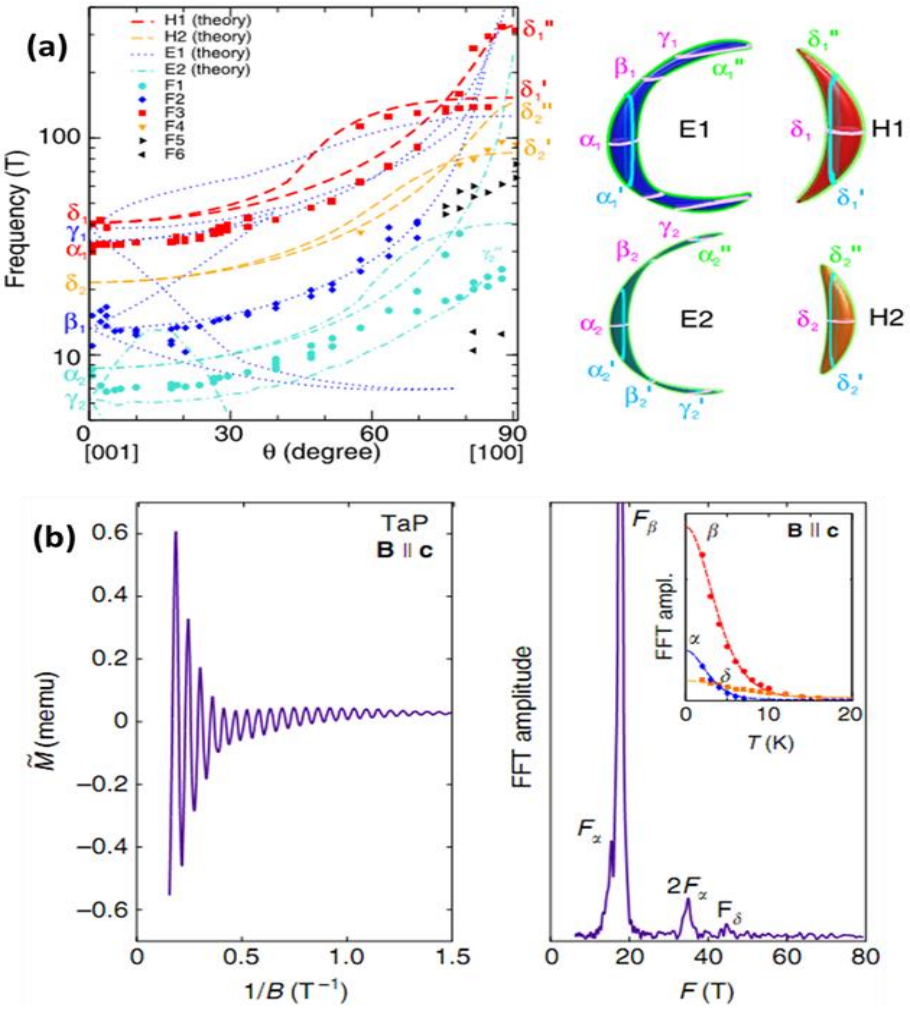

Figure 5.1 Representative results from literature in Weyl semimetals based on dHvA measurements. ***(a)*** *The angular dependence of the quantum oscillation frequencies in NbP, and the calculated Fermi surface cross sections are used to map the electron and hole pockets. Adapted from Klotz et al* [114]. ***(b)*** *The dHvA oscillations and the frequency spectra in TaP, as adapted from Arnold et al* [115]. *The temperature dependence of the oscillation amplitude is fitted with Lifshitz - Kosevich formula as shown in the inset.*

In this chapter, we present the results of de Haas - van Alphen experiments in $TaAs_2$ and $NbAs_2$. These investigations have been carried out with the limited objective of providing support to the magneto-resistance measurements presented in Chapters 3 and 4, rather than to investigate the Fermiology. In particular, we investigate the effect of irradiation and also obtain the transport parameters. We also analyze the data to see if the di-pnictides have topological features, viz., the Berry phase.

Towards this, we have carried out the temperature dependent measurements of de Haas - van Alphen oscillations in $TaAs_2$ and $NbAs_2$. The fast Fourier transform (FFT) technique has been employed to obtain the dHvA frequencies. The field variation of oscillation amplitude was analyzed using the Lifshitz - Kosevich equation to extract various transport parameters. In addition, the oscillation features have also been extracted from Shubnikov - de Haas measurements in the pristine samples.

5.2. Apparatus and Experimental Methodology

The magnetic measurements were performed using the Quantum Design make liquid cryogen-free (2 K, 7 T) Magnetic Property Measurement System SQUID Vibrating Sample Magnetometer (MPMS SQUID VSM). This system combines the speed of a vibrating sample magnetometer (VSM) and the superior sensitivity of a Superconducting Quantum Interference Device (SQUID) magnetometer. A photograph of the facility is shown in Figure 5.2. The main cabinet houses the magnet power supply, system control electronics, computer control system and the 7 T superconducting magnet shielded with the nitrogen jacket. The collection of high precision data is accomplished with a superconducting rapid switching element that changes between superconducting and normal states within a second. The temperature control allows cooling the sample from room temperature to 1.8 K in 30 minutes. Cold helium gas, driven by a pulse tube refrigerator (shown in the inset of Figure 5.2) is passed to the sample chamber through a

variable flow valve. A turbo-molecular pump generates vacuum in the sample chamber and the pump console can be seen at the bottom right in Figure 5.2.

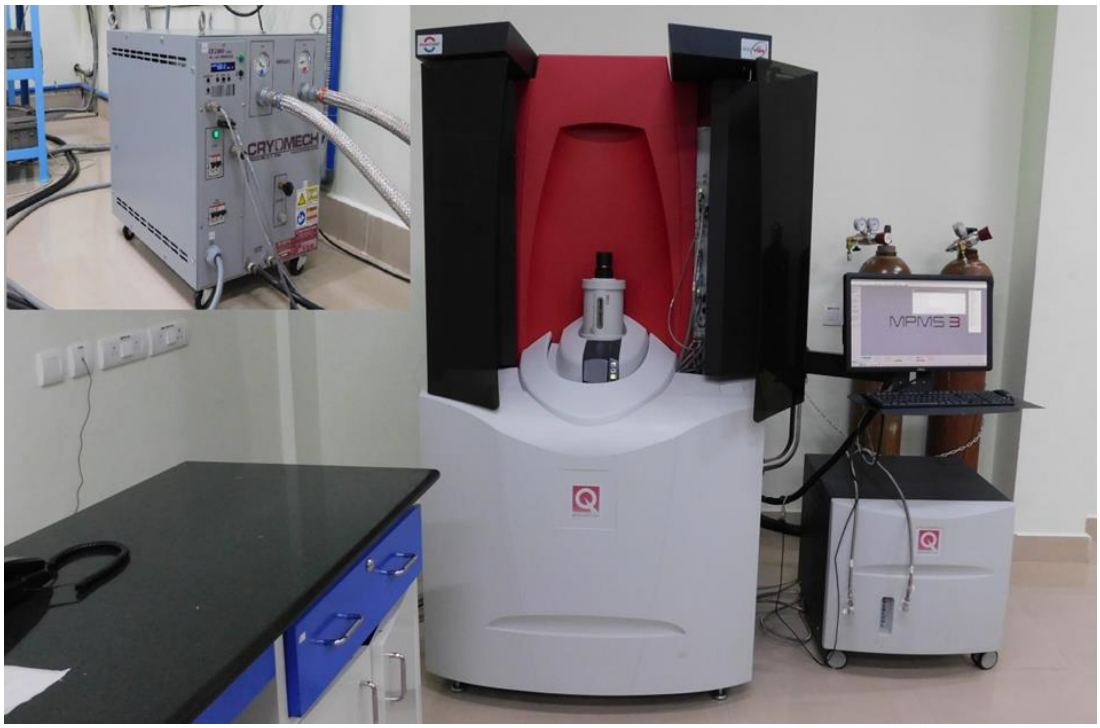

Figure 5.2 A photograph of the SQUID VSM facility. It shows the main cabinet along with electronics control unit, computer control system and the pump console. The top inset is the pulse tube cryo-cooler.

Figure 5.3a shows the photograph of the sample mounting platform on which a quartz sample holder is placed. The sample holder is in the shape of a semi-cylindrical rod. In order to mount the sample, the holder is placed on the platform. The area of the quartz holder parallel to the white strips on the platform approximately comes within the pickup coil region in the magnetometer. Hence the sample is mounted within this length of the quartz holder. Well faceted single crystals, sonicated and cleaned in isopropyl alcohol, were used for measurements. Samples were handled with non-magnetic tweezers. The crystal was carefully mounted on the flat side of the holder, either parallel or perpendicular to the field using double sided sticky tape, under a microscope. It was wrapped around the quartz holder using teflon tape so that the crystal will not accidently fall in the cryostat during the VSM measurement. Care was taken to use minimum amount of sticky tape and

teflon to reduce the background signal in the collected data. The sample loading stick is in the shape of a long rod and is shown in Figure 5.3b. After mounting the sample, the quartz holder is attached to the bottom end (shown in Figure 5.3c) of the sample loading stick. The stick is inserted to the sample space through the airlock valve at the top of the cryostat chamber. The top end of the stick (Figure 5.3d) is magnetically coupled to the airlock opening.

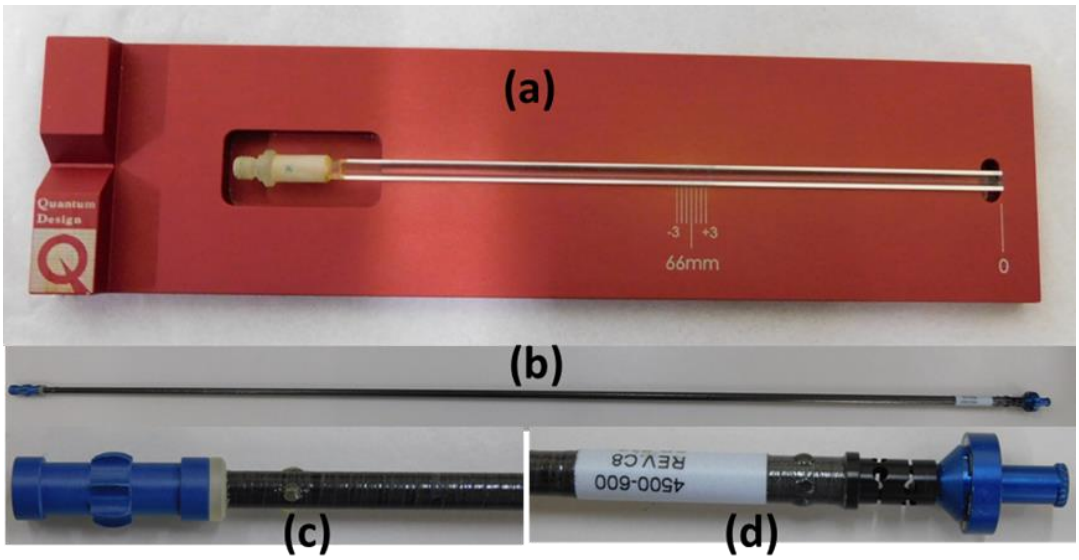

*Figure 5.3 Photographs of **(a)** sample mounting platform, quartz holder and the **(b)** sample loading stick. After mounting the sample, the quartz holder is attached to the bottom end of the stick, shown in **(c)**. The other end shown in **(d)** is magnetically coupled to the airlock valve after loading the stick into the cryostat chamber.*

The operation of the magnetometer and the collection of data are automated through a Windows based multiple document interface application called 'MPMS MultiVu'. It records the magnetic moment as the voltage output of the SQUID detector when the sample makes an upward movement during its vibration through the pickup coils. The measurements are taken with respect to the initialization position. At each position 'MultiVu' records several voltages, and averages them for improved measurement resolution. The MPMS system has typically a resolution > 10^{-8} emu. Once the sample is loaded, it needs to be centered properly within the pickup coils. For this, the

sample is moved in the vertical path (approximately 12 cm long) thorough the coils and the SQUID detector responses are recorded. This is done after applying an external magnetic field ~1000 Oe to 2000 Oe (0.1 T to 0.2 T). Since we have mounted the sample on the quartz within the range indicated by the sample loading platform, we can perform only a partial centering with pre-set position values. 'MultiVu' system scans the sample magnetic moment during the vertical motion and provides a voltage response profile as a function of the position. The sample is centered based on this output and subsequently start the measurement sequence. We have measured isothermal magnetic moment as a function of magnetic field at several temperatures from 2.5 K to room temperature. The magnetic field was applied in intervals of 0.01 T (100 Oe) from 0 to 7 T. The field was stabilized at each measuring point and five values of moments were recorded, and averaged them for accuracy. After each measurement, the remanent magnetic field was ramped to a few Oersted (~5 Oe) by oscillating the field in positive and negative cycles. The sample was warmed to room temperature (300 K) after every isothermal measurement.

5.3. Magnetization in $TaAs_2$: Low Temperature Measurements Exhibit Oscillations

Magnetization measurements on the pristine $TaAs_2$ sample have been carried out at several isothermal conditions from 2.5 K to 300 K in magnetic fields up to 7 T. Figure 5.4 shows the raw magnetization data (in units of emu/g) plotted against the applied field (in Tesla) for selected temperatures. It exhibits spectacular de Haas - van Alphen oscillations at low temperatures. The magnetic field was applied parallel to the *b*-axis of the crystal. The oscillations are seen to ride on a diamagnetic background. It is seen from Figure 5.4 that while the period of oscillations remains nearly the same across the temperature range, their amplitude successively dampens with an increase of temperature. The oscillations disappear completely beyond 30 K.

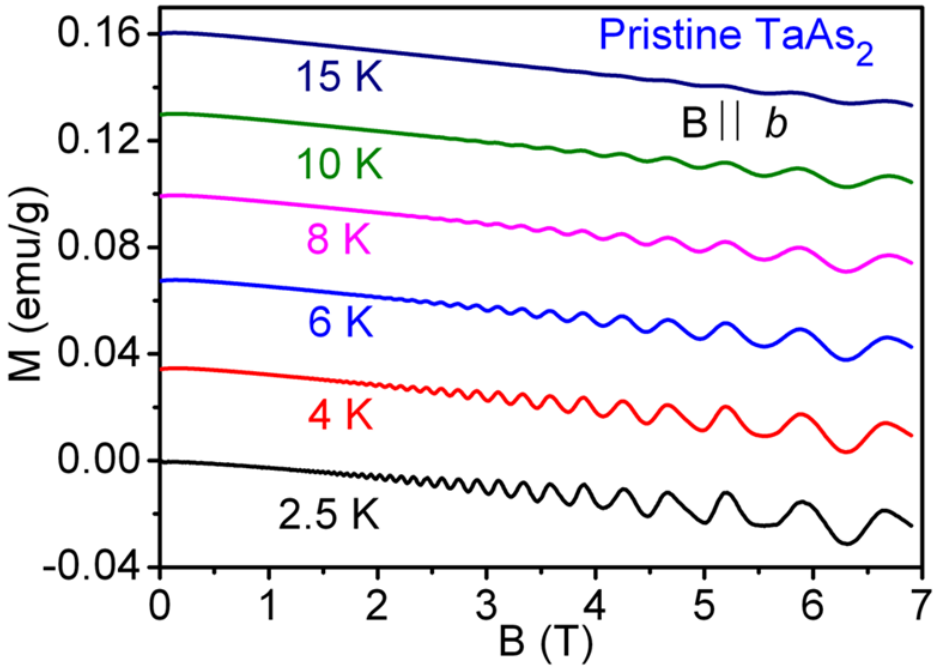

Figure 5.4 The raw magnetization data as obtained from the isothermal measurements in pristine $TaAs_2$ is plotted against the magnetic field applied parallel to the b-axis of the crystal. It displays clear de Haas - van Alphen oscillations riding on a diamagnetic background. The Y-axis is shifted upward in each curve except in 2.5 K for clarity of oscillations.

Figure 5.5a is the dHvA oscillations after subtracting a polynomial background from the data shown in Figure 5.4. The data were further analyzed using fast Fourier transform (FFT) technique to identify the frequencies of oscillations [111]. The resultant plots of FFT amplitude versus frequency from various isothermal measurements are given in Figure 5.5b. In order to obtain this, the data in Figure 5.5a was plotted against the inverse magnetic field ($\frac{1}{B}$). Then, an interpolation to 2048 points was performed to obtain equidistant data points in $\frac{1}{B}$. Fourier transform was carried out on this data. The peaks in the spectrum indicate the oscillation frequencies. The FFT spectra in Figure 5.5b shows that the main dHvA oscillation frequency is 46 T (for example, see the black curve corresponding to 2.5 K). Identical value (45 T) from Shubnikov - de Haas oscillation studies is reported in literature [31]. Besides we could observe one more frequency at 76 T. This frequency is quite weak compared to 46 T and disappears quickly as the

temperature is increased. It can be observed from Figure 5.5b that the first harmonic of 46 T at 92 T is also contained in the oscillations. The presence of multiple frequencies in FFT result indicates that $TaAs_2$ contains different carrier pockets across the Fermi level and is consistent with literature [13].

In addition, we have repeated the dHvA experiments with another pristine $TaAs_2$ sample of the same batch and obtained 39 T as the main oscillation frequency. In all the literature based on SdH studies, two prominent frequencies are observed. Wu et al [13] reported 190.5 T and 212.5 T, while Yuan et al [30] identified smaller frequencies at 39 T and 54 T. Similar values, 39 T and 56 T, were seen by Rao et al [116]. The major frequencies observed in Wang et al's [31] experiments are 45 T and 158 T. The only previous work from the dHvA studies lists 41 T, 54 T, 85 T and 130 T as the frequencies obtained [62]. The frequencies from our experiments are presented in Table 5.1, where a comparison with literature values is also presented.

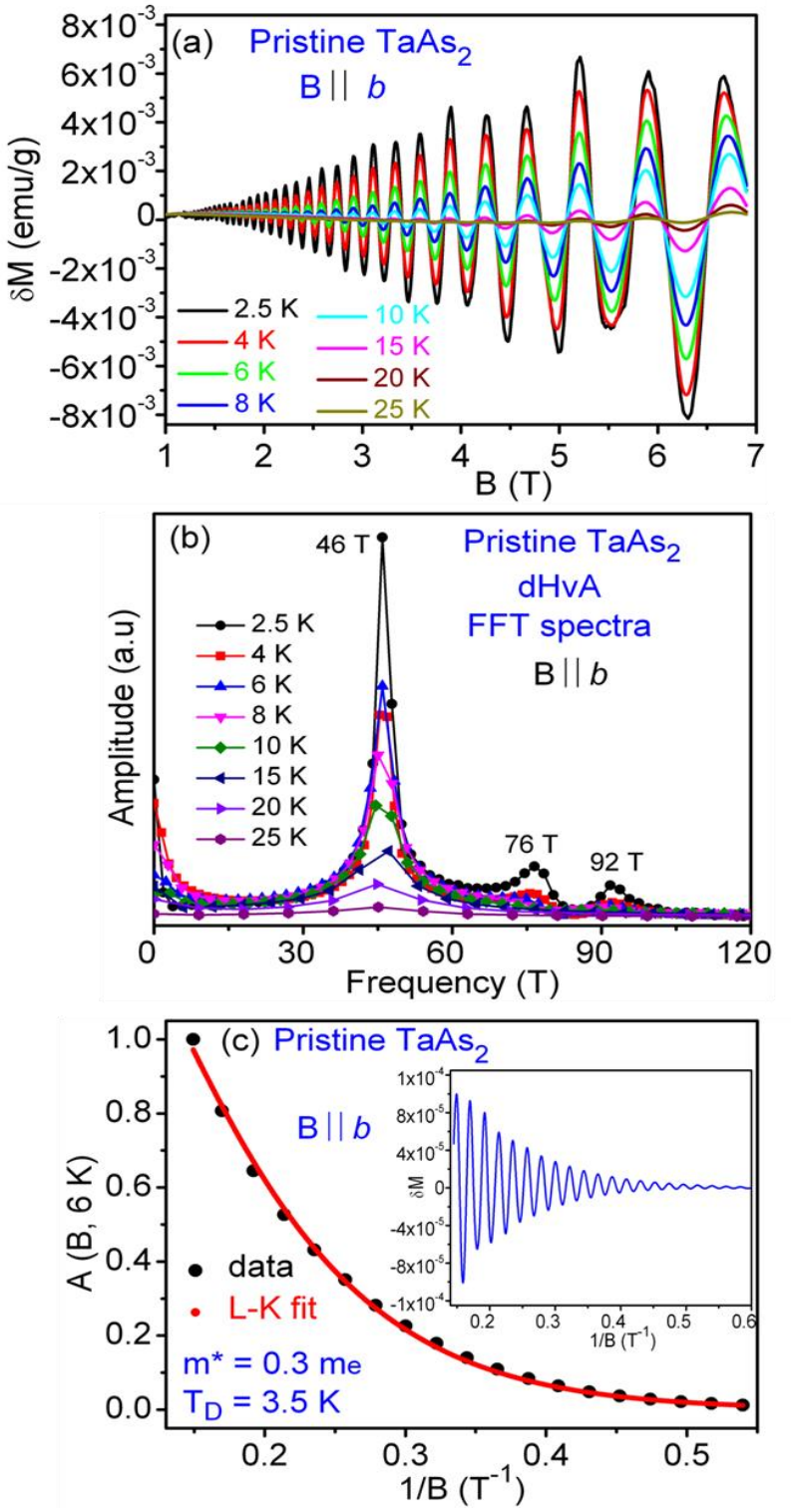

Figure 5.5 ***(a)*** *Polynomial background subtracted magnetization data of pristine $TaAs_2$ at various temperatures is plotted against the magnetic field (parallel to b-axis). It displays dHvA oscillations up to 25 K.* ***(b)*** *FFT spectra of data show various oscillation frequencies.* ***(c)*** *The Lifshitz - Kosevich fit of the oscillation amplitudes in a varying magnetic field obtained at 6 K to estimate effective carrier mass and Dingle temperature. The inset is the background subtracted residual magnetization versus inverse field plot, showing the weakening of oscillation amplitudes with decrease of field.*

In order to obtain the effective carrier mass (cyclotron mass) and Dingle temperature in pristine $TaAs_2$, we have analyzed the dHvA oscillations presented in Figure 5.5a using the Lifshitz - Kosevich (L-K) formula. Following Shen et al [29] the amplitude variation of oscillation in a varying magnetic field (B), measured at a given temperature (T), is given as [111]

$$A\,(B,T) \propto \frac{\frac{\alpha T m^*}{B}}{sinh\left(\frac{\alpha T m^*}{B}\right)}\; exp\left(-\frac{\alpha T_D m^*}{B}\right) \qquad \textbf{(5. 2)}$$

Here $A\,(B,T)$ is the normalized oscillation amplitude at a given T, $\alpha = \frac{2\pi^2 k_B m_e}{e\hbar} = 14.69\,T/K$, m^* is the effective carrier mass and T_D is the Dingle temperature. The relaxation time is related to the Dingle temperature through $\tau_q = \frac{\hbar}{2\pi k_B T_D}$. An L-K fit of the oscillations obtained at 6 K is given in Figure 5.5c. The residual oscillations (δM) plotted against $\frac{1}{B}$ are depicted in the inset of Figure 5.5c. The fit resulted in an estimation of cyclotron mass (m^*) as $0.3\,m_e$ in units of electron rest mass (m_e) and Dingle temperature as 3.5 K [48]. The value of m^* is comparable with that reported from SdH measurements ($0.17\,m_e$ to $0.34\,m_e$) [13, 30, 31].

The magnetization measurements were also carried out by applying the field parallel to the *a*-axis of the sample. But the oscillation amplitudes, shown in Figure 5.6a, were not as distinct as that observed when the field was parallel to *b*-axis (See Figure 5.5a). The FFT spectrum in the inset of Figure 5.6a shows that it has two prominent frequencies at 83 T and 129 T, which are very close to the values viz., 85 T, 130 T earlier cited from literature [62]. A consolidation of all the dHvA frequencies obtained from our samples is given in Table 5.1. Figure 5.6b shows the L-K fit of the oscillation amplitudes measured at 4 K. In this case, a higher cyclotron mass, $1.45\,m_e$ was obtained, while the

Dingle temperature (3.3 K) remains more or less same. This implies that magneto-transport is anisotropic in $TaAs_2$ in agreement with our magneto-resistance results presented in Chapter 3 (Refer Section 3.8.2). Essentially, our studies show that the charge carriers in $TaAs_2$ are having low masses and also suggest an anisotropic Fermi surface in the material.

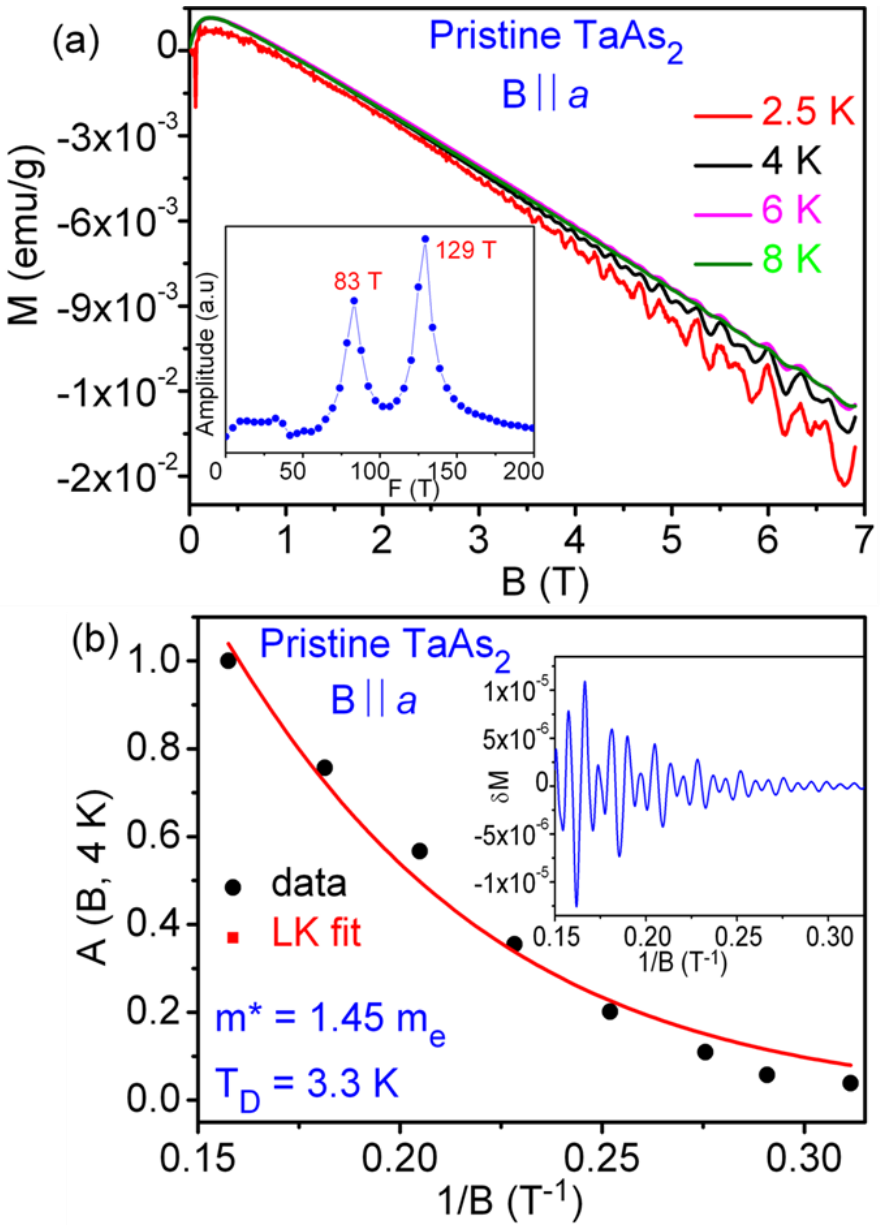

Figure 5.6 ***(a)*** *The dHvA oscillations exhibited by the pristine $TaAs_2$ when magnetic field was applied parallel to the a-axis. The oscillations are weaker than that when field was parallel to the b-axis. The inset is the FFT spectrum of oscillations at 4 K.* ***(b)*** *The Lifshitz - Kosevich fit shows an increase in carrier mass when magnetic field is parallel to the a-axis. Inset is the plot of residual magnetization versus inverse field at 4 K.*

5.4. Magnetization in $NbAs_2$: Multi-frequency Quantum Oscillations at Low Temperature

The isothermal magnetization measurements in pristine $NbAs_2$ have been carried out at various temperatures from 2.5 K to 30 K in magnetic fields up to 7 T. The magnetization plotted against magnetic field applied along the *b*-axis is given in Figure 5.7a. It displays de Haas - van Alphen oscillations up to 25 K. The diamagnetic nature of the magnetization signal is evident from the figure. The oscillations start appearing with a field as low as 0.7 T at 2.5 K. The dHvA amplitudes dampen with temperature and almost vanish by 30 K. The presence of various oscillation frequencies is clearly discernible at higher fields in $NbAs_2$ [117]. To analyze the oscillations in Figure 5.7a using fast Fourier transform, a polynomial background was subtracted from each of the isothermal pattern. The residual magnetization versus inverse field data was subjected to FFT analysis using the methodology described in the previous Section 5.3. The FFT spectra obtained for various isothermal measurements are shown in Figure 5.7b. It shows four distinct peaks viz., 32 T, 62T, 91 T, and 106 T with 32 T as the main oscillation frequency. The oscillation frequencies obtained in the present experiments and a comparison with the literature results are presented in Table 5.1.

Now let us briefly look at the literature for comparing the quantum oscillation frequencies observed in $NbAs_2$ with our results. First, we note that there are no reports of de Haas - van Alphen oscillation studies on $NbAs_2$. The density functional theory (DFT) calculations of Shen et al [29] and Yupeng Li et al [28] predict four carrier pockets in $NbAs_2$. The SdH studies by Shen et al distinguish three different frequencies (76 T, 122 T, 226 T) [11, 29] when field was perpendicular to *ab*-plane. Here, 122 T may be associated with the first harmonic of 62 T peak seen in the present investigation. Yupeng Li et al [28] lists 109.6 T, 234.3 T and 270.5 T as their SdH frequencies. In this case 109.6 T is close to 106 T while 270.5 T may be a harmonic of 91 T. Further, Peramaiyan et al [90] reported

32 T (which we have observed) and 266 T as their major SdH oscillation frequencies [90]. Experiments of Yuan et al [30] revealed 124 T (which in turn is the first harmonic of 62 T) and 224 T (the seventh harmonic of 32 T). Wang et al [31] identified 90 T (closer to our 91 T) and 204 T. Thus, the dHvA frequencies obtained from our experiments more or less match with the reported SdH frequencies [29-31, 90].

The amplitude variation of oscillations in pristine $NbAs_2$ was analyzed using Lifshitz - Kosevich formula (See Equation (5. 2)). The L-K fit of the data at 2.5 K is depicted in Figure 5.7c. The cyclotron mass and Dingle temperature were obtained as $0.47\ m_e$ and 2.1 K. The inset shows the beating pattern, when plotted between residual oscillations versus $\frac{1}{B}$, indicating multiple frequencies. de Haas – van Alphen oscillations were also seen with smaller amplitudes when magnetic field applied parallel to the *a*-axis. The FFT frequencies obtained are 113 T, 165 T and 322 T. The L-K analysis of oscillations at 2.5 K is shown in Figure 5.7d and the calculated m^* and T_D are $1.6\ m_e$ and 3.6 K respectively. The estimated cyclotron masses from both orientations are slightly larger than reported from SdH experiments (~ $0.15\ m_e$ to $0.35\ m_e$) [29-31, 90] and it may be due to the difference in the field directions between various experiments.

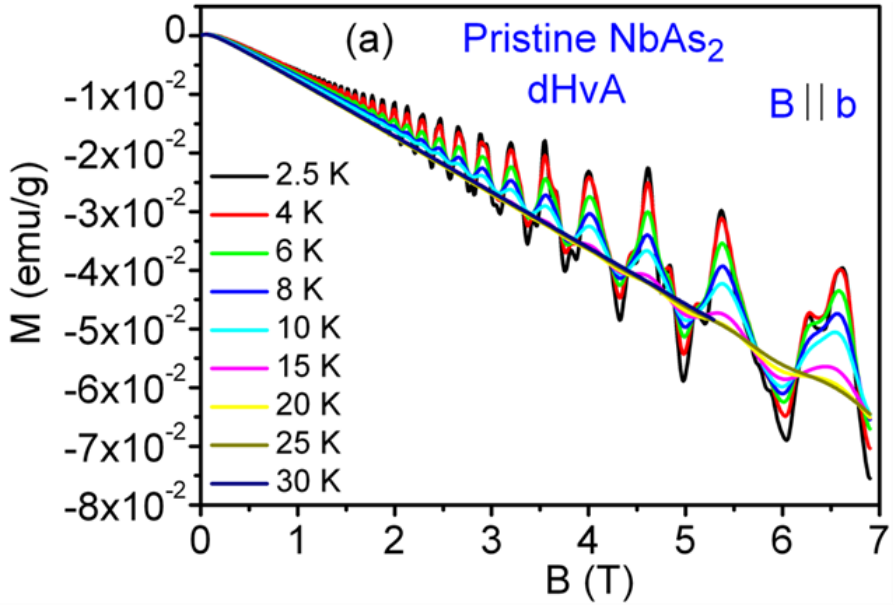
(a)
Pristine NbAs2
dHvA
B || b
M (emu/g)
0
-1x10-2
-2x10-2
-3x10-2
-4x10-2
-5x10-2
-6x10-2
-7x10-2
-8x10-2
2.5 K
4 K
6 K
8 K
10 K
15 K
20 K
25 K
30 K
0 1 2 3 4 5 6 7
B (T)

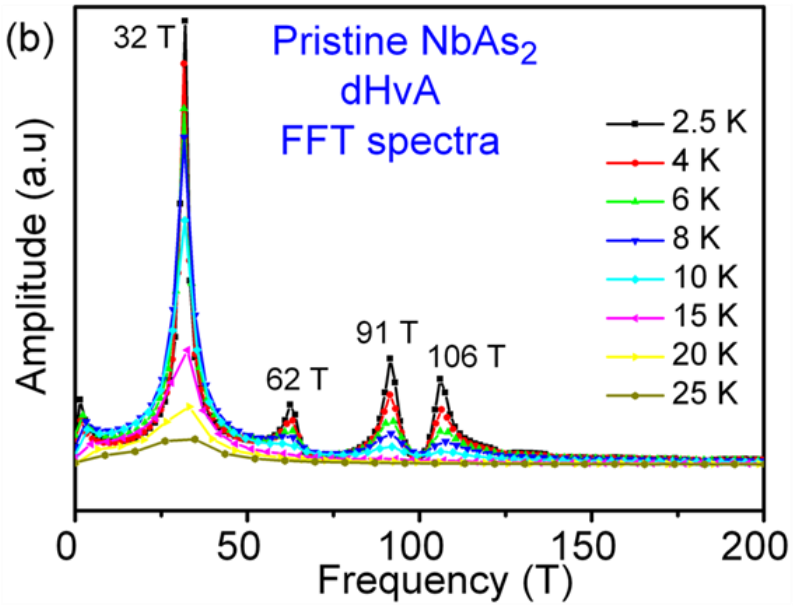
(b)
32 T
Pristine NbAs2
dHvA
FFT spectra
Amplitude (a.u)
62 T
91 T
106 T
2.5 K
4 K
6 K
8 K
10 K
15 K
20 K
25 K
0 50 100 150 200
Frequency (T)

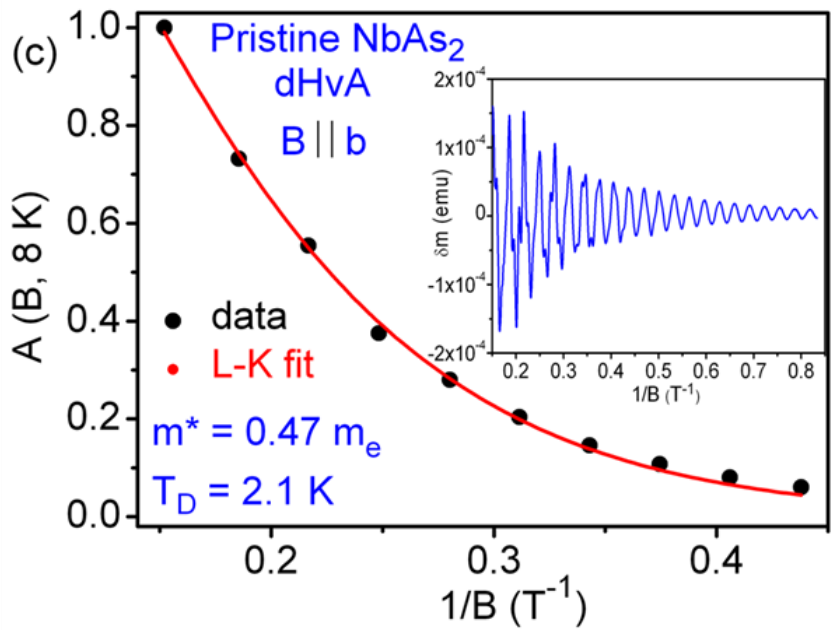
(c)
Pristine NbAs2
dHvA
B || b
A (B, 8 K)
1.0
0.8
0.6
0.4
0.2
0.0
data
L-K fit
m* = 0.47 me
TD = 2.1 K
0.2 0.3 0.4
1/B (T-1)
2x10-4
1x10-4
0
-1x10-4
-2x10-4
δm (emu)
0.2 0.3 0.4 0.5 0.6 0.7 0.8
1/B (T-1)

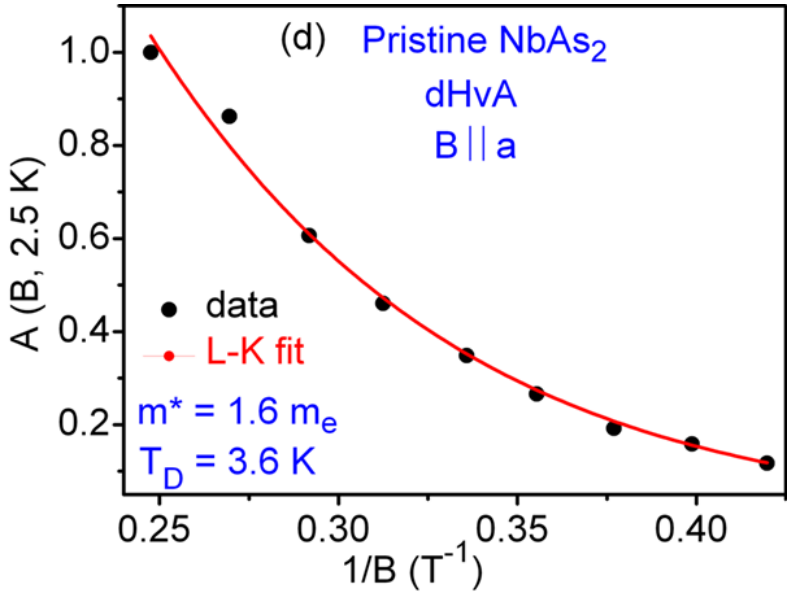

Figure 5.7 ***(a)*** *The dHvA oscillations obtained from the isothermal magnetization measurements on pristine $NbAs_2$. Magnetic field is along b-axis.* ***(b)*** *Fast Fourier transform spectra of oscillations, showing four distinct oscillation frequencies.* ***(c)*** *The Lifshitz - Kosevich analysis of field dependent amplitude variation results in the estimation of effective carrier mass and Dingle temperature.* ***(d)*** *The L-K fit of the oscillation amplitudes obtained when field was along a-axis. It reveals a higher cyclotron mass.*

5.5. Effects of Disorder: Irradiation Weakens the Oscillations

5.5.1. de Haas - van Alphen measurements in irradiated $TaAs_2$

In order to see the effects of disorder in the magneto-transport, we have carried out de Haas - van Alphen studies on the irradiated samples. The details of irradiation experiments were described in Section 2.2 of Chapter 2. The results from the experiments on irradiated $TaAs_2$ are given in Figure 5.8. Here, the isothermal magnetization measurements are plotted against the magnetic field applied along the *b*-axis. Figure 5.8a shows that de Haas - van Alphen effect has weakened significantly after irradiation in contrast to that of pristine sample observed from Figure 5.5a. It is seen that the diamagnetic background decreases, as the temperature is increased, and this is discussed in Section 5.9. Even at the lowest measured temperature 2.5 K, oscillations now appear only with high magnetic fields (~3 T and beyond). At 8 K, the dHvA effect reduced to a few ripples as seen from the blue line in the figure. The oscillations were analyzed using fast

Fourier transform. FFT spectrum of 2.5 K data is given as inset of Figure 5.8a. FFT peaks in the irradiated $TaAs_2$ appear at 54 T and 70 T in contrast to 46 T and 76 T in the pristine crystal. Moreover, there is a small peak at 171 T in the irradiated $TaAs_2$. The changes in the FFT frequency indicate that carrier density in $TaAs_2$ is altered upon irradiation which was clear from the Hall analysis (Refer Section 3.7 of Chapter 3). Further analysis (consolidated in Table 5.2) revealed that carrier density in the irradiated sample has marginally increased, which indicates swelling of the Fermi surface.

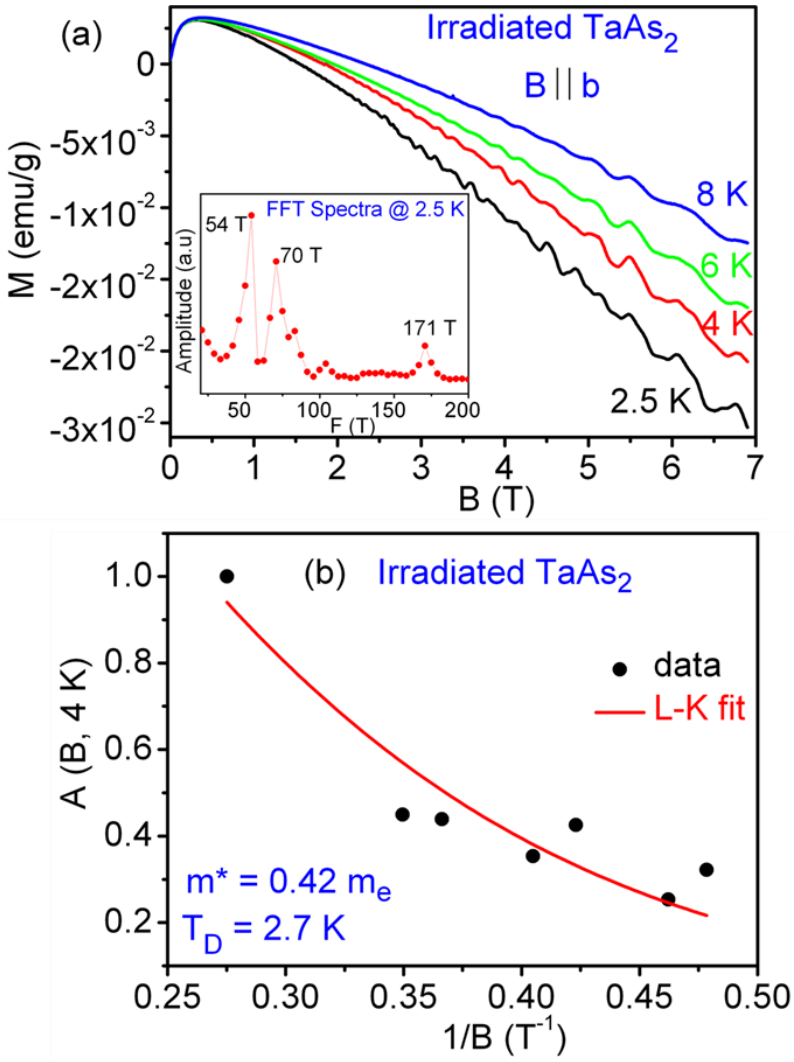

Figure 5.8 ***(a)*** *Isothermal magnetization experiments on irradiated $TaAs_2$ show weak de Haas - van Alphen oscillations. It also indicates an increasing paramagnetic background as the sample is warmed. Inset shows the FFT spectrum of oscillations at 2.5 K.* ***(b)*** *The Lifshitz - Kosevich fit indicates slightly increased carrier mass in the irradiated $TaAs_2$.*

The L-K fit from the field variation of dHvA amplitudes at 4 K in the irradiated $TaAs_2$ is shown in Figure 5.8b. Because of the large oscillation damping in the irradiated sample, the Lifshitz - Kosevich analysis was challenging. The estimated cyclotron mass $0.42\ m_e$ is higher than that in the pristine sample ($0.3\ m_e$). Dingle temperature is 2.7 K in the irradiated sample, as compared to 3.5 K in the pristine $TaAs_2$.

5.5.2. de Haas - van Alphen measurements in irradiated $NbAs_2$

The field variation of magnetization in the irradiated $NbAs_2$ crystal measured at various isothermal conditions between 2.5 K to 30 K is given in Figure 5.9a. Magnetic field was applied along the *b*-axis. The multi-frequency character of the oscillations is evident from the patterns at 2.5 K and 4 K depicted in the black and red curves in the figure. However, the amplitudes dampen quickly as the sample is warmed. Beyond 8 K, oscillations almost disappear completely. Importantly, there is an increasing paramagnetic background in the irradiated $NbAs_2$ with increase of temperature similar to that observed in irradiated $TaAs_2$ (See Figure 5.8a). The significance of the variation in the diamagnetic background is discussed later in Section 5.9.

The inset of Figure 5.9a shows the fast Fourier transform spectrum of oscillations in the irradiated $NbAs_2$ obtained at 2.5 K. Three distinct peaks viz., 104 T, 132 T and 229 T are seen in which 229 T is the major peak. There also exists a peak at 278 T whose amplitude is very small. The multiple frequencies in the FFT spectrum evidence the multi-carrier nature of the transport in the irradiated $NbAs_2$ sample. The peak positions in the irradiated sample are shifted to the high frequency side, which indicates an increase in the carrier density in $NbAs_2$ after irradiation. This may be due to self-electron doping by arsenic vacancies introduced by irradiation. This was earlier indicated in literature where sample dependent arsenic vacancies caused changes in the FFT spectra of di-pnictides [28].

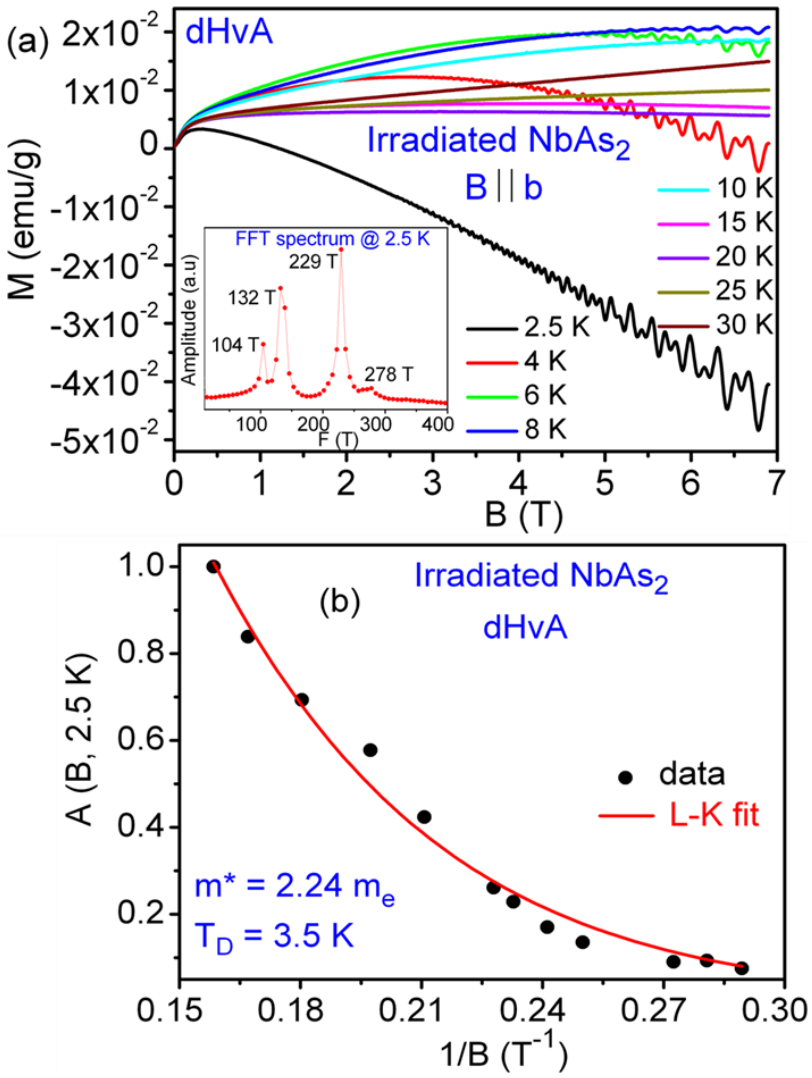

Figure 5.9 ***(a)*** *Results of the isothermal magnetization measurements on the irradiated $NbAs_2$. The irradiated sample retained dHvA oscillations with increasing paramagnetic background. Inset is the FFT spectrum of oscillations obtained at 2.5 K, indicating multiple frequencies.* ***(b)*** *The Lifshitz - Kosevich fit reveals an increased carrier mass in the irradiated sample.*

The Lifshitz - Kosevich analysis of the amplitude variation of oscillations in the irradiated $NbAs_2$ at 2.5 K is given in Figure 5.9b. The fit resulted in an estimate of cyclotron mass as 2.24 m_e and Dingle temperature as 3.5 K for the charge carriers. This carrier mass is quite large compared to that obtained from the pristine sample, $i.e$ 0.47 m_e (See Figure 5.7c). But the Dingle temperature show only a small increase from 3.2 K to 3.5 K (compare with Figure 5.7c). An increased carrier mass can result in a reduction in

the carrier mobility which we have seen in Chapter 4 (See Section 4.9 for Hall analysis) where the irradiated $NbAs_2$ exhibited lower mobility than that of the pristine sample.

5.6. Shubnikov - de Haas Measurements: Magneto-resistance oscillations at Low Temperature

5.6.1. SdH oscillations in $TaAs_2$

The de Haas - van Alphen technique is in general free from quantum interference effects and the noise from electrical contacts associated with resistivity measurements [118]. Hence it is possible to separate out small frequency components especially with low magnetic fields. Despite this, in addition to de Haas - van Alphen effect in magnetization, we have also used the magneto-resistance (MR) data to analyze for Shubnikov - de Haas (SdH) oscillations. Often SdH technique requires high magnetic fields compared to dHvA to see sharp and distinguishable frequencies. It is seen from Figure 5.10 and Figure 5.11 that the isothermal magneto-resistance measurements in $TaAs_2$ and $NbAs_2$ show Shubnikov - de Haas oscillations at low temperatures. Experiments were carried out at four different temperatures viz., 2.5 K, 5 K, 8 K and 12 K between ± 15 T using the 'Cryogenic Ltd make cryostat' described in Section 2.4.1 of Chapter 2.

The results from pristine $TaAs_2$ are summarized in Figure 5.10. The MR data were collected at closer intervals of magnetic field (0.02 T or 200 Oe). Figure 5.10a is the transverse magneto-resistivity versus magnetic field plot at 2.5 K showing the appearance of SdH oscillations at high magnetic fields (beyond ~6 T). The electric and magnetic fields were respectively along the *a*-axis and *c*-axis. Oscillations are riding on a parabolic resistance background and their amplitudes increase with increase of field. The large increase of magneto-resistance with increase of magnetic field make the oscillations less visible in the raw data compared to the dHvA effects seen earlier in Section 5.3. As the sample was warmed, the oscillations dampened very quickly compared to the dHvA oscillations. Even at 5 K, oscillation patterns were weak in the raw MR data. At 12 K, only

a few ripples were present in the high magnetic field range (above ~10 T). Hence, we could not carry out L-K analysis, as done earlier for the dHvA data.

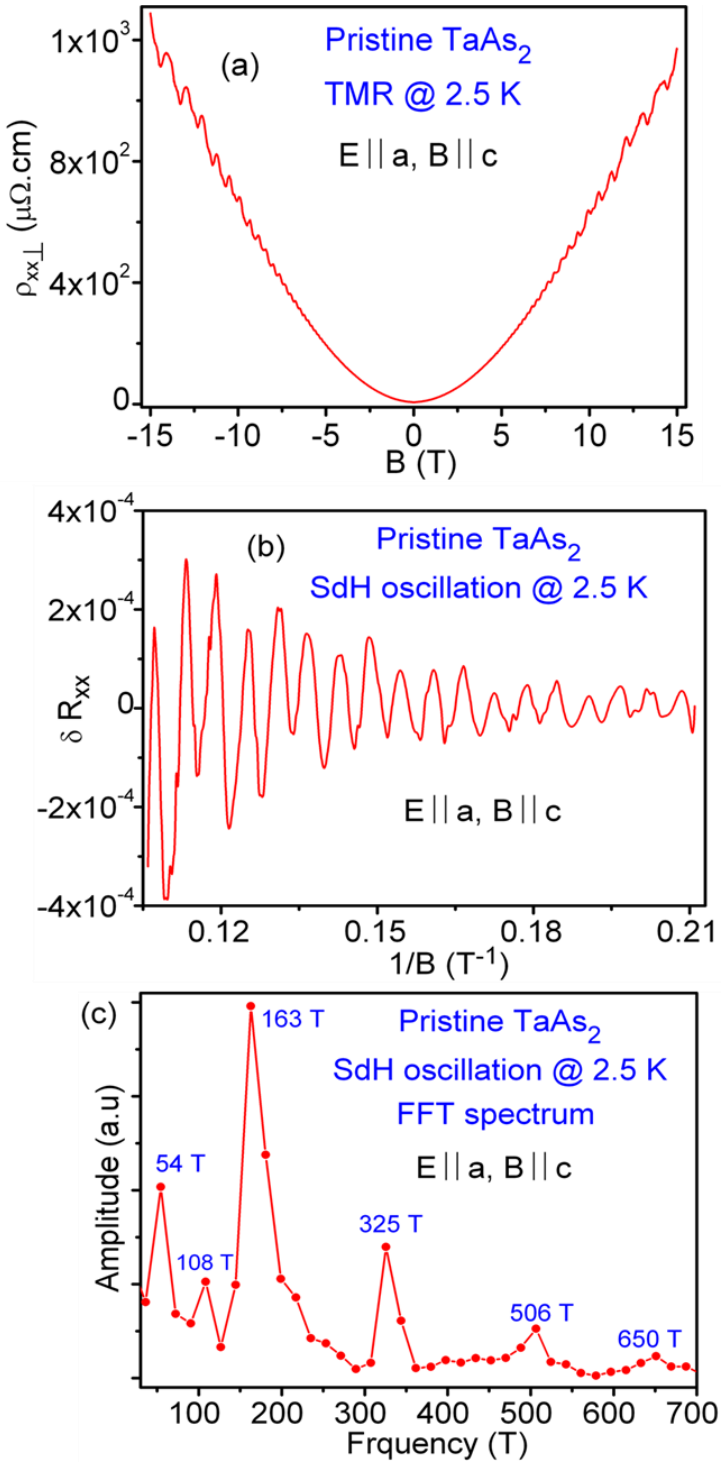

Figure 5.10 ***(a)*** *The isothermal transverse magneto-resistance in pristine $TaAs_2$ at 2.5 K is displaying Shubnikov - de Haas oscillations at high magnetic fields.* ***(b)*** *The residual resistance after removing the parabolic background is plotted against inverse field.* ***(c)*** *Fast Fourier transform spectrum of the oscillations showing main oscillation frequencies and their harmonics.*

The SdH oscillations in Figure 5.10a were analyzed by fast Fourier transform technique analogous to that adopted for dHvA analysis in the preceding sections. The resistance data from both directions of the magnetic field, $R_{xx}(+B)$ and $R_{xx}(-B)$, were properly averaged to $R_{xx}(B)$. A parabolic background was subtracted from $R_{xx}(B)$ and the residual resistance (δR_{xx}) is plotted against inverse magnetic field ($\frac{1}{B}$) in Figure 5.10b. The data were interpolated to large number of points (2048) to obtain equally spaced resistance values in inverse field. This was subjected to FFT to obtain the SdH oscillation frequencies and the FFT spectrum is given in Figure 5.10c. It shows dominant peaks at 54 T, 163 T and 325 T, the later could be harmonic of 163 T peak. The 54 T may correspond to the 46 T peak seen in dHvA results (See Figure 5.5b). The results are summarized in Table 5.1.

5.6.2. SdH oscillations in $NbAs_2$

The results of Shubnikov - de Haas measurements in pristine $NbAs_2$ at 2.5 K are given in Figure 5.11. The magneto-resistance data were collected in magnetic field intervals of 0.2 T (2000 Oe) between 0 T & ±6 T, and in 0.01 T (100 Oe) intervals afterwards up to ±15 T where strong oscillations were expected. Figure 5.11a shows the transverse magneto-resistivity versus magnetic field plot of the pristine $NbAs_2$, displaying SdH oscillations at high magnetic fields (above ~7 T). The magnetic field was applied along the *b*-axis and carried out in the geometry same as that of Section 4.4.1 for TMR. The oscillations appear with a large parabolic resistance background and its amplitude increases with increase in magnetic field.

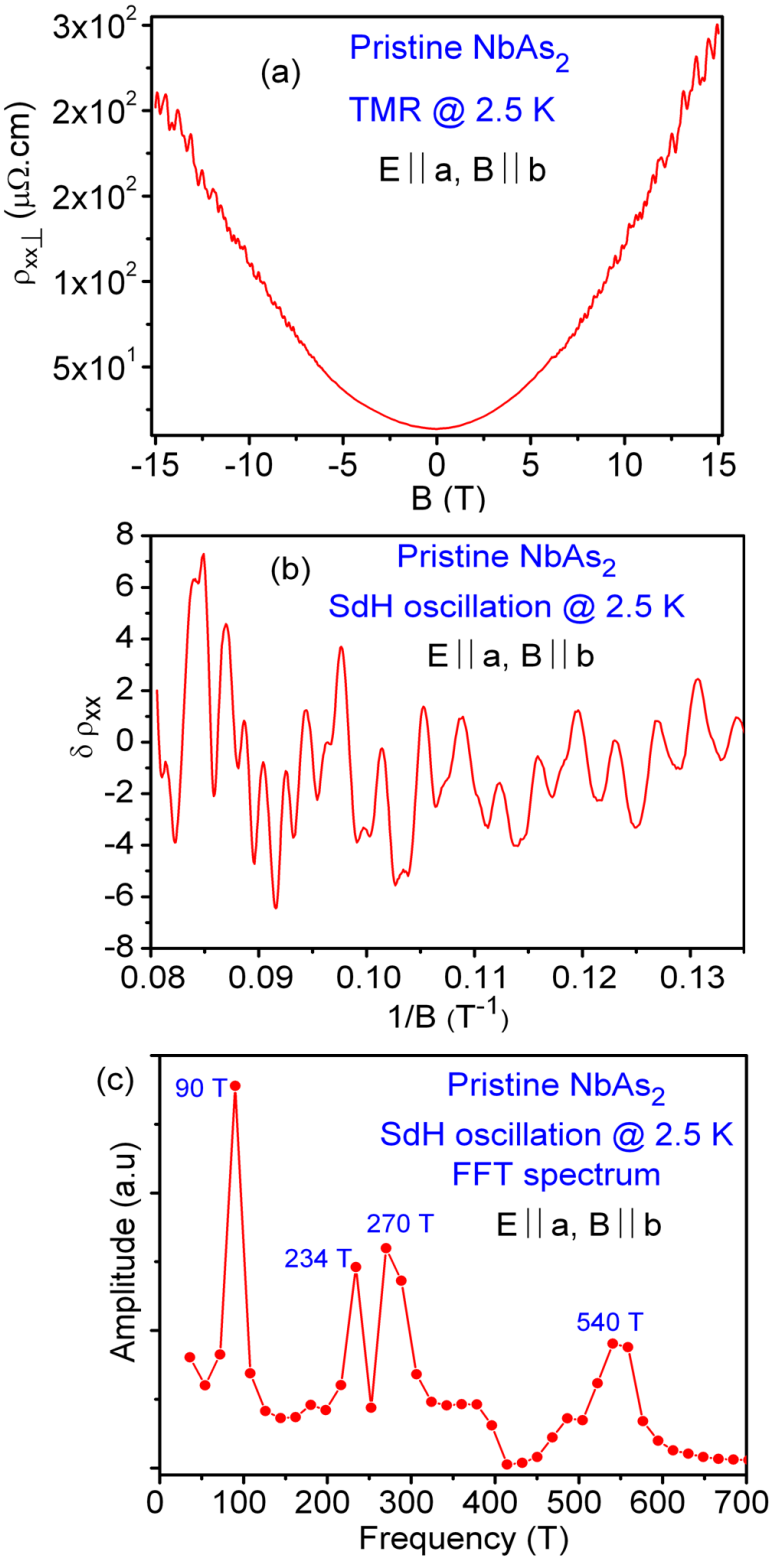

Figure 5.11 ***(a)*** *The Shubnikov - de Haas oscillations in pristine $NbAs_2$ observed at 2.5 K during the transverse magneto-resistance experiments.* ***(b)*** *The residual resistivity versus inverse magnetic field obtained after subtracting the parabolic resistance background from the magneto-resistance in the SdH effect. The beating pattern indicates the existence of multiple oscillation frequencies.* ***(c)*** *Fast Fourier transform of the beating pattern reveals several frequency elements and their harmonics contained in the oscillations.*

The oscillations were analyzed using the fast Fourier transform technique similar to the $TaAs_2$ data of the previous section. The residual resistivity ($\delta\rho_{xx}$) obtained after subtracting a parabolic background from the data in Figure 5.11a is plotted against inverse magnetic field in Figure 5.11b. The beating pattern indicates that the oscillation contains multiple frequencies, unlike the periodic variation in pristine $TaAs_2$, as seen in Figure 5.10b. The FFT spectrum of the beating pattern is given in Figure 5.11c. It shows distinct peaks at 90 T, 234 T, 270 T and 540 T, the later a harmonic of 270 T. Comparing with the dHvA results in $NbAs_2$ (Figure 5.7b), we note that 90 T is present.

It is noticed that harmonics are seen in the FFT analysis of SdH oscillations, while not so in dHvA experiments. This may be related to the fact that our SdH experiments have been carried out up to 15 T, as against 7 T in dHvA experiments. This may be related to magnetic breakdown [4]. It is well known [44] that charge carriers may tunnel from one cyclotron orbit to another and jump back to the original leading to form a bigger cyclotron orbit, hence leading to additional frequencies, equal to the sum or difference of two or more fundamental frequencies. This becomes more effective at high fields as the tunneling probability scales exponentially with the inverse field $\frac{1}{B}$ as $e^{-\frac{a}{B}}$ where 'a' is a material parameter relevant to the k-space separation of orbits. The additional frequencies ascribed to magnetic breakdown have been observed in several topological semimetals [44, 119]. Multi-harmonic frequencies are generally an indication of long transport lifetime [30] which will be seen in the next section.

Table 5.1 Consolidated list of oscillation frequencies obtained from the SdH and dHvA measurements on the pristine and irradiated samples of $TaAs_2$ and $NbAs_2$. The results from the literature are also indicated.

Sample	SdH Frequencies (T)		dHvA Frequencies (T)	
	Results	Literature values	Results	Literature values
Pristine $TaAs_2$	45, 54, 76, 83, 108, 163, 242, 325, 506, 651 (***B*** parallel to *c*-axis) 91, 273, 545, 818 (***B*** parallel to *b*-axis) 39, 55, 117, 137, 301, 313, 383, 625 (***B*** parallel to *a*-axis)	Yuan et al [30] 39, 54 Wang et al [31] 45, 158 Wu et al [13] 190.5, 212.5 Rao et al [116] 39, 56	39, 54, 65, 109, 163, 214, 235 46, 76, 92 (***B*** parallel to *b*-axis) 83, 129, 315 (***B*** parallel to *a*-axis)	Butcher et al [62] 41, 54, 85 130
Irradiated $TaAs_2$			39, 73, 163, 190, 235 Sample 2 54, 70, 171	
Pristine $NbAs_2$	32, 49, 81, 90, 146, 234, 248, 276, 287, 540, 828 38, 95, 210, 305, 362, 534, 591	Peramaiyan et al [90] 32, 266 Shen et al [29] 76, 122, 226 Wang et al [31] 90, 204 Yupeng Li [28] 109.6, 234.3, 270.5 Yuan et al [30] 124, 224	Sample 1 32, 62, 91, 106 Sample 1 (Orientation 2) 76, 120, 214, 245 Sample 2 149, 162, 239 Sample 2 (Orientation 2) 113, 165, 322	No dHvA studies
Irradiated $NbAs_2$			104, 132, 229, 278	

5.7. Transport Parameters from Quantum Oscillation Studies

Following other related works on the magneto-transport in semimetals [55, 71, 84, 120, 121], we have further analyzed the dHvA and SdH oscillations in $TaAs_2$ and $NbAs_2$ to estimate the transport parameters. From the FFT frequency (F), the extremal Fermi surface cross section area (A_F) was calculated using the Onsager relation $A_F = \frac{2\pi^2}{\varphi_0} F$, where φ_0 is the magnetic flux quantum [111]. The Fermi wave vector $k_F = \left(\frac{A_F}{\pi}\right)^{\frac{1}{2}}$ was estimated corresponding to each frequency, F [71]. Subsequently, assuming spherical Fermi pockets, the approximate carrier densities were obtained from the relation $n_F = \frac{k_F^3}{3\pi^2}$ [55]. The average values of A_F, k_F and n_F corresponding to all the dHvA frequencies in each sample are given in Table 5.2. It is seen that there is an increase in carrier density upon irradiation.

We have seen in earlier sections that the L-K analysis of the dHvA oscillations leads to the Dingle temperature T_D and the effective cyclotron mass m^*. From the Dingle temperature, the quantum relaxation time can be estimated using the relation [111] $\tau_q = \frac{\hbar}{2\pi k_B T_D}$. Using the carrier relaxation time and the effective mass, the mobility is evaluated using the relation $\mu_q = \frac{e\tau_q}{m^*}$. These are indicated in Table 5.2, for pristine and irradiated $TaAs_2$ and $NbAs_2$. It is seen that the mobility decreases on irradiation.

While the increase in carrier density and a decrease in mobility upon irradiation are consistent with the Hall data, the numbers do not match. Such a discrepancy between the transport relaxation time and the relaxation time estimated from Dingle temperature is to be expected [67]. Further, we mention that our mobility values for $TaAs_2$ and $NbAs_2$ are in the same ballpark as reported in the literature [27, 30, 90].

Table 5.2 The transport parameters of pristine and irradiated samples of $TaAs_2$ and $NbAs_2$ as estimated from the analysis of quantum oscillations observed during the transport experiments. The results from Hall data are also included for comparison. Here, A_F is the cross sectional area of the Fermi surface, k_F is the Fermi vector, n is the carrier density, m^* is the effective mass, T_D is the Dingle temperature, τ is the relaxation time and μ is the mobility. It is seen that the irradiation results in an increase in the carrier density and a decrease in mobility.

Parameter		Pristine $TaAs_2$	Irradiated $TaAs_2$	Pristine $NbAs_2$	Irradiated $NbAs_2$
A_F (10^{-3} Å^{-2})		6.8	9.4	6.9	17.7
k_F (10^{-2} Å^{-1})		4.6	5.3	4.6	7.4
n (10^{18} cm^{-3})	dHvA	3.5	6.1	3.7	15.1
	Hall (2.5 K)	52	60	52	238
m^* (m_e)		0.3	0.4	0.5	2.2
T_D (K)		3.5	2.7	2.2	3.5
τ (10^{-13} s)	dHvA (τ_q)	3.5	4.5	5.6	3.5
	Hall (τ_{tr}; 2.5 K)	100	43	6666	299
μ (cm^2. V^{-1}. s^{-1})	dHvA (μ_q)	2036	1885	2077	272
	Hall (μ_{tr}; 2.5 K)	1878	15157	1.2 x 10^6	52552

5.8. Landau Level - fan Diagram: Determination of the Berry phase

As mentioned in the introduction, the Berry phase, that is the additional geometrical phase factor acquired in the adiabatic evolution along a closed trajectory in the parameter space, is determined by the topological characteristics of the electron bands in the Brillouin zone. A non-zero Berry phase reflects the existence of band touching point such as Dirac nodes [122], and results in observable effects in quantum oscillations.

For the case of de Haas - van Aphen effect, the oscillations in magnetic moment is decomposed into sine components [43] viz.,

$$M = a_0 + \sum_{i=1}^{n} A_i \sin\left(2\pi F_i\left(\frac{1}{B}\right) - \varphi_i\right) e^{-d_i\left(\frac{1}{B}\right)} \quad \textbf{(5. 3)}$$

whereas the oscillations in the resistivity in the SdH experiments is broken into sum of cosine functions, which is important in the Berry phase calculation. When several frequencies are present, then the damped oscillation in magnetization/conductivity is decomposed into its Fourier components and the Berry phase is determined for each of the Fermi pockets, as for example done for TaP [42].

Alternatively, the Berry phase can be calculated by constructing the Landau level - fan diagram [113, 120] from the observed quantum oscillations that is periodic in inverse magnetic field $\frac{1}{B}$. This consists of plotting the index n of the Landau level (LL), corresponding to maxima, versus $\frac{1}{B_n}$. The intercept of this linear plot, obtained by extrapolation of the Landau level index (n) to the zero of inverse field $(\frac{1}{B})$ provides the information on the Berry phase. This method, wherein the maxima and minima are manually determined, works when only one oscillation frequency is present. This approach has been used in the case of topological insulators [122] and Dirac fermion systems with linear band dispersion. According Ando et al [122], the $\frac{1}{B_n}$ and the n^{th} minimum in the Landau - fan diagram are related as

$$2\pi\left(\frac{F}{B_N}-\frac{1}{2}+\ \beta\right)\ =(2N-1)\pi \qquad \textbf{(5. 4)}$$

in which β is the Berry phase.

The results obtained from the analysis of dHvA oscillations of the pristine $TaAs_2$ obtained at 4 K are given in Figure 5.12. The maxima (peaks) and minima (valleys) in the oscillations were indexed respectively with integer (n) and half integer $(n+\frac{1}{2})$ values following standard methods [122]. When plotted against the inverse magnetic field $(\frac{1}{B})$, the Landau level indices falls on a straight line, as shown by the dots (maxima) and circles (minima) in the figure. Extrapolating these values to the infinite magnetic field limit or the

quantum limit is indicated by the red line in Figure 5.12. The intercept on the n-axis can help in determining the value of Berry phase of the charge carriers [120, 122]. For the $TaAs_2$ data, shown in Figure 5.12, a linear fit with the slope 46.5 T and intercept 0.07 is obtained. The slope matches with the main frequency obtained in the FFT analysis (See Figure 5.5b). The intercept of 0.07 suggests trivial Berry phase.

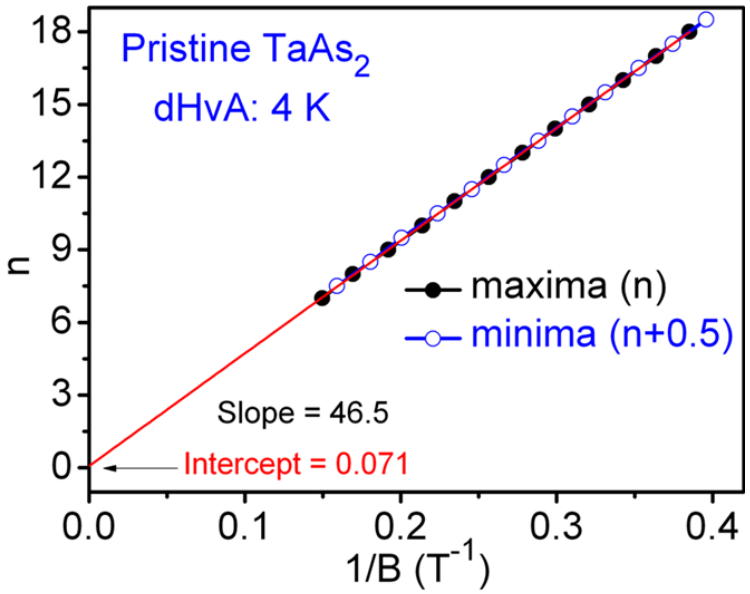

Figure 5.12 Landau level - fan diagram for pristine $TaAs_2$ sample obtained from the de Haas - van Alphen oscillations at 4 K. The obtained intercept suggests topologically trivial bands in the sample.

While we have determined the Berry phase through an analysis of LL – fan diagram, researchers [43] have pointed to the complications/uncertainties in this approach that arises from the presence of multiple oscillation frequencies due to the coexistence of Dirac and parabolic bands, and that to realize the signatures of a Berry phase, the Fermi level must be as close as possible to the Weyl point. We must mention that we have not done a similar LL - fan diagram analysis for $NbAs_2$, as it has manifestly multiple oscillation frequencies in the dHvA oscillations (See Figure 5.7b).

5.9. On the Diamagnetic Background in de Haas - van Alphen Oscillations

With the introduction of disorder, apart from the damping of de Haas - van Alphen oscillations, another feature that is seen in the magnetization data is the increase in the paramagnetic background. This is seen clearly in the Figure 5.13 below for irradiated and heat treated samples, when compared with the pristine samples, as also seen in earlier figures (Figure 5.8a and Figure 5.9a). This raises two questions: (1) Why is there a diamagnetic background in the pristine semimetal, and why does it decrease on the introduction of disorder? It is well known [5] that for an ordinary metal, the magnetic susceptibility consists of Pauli paramagnetism (spin term) and Landau diamagnetism (orbital term). The semimetals such as graphite and Bi show large diamagnetic susceptibility that cannot be explained within the framework of Landau - Peierls treatment, and it has been shown that one needs to consider band to band transition [123, 124].

In the case of novel topological semimetals, the magnetic susceptibility is quite distinct from the conventional Landau diamagnetism. Calculations of the magnetic susceptibility from Landau levels for the Weyl and Dirac Hamiltonian indicate [125] that for materials with spin-orbit coupling, there is an additional spin-orbit cross susceptibility, X_{SO} on top of the spin susceptibility and orbital susceptibility. It has been shown [125, 126] that X_{SO} is a monotonically increasing or decreasing function in the Fermi energy with different sign in the electron side and the hole side: The electron side is more paramagnetic or diamagnetic than the hole side, depending on the chirality of the spin texture. Further, these calculations [125-128] indicate a strong diamagnetism at the band touching point of Weyl and Dirac semimetal. X_{orb} is a logarithmic function which diverges at zero energy, and for the parameters in experimentally realized Dirac or Weyl

semimetals, it has been shown that X_{orb} is the dominant contribution to susceptibility. This is consistent with the diamagnetic signal seen in pristine samples.

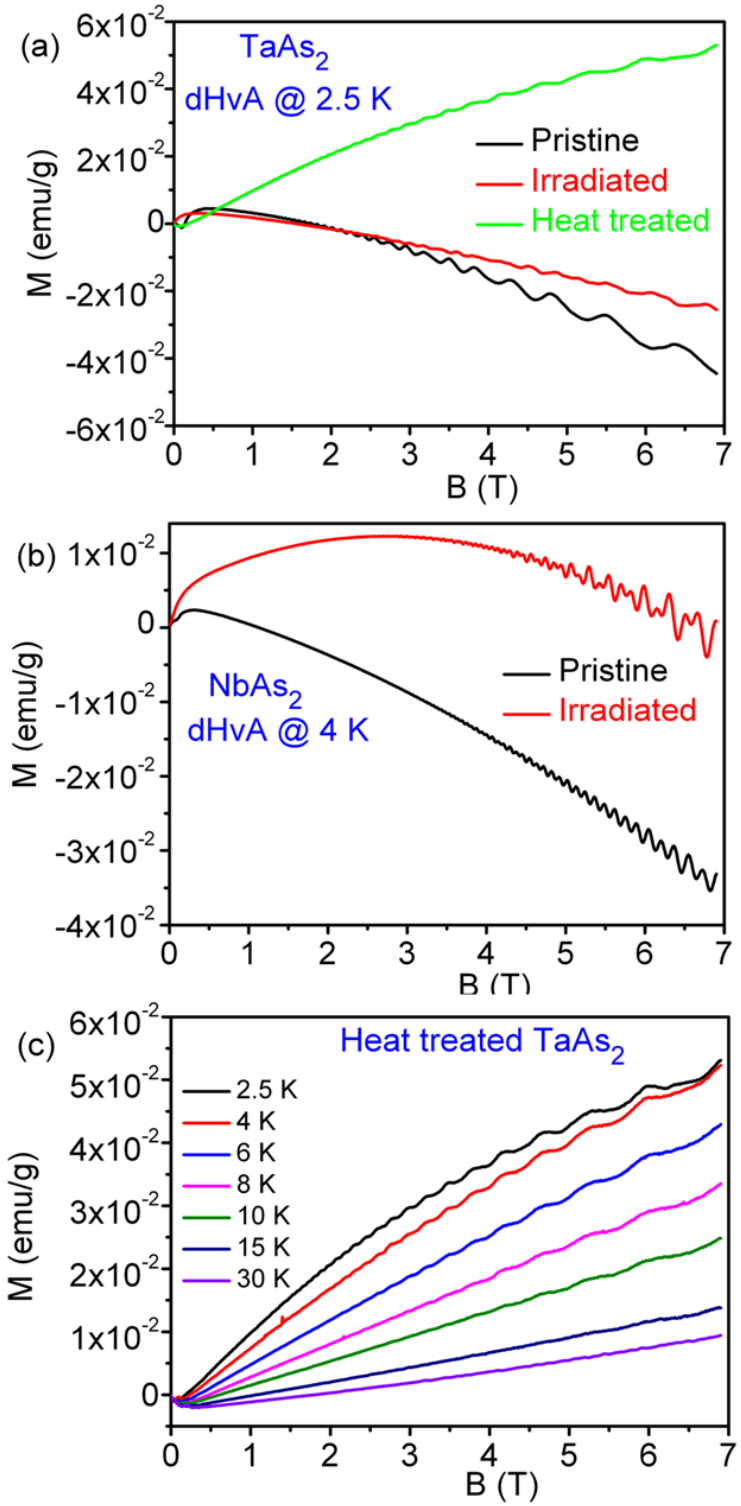

Figure 5.13 The reduction in the diamagnetic character and weakening of oscillations upon introducing defects or by introducing carriers via heat treatment and irradiation in ***(a)*** *$TaAs_2$* ***(b)*** *$NbAs_2$.* ***(c)*** *Variation of diamagnetic background with temperature in heat treated $TaAs_2$.*

With irradiation, the diamagnetic background decreases, along with the reduction in quantum oscillations. Such a reduction in diamagnetic background can arise due to reduction in the Landau contribution to the susceptibility that arises due to the cyclotron motion, with the introduction of defects, or a shift in the position of the Fermi level with the introduction of carriers. In the case of the heat treated sample, the diamagnetic background seen in the pristine sample changes over to a paramagnetic background that decreases with temperature (See Figure 5.13c). Thus, we see that there are systematic changes in the diamagnetic background that could be analyzed in detail to obtain information on the electronic structure.

5.10. Conclusions

Detailed de Haas – van Alphen measurements in pristine and irradiated samples of $TaAs_2$ and $NbAs_2$ evidenced the involvement of multiple carriers in the magneto-transport. Lifshitz - Kosevich analysis indicated the low effective masses of the carriers that can provide them high mobility. Extracted transport parameters helped to quantitatively understand the magneto-transport behaviour. The Berry phase obtained from the Landau level - fan diagram indicated the trivial nature of the band structure. Hence $TaAs_2$ and $NbAs_2$ are not topological semimetals.

References

[1] M.Z. Hasan, X. Su-Yang, B. Guang, Topological insulators, topological superconductors and Weyl fermion semimetals: discoveries, perspectives and outlooks, Physica Scripta, 2015 (2015) 014001.

[2] A.C. Potter, I. Kimchi, A. Vishwanath, Quantum oscillations from surface Fermi arcs in Weyl and Dirac semimetals, Nature Communications, 5 (2014) 5161.

[3] J.M. Ziman, Principles of the Theory of Solids, Cambridge University Press, Cambridge, 1972.

[4] A.B. Pippard, Magnetoresistance in metals, Cambridge University press, 1989.

[5] N.D.M. N W Ashcroft Solid State Physics, Cengage Learning India Private Limited, New Delhi, 1976.

[6] A.C. Ehrlich, D.J. Gillespie, T. California Institute of, L. jet Propulsion, G. Thermoelectric, Electronic structure of semimetals from transport and fermiology experiments, in: International conference; 15th, Thermoelectrics, IEEE;, 1996, pp. 397-401.

[7] A. Collaudin, B. Fauqué, Y. Fuseya, W. Kang, K. Behnia, Angle Dependence of the Orbital Magnetoresistance in Bismuth, Physical Review X, 5 (2015) 021022.

[8] X. Du, S.-W. Tsai, D.L. Maslov, A.F. Hebard, Metal-Insulator-Like Behavior in Semimetallic Bismuth and Graphite, Physical Review Letters, 94 (2005) 166601.

[9] D.V. Khveshchenko, Magnetic-Field-Induced Insulating Behavior in Highly Oriented Pyrolitic Graphite, Physical Review Letters, 87 (2001) 206401.

[10] Y. Kopelevich, J.H.S. Torres, R.R. da Silva, F. Mrowka, H. Kempa, P. Esquinazi, Reentrant Metallic Behavior of Graphite in the Quantum Limit, Physical Review Letters, 90 (2003) 156402.

[11] H. Lu, S. Jia, Crystal growth and electrical transport properties of niobium and tantalum monopnictide and dipnictide semimetals, Frontiers of Physics, 12 (2017) 1-17.

[12] B. Fauqué, X. Yang, W. Tabis, M. Shen, Z. Zhu, C. Proust, Y. Fuseya, K. Behnia, Magnetoresistance of semimetals: The case of antimony, Physical Review Materials, 2 (2018) 114201.

[13] D. Wu, J. Liao, W. Yi, X. Wang, P. Li, H. Weng, Y. Shi, Y. Li, J. Luo, X. Dai, Z. Fang, Giant semiclassical magnetoresistance in high mobility TaAs2 semimetal, Applied Physics Letters, 108 (2016) 042105.

[14] N. Luo, G.H. Miley, Kohler's rule and relaxation rates in high-Tc superconductors, Physica C: Superconductivity, 371 (2002) 259-269.

[15] M.K. Chan, M.J. Veit, C.J. Dorow, Y. Ge, Y. Li, W. Tabis, Y. Tang, X. Zhao, N. Barišić, M. Greven, In-Plane Magnetoresistance Obeys Kohler's Rule in the Pseudogap Phase of Cuprate Superconductors, Physical Review Letters, 113 (2014) 177005.

[16] Y.L. Wang, L.R. Thoutam, Z.L. Xiao, J. Hu, S. Das, Z.Q. Mao, J. Wei, R. Divan, A. Luican-Mayer, G.W. Crabtree, W.K. Kwok, Origin of the turn-on temperature behavior in WTe2, Physical Review B, 92 (2015) 180402.

[17] Y. Li, L. Li, J. Wang, T. Wang, X. Xu, C. Xi, C. Cao, J. Dai, Resistivity plateau and negative magnetoresistance in the topological semimetal TaSb2, Physical Review B, 94 (2016) 121115.

[18] F. Duan, J. Guojun, Introduction to Condensed Matter Physics, World Scientific publishing, Singapore, 2005.

[19] T. Graf, J.M. Lawrence, M.F. Hundley, J.D. Thompson, A. Lacerda, E. Haanappel, M.S. Torikachvili, Z. Fisk, P.C. Canfield, Resistivity, magnetization, and specific heat of YbAgCu4 in high magnetic fields, Physical Review B, 51 (1995) 15053-15061.

[20] N.H. Jo, Y. Wu, L.-L. Wang, P.P. Orth, S.S. Downing, S. Manni, D. Mou, D.D. Johnson, A. Kaminski, S.L. Bud'ko, P.C. Canfield, Extremely large magnetoresistance and Kohler's rule in PdSn4: A complete study of thermodynamic, transport, and band-structure properties, Physical Review B, 96 (2017) 165145.

[21] Y. Wu, N.H. Jo, M. Ochi, L. Huang, D. Mou, S.L. Bud'ko, P.C. Canfield, N. Trivedi, R. Arita, A. Kaminski, Temperature-Induced Lifshitz Transition inWTe2, Physical Review Letters, 115 (2015) 166602.

[22] A.A. Burkov, Topological semimetals, Nature Materials, 15 (2016) 1145.

[23] J. Gooth, G. Schierning, C. Felser, K. Nielsch, Quantum materials for thermoelectricity, MRS Bulletin, 43 (2018) 187-192.

[24] B. Yan, C. Felser, Topological Materials: Weyl Semimetals, Annual Review of Condensed Matter Physics, 8 (2017) 337-354.

[25] M.Z. Hasan, S.-Y. Xu, I. Belopolski, S.-M. Huang, Discovery of Weyl Fermion Semimetals and Topological Fermi Arc States, Annual Review of Condensed Matter Physics, 8 (2017) 289-309.

[26] K. Wang, D. Graf, L. Li, L. Wang, C. Petrovic, Anisotropic giant magnetoresistance in NbSb2, Scientific Reports, 4 (2014) 7328.

[27] Y. Luo, R.D. McDonald, P.F.S. Rosa, B. Scott, N. Wakeham, N.J. Ghimire, E.D. Bauer, J.D. Thompson, F. Ronning, Anomalous electronic structure and magnetoresistance in TaAs2, Scientific Reports, 6 (2016) 27294.

[28] Y. Li, Z. Wang, Y. Lu, X. Yang, Z. Shen, F. Sheng, C. Feng, Y. Zheng, Z.-A. Xu, Negative Magnetoresistance in Topological Semimetals of Transition-Metal Dipnictides with Nontrivial Z2 Indices, arXiv e-prints, (2016) arXiv:1603.04056.

[29] B. Shen, X. Deng, G. Kotliar, N. Ni, Fermi surface topology and negative longitudinal magnetoresistance observed in the semimetal NbAs2, Physical Review B, 93 (2016) 195119.

[30] Z. Yuan, H. Lu, Y. Liu, J. Wang, S. Jia, Large magnetoresistance in compensated semimetals TaAs2 and NbAs2, Physical Review B, 93 (2016) 184405.

[31] Y.-Y. Wang, Q.-H. Yu, P.-J. Guo, K. Liu, T.-L. Xia, Resistivity plateau and extremely large magnetoresistance in NbAs2 and TaAs2, Physical Review B, 94 (2016) 041103.

[32] G.S. Saini, L.D. Calvert, J.B. Taylor, Preparation and characterization of crystals of MX- and MX2-type arsenides of niobium and tantalum, Canadian Journal of Chemistry, 42 (1964) 630-634.

[33] C. Xu, J. Chen, G.-X. Zhi, Y. Li, J. Dai, C. Cao, Electronic structures of transition metal dipnictides XPn2 (X=Ta, Nb; Pn=P, As, Sb), Physical Review B, 93 (2016) 195106.

[34] D. Gresch, Q. Wu, G.W. Winkler, A.A. Soluyanov, Hidden Weyl points in centrosymmetric paramagnetic metals, New Journal of Physics, 19 (2017) 035001.

[35] N.P. Armitage, E.J. Mele, A. Vishwanath, Weyl and Dirac semimetals in three-dimensional solids, Reviews of Modern Physics, 90 (2018) 015001.

[36] P. Hosur, X. Qi, Recent developments in transport phenomena in Weyl semimetals, Comptes Rendus Physique, 14 (2013) 857-870.

[37] I.A. Leahy, Y.-P. Lin, P.E. Siegfried, A.C. Treglia, J.C.W. Song, R.M. Nandkishore, M. Lee, Nonsaturating large magnetoresistance in semimetals, Proceedings of the National Academy of Sciences, 115 (2018) 10570.

[38] C.-L. Zhang, S.-Y. Xu, I. Belopolski, Z. Yuan, Z. Lin, B. Tong, G. Bian, N. Alidoust, C.-C. Lee, S.-M. Huang, T.-R. Chang, G. Chang, C.-H. Hsu, H.-T. Jeng, M. Neupane, D.S. Sanchez, H. Zheng, J. Wang, H. Lin, C. Zhang, H.-Z. Lu, S.-Q. Shen, T. Neupert, M. Zahid Hasan, S. Jia, Signatures of the Adler–Bell–Jackiw chiral anomaly in a Weyl fermion semimetal, Nature Communications, 7 (2016) 10735.

[39] J. Cano, B. Bradlyn, Z. Wang, M. Hirschberger, N.P. Ong, B.A. Bernevig, Chiral anomaly factory: Creating Weyl fermions with a magnetic field, Physical Review B, 95 (2017) 161306.

[40] H.-Z. Lu, S.-Q. Shen, Quantum transport in topological semimetals under magnetic fields, Frontiers of Physics, 12 (2017) 127201.

[41] J. Hu, Y. Zhu, X. Gui, D. Graf, Z. Tang, W. Xie, Z. Mao, Quantum oscillation evidence for a topological semimetal phase in ZrSnTe, Physical Review B, 97 (2018) 155101.

[42] J. Hu, J.Y. Liu, D. Graf, S.M.A. Radmanesh, D.J. Adams, A. Chuang, Y. Wang, I. Chiorescu, J. Wei, L. Spinu, Z.Q. Mao, π Berry phase and Zeeman splitting of Weyl semimetal TaP, Scientific Reports, 6 (2016) 18674.

[43] P. Sergelius, J. Gooth, S. Bäßler, R. Zierold, C. Wiegand, A. Niemann, H. Reith, C. Shekhar, C. Felser, B. Yan, K. Nielsch, Berry phase and band structure analysis of the Weyl semimetal NbP, Scientific Reports, 6 (2016) 33859.

[44] J. Hu, S.-Y. Xu, N. Ni, Z. Mao, Transport of Topological Semimetals, Annual Review of Materials Research, 49 (2019) 207-252.

[45] V. Harimohan, A. Bharathi, R. Rajaraman, P. Magudapathy, C. David, C.S. Sundar, Magneto-resistance in pristine and irradiated TaAs2, AIP Advances, 9 (2019) 045020.

[46] V. Harimohan, A. Bharathi, P.D. Babu, R. Rajaraman, P. Magudapathy, C. David, C.S. Sundar, Validity of Kohler's rule for the magneto-resistance in pristine and irradiated NbAs2, Solid State Communications, 305 (2020) 113734.

[47] T.R. Devidas, E.P. Amaladass, S. Sharma, R. Rajaraman, D. Sornadurai, N. Subramanian, A. Mani, C.S. Sundar, A. Bharathi, Role of Se vacancies on Shubnikov-de Haas oscillations in Bi 2 Se 3 : A combined magneto-resistance and positron annihilation study, EPL (Europhysics Letters), 108 (2014) 67008.

[48] V. Harimohan, A. Bharathi, R. Rajaraman, C.S. Sundar, A magneto-resistance and magnetisation study of TaAs2 semimetal, AIP Conference Proceedings, 1942 (2018) 110019.

[49] V. Harimohan, A. Bharathi, P.D. Babu, R. Rajaraman, C.S. Sundar, Magneto-resistance study on single crystals of NbAs2 semimetal, AIP Conference Proceedings, 2115 (2019) 030430.

[50] M.D. Bachmann, N. Nair, F. Flicker, R. Ilan, T. Meng, N.J. Ghimire, E.D. Bauer, F. Ronning, J.G. Analytis, P.J.W. Moll, Inducing superconductivity in Weyl semimetal microstructures by selective ion sputtering, Science Advances, 3 (2017).

[51] B.J.P. Ziegler J.F, Treatise on Heavy-Ion Science in: D.A. Bromley (Ed.) Springer, Boston, MA, Springer, Boston, MA, Pergamon, New York, 1985, pp. 93-129.

[52] F. Jin, X. Ma, P. Guo, C. Yi, L. Wang, Y. Wang, Q. Yu, J. Sheng, A. Zhang, J. Ji, Y. Tian, K. Liu, Y. Shi, T. Xia, Q. Zhang, Raman scattering study of large magnetoresistance semimetals TaAs2 and NbAs2, Physical Review B, 94 (2016) 094302.

[53] C. Ltd, Cryogen-free Magnet System - User Manual, www.cryogenic.co.uk, January, 2010 (2010).

[54] T. David, I. Molchadsky, A. Somechi, R. Rosenbaum, Novel analog switching circuit for van der Pauw measurements, arXiv e-prints, (2005) cond-mat/0502182.

[55] C. Shekhar, A.K. Nayak, Y. Sun, M. Schmidt, M. Nicklas, I. Leermakers, U. Zeitler, Y. Skourski, J. Wosnitza, Z. Liu, Y. Chen, W. Schnelle, H. Borrmann, Y. Grin, C. Felser, B. Yan, Extremely large magnetoresistance and ultrahigh mobility in the topological Weyl semimetal candidate NbP, Nature Physics, 11 (2015) 645.

[56] S.-M. Huang, S.-Y. Xu, I. Belopolski, C.-C. Lee, G. Chang, B. Wang, N. Alidoust, G. Bian, M. Neupane, C. Zhang, S. Jia, A. Bansil, H. Lin, M.Z. Hasan, A Weyl Fermion semimetal with surface Fermi arcs in the transition metal monopnictide TaAs class, Nature Communications, 6 (2015) 7373.

[57] J. Sun, D.J. Singh, First-principles study of tantalum-arsenic binary compounds, Journal of Applied Physics, 121 (2017) 015101.

[58] O. Pavlosiuk, P. Swatek, D. Kaczorowski, P. Wiśniewski, Magnetoresistance in LuBi and YBi semimetals due to nearly perfect carrier compensation, Physical Review B, 97 (2018) 235132.

[59] M.N. Ali, J. Xiong, S. Flynn, J. Tao, Q.D. Gibson, L.M. Schoop, T. Liang, N. Haldolaarachchige, M. Hirschberger, N.P. Ong, R.J. Cava, Large, non-saturating magnetoresistance in WTe2, Nature, 514 (2014) 205.

[60] K.E. Tan, A.M. Bratkovsky, R.M. Harris, A.P. Horsfield, D. Nguyen-Manh, D.G. Pettifor, A.P. Sutton, Carbon vacancies in titanium carbide, Modelling and Simulation in Materials Science and Engineering, 6 (1998) 335.

[61] P.S. Dobal, R.S. Katiyar, Y. Jiang, R. Guo, A.S. Bhalla, Raman scattering study of a phase transition in tantalum pentoxide, Journal of Raman Spectroscopy, 31 (2000) 1061-1065.

[62] T.A. Butcher, J. Hornung, T. Förster, M. Uhlarz, J. Klotz, I. Sheikin, J. Wosnitza, D. Kaczorowski, Fermi surface investigation of the semimetal TaAs2, Physical Review B, 99 (2019) 245112.

[63] R. Jha, S. Onishi, R. Higashinaka, T.D. Matsuda, R.A. Ribeiro, Y. Aoki, Anisotropy in the electronic transport properties of Weyl semimetal WTe2 single crystals, AIP Advances, 8 (2018) 101332.

[64] S. Shanshan, W. Qi, G. Peng-Jie, L. Kai, L. Hechang, Large magnetoresistance in LaBi: origin of field-induced resistivity upturn and plateau in compensated semimetals, New Journal of Physics, 18 (2016) 082002.

[65] L. Guo, Y.-K. Liu, G.-Y. Gao, Y.-Y. Huang, H. Gao, L. Chen, W. Zhao, W. Ren, S.-Y. Li, X.-G. Li, S. Dong, R.-K. Zheng, Extreme magnetoresistance and SdH oscillation in compensated semimetals of NbSb2 single crystals, Journal of Applied Physics, 123 (2018) 155103.

[66] H.D. Drew, U. Strom, Electron Relaxation Rates in Bismuth at Microwave and Far-Infrared Frequencies, Physical Review Letters, 25 (1970) 1755-1758.

[67] W. Gao, N. Hao, F.-W. Zheng, W. Ning, M. Wu, X. Zhu, G. Zheng, J. Zhang, J. Lu, H. Zhang, C. Xi, J. Yang, H. Du, P. Zhang, Y. Zhang, M. Tian, Extremely Large Magnetoresistance in a Topological Semimetal Candidate Pyrite PtBi2, Physical Review Letters, 118 (2017) 256601.

[68] X. Huang, L. Zhao, Y. Long, P. Wang, D. Chen, Z. Yang, H. Liang, M. Xue, H. Weng, Z. Fang, X. Dai, G. Chen, Observation of the Chiral-Anomaly-Induced Negative Magnetoresistance in 3D Weyl Semimetal TaAs, Physical Review X, 5 (2015) 031023.

[69] Y. Kopelevich, J.C.M. Pantoja, R.R. da Silva, S. Moehlecke, Universal magnetic-field-driven metal-insulator-metal transformations in graphite and bismuth, Physical Review B, 73 (2006) 165128.

[70] Y. Luo, H. Li, Y.M. Dai, H. Miao, Y.G. Shi, H. Ding, A.J. Taylor, D.A. Yarotski, R.P. Prasankumar, J.D. Thompson, Hall effect in the extremely large magnetoresistance semimetal WTe2, Applied Physics Letters, 107 (2015) 182411.

[71] F. Fallah Tafti, Q. Gibson, S. Kushwaha, J.W. Krizan, N. Haldolaarachchige, R.J. Cava, Temperature−field phase diagram of extreme magnetoresistance, Proceedings of the National Academy of Sciences, 113 (2016) E3475.

[72] O. Pavlosiuk, P. Swatek, P. Wiśniewski, Giant magnetoresistance, three-dimensional Fermi surface and origin of resistivity plateau in YSb semimetal, Scientific Reports, 6 (2016) 38691.

[73] Z. Wang, Y. Li, Y. Lu, Z. Shen, F. Sheng, C. Feng, Y. Zheng, Z. Xu, Topological phase transition induced extreme magnetoresistance in TaSb2, eprint arXiv:1603.01717, (2016) arXiv:1603.01717.

[74] R.H. McKenzie, J.S. Qualls, S.Y. Han, J.S. Brooks, Violation of Kohler's rule by the magnetoresistance of a quasi-two-dimensional organic metal, Physical Review B, 57 (1998) 11854-11857.

[75] J. Sun, Y.-A. Soh, J. Kosel, Geometric factors in the magnetoresistance of n-doped InAs epilayers, Journal of Applied Physics, 114 (2013) 203908.

[76] K. Böning, H.J. Fenzl, E. Olympios, J.M. Welter, H. Wenzl, The kohler rule of magnetoresistance in neutron-irradiated aluminium at 4.6°K, physica status solidi (b), 34 (1969) 395-401.

[77] J.M. Harris, Y.F. Yan, P. Matl, N.P. Ong, P.W. Anderson, T. Kimura, K. Kitazawa, Violation of Kohler's Rule in the Normal-State Magnetoresistance of YBa_2Cu_3O_7-delta and La2SrCuO4, Physical Review Letters, 75 (1995) 1391-1394.

[78] Sudesh, P. Kumar, P. Neha, T. Das, S. Patnaik, Evidence for trivial Berry phase and absence of chiral anomaly in semimetal NbP, Scientific Reports, 7 (2017) 46062.

[79] H. Ehrenreich, F. Spaepen, Solid State Physics, Elsevier Science, 2001.

[80] P. Cheng, H. Yang, Y. Jia, L. Fang, X. Zhu, G. Mu, H.-H. Wen, Hall effect and magnetoresistance in single crystals of NdFeAsO_1-xF_xx=0 and 0.18, Physical Review B, 78 (2008) 134508.

[81] I.L. Spain, R.O. Dillon, Kohler's rule and other scaling relationships for the magnetoresistance of graphite, Carbon, 14 (1976) 23-26.

[82] A. Laboratory, Old rules apply in explaining extremely large magnetoresistance, ScienceDaily -, (2017).

[83] N. Ghosh, A. Bharathi, A.T. Satya, S. Sharma, A. Mani, R.M. Sarguna, D. Sornadurai, V.S. Sastry, C.S. Sundar, Kohler’s rule in Ba1−xKxFe2As2, Solid State Communications, 150 (2010) 1940-1943.

[84] N. Kumar, C. Shekhar, S.-C. Wu, I. Leermakers, O. Young, U. Zeitler, B. Yan, C. Felser, Observation of pseudo-two-dimensional electron transport in the rock salt-type topological semimetal LaBi, Physical Review B, 93 (2016) 241106.

[85] O. Pavlosiuk, M. Kleinert, P. Swatek, D. Kaczorowski, P. Wiśniewski, Fermi surface topology and magnetotransport in semimetallic LuSb, Scientific Reports, 7 (2017) 12822.

[86] A.A. Abrikosov, Quantum magnetoresistance, Physical Review B, 58 (1998) 2788-2794.

[87] P.S. Alekseev, A.P. Dmitriev, I.V. Gornyi, V.Y. Kachorovskii, B.N. Narozhny, M. Schütt, M. Titov, Magnetoresistance of compensated semimetals in confined geometries, Physical Review B, 95 (2017) 165410.

[88] J.R. Meyer, C.A. Hoffman, F.J. Bartoli, D.A. Arnold, S. Sivananthan, J.P. Fauri, Methods for magnetotransport characterization of IR detector materials, Semiconductor Science and Technology, 8 (1993) 805.

[89] C.M. Hurd, The Hall effect in metals and alloys, Plenum Press, London, 1972.

[90] G. Peramaiyan, R. Sankar, I.P. Muthuselvam, W.-L. Lee, Anisotropic magnetotransport and extremely large magnetoresistance in NbAs2 single crystals, Scientific Reports, 8 (2018) 6414.

[91] M. Andersson, M. Feuerbacher, Ö. Rapp, Magnetoresistance and Hall effect of the complex metal alloy Mg2Al3, Physical Review B. Condensed Matter and Materials Physics, 78 (2008).

[92] A.A. Burkov, Negative longitudinal magnetoresistance in Dirac and Weyl metals, Physical Review B, 91 (2015) 245157.

[93] R.D.d. Reis, M.O. Ajeesh, N. Kumar, F. Arnold, C. Shekhar, M. Naumann, M. Schmidt, M. Nicklas, E. Hassinger, On the search for the chiral anomaly in Weyl semimetals: the negative longitudinal magnetoresistance, New Journal of Physics, 18 (2016) 085006.

[94] A. Pariari, R. Singha, S. Roy, B. Satpati, P. Mandal, Anisotropic transverse magnetoresistance and Fermi surface in TaSb2, Scientific Reports, 8 (2018) 10527.

[95] X.-Y. Liu, J.-L. Wang, W. You, T.-T. Wang, H.-Y. Yang, W.-H. Jiao, H.-Y. Mao, L. Zhang, J. Cheng, Y.-K. Li, Anisotropic Magnetoresistivity in Semimetal TaSb 2, Chinese Physics Letters, 34 (2017) 127501.

[96] B. Wan, F. Schindler, K. Wang, K. Wu, X. Wan, T. Neupert, H.-Z. Lu, Theory for the negative longitudinal magnetoresistance in the quantum limit of Kramers Weyl semimetals, Journal of Physics: Condensed Matter, 30 (2018) 505501.

[97] H.K. Pal, D.L. Maslov, Necessary and sufficient condition for longitudinal magnetoresistance, Physical Review B, 81 (2010) 214438.

[98] F. Hulliger, New Representatives of the NbAs2 and ZrAs2 Structures, Nature, 204 (1964) 775-775.

[99] W. Bensch, W. Heid, NbAs2, Acta Crystallographica Section C, 51 (1995) 2205-2207.

[100] Y. Shao, Z. Sun, Y. Wang, C. Xu, R. Sankar, A.J. Breindel, C. Cao, M.M. Fogler, A.J. Millis, F. Chou, Z. Li, T. Timusk, M.B. Maple, D.N. Basov, Optical signatures of Dirac nodal lines in NbAs2, Proceedings of the National Academy of Sciences, 116 (2019) 1168.

[101] V. Harimohan, A. Bharathi, P.D. Babu, R. Rajaraman, C.S. Sundar, A clue to the large magneto-resistance in the NbAs2 semimetal, AIP Conference Proceedings, 2265 (2020) 030428.

[102] J. Hu, Z. Tang, J. Liu, X. Liu, Y. Zhu, D. Graf, K. Myhro, S. Tran, C.N. Lau, J. Wei, Z. Mao, Evidence of Topological Nodal-Line Fermions in ZrSiSe and ZrSiTe, Physical Review Letters, 117 (2016) 016602.

[103] N. Kumar, Y. Sun, N. Xu, K. Manna, M. Yao, V. Süss, I. Leermakers, O. Young, T. Förster, M. Schmidt, H. Borrmann, B. Yan, U. Zeitler, M. Shi, C. Felser, C. Shekhar, Extremely high magnetoresistance and conductivity in the type-II Weyl semimetals WP2 and MoP2, Nature Communications, 8 (2017) 1642.

[104] S. Zhang, Q. Wu, Y. Liu, O.V. Yazyev, Magnetoresistance from Fermi surface topology, Physical Review B, 99 (2019) 035142.

[105] A.C. Niemann, J. Gooth, S.-C. Wu, S. Bäßler, P. Sergelius, R. Hühne, B. Rellinghaus, C. Shekhar, V. Süß, M. Schmidt, C. Felser, B. Yan, K. Nielsch, Chiral magnetoresistance in the Weyl semimetal NbP, Scientific Reports, 7 (2017) 43394.

[106] L.R. Thoutam, Y.L. Wang, Z.L. Xiao, S. Das, A. Luican-Mayer, R. Divan, G.W. Crabtree, W.K. Kwok, Temperature-Dependent Three-Dimensional Anisotropy of the Magnetoresistance in WTe2, Physical Review Letters, 115 (2015) 046602.

[107] P. Hosur, S.A. Parameswaran, A. Vishwanath, Charge Transport in Weyl Semimetals, Physical Review Letters, 108 (2012) 046602.

[108] J. Wang, H. Yang, L. Ding, W. You, C. Xi, J. Cheng, Z. Shi, C. Cao, Y. Luo, Z. Zhu, J. Dai, M. Tian, Y. Li, Angle-dependent magnetoresistance and its implications for Lifshitz transition in W2As3, npj Quantum Materials, 4 (2019) 58.

[109] H. Pfau, R. Daou, S. Lausberg, H.R. Naren, M. Brando, S. Friedemann, S. Wirth, T. Westerkamp, U. Stockert, P. Gegenwart, C. Krellner, C. Geibel, G. Zwicknagl, F. Steglich, Interplay between Kondo Suppression and Lifshitz Transitions in YbRh2Si2 at High Magnetic Fields, Physical Review Letters, 110 (2013) 256403.

[110] I. Pletikosić, M.N. Ali, A.V. Fedorov, R.J. Cava, T. Valla, Electronic Structure Basis for the Extraordinary Magnetoresistance in WTe2, Physical Review Letters, 113 (2014) 216601.

[111] D. Schoenberg, Magnetic Oscillations in Metals, Cambridge University Press, Cambridge, 2009.

[112] I.M. Lifshitz, A.M. Kosevich, Theory of magnetic susceptibility in metals at low temperatures, Sov. Phys. JETP, 2 (1956) 636-645.

[113] A. Pariari, P. Dutta, P. Mandal, Probing the Fermi surface of three-dimensional Dirac semimetal Cd3As2through the de Haas--van Alphen technique, Physical Review B, 91 (2015) 155139.

[114] J. Klotz, S.-C. Wu, C. Shekhar, Y. Sun, M. Schmidt, M. Nicklas, M. Baenitz, M. Uhlarz, J. Wosnitza, C. Felser, B. Yan, Quantum oscillations and the Fermi surface topology of the Weyl semimetal NbP, Physical Review B, 93 (2016) 121105.

[115] F. Arnold, C. Shekhar, S.-C. Wu, Y. Sun, R.D. dos Reis, N. Kumar, M. Naumann, M.O. Ajeesh, M. Schmidt, A.G. Grushin, J.H. Bardarson, M. Baenitz, D. Sokolov, H. Borrmann, M. Nicklas, C. Felser, E. Hassinger, B. Yan, Negative magnetoresistance without well-defined chirality in the Weyl semimetal TaP, Nature Communications, 7 (2016) 11615.

[116] X. Rao, X. Zhao, X.Y. Wang, H.L. Che, L.G. Chu, G. Hussain, T.L. Xia, X.F. Sun, Quantum oscillation of thermal conductivity and violation of Weidemann-Franz law in TaAs2 and NbAs2, arXiv e-prints, (2019) https://arxiv.org/abs/1906.03961.

[117] Y. Shao, Z. Sun, Y. Wang, C. Xu, R. Sankar, A.J. Breindel, C. Cao, M.M. Fogler, A.J. Millis, F. Chou, Z. Li, T. Timusk, M.B. Maple, D.N. Basov, Optical signatures of Dirac nodal lines in NbAs<sub>2</sub&gt, Proceedings of the National Academy of Sciences, 116 (2019) 1168.

[118] R. Singha, B. Satpati, P. Mandal, Fermi surface topology and signature of surface Dirac nodes in LaBi, Scientific reports, 7 (2017) 6321-6321.

[119] S. Onishi, R. Jha, A. Miyake, R. Higashinaka, T.D. Matsuda, M. Tokunaga, Y. Aoki, Deviation from the Kohler's rule and Shubnikov–de Haas oscillations in type-II Weyl semimetal WTe2: High magnetic field study up to 56 T, AIP Advances, 8 (2018) 101330.

[120] F. Fei, X. Bo, R. Wang, B. Wu, J. Jiang, D. Fu, M. Gao, H. Zheng, Y. Chen, X. Wang, H. Bu, F. Song, X. Wan, B. Wang, G. Wang, Nontrivial Berry phase and type-II Dirac transport in the layered material PdTe2, Physical Review B, 96 (2017) 041201.

[121] Y. Luo, N.J. Ghimire, M. Wartenbe, H. Choi, M. Neupane, R.D. McDonald, E.D. Bauer, J. Zhu, J.D. Thompson, F. Ronning, Electron-hole compensation effect between topologically trivial electrons and nontrivial holes in NbAs, Physical Review B, 92 (2015) 205134.

[122] Y. Ando, Topological Insulator Materials, Journal of the Physical Society of Japan, 82 (2013) 102001.

[123] J.W. McClure, Diamagnetism of Graphite, Physical Review, 104 (1956) 666-671.

[124] F.A. Buot, J.W. McClure, Theory of Diamagnetism of Bismuth, Physical Review B, 6 (1972) 4525-4533.

[125] H. Intan Fatimah, Theory of magnetic response in nodal semimetals, in: Department of Physics, Graduate School of Science Tohoku University, 2018.

[126] Y. Fuseya, M. Ogata, H. Fukuyama, Transport Properties and Diamagnetism of Dirac Electrons in Bismuth, Journal of the Physical Society of Japan, 84 (2014) 012001.

[127] M. Koshino, I.F. Hizbullah, Magnetic susceptibility in three-dimensional nodal semimetals, Physical Review B, 93 (2016) 045201.

[128] M. Koshino, T. Ando, Anomalous orbital magnetism in Dirac-electron systems: Role of pseudospin paramagnetism, Physical Review B, 81 (2010) 195431.

Thesis Highlights

Name of the Student: Harimohan V
Name of CI: IGCAR, Kalpakkam Enrolment No.: PHYS 02 2014 04 010
Thesis Title: Magneto-transport Studies on the Single Crystals of $TaAs_2$ and $NbAs_2$ Semimetals
Discipline: Physical Sciences Sub-Area of Discipline: Condensed Matter Physics/Material Science
Date of viva-voce: 13/04/2021

The thesis work is aimed at understanding the magneto-transport phenomena in di-pnictides, $TaAs_2$ and $NbAs_2$. Experiments have been carried out in Raman characterized pristine, heat treated and low energy (Ar^+ ion) irradiated single crystals, the later with a view to affect the surface states and alter the mobility.

The temperature variation of resistance in semimetals $TaAs_2$ and $NbAs_2$ under applied magnetic fields shows the characteristic resistivity minima and plateaus at very low temperatures. We have rationalized the observed magneto-resistance (MR) behaviour using the semi-classical Kohler's rule, thereby ruling out a field induced metal to insulator behaviour. Field variation of MR exhibited non-saturating and parabolic growth, reaching ~10^5 % at 3 K with 15 T that also could be scaled with Kohler's rule as shown in Fig.1.

The angle dependent measurements did not show negative MR, a characteristic of Weyl semimetals, including in the longitudinal configuration where the electric and magnetic fields are parallel (See Fig.2). Angular variation of MR at fixed field and temperature exhibited dipolar behaviour. This has been verified over wide intervals of temperature and magnetic fields which indicates that the di-pnictides retains the centro-symmetric crystal structure. This helped us to negate a probable electronic structure change in the material brought about by a possible temperature or field induced Liftshitz transition.

Hall resistance measurements in $TaAs_2$ and $NbAs_2$ indicated the role of multi-carrier transport with electrons and holes. The temperature dependence of MR was found to follow the corresponding variation of carrier mobility (See Fig.3) that points to the fact that the source of the extremely large MR in these semimetals is strongly linked with the charge carrier mobility.

The isothermal MR and magnetization measurements at low temperatures respectively displayed spectacular Shubnikov-de Haas and de Haas-van Alphen (dHvA) oscillations (See Fig.4). Important transport parameters have been estimated from the analysis of dHvA oscillations based on the Liftshitz-Kosevich formalism. The Landau Level-fan diagram indicated a trivial Berry phase which suggests that $TaAs_2$ and $NbAs_2$ are not topological semimetals.

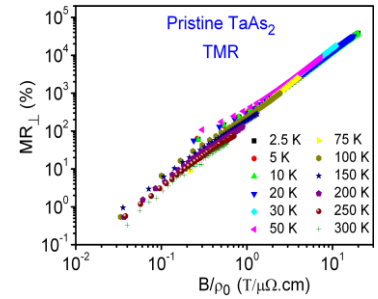

Figure 1. MR of $TaAs_2$ measured at various fixed temperatures collapse onto a single line, validating Kohler's scaling rule.

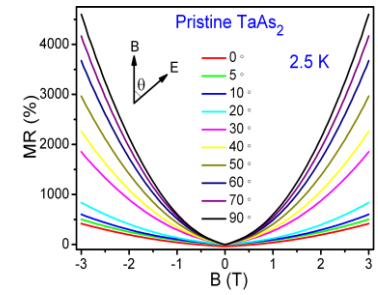

Figure 2. Field dependent MR in $TaAs_2$ at various angles between electric & magnetic fields.

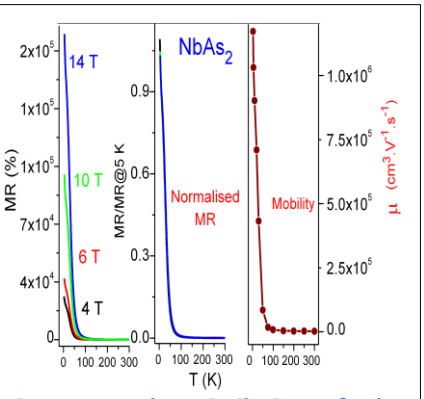

Figure 3. The similarity of the temperature dependence of normalized MR with mobility from Hall measurements in $NbAs_2$.

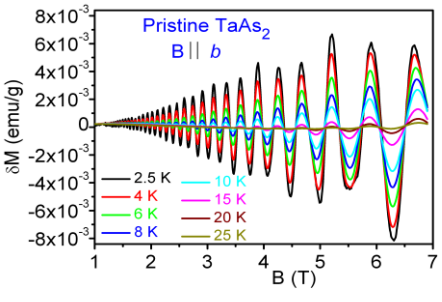

Figure 4. The de Haas - van Alphen oscillations in $TaAs_2$ after removing the diamagnetic background.